Studies of Time Projection Chambers using micro-pattern detectors for the DUNE experiment

Pierre Granger

▶ To cite this version:

Pierre Granger. Studies of Time Projection Chambers using micro-pattern detectors for the DUNE experiment. High Energy Physics - Experiment [hep-ex]. Université Paris-Saclay, 2022. English. NNT : 2022UPASP058 . tel-03771338

HAL Id: tel-03771338
https://theses.hal.science/tel-03771338

Submitted on 7 Sep 2022

Studies of Time Projection Chambers using micro-pattern detectors for the DUNE experiment

Etudes de Chambres à Projections Temporelles utilisant des détecteurs à micro-structures pour l'expérience DUNE

Thèse de doctorat de l'université Paris-Saclay

École doctorale n° 576, Particules, hadrons, énergie et noyau :
instrumentation, imagerie, cosmos et simulation (PHENIICS)
Spécialité de doctorat: physique des particules
Graduate School : Physique, Référent: Faculté des sciences d'Orsay

Thèse préparée dans l'unité de recherche
Département de Physique des Particules (Université Paris-Saclay, CEA),
sous la direction de **Sara BOLOGNESI**, ingénieure-chercheuse au CEA

Thèse soutenue à Paris-Saclay, le 27 juin 2022, par

Pierre GRANGER

Composition du jury

Alessandra TONAZZO Professeure, Université Paris Cité	Présidente
Olivier DRAPIER Directeur de recherche, Laboratoire Leprince-Ringuet	Rapporteur & Examinateur
Claudio GIGANTI Chargé de recherche, HDR, Laboratoire de physique nucléaire et de hautes énergies	Rapporteur & Examinateur
Justyna LAGODA Professeure associée, National Centre for Nuclear Research	Examinatrice
Boris TUCHMING Ingénieur-chercheur, HDR, Université Paris-Saclay, CEA IRFU	Examinateur
Sara BOLOGNESI Ingénieure-chercheuse, HDR, Université Paris-Saclay, CEA IRFU	Directrice de thèse

THESE DE DOCTORAT

NNT : 2022UPASP058

université
PARIS-SACLAY

ÉCOLE DOCTORALE
Particules, hadrons, énergie et noyau :
instrumentation, imagerie, cosmos
et simulation (PHENIICS)

Titre: Etudes de Chambres à Projections Temporelles utilisant des détecteurs à micro-structures pour l'expérience DUNE

Mots clés: Oscillations des neutrinos, TPC à argon liquide, Détecteurs à micro-structures

Résumé: La découverte des oscillations de neutrinos a permis de mettre en évidence le fait que les neutrinos possèdent une masse, ce qui n'est actuellement pas expliqué par le Modèle Standard. Les futures expériences d'oscillations de neutrinos vont se concentrer principalement sur la mesure de la hiérarchie de masse des neutrinos ainsi que sur la possible découverte de la violation de CP dans le secteur leptonique. L'expérience DUNE qui est traitée dans cette thèse se propose notamment de mesurer ces deux paramètres. Plusieurs solutions technologiques à base de TPCs pour l'expérience DUNE sont discutées dans cette thèse. L'opération d'un prototype de TPC double-phase, protoDUNE-DP, y est décrite ainsi que l'analyse de ses données afin de caractériser la stabilité et les performances de cette nouvelle technologie à grande échelle. En outre, l'étude d'un design pour un détecteur proche de DUNE, SAND, mettant en jeu des TPCs instrumentées avec des MicroMegas résistifs ainsi qu'un détecteur scintillant à haute granularité et à lecture 3D. L'adéquation du design des TPCs avec le faisceau de DUNE y est étudiée ainsi que la caractérisation des performances des TPCs à l'aide de simulations numériques. La capacité de détection des neutrons du détecteur scintillant est démontrée, et son impact positif sur la reconstruction de l'énergie des neutrinos est mise en exergue.

Title: Studies of Time Projection Chambers using micro-pattern detectors for the DUNE experiment

Keywords: Neutrino oscillations, Liquid argon TPC, Micro-pattern detectors

Abstract: The discovery of neutrino oscillations highlighted that the neutrinos are massive, which is currently not explained by the Standard Model. Future neutrino oscillation experiments will mainly focus on measuring both the neutrino mass hierarchy and discovering a possible CP violation in the lepton sector. The DUNE experiment, which is treated in this thesis, proposes in particular to measure these two parameters. Several technological solutions based on TPCs for the DUNE experiment are discussed in this thesis. The operation of a dual-phase liquid argon TPC prototype, protoDUNE-DP, is described, as well as, the analysis of its data in order to characterize the stability and performances of this technology at a large scale. In addition, the study of a design for the SAND near detector of DUNE, involving resistive MicroMegas TPCs and a highly granular 3D scintillating detector, is studied. The adequation of the TPCs design with the DUNE beam and their impressive performances are demonstrated through numerical simulations. The neutron detection capabilities of the scintillating detector are established, and their beneficial impact on the neutrino energy reconstruction are highlighted.

Résumé

Les neutrinos forment le deuxième type de particule le plus abondant de l'univers, après les photons. Leur existence n'a néanmoins été découverte que tardivement étant donné leur faible propension à interagir avec la matière qui nous entoure. L'existence du neutrino a été postulée pour la première fois en 1930 par Wolfgang Pauli afin d'expliquer le spectre en énergie des électrons émis par désintégration β. Le neutrino décrit par Pauli (à l'époque appelé neutron avant qu'Enrico Fermi ne découvre le neutron) est une particule neutre, de très faible masse, et de spin 1/2. Il faudra ensuite attendre 30 ans avant la première découverte expérimentale du neutrino par Reines et Cowan via le processus de réaction β inverse dans lequel un antineutrino, émis dans leur expérience par la centrale nucléaire de Savannah River, transmute un proton en neutron avec l'émission conjointe d'un électron.

Cette première détection expérimentale du neutrino par Reines et Cowan ne fut que le début d'une longue série de découvertes. Parmi les découvertes les plus récentes, se trouve l'oscillation des neutrinos entre les 3 saveurs connues au cours de leur propagation. Ces oscillations de neutrinos démontrent la nature massive de ces particules bien que le modèle standard, tel qu'il est actuellement formulé, implique une masse nulle pour les neutrinos. Différents processus sont postulés pour tenter d'expliquer la très faible masse des neutrinos. Mesurer finement les différents paramètres d'oscillation peut permettre de discriminer ces différentes théories. En outre, les probabilités d'oscillations des neutrinos peuvent présenter une asymétrie entre les neutrinos et les antineutrinos, réalisant ainsi une possible violation de la symétrie CP dans le secteur leptonique. Une telle violation de CP pourrait contribuer à expliquer l'asymétrie observée entre matière et antimatière dans l'univers.

Au cours de ma thèse, j'ai étudié différentes propositions de détecteurs pour l'expérience d'étude d'oscillations de neutrinos DUNE. Cette expérience vise à mesurer la valeur de la phase décrivant la violation de CP dans le secteur leptonique, ainsi qu'à établir la hiérarchie de masse des neutrinos. DUNE prendra place aux États-Unis avec la production d'un faisceau de neutrinos à Fermilab et leur détection dans une mine du Dakota du Sud, 1300 km plus loin. DUNE mesurera les paramètres d'oscillation en observant les probabilités d'apparence et de

disparition des différentes saveurs entre un détecteur proche et un détecteur lointain. L'acquisition des premières données est attendue avant 2030. Le détecteur lointain sera composé de 4 modules remplis avec 10 kt d'argon liquide chacun. Plusieurs détecteurs proches seront utilisés afin de mesurer précisément les paramètres de flux et de section efficaces.

La technologie des Chambres à Projection Temporelle (TPC) sera utilisée pour les modules du détecteur lointain et dans certains détecteurs proches. Cette technologie a été pour la première fois introduite par David Nygren en 1974. Dans les TPCs, le milieu de détection est ionisé par le passage de particules chargées. Les électrons d'ionisation sont dérivés vers un plan de lecture via l'application d'un champ électrique. Ces détecteurs permettent ainsi de reconstruire en 3D les trajectoires des particules chargées qui les traversent en utilisant la position mesurée sur le plan de détection ainsi que le temps de dérive. Cette reconstruction en 3D des traces permet d'accéder à la cinématique des interactions. On peut distinguer deux principaux types de TPCs. Tout d'abord les TPC gazeuses qui influent faiblement sur les trajectoires des particules et permettent de mesurer leur cinématique avec précision. L'application d'un champ magnétique parallèle au champ de dérive permet de mesurer l'impulsion des particules en mesurant leur courbure dans le plan transverse à la direction de dérive. Etant donné la faible densité du gaz, les probabilités d'interaction de particules à l'intérieur de la TPC sont faibles, ainsi ces TPCs sont surtout utilisées pour mesurer les trajectoires de particules produites à l'extérieur d'elles. Il existe aussi des TPCs remplies de liquide ce qui permet de les utiliser directement comme cible. Etant donné leur densité plus élevée, l'énergie des particules peut être mesurée par calorimétrie en observant l'énergie déposée dans le liquide.

Au cours de ma thèse, j'ai travaillé sur l'étude du prototype de TPC à argon liquide double phase construit au CERN: ProtoDUNE-DualPhase (PDDP). Le volume actif de PDDP est un cube de 6 m de côté situé dans un cryostat. La technologie de TPC double-phase vise à utiliser une grande masse d'argon liquide comme matériau cible pour les interactions neutrinos ainsi que comme milieu ionisable dans lequel les particules chargées déposent de l'énergie de façon continue. Les électrons d'ionisations produits sont ensuite dérivés par un fort champ électrique vers le sommet de la TPC. L'argon liquide est surmonté d'argon gazeux, d'où l'appellation de TPC double-phase. Les électrons sont extraits depuis le liquide vers le gaz grâce à l'application d'un important champ électrique. Une fois extraits dans le gaz, les électrons peuvent être amplifiés par effet d'avalanche par des dispositifs dédiés, les LEMs, avant d'être lus sur des anodes 2D. La principale force de la technologie double-phase est de pouvoir proposer à la fois une masse active importante via la phase liquide et une amplification du signal via des effets d'avalanche produits dans la phase gazeuse. Plusieurs prototypes de TPC à argon double-phase ont été précédemment testés avec succès mais à plus petite échelle.

PDDP a été construit afin de démontrer la possibilité d'utiliser la technologie double-phase afin d'instrumenter un module du détecteur lointain de DUNE. Pour ce faire, il était nécessaire de montrer que ce type de détecteur peut être opéré de façon stable à grande échelle, et qu'une grande pureté de l'argon liquide ainsi que des gains suffisants peuvent être atteints. En outre, ce prototype permettait de tester les solutions techniques proposées pour l'acheminement de la haute tension ainsi que pour le cryostat. Néanmoins, plusieurs difficultés sont apparues au cours des opérations du détecteur et il n'a pas été possible de démontrer la possibilité d'opérer un détecteur d'une telle taille de façon stable. Un court-circuit au niveau du composant chargé de l'acheminement de la haute tension jusqu'à la cathode a fortement limité le volume actif du détecteur tout en créant de fortes inhomogénéités dans le champ de dérive. Ces éléments ont été très préjudiciables à l'analyse des données du détecteur. Une seconde difficulté rencontrée a été l'instabilité de l'interface entre argon liquide et gazeux notamment causée par la formation de bulles de gaz au sein de l'argon liquide explosant à la surface. Certaines solutions temporaires ont pu être trouvées afin d'obtenir une interface relativement stable durant un certain temps permettant l'acquisition de données. La quantité de données acquise au cours des opérations de PDDP est cependant relativement faible. Des taux de spark inférieurs à 1 par CRP par heure n'ont pu être observés sur les LEMs que pour des champs d'amplification inférieurs ou égaux à 2.9 kV ne permettant pas d'atteindre des gains de l'ordre de 6 qui étaient attendus. Les LEMs avaient cependant pu être opérés précédemment à des champs d'amplification plus élevés avec une plus grande stabilité dans la coldbox qui présentait une surface d'argon liquide parfaitement stable et plane. Cela semble indiquer que la cause principale des instabilités des LEMs observées provient de l'instabilité des conditions cryogéniques au sein du détecteur.

Les données collectées m'ont permis de conduire de multiples analyses malgré les difficultés évoquées précédemment. Néanmoins, aucune calibration de l'électronique n'a été réalisée au sein du détecteur ce qui a compliqué l'interprétation des résultats. L'analyse des traces de muons atmosphériques m'a permis de mesurer le temps de vie des électrons dans la TPCs. Ces mesures ont permis de démontrer que l'argon liquide a pu être purifié jusqu'à obtenir un temps de vie des électrons supérieur à 3 ms, valeur requise pour opérer un détecteur lointain de DUNE. L'analyse des traces a aussi permis de caractériser les gains des LEMs en fonction du champ d'amplification. Cette analyse a mis en évidence une inhomogénéité des gains entre les différents LEMs qui a pu être expliquée par des différences d'épaisseur.

Etant donné les instabilités mises en évidence au cours des opérations de PDDP, la collaboration DUNE a pris la décision de considérer un design alternatif à PDDP: le Vertical-Drift. Ce nouveau design propose d'effectuer la lecture de charge directement dans l'argon liquide en retirant l'étage d'amplification qui était présent dans le gas. Il n'y a ainsi plus de problèmes d'instabilité de l'interface liquide-gaz étant donné que le détecteur n'opère que dans l'argon liquide. Néanmoins le gain en stabilité obtenu sera au détriment de l'amplification du signal qui était possible dans le design double phase.

Une seconde partie de mon travail de thèse a été réalisée sur l'étude d'une proposition de design pour un détecteur proche de DUNE: SAND. Ce détecteur proche aura un rôle essentiel dans l'analyse d'oscillation que réalisera DUNE. En effet, SAND fournira une mesure très précise du flux de neutrinos et antineutrinos émis par le faisceau. SAND sera en outre capable de détecter les variations de flux au cours du temps. Le design sur lequel j'ai travaillé proposait de s'inspirer très fortement des développements réalisés pour l'amélioration du détecteur proche de T2K : ND280. En effet, il était proposé de réutiliser les mêmes technologies afin de bénéficier de toute la recherche et des développements déjà réalisés pour T2K. Cette proposition de design impliquait les sous-détecteurs suivants placés dans un solénoïde fournissant un champ magnétique :

- un calorimètre électromagnétique (réutilisé de l'expérience KLOE) ;
- un détecteur scintillant à haute granularité, le 3DST ;
- trois TPCs instrumentées avec des MicroMegas résistifs.

Le 3DST est un détecteur composé de cubes scintillants d'1 cm de côté lus dans les trois directions de l'espace par des fibres scintillantes. Ce détecteur propose une masse importante qui lui permet de servir de cible pour l'interaction des neutrinos. Les différentes particules chargées peuvent ensuite être détectées et leurs trajectoires reconstruites en 3D grâce à l'importante granularité du détecteur. Le 3DST est entouré par trois TPCs qui permettent de mesurer précisément l'impulsion des particules chargées qui quittent le 3DST, en observant la courbure des traces dans le champ magnétique, ainsi que d'identifier les différents types de particules. L'utilisation de MicroMegas résistifs afin de faire la lecture de charge dans les TPCs permet d'améliorer la résolution spatiale des traces en étalant la charge sur plusieurs cellules, ce qui permet une meilleure reconstruction de la position de chaque coup.

J'ai développé une simulation des TPCs afin d'évaluer leurs performances dans le contexte de SAND. J'ai pu démontrer que le design proposé devrait permettre d'atteindre des performances largement supérieures à celles requises pour l'opération de SAND, notamment en ce qui concerne la résolution en impulsion. J'ai aussi pu démontrer la nécessité d'avoir une bonne connaissance du champ magnétique du solénoïde afin de pouvoir tirer les meilleures performances du détecteur. En effet, le champ magnétique produit par l'électro-aimant de KLOE est relativement inhomogène, notamment aux bords de l'aimant. J'ai ainsi pu développer une reconstruction prenant en compte ces effets d'inhomogénéité de champ magnétique. J'ai également travaillé avec des simulations de 3DST afin d'évaluer les capacités de ce détecteur à détecter les neutrons produits par les interactions avec des antineutrinos. Les neutrons sont typiquement complexes à détecter étant des particules neutres ne déposant pas d'énergie par ionisation. Ils déposent de l'énergie de façon sporadique dans le détecteur via des interactions de recul de proton notamment. Ainsi, le design hautement granulaire du 3DST permet de détecter les interactions des neutrons comme des clusters isolés. La détection de ces clusters isolés permet de calculer le temps de vol et la distance parcourue par les électrons, et par ce biais donne accès à leur énergie. J'ai pu démontrer avec mon travail que la détection des neutrons dans le 3DST permet d'améliorer de façon significative la reconstruction de l'énergie des antineutrinos. De plus, cela donne accès à une information cinématique supplémentaire qui peut permettre de sélectionner des événements pour lesquels les effets nucléaires lors de l'interaction sont les plus faibles. Il faut noter que la détection directe des neutrons émis par l'interaction des antineutrinos dans le détecteur est une révolution permettant de s'affranchir d'estimations dépendantes de modèles spécifiques. En effet, l'estimation de l'énergie de ces neutrons est la seconde incertitude la plus élevée dans l'expérience d'oscillation NOνA. Bien que le design proposé possède toutes les qualités requises pour pouvoir être implémenté dans SAND, des raisons politiques ont amené au choix d'un design alternatif. Tout le travail effectué sur ce projet n'a cependant pas été vain. En effet, un design extrêmement similaire est en cours d'installation au détecteur proche de T2K, ND280. Ainsi les études réalisées pourront servir aux analyses futures qui seront réalisées par la collaboration T2K. En outre, l'analyse sur les capacités de détection des neutrons d'un détecteur tel que 3DST démontre que ce type de détecteur scintillant hautement granulaire pourra être utilisé avantageusement par de futures expériences.

Malgré les choix spécifiques faits par la collaboration DUNE, j'ai pu démontrer au cours de ma thèse le rôle inestimable que les TPCs continueront de jouer dans les expériences de mesures d'oscillation de neutrinos d'accélérateurs. Ce type d'expérience ainsi que la technologie des TPCs ont tous deux un futur prometteur et l'étude de solutions innovantes, telles que la TPC à argon double-phase ou les Micromegas résistifs, est cruciale afin de façonner un tel avenir pour la discipline.

Contents

List of Figures

List of Tables

Introduction

Despite being the second most abondant particle in the universe, after the photon, the existence of the neutrino was only postulated in 1930 by Wolfgang Pauli to explain the continuous energy spectrum of the beta decay electron. The scientific community had to wait for 30 years more before the experimental discovery of neutrino by Reines and Cowan. Several additional discoveries followed, among which the existence of neutrinos and anti-neutrinos, both existing in three different flavours related to the three lepton families. The neutrino sole sensitivity to the weak interaction, coped with its extremely low mass, make its experimental detection particularly difficult. In the Standard Model, that has until now proven to be the most accurate description of particle physics, the neutrino is massless. However the SuperKamiokande and SNO experiments clearly demonstrated, more than 20 years ago, that the neutrinos could oscillate between different flavour states during their propagation. This observation is only compatible with the existence of neutrino mass states, different from the flavour states, with non-degenerate masses. This is a striking observed deviation from the Standard Model, and therefore one of the most scrutinized field in the search for physics beyond the standard model.

The different neutrino flavours are mixed by three mixing angles θ_{12}, θ_{13}, θ_{23} that have all been measured with different precisions (13.8 $\%$, 8.8 $\%$ and 21 $\%$ respectively considering the 3 σ intervals). The absolute square mass differences between the three mass states have also been experimentally determined with a certain precison (16.5 $\%$ for Δm^2_{21} and 7.4 $\%$ for Δm^2_{32} considering the 3 σ intervals). However two main unknowns remain: the value of the CP violating phase (δ_{CP}) and the neutrino mass ordering. The existence of CP-violation in the lepton sector could be connected to the matter-antimatter asymmetry we observe in the universe. The determination of the mass ordering would dismiss some beyond the standard model theories and limit the range of possible values for specific processes, such as the neutrinoless double beta decay.

Both the mass ordering and the value of δ_{CP} can be determined in long baseline oscillation neutrino experiments featuring intense neutrino beams. The comparison of the neutrino flux near the emission point measured with "near-detectors" with the oscillated flux at a "far detector" allows to estimate the oscillation parameters.

The DUNE experiment that is expected to start taking data before 2030 aims at measuring both the mass ordering and δ_{CP}. This will be accomplished by measuring the electron (anti)neutrino apparition probability in a muon (anti)neutrino dominated beam between a near detector complex at Fermilab and a far detector complex, 1300 km further away, composed of 4 modules of 10 kt each. The neutrino oscillation is an energy-dependant phenomenon, and precisely measuring the probability of ν_μ disappearance versus the energy will allow high-precision measurements of Δm^2_{32} and θ_{23}. A short history of neutrino physics, as well as, a short description of neutrino oscillation theory and of the experimental measurements of neutrino oscillations are presented in the first chapter of this thesis. The DUNE experiment is described in the same chapter together with examples of other next-generation neutrino experiments.

The realisation of these measurements will be very challenging and DUNE will rely on relatively new technologies to achieve its physics program. Among the technological innovations of DUNE, there is the use of Liquid Argon TPCs (LArTPCs) for the far detectors. The second chapter of this thesis therefore proposes an overview of the physics of Time Projection Chambers in order to introduce the technology that was at the heart of my thesis work. A short history of this technology is presented before focusing on the different physical processes involved from the ionization of the detector medium by a charge particle to the formation of an electronic signal.

Two large scale prototypes have been built at CERN to evaluate the performances of two different LArTPC technologies: ProtoDUNE-SinglePhase and ProtoDUNE-DualPhase. ProtoDUNE-SinglePhase is relying on a new implementation of a technology already tested in ICARUS and MiniBoone. The dual-phase technology is more innovative and has never been tested at such scales. It relies on the use of LAr as a ionization medium while allowing for the amplification of the electrons in a topping gaseous Argon phase, after extraction of the electrons, thus providing higher gains but at the cost of a higher complexity. Moreover, a dual-phase detector allows to use a single large fiducial volume, is easier to build and provides accessibility to the electronics located at the top of the detector. My work to characterize the performances of protoDUNE Dual-Phase, as well as, a description of the detector operations are presented in the third chapter.

In order to reach the expected sensitivities in the measurement of the oscillations, DUNE will need to efficiently constrain various systematic uncertainties. This will be achieved with an ambitious near detector complex featuring a liquid argon TPC and a high pressure gaseous argon TPC, able to move together at different off-axis angles, and an on-axis detector, SAND, responsible for the neutrino flux monitoring. An innovative solution has been proposed as the inner tracker for SAND. The proposed design makes use of the fined grained 3D scintillating technology (3DST detector) and the resistive MicroMegas TPCs chosen to instrument the ND280 near detector of T2K after its upgrade. The 3DST allows for the detection of neutrons from neutrino interactions and thus the impromevent of the neutrino energy resolution, as well as, a uniform efficiency and resolution versus rack angle and a low tracking threshold. The TPCs instrumented with resistive MicroMegas have improved spatial resolution thus improving the measurement of the momentum of charged particles. The last chapter of this thesis describes several physics analyses that I conducted to demonstrate the performance of this SAND design.

Finally a short conclusion closes this thesis.

Chapter 1

Introduction on neutrino physics

This short introduction on neutrino physics provides a short overview on the neutrino discovery and oscillation theory before focusing an experiments for neutrino oscillations. Many neutrino physcics topics such as the neutrinoless double beta decay or the search for sterile neutrinos will not be discussed.

1.1 The discovery of the neutrino

1.1.1 The β decay spectrum problem

β-decays are desintegrations of nuclei into more stable elements by the conversion of a neutron into a proton (and conversely) and the emission of an electron (positron). The characterization of this nuclear effect occured in several steps through time. The radioactivity itself was first discovered in uranium by Hernri Becquerel in 1896 [1] and then studied by Marie Curie on additional elements [2]. Ernest Rutherford showed in 1899 that the radioactive emissions could be separated into two distinct types based on their penetration capabilities: α and β particles [3]. The gamma rays were identified one year later by Paul Villard [4]. By measuring the mass to charge ratio of the β particle, Becquerel found the same value as J.J. Thomson with cathode rays (electron beam observed in discharge tubes), thus hinting that the β particle was the electron [5]. Finally in 1902, Rutherford and Frederick Soddy showed that the radioactivity was associated with the transmutation of elements [6]. With all these previous knowledges and the availability of more data on the different possible radioactive decays, Soddy proposed in 1913 [7] the process known as the β decay:

$$ {}^{\mathrm{N}}_{\mathrm{Z}}\mathrm{X} \rightarrow {}_{\mathrm{Z+1}}{}^{\mathrm{N}}\mathrm{Y} + \mathrm{e}^{-} \tag{1.1} $$

transmutting the nucleus Z into Y via the decay of a neutron into a proton and an electron.

The only detectable particle at the time was the electron and the β decay was, as a consequence, considered to be a 2 body decay, thus implying a constant energy of the emitted electron:

$$ E = \frac{m_X^2 - m_Y^2 + m_e^2}{2m_X} \tag{1.2} $$

with m_X, m_Y, and m_e being the masses of the X nucleus, Y nucleus, and electron respectively.

As soon as 1914, James Chadwick however discovered that the energy of the emitted electron was not fixed and followed a specific energy spectrum [8], as shown in Figure 1.1. This observation was at first rejected by the scientific community but other experiments ended up with the same conclusion. This continuous spectrum of the electron was first explained as a loss of energy of the electron in-between its emission and its detection either by scattering or γ-ray emission. However, this possibility was finally rejected after more careful investigations and the continuous nature of the decay electron spectrum had to be accepted. This discovery led to multiple debates inside the scientific community, some even proposing to discard the conservation of energy principle itself, as this new process didn't seem to conserve energy. In order to save the energy conservation, Wolfgang Pauli proposed, in his famous letter adressed to the *Radioactive Ladies and Gentlemen*, to introduce another particle produced in the β-decay, thus making it a three-body decay and explaining the continuous energy spectrum of the decay electron. He therefore postulated the existence of "electrically neutral particles [...] that have spin 1/2 and obey the exclusion principle" inside the nucleus. This postulated particle was first named neutron before eventually becoming the neutrino after the discovery of a neutral particle inside the nucleus in 1932 by Chadwick [9] that took the name of neutron. In this new three-body framework, Equation 1.1 becomes:

$$ {}^{\mathrm{N}}_{\mathrm{Z}}\mathrm{X} \rightarrow {}_{\mathrm{Z+1}}{}^{\mathrm{N}}\mathrm{Y} + \mathrm{e}^{-} + \nu \tag{1.3} $$

1.1.2 The neutrino discovery

Right after his suggestion for a new particle, Pauli considered that he did a terrible thing by postulating the existence of a particle that could never be detected. Enrico Fermi that formulated in 1933 the theory of the

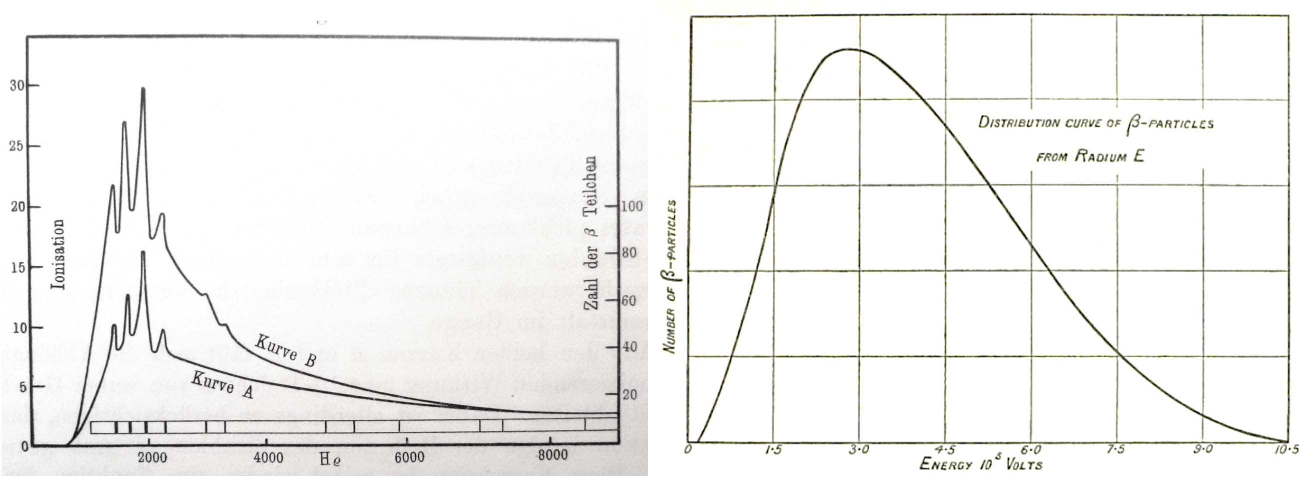

Figure 1.1: First β spectrum measured by James Chadwick in 1914 on radium decay (left) and β spectrum measured by Ellis and Wooster with a radium β-radioactive source in 1927.

β-decay [10], introducing the neutrino in the process, calculated the neutrino's cross-section to be so small that it could travel across the whole Earth without interacting. The possibility to ever detect the neutrino seemed therefore unachievable at the time.

However, what seemed unachievable in the 30's with simple β-decay emitters was made possible more than a decade later with the rise of nuclear reactors proving intense sources ($\sim 10^{20}\,\bar{\nu}_e$ per second) of electron antineutrinos through the fission processes as unstable nuclei undergo β^- decays. The Fermi theory of the β decay implied the existence of its reverse process, the Inverse Beta Decay (IBD) in which the interaction of an antineutrino with a proton creates a positron and a neutron:

$$\bar{\nu} + p \rightarrow \mathrm{e}^+ + \mathrm{n} \tag{1.4}$$

Reines and Cowan set up an experiment near the Savannah River power plant in the United States to detect reactor $\bar{\nu}$ using the IBD process. They built two tanks filled with 200 liters of water in which was dissolved 40 kg of cadmium chloride ($CdCl_2$). Liquid scintillator detectors instrumented with photomultipliers were installed above and below the water tanks. The experimental setup aimed at detecting IBD occuring inside the water tank by measuring delayed coincidences between the e^+ annihilation signal in two 511 keV gammas:

$$e^+ + e^- \rightarrow 2\gamma \tag{1.5}$$

and the capture of the thermalized neutron on a cadmium nucleus leading to the emission of de-excitation gammas:

$$\mathrm{n} + {}^{108}\mathrm{Cd} \rightarrow {}^{109}\mathrm{Cd} + \gamma \tag{1.6}$$

The delay between the e^+ annihilation and the cadmium de-excitation after neutron capture is due to the neutron thermalization and was typically around 5 µs. This setup allowed Reines and Cowan to observe around 3 events per hour, as expected from the predicted IBD cross-section of $6.4 \times 10^{-44}\,\mathrm{cm}^2$, with an excellent signal over noise ratio of 20 [11]. The Nobel Prize in physics was awarded to Reines in 1995 for this first experimental detection of the neutrino.

1.1.3 Additional neutrino flavours

After the experimental discovery of the neutrino by Reines and Cowan, the physicists wondered if the neutrino emitted in the pion decay was of the same nature than the neutrino from the β decay. An answer was brought to this question in 1962 by Lederman, Schwartz and Steinberger that produced the first neutrino beam from pion decay [12]. A proton beam was directed onto a beryllium target leading to the production of pions decaying into neutrinos. A 10 ton spark chamber filled with neon gas was placed on the neutrino beam to detect neutrino interactions. 29 muon events were observed in a few weeks of operation, thus confirming the existence of a second neutrino species coupled to the muon: the muon neutrino. This discovery of a second neutrino flavour was awarded the Nobel Prize in 1988.

After the discovery of the τ lepton at the SLAC e^+e^- collider in 1975 [13], an eventual ν_τ was searched for, given the previously developed theory of flavour symmetry. The ν_τ was discovered by the DONUT experiment, 25 years after the discovery of the τ, at Fermilab. A beam mainly composed of ν_τ was produced by τ decays, themselves produced by the decay of D_S mesons created by the interactions of 800 GeV protons on tungstene. The ν_τ were identified in an emulsion detector by observing their charged-current interactions leading to the production of the τ lepton, whose decays present a characteristic track-kink that could be observed. Four events were observed in agreement with the predicted cross-section, thus acting the ν_τ discovery.

The combined results from the ALEPH, DELPHI, L3 and OPAL experiments at CERN on e^+e^- collisions allow to precisely measure the Z boson resonance. Any additional family of neutrino coupled to the weak interaction will allow for a $Z \rightarrow \nu\bar{\nu}$ invisible decay that will result in a smaller number of visible Z events. Their results are in perfect agreement with the existence of only three neutrino flavors coupling to the weak interaction with a

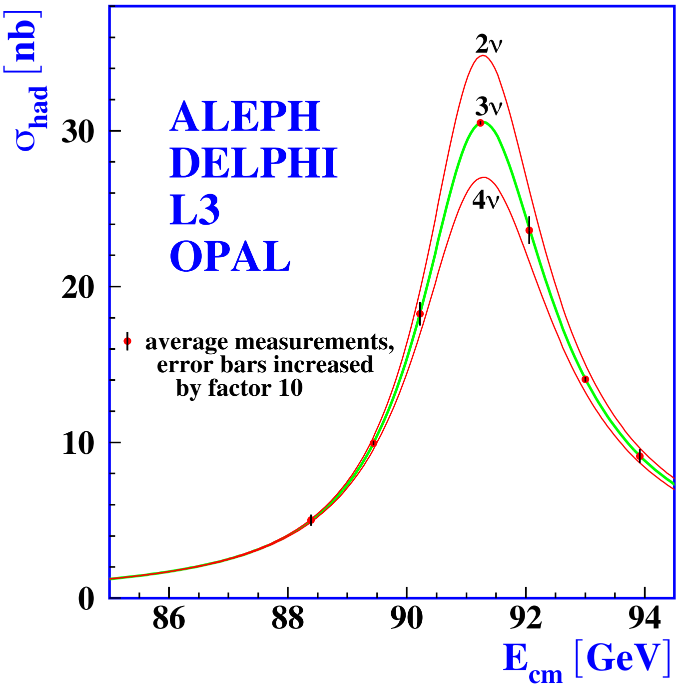

Figure 1.2: ALEPH, DELPHI, L3 and OPAL combined results showing the hadron production cross-section around the Z resonance. (reproduced from [14])

mass below half the mass of the Z, as shown in Figure 1.2, with a number of light neutrinos determined to be $N_\nu = 2.9841(83)$ [14]. This result definitively sets the number of low-mass active neutrinos to three.

1.2 The theory of neutrino oscillations

The idea of neutrino oscillations first appeared in 1957 when Pontecorvo suggested the possibility of neutrino-antineutrino oscillations if the violation of the lepton number was allowed in a similar way as the kaon-antikaon oscillations. The neutrino flavour mixing idea emerged only later, after the discovery of the muon neutrino, in a paper by Maki, Nakagawa and Sakata [15]. After that, the neutrino flavour oscillation was proposed by Pontecorvo in 1967 [16] and described in the formalism that we know today by Gribov and Pontecorvo in 1969 [17].

A lot of experimental evidences of neutrino oscillation have since been shown, as described in the next section, after a brief description of the theory of flavour mixing.

1.2.1 Lepton flavour mixing

Neutrinos can oscillate while propagating in vacuum, without requiring any interaction, by a quantum-mechanical phenomenon made possible by the existence of non-degenerate neutrino masses and lepton flavour mixing. The flavor mixing in the lepton sector arises from the mismatch between the basis of weak gauge eigenstates, governing the neutrino interactions, and the basis of mass eigenstates, governing the neutrino propagation. The neutrino mass matrix is therefore not diagonal when expressed in the flavour basis which correspond to the neutrino weak eigenstates coupling to the associated charged leptons e, μ and τ. The same process occurs in the quark-sector where the free quark eigenstates differ from the quarks weak gauge eigenstates. The flavour eigenstates are related to the mass eigenstates of the left-handed neutrino fields by a unitary matrix, the so-called *lepton mixing matrix* known as the PMNS (Pontecorvo-Maki-Nakagawa-Sakata) matrix, similarly to what is done in the quark sector with the CKM (Cabibbo-Kobayashi-Maskawa) matrix. This gives the following relation:

$$\begin{pmatrix} \nu_e \\ \nu_\mu \\ \nu_\tau \end{pmatrix}_L = \begin{pmatrix} U_{e1} & U_{e2} & U_{e3} \\ U_{\mu 1} & U_{\mu 2} & U_{\mu 3} \\ U_{\tau 1} & U_{\tau 2} & U_{\tau 3} \end{pmatrix}_L \begin{pmatrix} \nu_1 \\ \nu_2 \\ \nu_3 \end{pmatrix}_L \tag{1.7}$$

with ν_1, ν_2, and ν_3 the neutrino mass eigenstates, and, ν_e, ν_μ, and ν_τ the left-handed neutrinos flavour eigenstates.

The PMNS is a unitary matrix as it relates two different basis, thus implying the following unitarity relation:

$$\sum_i U_{\alpha i} U^*_{\beta i} = \delta_{\alpha\beta} \tag{1.8}$$

After accounting for the possible rephasings of the lepton fields, the PMNS matrix U can be parametrized by three mixing angles θ_{12}, θ_{13} and θ_{23}, and, one CP-violating phase. The PMNS matrix can be written as the product of three rotations, one of which depends on the Dirac CP-violating phase δ_{CP}, and a diagonal matrix of phases P including the possible Majorana phases that reduces to the identity matrix in the Dirac case:

$$
\begin{aligned}
U &= \begin{pmatrix} 1 & 0 & 0 \\ 0 & c_{23} & s_{23} \\ 0 & -s_{23} & c_{23} \end{pmatrix} \begin{pmatrix} c_{13} & 0 & s_{13}e^{-i\delta_{\text{CP}}} \\ 0 & 1 & 0 \\ -s_{13} & 0 & c_{13} \end{pmatrix} \begin{pmatrix} c_{13} & s_{12} & 0 \\ -s_{12} & c_{12} & 0 \\ 0 & 0 & 1 \end{pmatrix} P \\
&= \begin{pmatrix} c_{12}c_{13} & s_{12}c_{13} & s_{13}e^{-i\delta_{\text{CP}}} \\ -s_{12}c_{23} - c_{12}s_{13}s_{23}e^{i\delta_{\text{CP}}} & c_{12}c_{23} - s_{12}s_{13}s_{23}e^{i\delta_{\text{CP}}} & c_{13}s_{23} \\ s_{12}s_{23} - c_{12}s_{13}c_{23}e^{i\delta_{\text{CP}}} & -c_{12}s_{23} - s_{12}s_{13}c_{23}e^{i\delta_{\text{CP}}} & c_{13}c_{23} \end{pmatrix} P
\end{aligned}
\tag{1.9}
$$

using the short notations $s_{ij} \equiv \sin\theta_{ij}$ and $c_{ij} \equiv \cos\theta_{ij}$.

1.2.2 Neutrino oscillations in vacuum

An oscillation experiment consists of three different steps: the creation of the neutrino in a specific weak eigenstate which is a coherent superposition of the mass states, the propagation of the different mass states, and finally the weak interaction of the neutrino and the detection of a specific flavour via charged-current interaction.

The produced neutrino is initially in the flavour eigenstate α which is a coherent superposition of the three mass eigenstates with coefficients taken from the PMNS matrix:

$$
\left|\nu(t=0)\right\rangle = |\nu_\alpha\rangle = \sum_i U^*_{\alpha i} |\nu_i\rangle \tag{1.10}
$$

Each mass eigenstate composing $|\nu_\alpha\rangle$ then evolves differently as a plane wave picking up its own phase $e^{i\vec{\mathbf{p}}_\mathbf{i}\cdot\vec{\mathbf{x}}}|\nu_i\rangle$ with $p_i = \sqrt{E^2 - m_i^2}$ supposing an identical energy E for all the mass states.

$$
\left|\nu(\vec{\mathbf{x}})\right\rangle = \sum_i U^*_{\alpha i} e^{i\vec{\mathbf{p}}_\mathbf{i}\cdot\vec{\mathbf{x}}} |\nu_i\rangle = \sum_i U^*_{\alpha i} e^{i\vec{\mathbf{p}}_\mathbf{i}\cdot\vec{\mathbf{x}}} \sum_\beta U_{\beta i} \left|\nu_\beta\right\rangle \tag{1.11}
$$

The final detection of the flavour occurs via charged-current interaction and collapses the neutrino back in a weak eigenstate. The probability of detecting a neutrino of flavor β after the propagation of the neutrino of flavour α is then given by:

$$
\mathcal{P}(\nu_\alpha \to \nu_\beta) = \left|\left\langle \nu_\beta \middle| \nu(t) \right\rangle\right|^2 = \left| \sum_i U_{\beta i} U^*_{\alpha i} e^{i\vec{\mathbf{p}}_\mathbf{i}\cdot\vec{\mathbf{x}}} \right|^2 \tag{1.12}
$$

For a relativistic neutrino of mass m_i, which is the case in any practical experimental conditions, we have

$$p_i = \sqrt{E^2 - m_i^2} \simeq E - \frac{m_i^2}{2E} \tag{1.13}$$

Using this approximation yields the following formula for the oscillation probability:

$$\begin{aligned}\mathcal{P}(\nu_\alpha \to \nu_\beta) = \delta_{\alpha\beta} &- 4\sum_{i<j} \mathrm{Re}\,[U_{\alpha i}U^*_{\beta i}U^*_{\alpha j}U_{\beta j}]\sin^2\left(\frac{\Delta m^2_{ji}L}{4E}\right) \\ &+ 2\sum_{i<j} \mathrm{Im}\,[U_{\alpha i}U^*_{\beta i}U^*_{\alpha j}U_{\beta j}]\sin\left(\frac{\Delta m^2_{ji}L}{2E}\right)\end{aligned} \tag{1.14}$$

where $\Delta m^2_{ji} = m_j^2 - m_i^2$ is the squared-mass splitting between the mass states i and j.

For the sake of simplicity, and as it allows to recover the proper oscillation formula, several simplifying assumptions were made in this derivation. The different mass states composing the neutrino are assumed to all have the same energy whereas this contradicts Lorentz-invariance. A proper derivation of the neutrino oscillation formulas has to be done in the framework of the wave-packet formalism as explained in [18].

Equation 1.14 shows that neutrino oscillations can only appear in the case of non-degenerate masses ($\Delta m^2_{ji} \neq 0$). The oscillation probability depends on the three mixing angles and two squared-mass differences (as we have by construction $\Delta m^2_{32} + \Delta m^2_{21} = \Delta m^2_{31}$). The oscillation probability also depends on the Dirac CP-violating phase, δ_{CP}, but is blind to the Majorana phases as the pairs of the form $U_{\alpha i}U^*_{\beta i}$ have cancelling Majorana phase terms. This implies that the neutrino oscillation phenomenon is identical for Dirac and Majorana neutrinos, which makes sense as the Majorana nature of the neutrino should be revealed by processes violating the total lepton number, such as the neutrinoless double beta decay, which the oscillation phenomenon does not.

Given that $U_{\alpha i}U^*_{\beta i}U^*_{\alpha j}U_{\beta j}$ is real for $\alpha = \beta$, the survival probability, that is the probability for the neutrino to be detected in the same flavour eigenstate as it was emitted, is equivalent for neutrinos and antineutrinos:

$$\mathcal{P}(\nu_\alpha \to \nu_\alpha) = \mathcal{P}(\bar{\nu}_\alpha \to \bar{\nu}_\alpha) = 1 - 4\sum_{i<j} \left|U_{\alpha i}U_{\alpha j}\right|^2 \sin^2\left(\frac{\Delta m^2_{ji}L}{4E}\right) \tag{1.15}$$

Any CP-violation effect in the lepton sector can therefore only be measured by detecting neutrino appearance, namely the non-oscillation of the neutrino into a different flavour state.

$$\mathcal{P}(\nu_\alpha \to \nu_\beta) = \mathcal{P}(\bar{\nu}_\alpha \to \bar{\nu}_\beta) = 1 - 4\sum_{i<j} \left|U_{\alpha i}U_{\alpha j}\right|^2 \sin^2\left(\frac{\Delta m^2_{ji}L}{4E}\right) \tag{1.16}$$

In many experimental situations, a two-neutrino oscillation framework is a good approximation of the neutrino oscillations and allows to better understand the results. This two-neutrino model only includes a single mass-square difference, Δm^2 and a single mixing angle θ. In this model, the oscillation probability for $\alpha \neq \beta$ becomes:

$$\mathcal{P}(\nu_\alpha \to \nu_\beta) = \mathcal{P}(\bar{\nu}_\alpha \to \bar{\nu}_\beta) = \sin^2(2\theta)\sin^2\left(\frac{\Delta m^2 L}{4E}\right) \tag{1.17}$$

with a survival probability:

$$\mathcal{P}(\nu_\alpha \to \nu_\alpha) = 1 - \mathcal{P}(\bar{\nu_\alpha} \to \bar{\nu_\alpha}) = 1 - \sin^2(2\theta)\sin^2\left(\frac{\Delta m^2 L}{4E}\right) \tag{1.18}$$

In this framework, the oscillation probability has an amplitude driven by $\sin^2(2\theta)$ and an oscillation length proportional to $\Delta m^2/E$. Defining this oscillation length as

$$L_{\text{osc.}}[km] = 2.48E[\text{GeV}]/\Delta m^2[\text{eV}^2] \tag{1.19}$$

we have:

$$\mathcal{P}(\nu_\alpha \to \nu_\beta) = \sin^2(2\theta)\sin^2\left(\pi\frac{L}{L_{\text{osc.}}}\right) \tag{1.20}$$

Many of the first oscillation experiments made use of the two-flavour formula as they were not sensitive to the subleading effects of the neutrino oscillations. The solar neutrino oscillations have been described with a solar mixing angle θ_{sol} and a square-mass difference Δm^2_{sol} and the atmospheric neutrino oscillations have ben described with an atmospheric mixing angle θ_{atm} and a square mass difference Δm^2_{atm}, defining:

$$\Delta m^2_{\text{sol}} = \Delta m^2_{21} \ll \left|\Delta m^2_{31}\right| \simeq \left|\Delta m^2_{32}\right| \simeq \left|\Delta m^2_{\text{atm}}\right| \tag{1.21}$$

The mass ordering between m_3 and m_2 is however not defined and two possibilities exist: either $m_1 < m_2 < m_3$, the so-called normal mass ordering (or hierarchy), or $m_3 < m_1 < m_2$ refered to as the inverted mass ordering (or hierarchy), as shown in Figure 1.3.

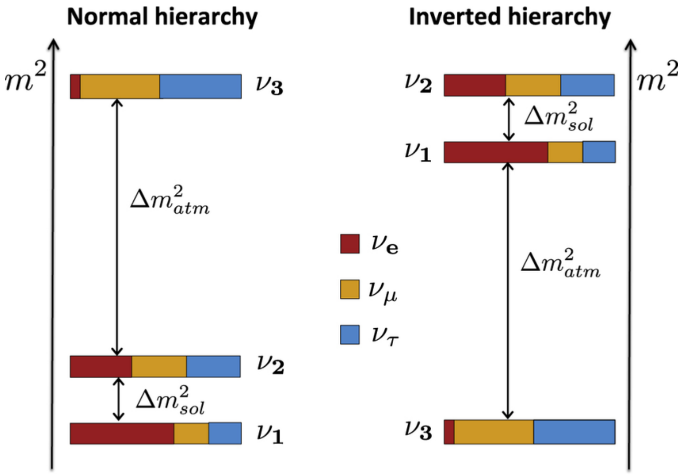

Figure 1.3: Scheme of the two different mass hierarchies with the composition in the different flavour eigenstates of the mass eigenstates.

1.2.3 Matter effects

In the previous section, the phenomenon of neutrino oscillation is described for neutrinos propagating in the vacuum. However when neutrinos propagate in matter such as the Earth, they interact with it despite the weak nature of the interaction. The propagation of the neutrinos in matter is a quantum-mechanical effect that can be described with the Schrödinger equation:

$$i\frac{\mathrm{d}}{\mathrm{d}t}\left|\nu(t)\right\rangle = H\left|\nu(t)\right\rangle \tag{1.22}$$

with $H = H_0 + V$, the Hamiltonian than can be separated into a free part H_0 corresponding to the kinetic energy of the neutrino, and a potential term V due to the interactions of the neutrino with matter during its propagation. In this case, the mass eigenstates are not the propagation eigenstates anymore.

The neutrino momentum can be left unchanged while interacting with the matter by coherent forward scatterings on electrons or nucleons. This interaction can be mediated by a Z boson (neutral current) for all neutrinos and by W boson (charged current) only for $\overset{(-)}{\nu}_e$. The matter potential component due to neutral current is identical for all the flavours:

$$V_{\mathrm{NC}} = -\frac{G_F}{\sqrt{2}} n_n(x) \tag{1.23}$$

where $n_n(x)$ is the location-dependant neutron density of the medium and $G_F = 1.166 \times 10^{-5}\,\mathrm{GeV}^{-2}$ is the Fermi constant. On the contrary, the charged current term of the potential only applies to $\overset{(-)}{\nu}_e$ as

$$V_{\text{CC}} = \pm\sqrt{2}G_F n_e(x) \tag{1.24}$$

where $n_e(x)$ is the location-dependant electron density. The charged current term is positive for ν_e and negative for $\bar{\nu}_e$.

One has to diagonalize the Hamiltonian in order to find the new propagation eigenstates associated to the neutrino in matter. This derivation is made in multiple references, among which [19]. Several key features of the neutrino oscillation appear with the addition of matter effects.

- The oscillation parameters are modified with the introduction of new mixing angles in matter θ_{ij}^m;
- As the matter does not contain any antimatter, the oscillation parameters are modified differently for the neutrinos and the antineutrinos, thus introducing an oscillation asymmetry that can resamble CP-violation;
- Adiabatic flavour conversion of neutrinos crossing mediums with varying densities, like the sun leading to the conversion of a neutrino in a flavour state, sum of multiple mass eigenstates, into a neutrino in a specific mass eigenstate. This is the so-called Mikheev-Smirnov-Wolfenstein (MSW) effect.

1.2.4 CP-violation

Eventual CP-violation in the lepton sector depends on the δ_{CP} phase of the PMNS matrix. CP-violation implies different oscillation probabilities for neutrinos and antineutrinos.

CP-violation arises from the CP-odd part in the Equation 1.14. The CP-violation effect can therefore be described by introducing the quantity $\Delta P_{\alpha\beta} \equiv P(\nu_\alpha \to \nu_\beta) - P(\bar{\nu}_\alpha \to \bar{\nu}_\beta)$. This can be expressed as

$$\Delta P_{\alpha\beta} = \pm 16 J \sin\left(\frac{\Delta m_{21}^2 M}{4E}\right)\sin\left(\frac{\Delta m_{31}^2 M}{4E}\right)\sin\left(\frac{\Delta m_{32}^2 M}{4E}\right) \tag{1.25}$$

with J the Jarlskog invariant equal to

$$J = \frac{1}{8}\cos\theta_{13}\sin(2\theta_{12})\sin(2\theta_{13})\sin(2\theta_{23})\sin\delta_{\text{CP}} \tag{1.26}$$

Equations 1.25 and 1.26 give us three conditions necessary to the existence of CP-violation:

- All the three mixing angles must be non-zero: $\theta_{ij} \neq 0$;

- The CP violating phase δ_{CP} must differ from 0 and π;

- The three neutrinos masses must be different: $m_1 \neq m_2 \neq m_3$.

We can also see that the CP-violating term is independant of the considered neutrino channel, up to a sign. Moreover, the dependance of the CP-violation effect on $\sin\left(\frac{\Delta m^2_{21} M}{4E}\right)$ implies that its observation requires long baselines of several hundreds of km and also intense neutrino flux, as well as, large detector volumes given that the effect is small.

1.3 Detecting the neutrino oscillations

1.3.1 Solar neutrino oscillations

The Sun is a major source of neutrinos. Indeed, the Sun fights gravity by fusioning hydrogen in its core, according to the following overall process:

$$4p \to {}^{4}\mathrm{He} + 2\,\mathrm{e}^{+} + 2\,\nu_e \tag{1.27}$$

thus emitting neutrinos. Solar models provide estimations of the solar neutrino flux on Earth with a typical value of $\phi = 6.5 \times 10^{10}\,\mathrm{cm}^{-2}\,\mathrm{s}^{-1}$. Different reactions inside the sun lead to the emission of neutrinos as this can be seen in Figure 1.4. Most of the neutrinos that make the solar neutrino flux are produced by the pp fusion and have a low energy $< 0.42\,\mathrm{MeV}$. Neutrinos at higher energies are emitted in the ^{8}B reaction ($^{8}_{5}\mathrm{B} \to {}^{8}_{4}\mathrm{Be} + \mathrm{e}^{+} + \nu_e$), up to 15 MeV, but with a way smaller flux. Several mono-energetic sources of neutrinos are also present, with two emission rays at 0.38 MeV and 0.86 MeV due to electron capture in ^{7}Be, and a 1.44 MeV ray due to pep reaction ($\mathrm{p} + \mathrm{p} + \mathrm{e}^{-} \to {}^{2}_{1}\mathrm{H}^{+} + \nu_e$).

The counting experiments

The first experiments conceived to detect neutrinos rely on the inverse beta decay reaction. This detection method was suggested by Pontecorvo as early as in 1946 [20]. He proposes in his report the inverse beta decay on chlorine:

$$\nu_e + {}^{37}\mathrm{Cl} \to {}^{37}\mathrm{Ar} + \mathrm{e}^{-} \tag{1.28}$$

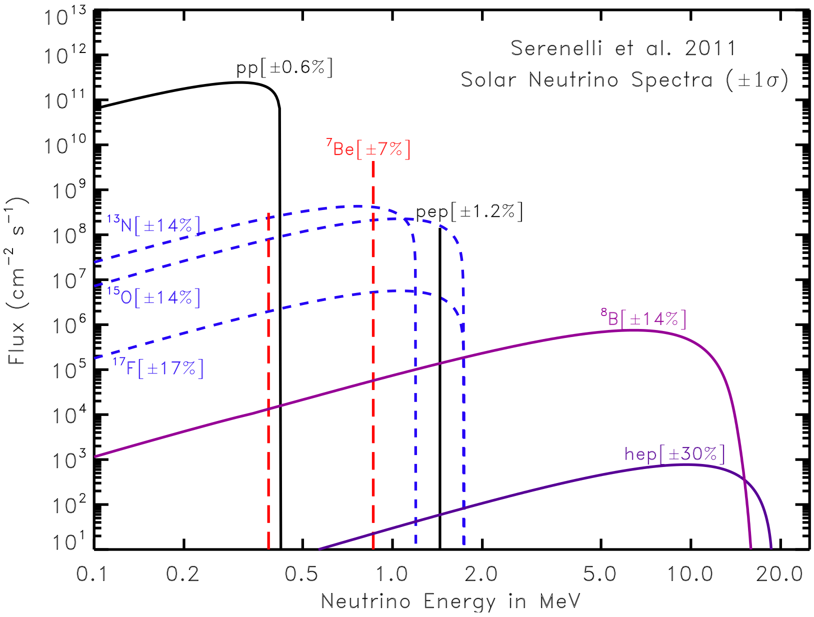

Figure 1.4: Solar neutrino spectrum including the SSM uncertainties.

This reaction has an energy thershold of 0.814 MeV, since mass is created in the process. This makes it sensitive to only a small part of the solar spectrum, mainly neutrinos produced by the ^{8}B and ^{7}Be processes. Ray Davis decided to build an experiment using this process to detect solar neutrinos, deep underground at Homestake in South Dakota, using 615 t of perchloroethylene (C_2Cl_4) as a target. The data taking started in 1968 and ended in 2002 [21]. The rate of Argon produced by solar neutrinos was 0.48 per day while the production rate by cosmogenics background was 0.09 per day. The half life of ^{37}Ar being 35 days, the C_2Cl_4 cuve was exposed to the neutrinos for 60 to 70 days before the extraction of its content to measure the number of created ^{37}Ar atoms. The ^{37}Ar, that decays by electron capture, emits Auger electrons that are detected by gas proportional counters. The result obtained by the Homestake experiment for the neutrino capture rate is:

$$(\sigma\phi)_{\mathrm{Cl}} = 2.56 \pm 0.16 \pm 0.16\,\mathrm{SNU} \tag{1.29}$$

where SNU stands for Solar Neutrino Units with 1 SNU $= 1 \times 10^{-36}$ captures/nucleus/second.

This measurement was about 3 times smaller than what was predicted by the GS98-SFII solar model [22]: 8.00(97) SNU. This large difference between the expected and measured values led to large debates whitin the scientific community with many physicists suggesting that the solar model might be incorrect. Indeed, the SSM model was not confirmed yet by helioseosmological data and the production rate of ^{8}B neutrinos in the core of the sun has a temperature dependance that goes as T^{22} [23]. The observed smaller rate could therefore be explained with a slight temperature difference of the Sun's core with respect to what is predicted by the solar model.

Years later, other experiments started to investigate the solar neutrino flux: the Soviet-American Gallium Experiment (SAGE) [24] from 1989 to 2007 in the Baksan laboratory in Russia, and the Gallium Experiment (Gallex) [25] from 1991 to 1997 in the Gran Sasso Laboratory in Italy, later joined by the Gallium Neutrino Observatory (GNO) [26] from 1998 to 2003. These three experiments made also use of the inverse beta decay process to detect the neutrinos, but this time on Gallium:

$$\nu_e + {}^{71}\mathrm{Ga} \rightarrow {}^{71}\mathrm{Ge} + \mathrm{e}^- \tag{1.30}$$

The advantage of using gallium over chlorine is the lower momentum threshold for the reaction (0.233 MeV) that gives access to a larger part of the neutrino spectrum, namely the pp neutrinos, largely improving the part of the flux that the experiments are sensitive to. These experiments all confirmed the solar neutrino deficit first witnessed by Homestake, however with a larger reduction factor with respect to the SSM prediction (126.6(42) SNU) around 50 %:

$$\begin{aligned}(\sigma\phi)_{\mathsf{SAGE}} &= 65.4\,\mathrm{SNU}\\ (\sigma\phi)_{\mathsf{GALLEX}} &= 73.4\,\mathrm{SNU}\\ (\sigma\phi)_{\mathsf{GNO}} &= 62.9\,\mathrm{SNU}\end{aligned} \tag{1.31}$$

The new measurements provided by all these gallium-based experiments clearly showed that the suppression factor depends on the neutrino energy thanks to their energy threshold different from the Homestake experiment, thus hinting towards a neutrino oscillation phenomenon.

This first series of experiments relying on radiochemical measurements only gave access to interaction rates without giving any possibility to detect directly the interactions and measure the neutrino characteristics.

Real time experiments

Subsequent experiments aimed at observing directly the neutrino interactions by detecting the children particles and measure their kinematics. The first experiment of this kind was the Kamioka Nucleon Decay Experiment (Kamiokande), later renamed Kamioka Neutrino Detection Experiment, a 2.14 kt water Cherenkov detector

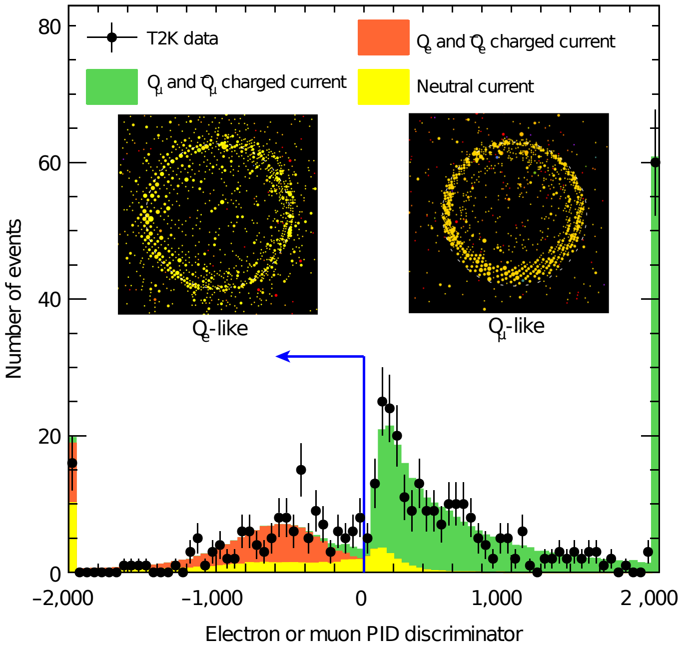

Figure 1.5: Super-Kamiokande PID discriminator based on the sharpness of the Cherenkov ring. (reproduced from [27])

located in Japan. The first aim of the experiment was to detect proton decays that can only be a rare event (if it exists), thus requiring high capabilities to constrain the background. This feature is a big advantage for neutrino detection. Kamiokande operated from 1987 to 1995, providing measurements of the solar neutrino flux in its phases II and III.

This detector relies on the Cherenkov effect that takes place when charged particles move faster than the speed of light in a given medium. This leads to the emission of Cherenkov photons along a cone centered on the particle direction with an opening angle equal to $\arccos{(n\beta)^{-1}}$ (42° for ultra-relativistic particles in water) for particles with a relative speed β in a medium with refractive index n. These Cherenkov photons can be detected by photomultipliers located on the walls of the detector allowing the reconstruction of the Cherenkov rings. The dependance of the ring opening angle on the particle momentum can be used to measure the momentum of the charged particles. Moreover, particle identification (PID) can be performed to discriminate electrons from muons by looking at the sharpness of the Cherenkov ring as shown in Figure 1.5. Indeed, as electrons are lighter particles they are more susceptible to undergo multiple scattering when traveling inside the water leading to multiple changes in their trajectories that translate into fuzzy Cherenkov rings.

As neutrino interactions often lead to the production of relativistic charged particles, Cherenkov detectors can be used to detect the interaction products and thus reconstruct the kinematic and flavor parameters of the interacting neutrinos.

Kamiokande could detect neutrino elastic scattering on electrons, a process mainly sensitive to electron neutrinos, with a threshold of 9 MeV that was progressively lowered to 7 MeV [28]. For kinematic reasons, the scattered electron is emitted preferentially in the initial neutrino direction allowing for the measurement of the neutrino direction. The neutrino direction can therefore be correlated with the Sun position to ensure the selection of solar neutrinos. The result obtained by Kamiokande [29] is

$$\phi(^{8}\mathrm{B}) = [2.80 \pm 0.19(\text{stat.}) \pm 0.33(\text{sys.})] \times 10^{6}\,\text{cm}^{-2}\text{s}^{-1} \tag{1.32}$$

indicating once again a large supression of the solar neutrino flux with respect to the solar model prediction.

Following the success of the Kamiokande experiment at detecting neutrinos, the Super-Kamiokande water Cherenkov detector was built under the Mozomi zinc mine, near Kamioka, in Japan. Its installation below 1000 m of rocks (2700 m equivalent of water) allows for the reduction of cosmogenics induced background. Since its commissioning in 1996, Super-Kamiokande remains the largest (enclosed) water Cherenkov detector in the world. It contains 50 kt of ultra-pure water in a stainless steel tank of around 40 m of diameter. The volume is fiducialized with an inner detector containing 22.5 kt of water instrumented with 11146 20-inch PhotoMultiplier Tubes (PMTs), and an outer detector instrumented with 1885 8-inch PMTs.

Super-Kamiokande started taking data in 1996 with a momentum threshold of 7 MeV, now reduced to 3.5 MeV, and is still taking data nowadays. Its latest solar neutrino results are the following [30]

$$\phi(^{8}\mathrm{B}) = [2.308 \pm 0.020(\text{stat.}) \pm {}^{+0.040}_{-0.040}(\text{sys.})] \times 10^{6}\,\text{cm}^{-2}\text{s}^{-1} \tag{1.33}$$

Super-Kamiokande was also able to observe for the first time a day-night asymmetry in the solar neutrino rate indicating Earth matter effects on neutrino propagation.

For solar neutrinos with energies of a few MeVs, the main interaction channel in water Cherenkov detectors is neutrinos scattering off electrons, with a cross-section about six time larger for electron neutrinos than the other flavors. Water Cherenkov detectors are therefore unable to distinguish between a ν_e deficit due to either a wrong SSM prediction, or neutrino oscillations. In order to do so, it is necessary to also estimate the flux of all the neutrinos independently of their flavor. This is what performed the Sudbury Neutrino Observatory (SNO) experiment, located in Canada, shown in Figure 1.6. This detector is also a Cherenkov detector, but filled with 1 kt of heavy water. The use of heavy water, in which hydrogen atoms are replaced by deuterium (d), composed of $1p$ and $1n$, gives access to three different channels for the measurement of the solar neutrino flux:

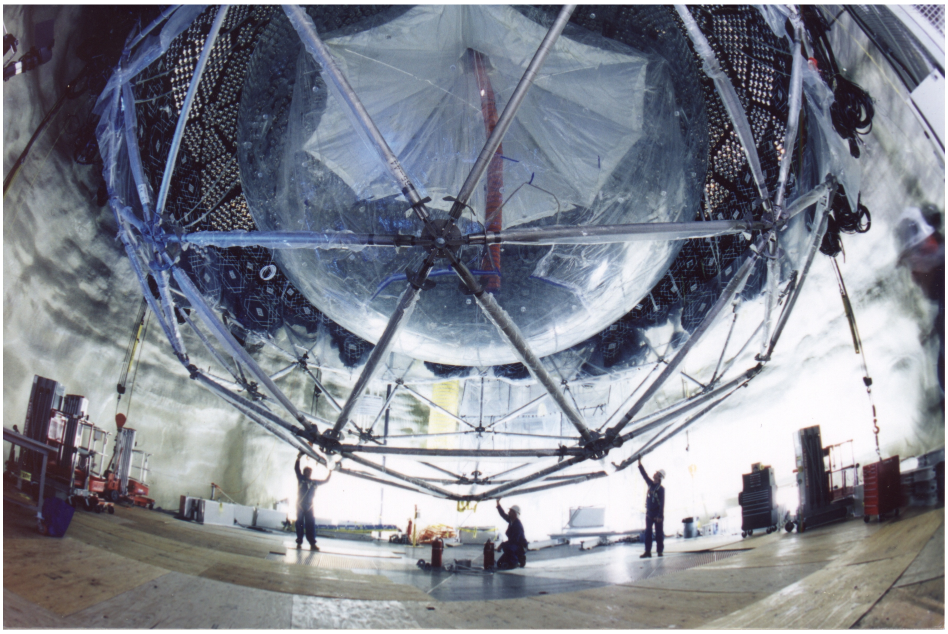

Figure 1.6: Picture of the SNO detector during its assembly. The heavy water tank is located in the center while the PMTs are attached onto the metallic structure.

- Charged Current (CC) interactions on the deuterium neutron $\nu_e + d \rightarrow p + p + e^-$ lead to the production of an electron carrying most of the neutrino energy;
- Electron Scattering (ES) interactions on electrons $\nu + e^- \rightarrow \nu + e^-$, mainly sensitive to ν_e as in conventional water Cherenkov detectors;
- Neutral Current (NC) interactions $\nu + d \rightarrow \nu + p + n$, which are flavor independant.

The CC interaction channel allows to measure the flux of the ν_e and their energy spectrum. This information is completed by the ES channel that is mainly sensitive to ν_e. The NC channel however, allows to count all the neutrinos with an energy above the deuterium binding energy of 2.224 MeV.

The NC interaction has for effect to break apart the deuterium, thus emitting a neutron. The only way to detect this interaction is to measure the gamma rays emitted by a nucleus as it captures the thermalized neutron. The capture of neutrons directly on deuterium was used in a first operating phase but it is not a very efficient process. In a second phase of operations, NaCl was dissolved in the water to be able to detect neutron capture on ^{35}Cl nuclei with an improved capture efficiency and gamma identification. During a third and final operation phase, detectors filled with ^{3}He gas were installed inside SNO, providing a higher neutron capture cross-section. The SNO experiment was sensitive to ^{8}B neutrinos given its electron kinetic energy threshold of 5 MeV. The results obtained during the three phases of operations [31] were in agreement and the obtained total

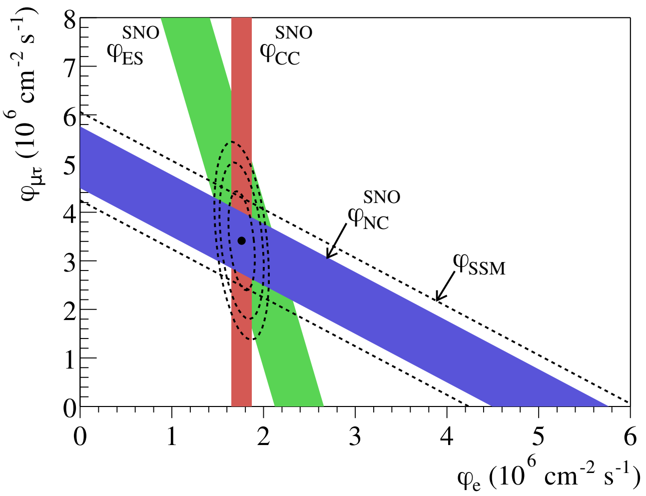

Figure 1.7: Measured ^{8}B solar neutrino fluxes by SNO in the different interaction channels. The bands represent the SNO measurements with 1 σ errors and the dashed lines correspond to the SSM predictions. (reproduced from [32])

solar neutrino flux is:

$$\phi_{\text{NC}}(^8\text{B}) = [5.25 \pm 0.16(\text{stat.}) \pm {}^{+0.11}_{-0.13}(\text{sys.})] \times 10^6\,\text{cm}^{-2}\text{s}^{-1} \tag{1.34}$$

This measurement is in agreement with the prediction of the solar models giving $\phi(^8\text{B}) = 5.05 \times 10^6\,\text{cm}^{-2}\text{s}^{-1}$. In addition, the ν_e flux was measured using CC interactions, obtaining:

$$\phi_{\text{CC}} = (0.301 \pm 0.033)\phi_{\text{NC}} \tag{1.35}$$

The combination of all the three interaction channels allows to measure the ν_e and $\nu_{\mu,\tau}$ ^{8}B solar neutrino fluxes as shown in Figure 1.7. This measurement is a clear, flux model independant, indication of ν_e oscillating into ν_μ and ν_τ. This 2001 discovery solved the solar anomaly puzzle but was not the first evidence of neutrino oscillation, that was actually discovered by Super-Kamiokande in 1998 with the measurement of atmospheric neutrino oscillations, as will be described in the next section.

Another experiment of large importance for the measurement of solar neutrinos is the Borexino experiment, a 278 t liquid scintillator detector located in the Gran Sasso laboratory in Italy, running from 2007 to 2021. Borexino mainly aims at conducting precise measurements of the multiple neutrino fluxes coming from the Sun. Thanks to the high light yield (10^4 photons/MeV) of its liquid scintillator and its high level of radiopurity, Borexino is able to detect neutrinos with an energy threshold of 200 keV. This low energy threshold allows Borexino to measure the ^{7}Be neutrino flux [33], as well as, the pep flux [34]. Moreover, Borexino has been able to detect pp neutrinos and put upper limits on the CNO neutrino flux. The constraints on the CNO neutrino flux, as well as, the other measurements allow to check the predictions of the solar models [35].

Reactor neutrinos

As explained previously, reactor neutrinos have been used in order to make the first experimental detection of the neutrino. Their high flux and the possibility to choose the distance between their emission and detection made them essential to probe the 1-2 oscillation sector in addition to the solar data. The typical energy of the produced $\bar{\nu}_e$ is of a few MeV. In this energy range, the $\bar{\nu}_e$ can interact on a proton leading to an IBD process $\bar{\nu}_e + p \rightarrow n + e^+$ which has an energy threshold of 1.8 MeV. The cross-section of the IBD process can be precisely calculated from the related neutron decay process [36]. Most of the neutrino energy is transfered to the positron with:

$$E_{e^+} = E_{\bar{\nu}_e} - (m_n - m_p) + m_e \tag{1.36}$$

where m_n, m_p and m_e are the neutron, proton and electron masses repectively. The IBD cross-section rises with energy while the $\bar{\nu}_e$ emission spectrum decreases rapidly with energy resulting in an interaction specrum peaking around 4 MeV as shown in Figure 1.8.

The emitted positron can be detected in any scintillation medium with a ionization of the medium followed by an anihilation signal of two gammas. The emitted neutron will thermalize in the medium and can be captured either on hydrogen or on specifically introduced nuclei with large capture cross-sections, such as gadolinium. This neutron capture results in gammas emission. The IBD decay can therefore be cleanly identified in a scintillation detector doped with gadolinium by measuring the positron ionization and annihilation in delayed coincidence with the neutron capture signal. Furthermore, the neutrino energy can be estimated from the positron ionization of the medium.

KamLAND is a 1 kt liquid scintillator experiment located in the former site of the Kamiokande detector in Japan. It performs reactor $\bar{\nu}_e$ detection using the IBD process. KamLAND is surrounded by multiple nuclear reactors that are at an average distance of 150 km, as shown in Figure 1.9, allowing to perform oscillation measurements. KamLAND provided the first evidence of $\bar{\nu}_e$ disappearance in 2002 [38]. This measurement demonstrated for the first time the oscillation behavior with respect to the L/E ratio, allowing to interprete the

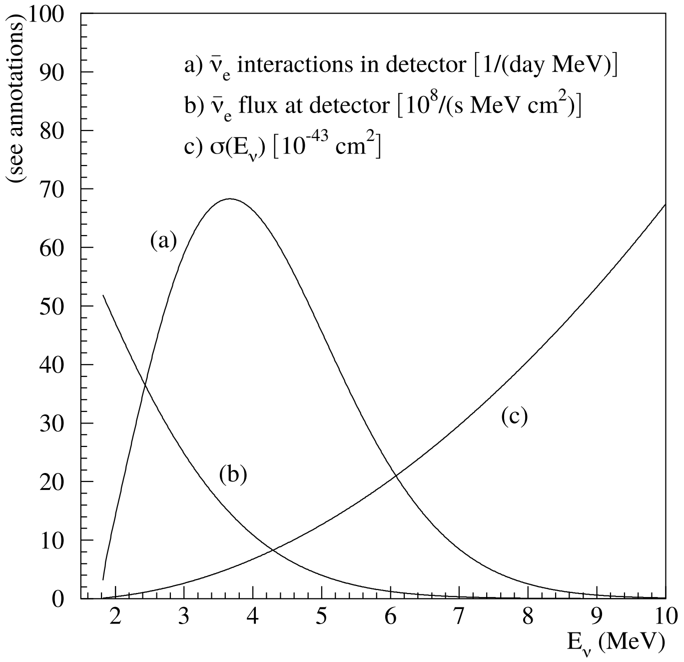

Figure 1.8: Reactor ν_e flux, IBD cross-section and resulting interaction spectrum for a 12 t fiducial mass detector located 0.8 km from a 12 GW_{th} reactor. (reproduced from [37])

solar neutrino data. The latest KamLAND results are presented in Figure 1.10. The combination of both the solar data and KamLAND data give the main contribution to the determination of Δm^2_{21} and θ_{12} in the NuFIT [39] global three-neutrino oscillation fit.

1.3.2 Atmospheric neutrino oscillation

We describe here the discovery of the 2-3 oscillations, often called atmospheric neutrino oscillations, as they were first discovered with atmospheric neutrinos before being later precisely measured by accelerator-based long baseline neutrino experiments.

Atmospheric neutrinos production

The interaction of cosmic rays, mainly composed of protons, with our atmosphere leads to the production of hadronic showers mainly composed of pions and kaons. The decays of these mesons produce a neutrino flux composed of ν_μ, $\bar{\nu}_\mu$, ν_e and $\bar{\nu}_e$:

$$\pi^\pm \to \mu^\pm + \overset{(-)}{\nu}_\mu \tag{1.37}$$

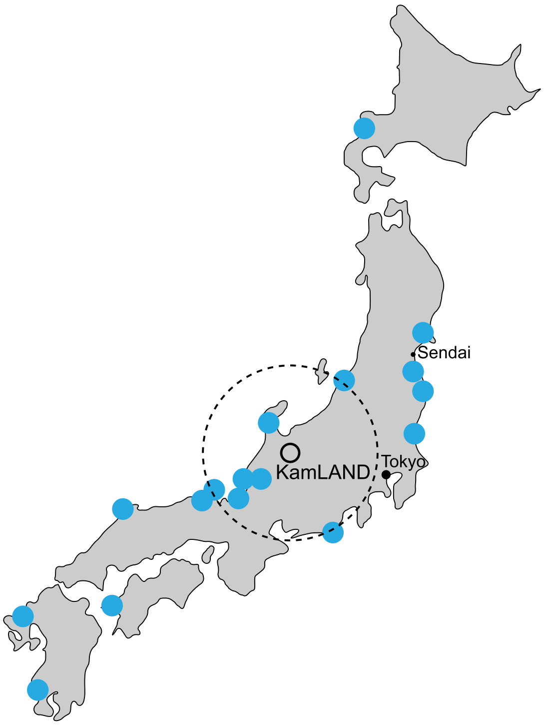

Figure 1.9: Location of the KamLAND experiment that measures the neutrino flux coming from multiple japanese reactors (in blue).

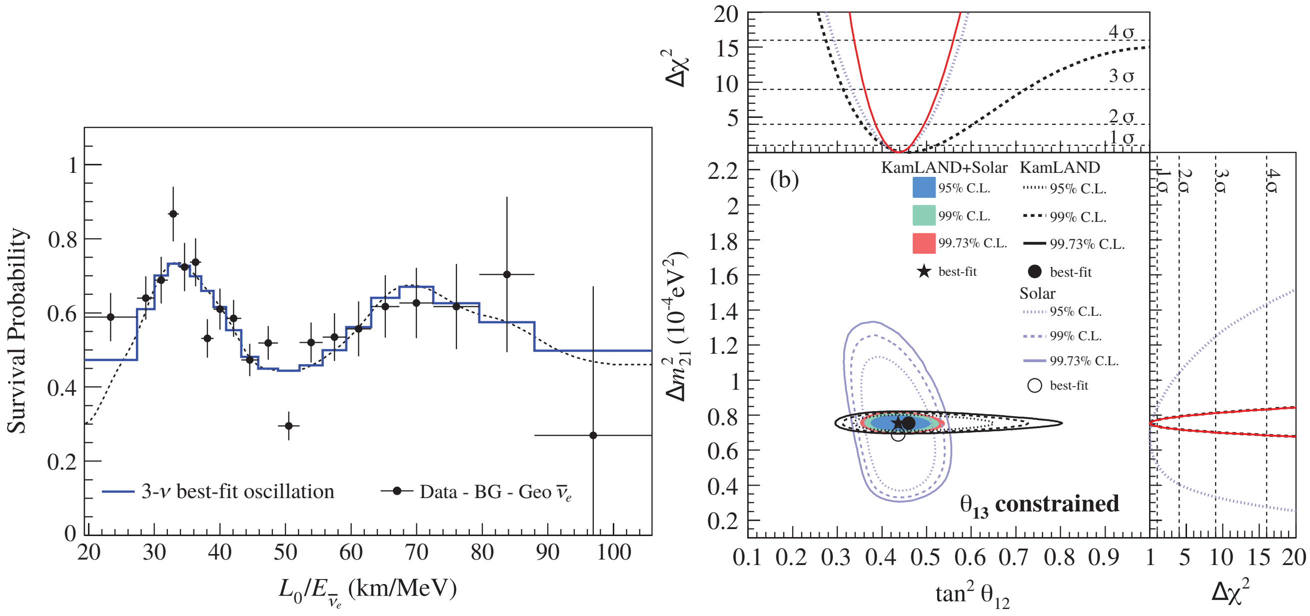

Figure 1.10: Ratio of the observed $\bar{\nu}_e$ spectrum to the expectation for no-oscillation as a function of L/E in in KamLAND (left) and allowed region for neutrino oscillation parameters combining solar neutrino experiments with in KamLAND data (right). (reproduced from [40])

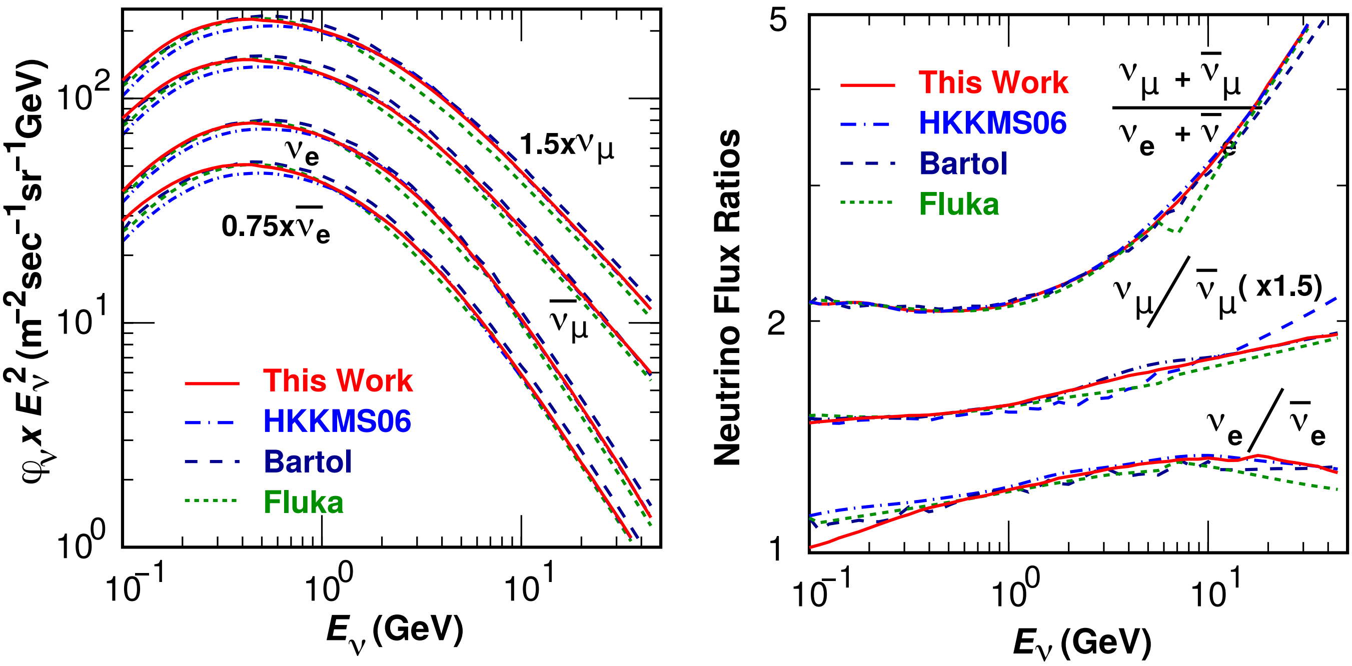

Figure 1.11: Predicted flux of atmospheric neutrinos at Kamioka with different models (left) and the implied flux ratios (right). (reproduced from [41])

$$\mu^\pm \to e^\pm + \overset{(-)}{\nu}_e + \overset{(-)}{\nu}_\mu \tag{1.38}$$

The fluxes of the produced neutrinos follow a power-law spectrum as a function of the energy above 1 GeV ($\sim E^{-2.7}$) as shown in Figure 1.11. Given the multiple parameters affecting the neutrino fluxes, such as the cosmic ray flux and composition, the nuclear interaction cross-section or the Earth magnetic field, the precision of the various models are typically above 7 % [41]. The uncertainties on the $(\nu_\mu + \bar{\nu}_\mu)/(\nu_e + \bar{\nu}_e)$ ratio is however smaller, of the order of 2 % [41] as some uncertainties cancel.

Atmospheric neutrino disappearance

In 1988, an anomaly in the ν_μ atmospheric flux was reported by the Kamiokande experiment. Indeed, according to Figure 1.11, the expected atmospheric ν_μ flux is twice larger than the ν_e flux in the GeV region, whereas Kamiokande measured a ratio around 1. This ν_μ deficit was also observed by other experiments such as IMB [42] or MACRO [43]. This situation was called the atmospheric-neutrino anomaly.

This anomaly was further investigated with the advent of Super-Kamiokande in 1996 that allowed to rapidly accumulate a large amount of data by reconstructing the momentum and flavour of atmospheric neutrinos. Moreover the propagation length of the atmospheric neutrinos can vary from a few km to around 10^4 km.

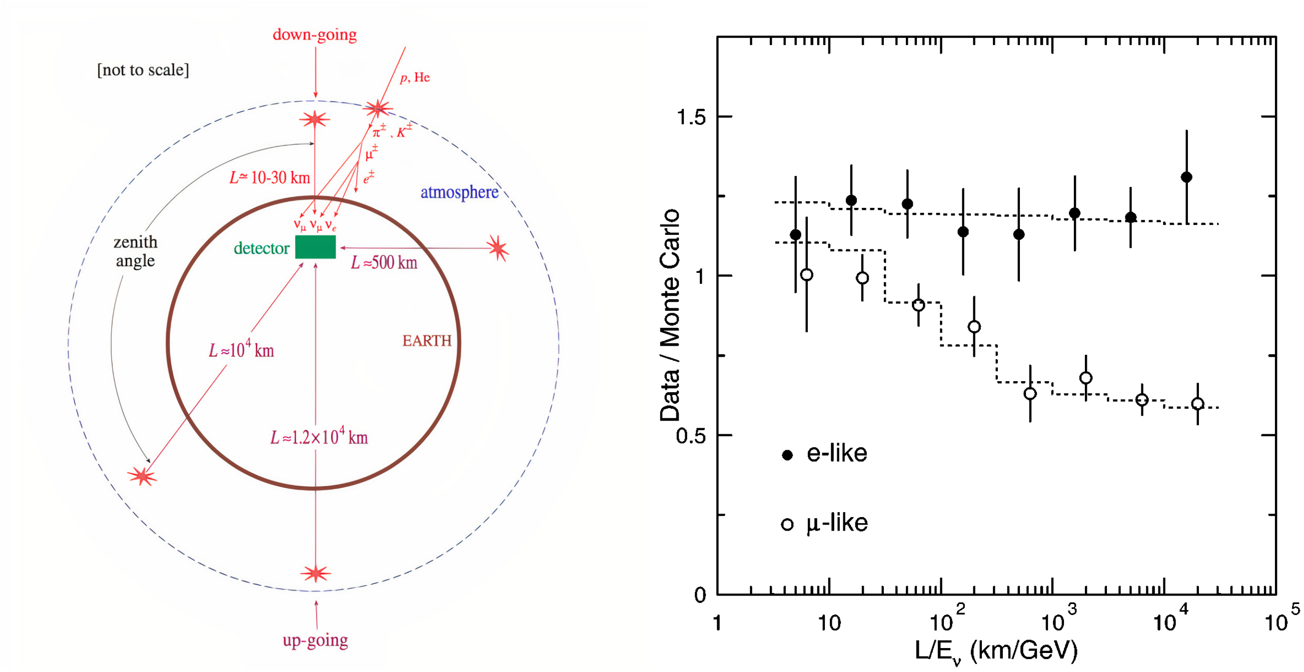

Figure 1.12: Scheme of the Super-Kamiokande atmospheric neutrino detection (left) and ratio of data to Monte Carlo ratios for atmospheric ν_μ and ν_e showing ν_μ deficit at large L/E.

Indeed, the atmospheric neutrinos detected can come from any side of the Earth and the lepton momentum angle with respect to the zenith allows to reconstruct the distance travelled by the neutrino between its creation and interaction inside the detector as shown in Figure 1.12 (left). Reconstructing both the neutrino zenith angle (and thus the neutrino travelled length) and the neutrino energy allows to measure the ν_e and ν_μ fluxes as a function of L/E and thus observe atmospheric neutrino oscillations. The first Super-Kamiokande results on atmospheric neutrinos showing evidence of atmospheric neutrino oscillations were published in 1998 [44]. These results are shown in Figure 1.12 (right) displaying a clear ν_μ deficit as L/E increases.

In the two-neutrino framework where the ν_μ disappearance probability is governed by Eq 1.18, we have:

$$\mathcal{P}(\nu_\mu \to \nu_\mu) \approx 1 - \sin^2(2\theta_{23}) \sin^2\left(\frac{\Delta m^2_{31} L}{4E}\right) \tag{1.39}$$

For large L/E, the oscillations average out and the ν_μ survival probability becomes $1 - \frac{1}{2}\sin^2(2\theta_{23})$. Therefore, the large ν_μ disappearance observed by Super-Kamiokande (survival fraction near 0.5) indicates a mixing close to maximal with $\theta_{23} \approx \frac{\pi}{4}$. The Nobel Prize in physics has been awarded in 2015 to both T. Kajita, for Super-Kamiokande, and A.B. McDonald, for SNO, for the discovery of neutrino oscillations.

Precise measurements with accelerator-based long baseline neutrino experiments

After the discovery of neutrino oscillations, their precise measurements require the usage of better controlled neutrino sources. The ideas of accelerator-based neutrino oscillation experiments thus arose. Neutrino beams are created by sending high energy and high intensity proton beams on a target where they interact to produce mesons that give rise to neutrinos through their decays. The produced beam is mainly composed of ν_μ or $\bar{\nu}_\mu$ depending on the selected charge sign of the produced mesons, mostly π and K. This selection is conducted by focusing horns that are pulsed with a very intense current to focus the positevely or negatively charged mesons while the others are discarded.

The great strength of accelerator-based experiments is the possibility to adjust both the distance of the detector to the source and the neutrino energy spectrum, which is impossible with natural neutrino sources. This allows to select the right parameters in order for the detectors to observe the oscillations maxima, where the oscillation parameters can be best measured. Moreover, the neutrino beam can be probed at multiple locations with "near" and "far" detectors in order to directly measure the non-oscillated and oscillated fluxes and observe oscillations with small systematic uncertainties.

The ν_μ or $\bar{\nu}_\mu$ beams produced by the accelerators are not totally pure. Indeed, they include $\nu_e/\bar{\nu}_e$ due to muon and kaon decays. The antineutrino beams are also contamined by a non negligeable fraction of neutrinos, and conversely, because the focusing of the horns is never perfect. This effect is more important in anti-neutrino beams as more π^+ than π^- are produced in the proton-carbon interactions in the target. Moreover, the neutrino interaction cross-sections are larger than those of anti-neutrinos, implying that even a slight contamination can lead to the observation of a sizeable amount of neutrino events in an anti-neutrino beam. The beam purity can be measured by magnetized near detectors able to discriminate the lepton charge and thus deduce the neutrino or anti-neutrino nature of the interacting particle.

The first long-baseline neutrino experiment was KEK-to-Kamioka (K2K) [46] that operated from 1999 to 2004. A neutrino beam was produced 250 km away from the Super-Kamiokande detector, used as far detector. K2K observed the ν_μ disappearance, following the Equation 1.39, with a $4.3\,\sigma$ significance [46]. With the same goal of measuring ν_μ disappearance, the MINOS experiment [47] operated from 2005 to 2012 with the NUMI beam [48] at Fermilab.

T2K and NOνA are presently running long-baseline experiments. The T2K experiment uses Super-Kamiokande as far detector with a beam produced at Tokai, 295 km away. The NOνA experiment is using the NUMI beam

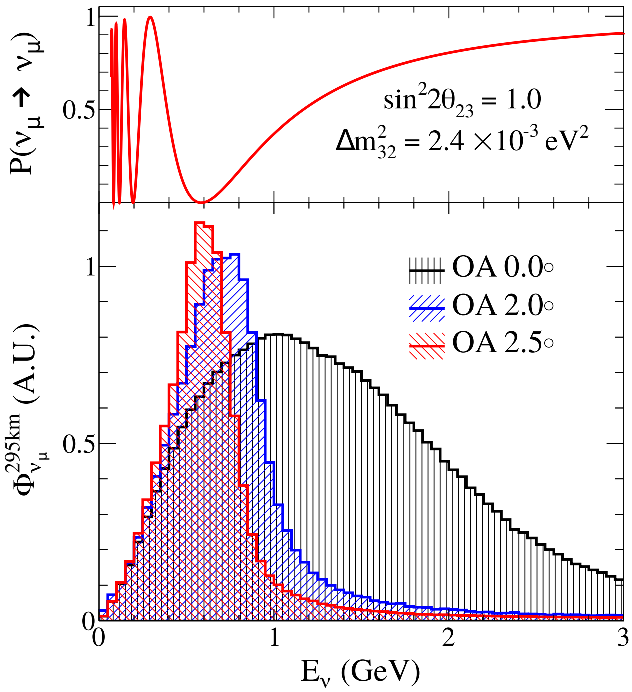

Figure 1.13: ν_μ survival probability at T2K (top) and neutrino energy spectrum at difference off-axis angles (bottom). (reproduced from [45])

produced at Fermilab and the far detector is located at 810 km in Ash River. Its 14 kt detector is segmented into multiple volumes filled with liquid scintillator. These two experiments are located off-axis, meaning that they are not positioned directly on the beamline axis but a few tens of mrad on the side. Placing the detector off-axis allows to focus the neutrino energy range on the oscillation maximum, however at the cost of a reduced flux. Indeed, the neutrinos are mostly produced by pion decays, a two body decay for which the neutrino angle with the beam and the neutrino energy are closely related. This can be clearly seen in Figure 1.13 that shows the T2K neutino energy spectrum for different off-axis angles.

T2K and NOνA both measure the $\overset{(-)}{\nu}_\mu$ disappearance and $\overset{(-)}{\nu}_e$ appearance. The latest results of the T2K and NOνA collaborations in the Δm^2_{32} versus $\sin^2\theta_{23}$ plane are reproduced in Figure 1.14.

Observations of ν_τ appearance

The atmospheric oscillation phenomenon can be established by ν_μ disappearance and ν_e appearance as discussed previously, but also by detecting ν_τ appearance. The main experiment that aimed at detecting this apparition of ν_τ was OPERA [50] that operated between 2008 and 2012 with an Emulsion Cloud Chamber [51] located in the Gran Sasso laboratory on a CERN neutrino beamline. The use of an emulsion cloud chamber allows to reach a

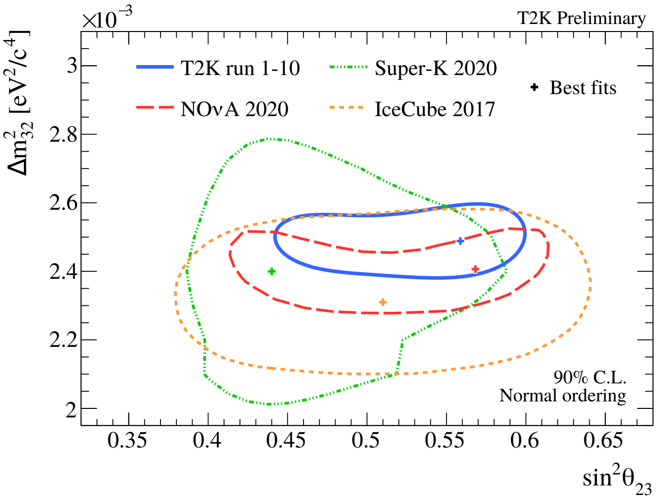

Figure 1.14: Confidence regions in the Δm^2_{32} versus $\sin^2\theta_{23}$ plane for different neutrino oscillation experiments. (reproduced from [49])

sub-micrometric track resolution, necessary to precisely study the interaction vertex and detect the τ lepton that has a short lifetime ($c\tau = 87\,\mu\text{m}$). This detection of the τ relies on the characteristic track kink that arises when it decays. OPERA observed 5 ν_τ candidate events [50] with a background of 0.25 events, thus implying a 5.1 σ discovery of ν_τ appearance by ν_μ oscillation. One of the observed event is reproduced in Figure 1.15. A further improved multivariate approach found a 6.1 σ significance [52].

1.3.3 The 1-3 sector

Early searches for neutrino oscillations in the $\bar{\nu}_e$ disappearance channel were performed in the 1980s by placing detectors close to nuclear reactors, but their searches were infructuous. Solar and atmospheric neutrino oscillations were then discovered letting θ_{13} as the only unmesured mixing angle. The results obtained on solar and atmospheric oscillations allowed to estimate the optimal distance for reactor-detector to measure θ_{13} that is around 2 km. Upper limits on $\sin^2(2\theta_{13})$ were obtained by the Chooz experiment [53]. The first evidence of $\theta_{13} > 0$ was brought by T2K with the indication of ν_e appearance in a ν_μ beam [54]. The precision measurement of θ_{13} was finally conducted by Daya Bay [55] in 2012 and soon confirmed by the Reno [56] and Double Chooz experiments [57].

In the 2-flavor oscillation framework, the $\bar{\nu}_e$ survival probability is governed by Equation 1.18:

$$\mathcal{P}(\bar{\nu}_e \rightarrow \bar{\nu}_e) \approx 1 - \sin^2(2\theta_{13})\sin^2\left(\frac{\Delta m^2_{31} L}{4E}\right) \tag{1.40}$$

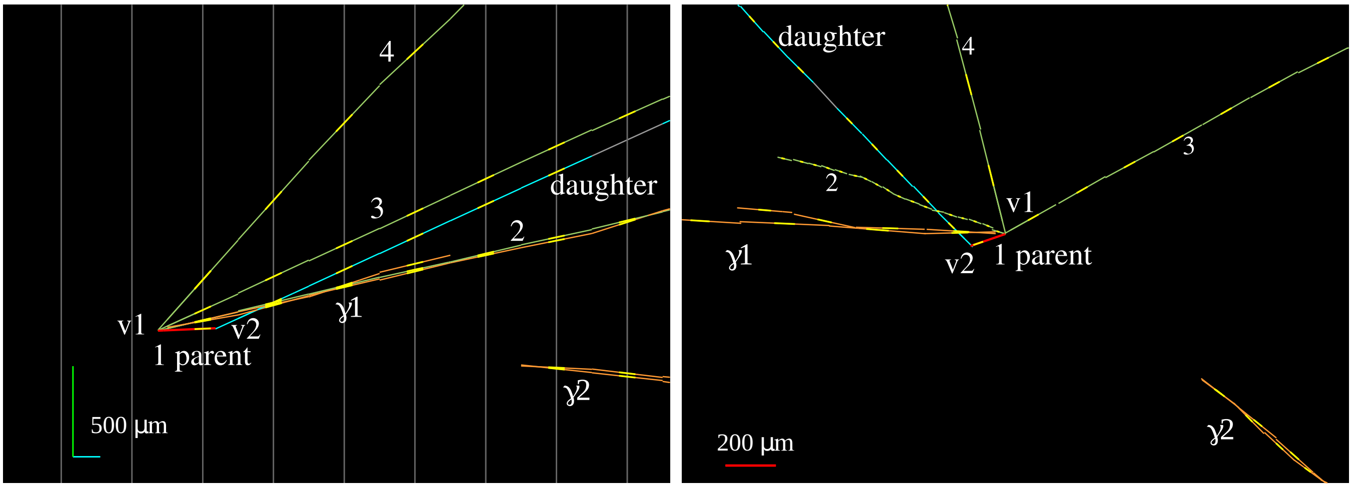

Figure 1.15: Event display of a ν_τ candidate, in OPERA, in a plane longitudinal to the neutrino direction (left) and transverse to the neutrino direction (right) with v_1 and v_2 indicating the primary and decay vertices respectively. (reproduced from [50])

The oscillation analysis is performed by comparing the $\bar{\nu}_e$ fluxes measured at near detectors, and far detectors 2 km away, as shown in Figure 1.16. The obtained value for θ_{13} by Daya Bay is the following [55]:

$$\sin^2(2\theta_{13}) = 0.084 \pm 0.005 \tag{1.41}$$

making θ_{13} the best known mixing angle of the PMNS matrix.

1.3.4 Measuring δ_{CP}

As all the mixing angles have been measured to be non-zero and all the masses different, CP-violation is possible in the lepton sector if δ_{CP} is different from 0 and π. This possible CP-violation can be probed by the long-baseline neutrino experiments by measuring the probabilities for electron neutrino and antineutrino appearance in a beam of muon neutrinos and antineutrinos. Taking into account the matter effects, the probability for the appearance of ν_e in a ν_μ beam can be approximated by [58]:

$$\begin{aligned}\mathcal{P}(\nu_\mu \to \nu_e) \approx{}& \sin^2\theta_{23}\sin^2(2\theta_{13})\frac{\sin^2(\Delta_{31}-aL)}{(\Delta_{31}-aL)^2}\Delta_{31}^2 \\ &+ \sin(2\theta_{23})\sin(2\theta_{13})\sin(2\theta_{12})\frac{\sin(\Delta_{31}-aL)}{(\Delta_{31}-aL)}\Delta_{31}\frac{\sin(aL)}{aL}\Delta_{21}\cos(\Delta_{31}+\delta_{\text{CP}}) \\ &+ \cos^2\theta_{23}\sin^2(2\theta_{12})\frac{\sin^2(aL)}{(aL)^2}\Delta_{21}^2\end{aligned} \tag{1.42}$$

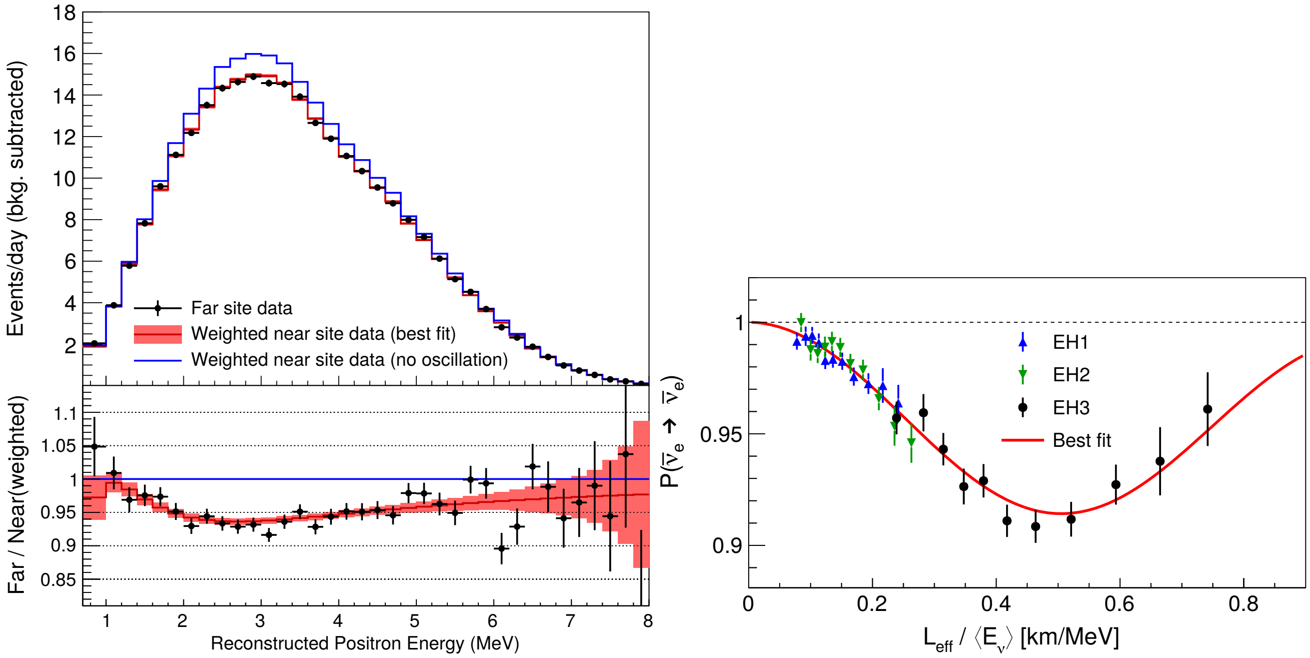

Figure 1.16: Daya Bay reconstructed positron energy spectrum compared with the expected values dervied from the near detectors without and with oscillations (upper left), ratio of the measured spectrum with the no-oscillation case with its systematic uncertainty (lower left), and $\bar{\nu}_e$ survival probability masured as function of L/E (right). (reproduced from [55])

where $\Delta_{ij} = \frac{\Delta m^2_{ij} L}{4E}$ and $a = \frac{G_F N_e}{\sqrt{2}}$ with N_e the electron density of earth. $\mathcal{P}(\bar{\nu}_\mu \to \bar{\nu}_e)$ can be obtained by reversing the signs of δ_{CP} and a. We can see that it is in theory possible to measure both δ_{CP} and the sign of Δm^2_{31} by observing only $\mathcal{P}(\nu_\mu \to \nu_e)$ given that it is directly impacted by both a and δ_{CP}. However, in order to increase the sensitivity and directly prove the CP-violation, long baseline neutrino experiments measure the difference between $\mathcal{P}(\nu_\mu \to \nu_e)$ and $\mathcal{P}(\bar{\nu}_\mu \to \bar{\nu}_e)$. Shorter baseline experiments such as T2K are less impacted by the matter effects and provide clean measurement of δ_{CP}.

On the contrary, longer baseline experiments such as NOνA and DUNE can probe also the mass hierarchy. T2K and NOνA will keep running but will only be able to reach at best a $3\,\sigma$ confidence on CP-violation or mass hierarchy. New generation experiments are necessary for a jump in statistics and accuracy.

Figure 1.17 shows the latests T2K and NOνA results on δ_{CP}.

1.3.5 Current knowledge of the PMNS parameters

Most of the parameters of the PMNS matrix have been measured since the first discovery of neutrino oscillations. Figure 1.18 shows the latest results of NuFIT [39] performing a combined fit of solar, atmoshperic and reactor neutrino oscillation data.

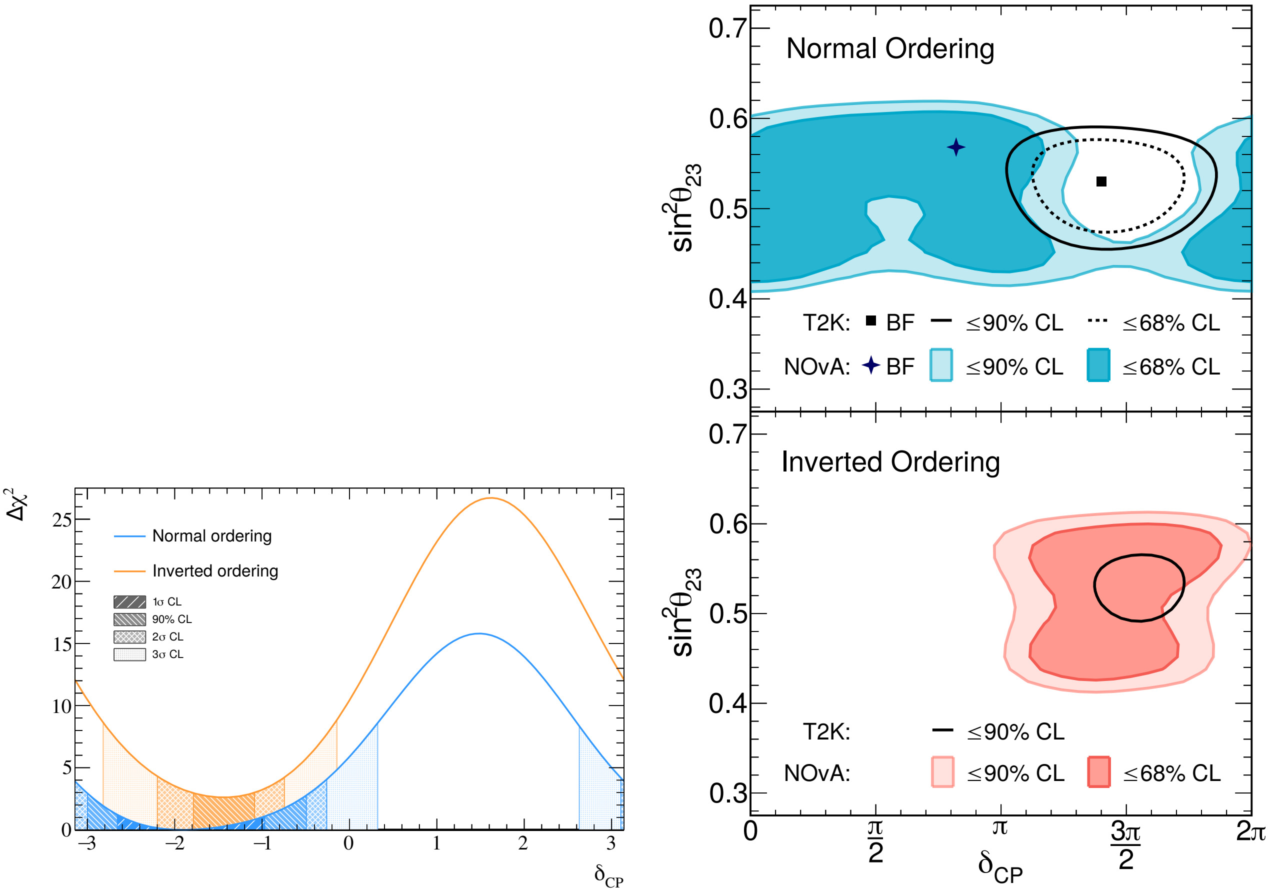

Figure 1.17: $\Delta\chi^2$ distribution of T2K best fit as a function of $\delta_{\rm CP}$ (left) and contours in the $\sin^2\theta_{23}$ versus $\delta_{\rm CP}$ plane obtained by NOνA and T2K. (reproduced from [59, 60])

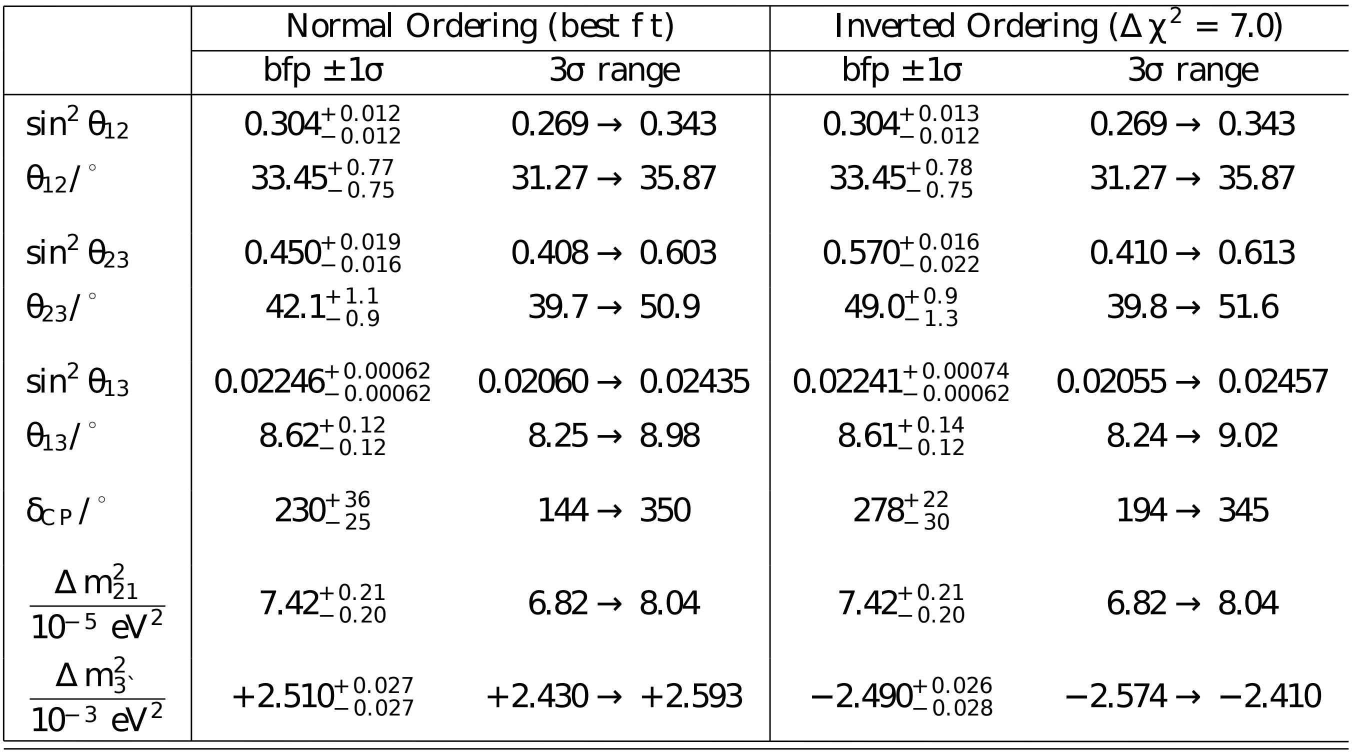

	Normal Ordering (best fit)		Inverted Ordering ($\Delta\chi^2 = 7.0$)	
	bfp $\pm 1\sigma$	3σ range	bfp $\pm 1\sigma$	3σ range
$\sin^2\theta_{12}$	$0.304^{+0.012}_{-0.012}$	$0.269 \rightarrow 0.343$	$0.304^{+0.013}_{-0.012}$	$0.269 \rightarrow 0.343$
$\theta_{12}/^\circ$	$33.45^{+0.77}_{-0.75}$	$31.27 \rightarrow 35.87$	$33.45^{+0.78}_{-0.75}$	$31.27 \rightarrow 35.87$
$\sin^2\theta_{23}$	$0.450^{+0.019}_{-0.016}$	$0.408 \rightarrow 0.603$	$0.570^{+0.016}_{-0.022}$	$0.410 \rightarrow 0.613$
$\theta_{23}/^\circ$	$42.1^{+1.1}_{-0.9}$	$39.7 \rightarrow 50.9$	$49.0^{+0.9}_{-1.3}$	$39.8 \rightarrow 51.6$
$\sin^2\theta_{13}$	$0.02246^{+0.00062}_{-0.00062}$	$0.02060 \rightarrow 0.02435$	$0.02241^{+0.00074}_{-0.00062}$	$0.02055 \rightarrow 0.02457$
$\theta_{13}/^\circ$	$8.62^{+0.12}_{-0.12}$	$8.25 \rightarrow 8.98$	$8.61^{+0.14}_{-0.12}$	$8.24 \rightarrow 9.02$
$\delta_{CP}/^\circ$	230^{+36}_{-25}	$144 \rightarrow 350$	278^{+22}_{-30}	$194 \rightarrow 345$
$\frac{\Delta m^2_{21}}{10^{-5}\ \text{eV}^2}$	$7.42^{+0.21}_{-0.20}$	$6.82 \rightarrow 8.04$	$7.42^{+0.21}_{-0.20}$	$6.82 \rightarrow 8.04$
$\frac{\Delta m^2_{3\ell}}{10^{-3}\ \text{eV}^2}$	$+2.510^{+0.027}_{-0.027}$	$+2.430 \rightarrow +2.593$	$-2.490^{+0.026}_{-0.028}$	$-2.574 \rightarrow -2.410$

Figure 1.18: Latest three-flavour oscillation parameters obtained by a global fit from [61].

The solar and reactor parameters are determined to a good precision and can be used to constrain the oscillation parameters in the long baseline experiments. The atmospheric parameters are less well known. The least known parameter is δ_{CP}. T2K was however able to provide first hints of CP-violation in the lepton sector by excluding the two CP-conserving values of 0 and π with a 95 % confidence level.

The two main unresolved questions about neutrino oscillations are the mass ordering and the value of the CP-violating phase δ_{CP}. The existence of CP-violation in the lepton sector could contribute to the explanation of the matter-antimatter asymmetry we observe in the universe, while discovering the right mass ordering might constrain new models beyond the standard model able to motivate the existence of a non-zero mass of neutrinos and of the flavour mixing.

1.4 DUNE as a next-generation experiment

The DUNE experiment, illustrated in Figure 1.19 aims at dermining the mass hierarchy and investigate CP-violation in the lepton sector. To do so, DUNE will measure the oscillation appearance probability $\mathcal{P}\left(\overset{(-)}{\nu}_\mu \rightarrow \overset{(-)}{\nu}_e\right)$ and the survival probility $\mathcal{P}\left(\overset{(-)}{\nu}_\mu \rightarrow \overset{(-)}{\nu}_\mu\right)$ of accelerator neutrinos produced at Fermilab and detected at Sanford, South Dakota. Its 1300 km-long baseline induces large matter effects, enhancing the sensitivity to the mass

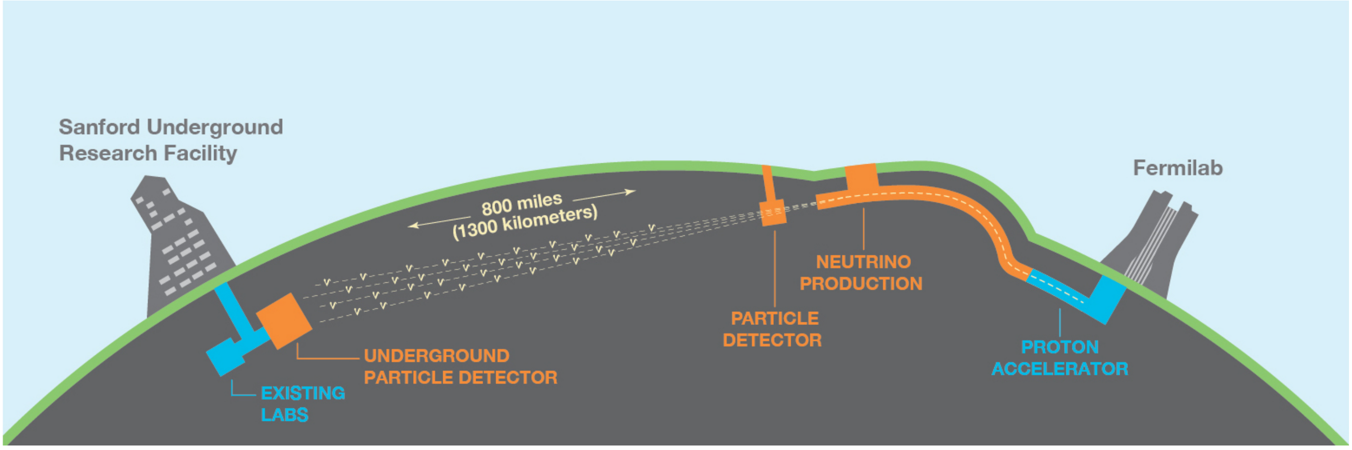

Figure 1.19: Illustration of the DUNE experiment. The DUNE experiment will be located in the US and will measure the neutrino oscillations 1300 km away from a ν_μ neutrino beam produced at Fermilab.

hierarchy. The neutrinos energy will be in the 0.5 GeV to 5 GeV range, allowing to cover two oscillation maxima in order to better discriminate CP-violation and matter effects, and to perform very precise measurements of oscillation parameters.

The DUNE far detector facility will be located in a South Dakota mine to reduce the cosmogenics-induced background. It is expected to be composed of 4 individual Liquid Argon Time Projection Chambers (LArTPCs), cumulating a total active mass of 40 kt. In the initial plan, two modules were foreseen to use the LArTPC technology successfuly tested in the context of the ICARUS and MicroBooNE experiments, while a third module would make use of the newly developed LAr Dual-Phase technology. The technology of the fourth and last module has not been yet decided. All the modules are expected to be progressively deployed in the far detector complex with a first data taking phase occuring with the two first modules installed. In order to test these two LArTPC technologies in detail before the construction of any DUNE module, two LArTPC prototypes were constructed during 2018 and 2019 at CERN: one LArTPC named ProtoDUNE-SinglePhase and a second protype based on the dual-phase technology referred to as ProtoDUNE-DualPhase.

Given its ambitious physics program, that we will discuss below, DUNE needs to be able to strongly constrain its systematics uncertainies on the beam flux and composition, and on the neutrino interaction cross-sections. DUNE will therefore feature a near detector complex aiming at monitoring the beam and constraining the various systematic uncertainties with multiple independant detection methods. The DUNE near detector complex will include the following detectors:

ND-Lar a liquid argon TPC using the ArgonCube technology [62]. It will provide the same target nucleus as the far detectors and use the same fundamental detection principle.

ND-Gar a high pressure gaseous argon TPC surrounded by an electromagnetic calorimeter (ECal) in a 0.5 T field. ND-Gar can access features at lower momentum threshold than ND-Lar allowing to precisely study the activity near the neutrino interaction vertex. Moreover, ND-Gar serves as a magnetic spectrometer for uncontained ND-Lar muons.

SAND System for on-Axis Neutrino Detection used to monitor precisely the beam flux. This detector is discussed in details in Chapter 4.

Unlike SAND, ND-Lar and ND-Gar can be moved in order to scan multiple off-axis angles and have access to different neutrino spectra according to the DUNE-PRISM (Precision Reaction-Independant Spectrum Measurement) paradigm. The DUNE-PRISM concept arose from the observation that the neutrino energy spectra measured at the near and far detector are intrinsically different as neutrinos have oscillated. As a consequence, the features measured on the near detector spectrum cannot be trivially extrapolated to the far detector spectrum. To cope with this issue, DUNE-PRISM proposes to measure the neutrino spectrum at various off-axis locations in the near detector complex and to linearly combines these spectra in order to match the observed oscillated spectrum at the far detectors. This linear combination of observations at different off-axis positions should allow to better cancel the various uncertainties in the near and far detectors ratio when performing the oscillation analysis.

A complete review of the DUNE near detector complex can be found in DUNE ND CDR [63].

In parallel, the main NuMI injector at Fermilab, that provided neutrino beams for the NOνA and MINOS experiments, is expected to be upgraded under the PIP-II project that should allow to reach a beam power of 1 MW by 2026. An additional upgrade, PIP-III, is already foreseen after 2030 in order to reach a beam power of 2.4 MW.

The main scientific cases of DUNE are:

- The determination of the CP-violation in the lepton sector and the determination of the neutrino mass ordering. Figure 1.20 shows the sensitivity if the DUNE experiment to the neutrino mass hierarchy and CP-violation as a function of the true δ_{CP} value for different exposures. DUNE will be able to establish the neutrino mass hierarchy at a $5\,\sigma$ confidence level for all the possible δ_{CP} values with 100 kt MW years exposure. With this same exposure, DUNE can also observe CP-violation with $3\,\sigma$ confidence in the case of maximal CP-violation. CP-violation can be observed with 5 σ significance with a 350 kt MW years exposure if $\delta_{\text{CP}} = -\pi/2$ and after a 700 kt MW years exposure for 50 % of δ_{CP} values, as shown in Figure 1.20.

- Conduct precise measurements of the neutrino oscillation parameters. Figure 1.21 shows the expected DUNE sensitivity as a function of the exposure for Δm^2_{32}, δ_{CP}, $\sin^2(2\theta_{13})$ and $\sin^2(2\theta_{23})$.
- The detection of rare events such as the search for supernovae neutrinos or of proton decay.

Several additional secondary scientific goals are pursued by the DUNE collaboration: the search for neutrino non-standard interactions, the search for sterile neutrinos, the observation of ν_τ appearance, or the detection of atmospheric neutrinos.

DUNE physics program is very challenging and therefore necessitates new technologies. DUNE will feature a new beam of high power and will make use of relatively new technology deployed to an unprecedented scale for its detectors. This thesis will focus on some of the technological innovations for DUNE.

1.5 Other next-generation oscillation experiments

DUNE is not the only planned neutrino oscillation experiments for the coming years. Other experiments aim at detecting the CP-violation in the lepton sector and establish the neutrino mass hierarchy.

1.5.1 JUNO and KM3NeT/ORCA

JUNO and KM3NeT/ORCA are two complementary next-generation neutrino detetors aiming at establishing the neutrino mass hierarchy.

The Jiangmen Underground Neutrino Observatory [66] is a medium-baseline (~ 53 km) reactor neutrino experiment that will aim at measuring the $\bar{\nu}_e$ disappearance channel with a L/E range where both Δm^2_{32} and Δm^2_{31} are significant. The strength of the JUNO measurement will be its independance on the value of δ_{CP}. The JUNO detector will be composed of 3 parts: a Central Detector filled with 20 kton of liquid scintillator detecting IBD interactions, and two outer detectors (a water Cherenkov detector and a Top Tracker) serving as a veto for the cosmics muon background. JUNO will also include a near detector (JUNO-TAO) placed at a distance of 30 m from the reactor in order to precisely determine the unoscillated $\bar{\nu}_e$ spectrum. The JUNO detector is expected to be completed in the coming years.

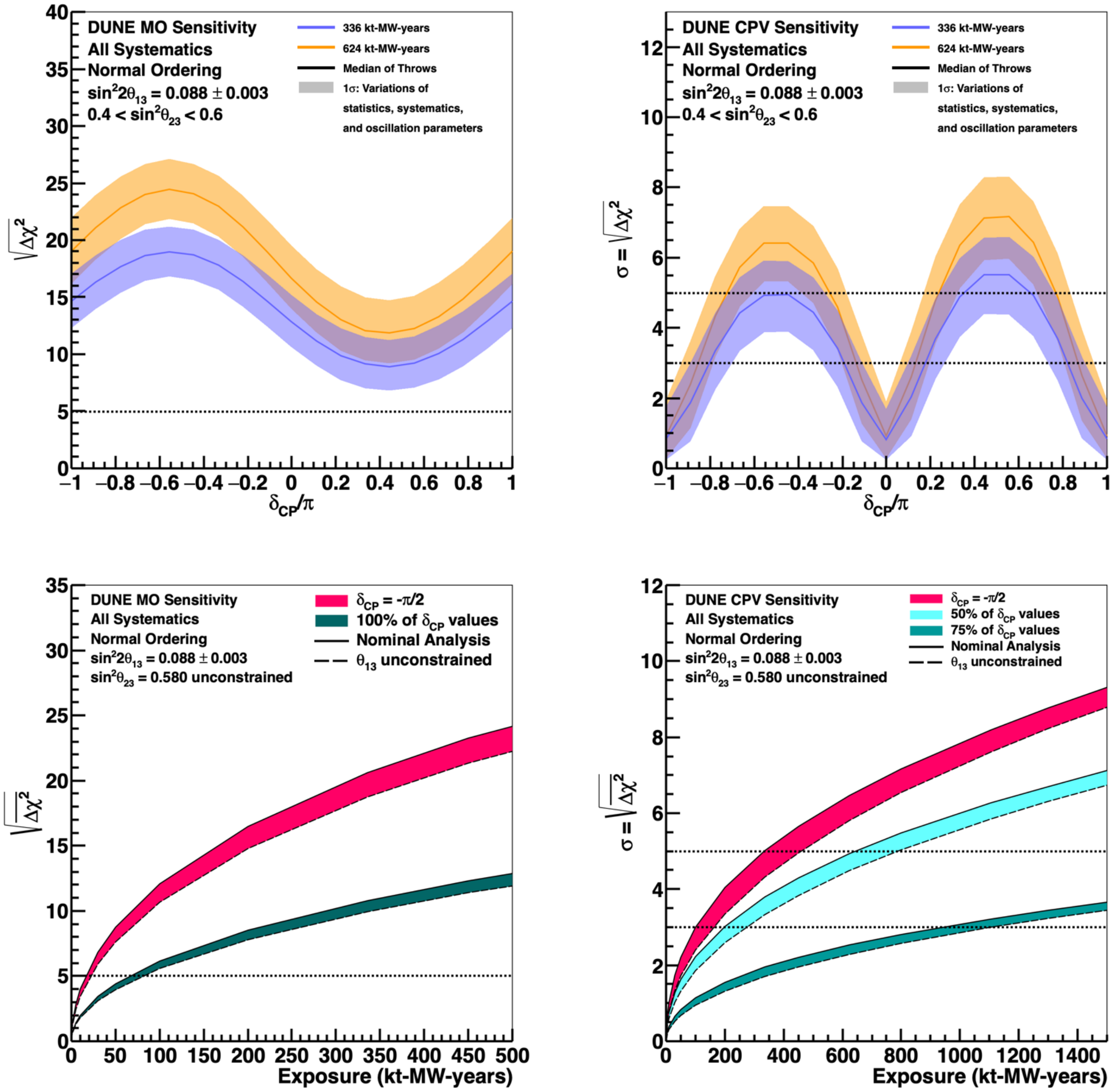

Figure 1.20: Sensitivity of the DUNE experiment to the neutrino mass ordering (left) and CP-violation (right) as a function of the true δ_{CP} value for several exposures (top) or as a function of exposure (bottom). (reproduced from [64])

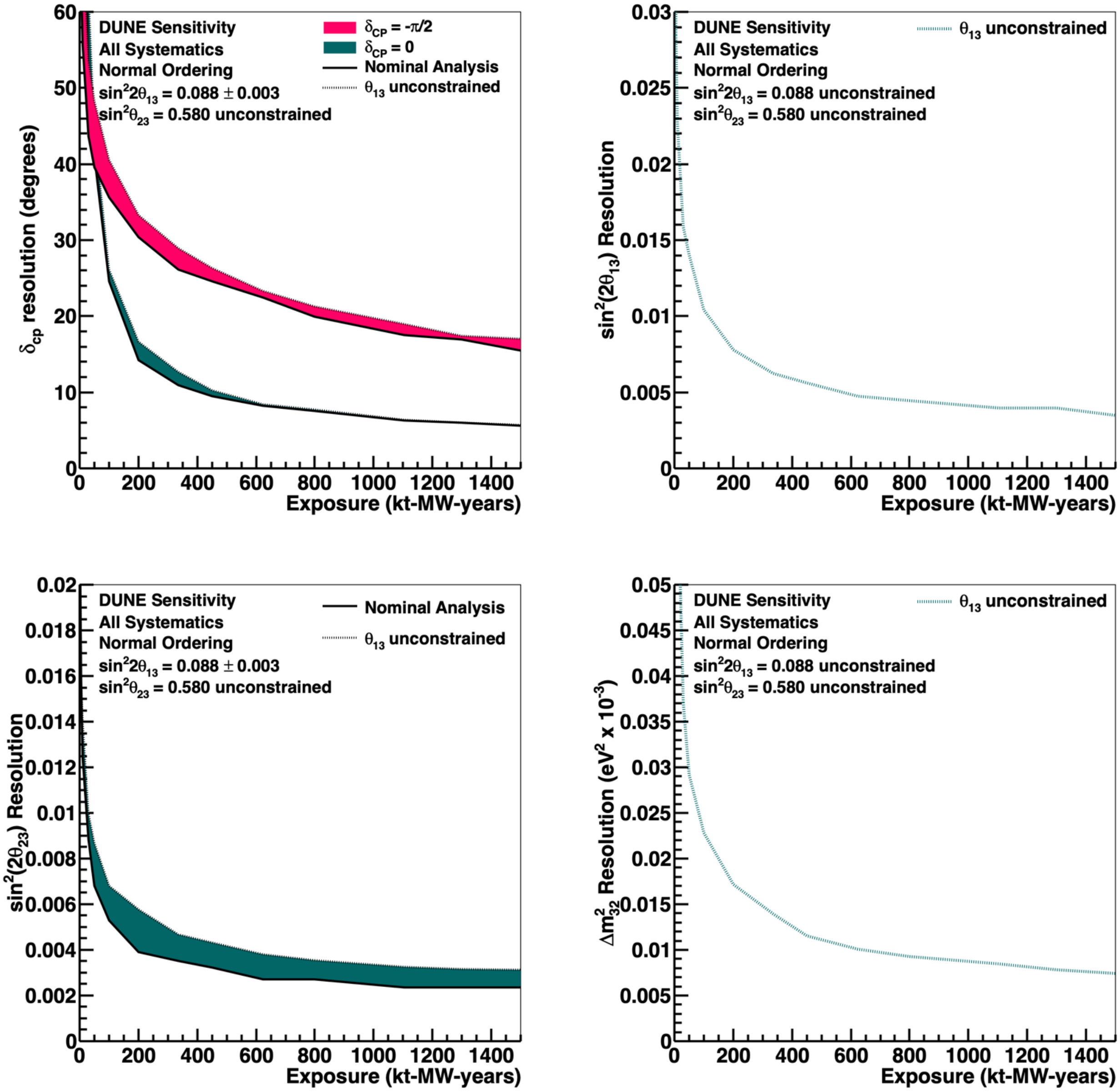

Figure 1.21: Sensitivity of the DUNE experiment as function of the exposure on δ_{CP} (top left), $\sin^2(2\theta_{13})$ (top right), $\sin^2(2\theta_{13})$ (bottom left) and Δm^2_{32} (bottom right). (reproduced from [65])

ORCA is the low-energy branch of the KM3NeT network of water Cherenkov neutrino telescopes. ORCA will probe mass hierarchy through the Earth matter effects on the atmospheric neutrino oscillations in the GeV energy range. The KM3NeT network is a set of water Cherenkov detectors installed in the Mediterranean sea, using the sea water as interacting medium. Two tridimensionnal PMTs arrays compose KM3NeT: ARCA (Astroparticle Research with Cosmics in the Abyss) and ORCA (Oscillation Research with Cosmics in the Abyss). ARCA will search for astrophysical neutrinos with energies above the TeV, while ORCA features a denser and smaller array of PMTs optimized for the analysis of atmospheric neutrinos oscillations above 1 GeV. The ORCA detector is expected to be composed of 115 detection lines. Some of them are already installed and their number will be gradually increased until 2025.

These two experiments are expected to be able to combine their results efficiently as they will take place on similar timelines, and more importantly, as they provide two different complementary approaches to the determination of the mass hierarchy, which enable an increased combined sensitivity. Indeed, when assuming a wrong mass ordering, the best fits for $|\Delta m^2_{31}|$ of ORCA and JUNO, that rely on the ν_μ amd $\bar{\nu}_e$ disappearance respectively, should lead to a tension, thus allowing to reject the wrong mass hierarchy. Studies have been conducted in order to evaluate the sensitivity to the neutrino mass ordering obtained from the combination of the results of the two experiments [67]. The estimated sensitivities are reproduced in Figure 1.22, where we can see an expected sensitivity above $5\,\sigma$, independantly of the true mass ordering, with 6 years of data taking of each experiment.

1.5.2 HyperKamiokande

The HyperKamiokande experiment is proposed as a T2K and SuperKamiokande successor, using the already acquired experience on the water Cherenkov technique and on the J-PARC beam.

HyperKamiokande will be a water Cherenkov detector enclosed in a cylindrical tank of 78 m height and 74 m diameter located in the Tochibora mine in Japan, with the same off-axis angle as SuperKamiokande with respect to the J-PARC neutrino beam. Its design will be similar to SuperKamiokande with an inner detector instrumented with a dense array of 20000 50 cm diameter PMTs, and an outer detector instrumented with ~ 5000 20 cm diameter PMTs used to reject background events. The total detector water mass will be of 258 kt with a fiducial volume of 187 kton.

HyperKamiokande will serve as a far detector of a J-PARC upgraded beamline with a beam power of 1.3 MW. The current INGRID and ND280 (in its upgraded design) will be kept as near detectors in order to constrain

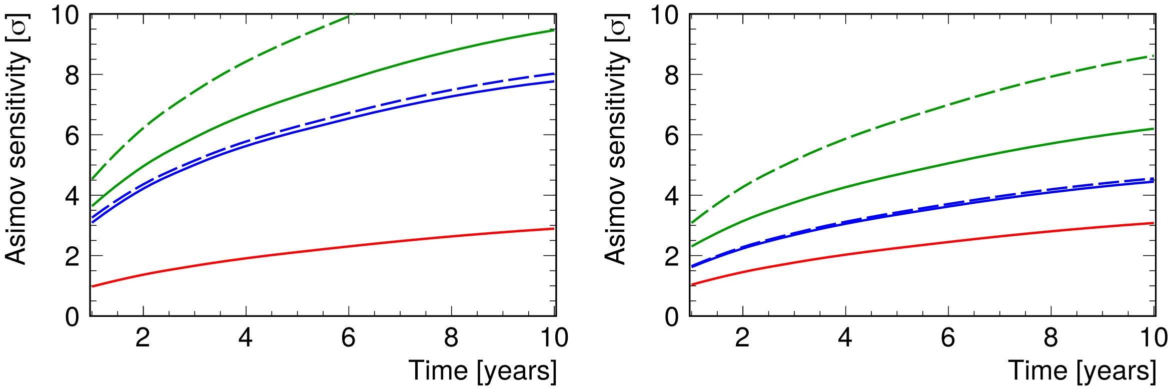

Figure 1.22: Sensitivity to the neutrino mass ordering as a function of time for JUNO alone, ORCA alone and the combination of both experiments in the case of the normal ordering (left) and inverted ordering (right). (reproduced from [67])

systematics error. An additional intermediate water Cherenkov detector (IWCD) is also proposed to be placed 1 km away from the beam source to take data in various off-axis positions. HyperKamiokande will also study atmospheric neutrino oscillations as SuperKamiokande is now doing.

The main goal of HyperKamiokande will be to discover CP-violation. HyperKamiokande is expected to discover CP-violation at a $5\,\sigma$ confidence level in around 2 years of operations for maximal CP-violation ($\delta_{\text{CP}} = \pm\pi/2$), and after ten years of operations, for more than $60\,\%$ of δ_{CP} values, as shown in Figure 1.23.

Given the relatively short baseline, identical to T2K, HyperKamiokande cannot measure the mass hierarchy with beam neutrinos. However, HyperKamiokande can benefit from its studies on atmospheric neutrinos oscillation in order to conduct a combined analysis allowing to determine CP-violation and establish the right mass hierarchy. This effect of increased sensitivity combining beam and atmospheric neutrinos is shown in Figure 1.24.

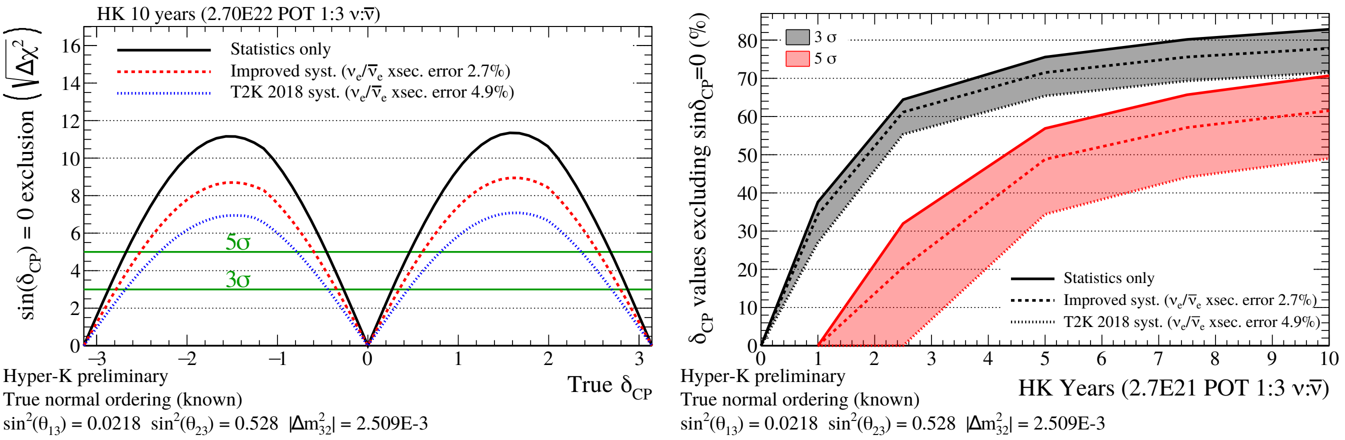

Figure 1.23: Sensitivity to CP-violation as a function of the true value of δ_{CP} in HyperKamiokande (left) and proportion of δ_{CP} values excluding CP conservation with $3\,\sigma$ and $5\,\sigma$ significances as a function of HyperKamiokande accumulated data (right). (reproduced from [68])

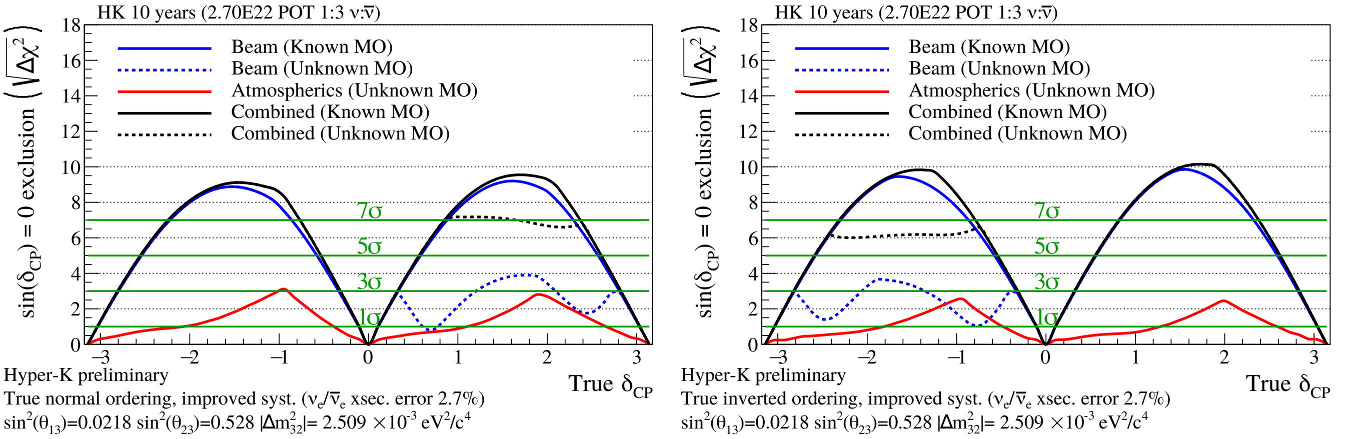

Figure 1.24: Sensitivity to CP-violation using beam neutrinos, atmospheric neutrinos and the combination of both assuming the normal mass ordering (left) or the inverted mass ordering (right). (reproduced from [68])

Chapter 2

The physics of Time Projection Chambers

Time Projection Chambers are a class of detectors that have proven their efficiency at precisely tracking charged particles. Constant improvements have been made since their first introduction in 1974, mainly on the amplification and readout side. A short review and the history and physics of Time Projection Chambers is proposed in this chapter.

2.1 History and working principle of Time Projection Chambers

2.1.1 History

Gaseous detectors have been used for more than a century now, starting with the experiment of Geiger and Rutherford in 1908 that led to the later invention of the Geiger-Müller counter, still in use nowadays. Gaseous detectors have then been largely used for particle tracking in the form of cloud chambers, for example, allowing to detect visually the paths of charged particles.

One major revolution in detector physics came from George Charpak in 1968, who received the Nobel Prize in 1992 for his work, with the invention of the Multi-Wire Proportional Chamber (MWPC) that allowed to transition to the era of electronics readout for particle physics detectors. Indeed, the previous detectors relied on an optical readout of the tracks (bubble chamber, cloud chamber, emulsions), limiting the achievable rates. MWPC allowed to reach detection rates of around 1 kHz while bubble chambers were limited to rates of 1 Hz

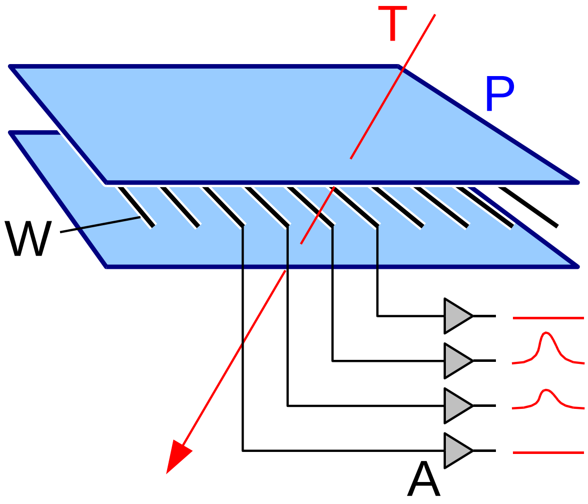

Figure 2.1: Scheme of a MWPC readout plane.

to 2 Hz. The MWPC, pushed by the rise of the semiconductor technology, allowed to economically cover large detectors thanks to their design made of parallel planes of conducting wires, as shown in Figure 2.1. A series of finely pitched wires (W) is used as an anode between cathode plates (P), creating a drift field under which the ionization electrons produced by charged tracks get collected on the wires. Moreover, MPWCs were able to provide signal amplification by relying on the electron Townsend avalanche phenomenon nearby the high voltage wires in the gas. To achieve particle tracking in 3D, MWPC required to use several wire plans in the whole chamber volume.

This need for a large number of planes in order to instrument a full volume was solved with introduction of the Time Projection Chamber (TPC) in 1974 by David Nygren. The TPC is a detector allowing to measure directly a track in three-dimensions by gathering simulteanously the x, y and z coordinates for each energy deposition, only requirind a single readout plane. To achieve this, the tracks are projected on the readout plane by drifting the ionization electrons produced in the whole TPC thanks to an electric field. Considering a drift direction along z, the readout plane allows to measure directly the (x, y) coordinate while the signal timing can be used to reconstruct the z position of any energy deposition which corresponds to the drift distance. The electron drift is ensured by applying a difference of potential between the readout anode and a high voltage cathode located on the other side of the TPC as shown in Figure 2.2.

The first TPC was used for the PEP4 spectrometer to study electron-positron collisions in the Stanford Linear Accelerator Center (SLAC). Since this first TPC, many of them have been built and used as particle trackers, especially at colliders. The working principle remains the same since the beginning, improvements were however

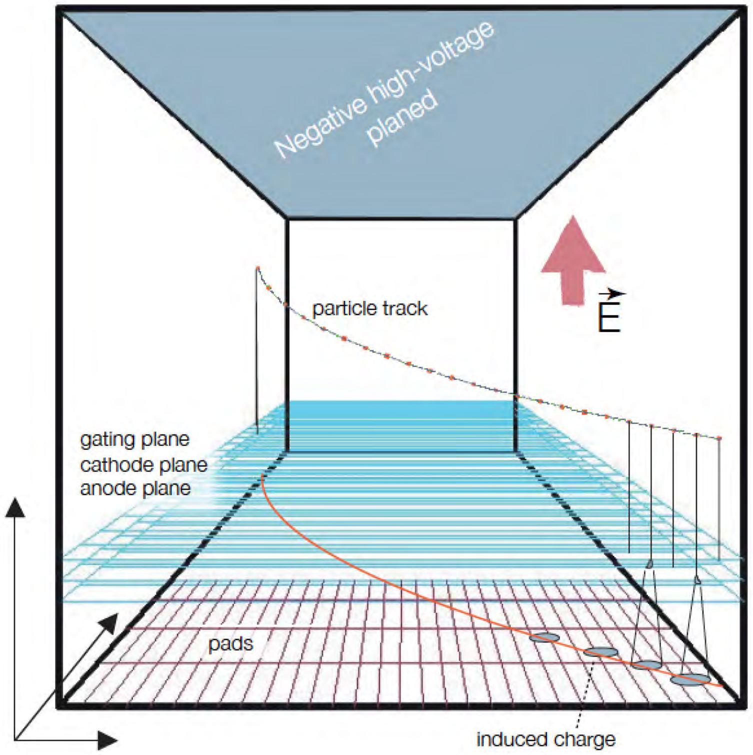

Figure 2.2: Scheme of a TPC.

made on the design of the readout planes to obtain higher amplifications and sustain higher rates. TPCs can also be used as a tracking target, most notably in nuclear physics for gaseous TPCs. Liquid TPCs can also be used as tracking targets, filled with cooled Argon or Xenon, to detect rare events such as neutrino interactions or dark matter. The necessity to transition to liquid phase for this kind of experiments comes from the increased density of the liquid phase (around 10^3 factor) allowing for more interactions to occur.

2.1.2 TPCs advantages

The main advantage of a TPC detector is its ability to directly reconstruct 3D tracks based on the hits location and time. The 3D reconstruction of the event topologies allows for the detection of specific interaction patterns. These patterns can help to clearly separate the seeked signals from any background and is a precious information allowing, for example, to reconstruct interaction vertices. Depending on the straightness of the track, one can evaluate the momentum of the particle with a fuzzy track indicating a low energy particle whereas a straight track is the sign of a higher energy particle as the multiple scattering angle will depend on the particle's momentum. This effect was for example used to determine the the momentum of muons in the ICARUS LArTPC [69]. In the presence of a magnetic field, the curvature of the track can also allow to directly measure the particle transverse

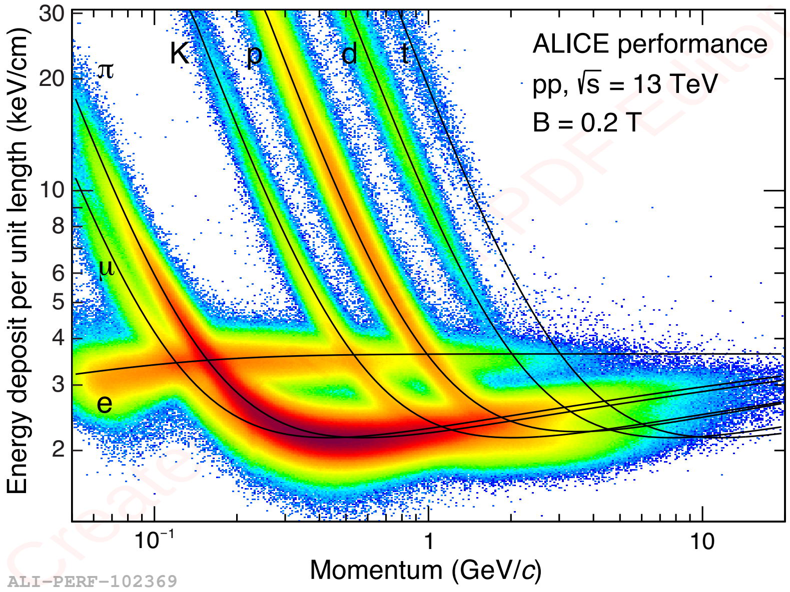

Figure 2.3: PID capabilities of the ALICE TPC in the $\frac{\mathrm{d}E}{\mathrm{d}x}$ vs. P plane.

momentum and its charge from its curvature radius. Indeed the radius of curvature of the track R depends directly on the particle transverse momentum p_T, charge q and magnetic field B:

$$R = \frac{p_T}{qB} \implies p_T[\text{GeV}] = 0.3B[\text{T}]\,R[\text{m}] \tag{2.1}$$

The differential energy loss of the ionising particles can also be measured along the tracks. This feature allows to perform particle identification (PID) as the differential energy loss at a certain particle energy is charecteristics of a particle type. The PID capabilities of the ALICE TPC are for example shown in Figure 2.3. Moreover, the ionizing profile along the track can be studied in order to detect, for example, a high ionization density at the end of the track, sign of a Bragg peak.

2.2 Energy deposition

2.2.1 Primary ionisation

Charged particle crossing the dectector loose energy both by excitation and ionization of the medium. The mean energy loss rate for charged particles can be described by the modified Bethe-Bloch equation [70]:

$$< \frac{\mathrm{d}E}{\mathrm{d}x} >= Kz^2 \frac{Z}{A} \frac{1}{\beta^2} \left[0.5 \ln \frac{2m_e c^2 \beta^2 T_{\text{max}}}{I^2} - \beta^2 - \frac{\delta}{2} \right] \tag{2.2}$$

Table 2.1: Parameters of Bethe-Bloch equation.

Symbol	Parameter	Value
N_A	Avogadro constant	$6.02 \times 10^{23}\,\mathrm{mol}^{-1}$
m_e	electron mass	$9.11 \times 10^{-31}\,\mathrm{kg}$
r_e	electron classical radius	$2.82 \times 10^{-15}\,\mathrm{m}$
c	speed of light in vacuum	$3.00 \times 10^{8}\,\mathrm{m\,s}^{-1}$
K	Coefficient for $\frac{\mathrm{d}E}{\mathrm{d}x}$	$4\pi N_A r_e^2 m_e c^2$
M	particle mass	
γ	particle lorentz factor	
β	Speed ratio	$\frac{1}{\gamma}\sqrt{\gamma^2 - 1}$
T_{max}	maximal energy transfer	$\frac{2m_ec^2\beta^2\gamma^2}{1+2\gamma\frac{m_e}{M}+\frac{m_e^2}{M^2}}$
A	material mass number	
Z	material atomic number	
I	material mean excitation energy	
δ	density correction term	

where the relevant parameters are reported in Table 2.1. The energy loss depends mostly on the β value of the charged particle. The rate of energy loss in shown in Figure 2.4 for muons in copper. Minimum Ionizing Particles (MIPs), that have $\beta\gamma \sim 3$ have a minimum energy loss per cm of 1 MeV/g cm^2 to 2 MeV/g cm^2 for all the materials except for hydrogen were the energy loss is 4 MeV/g cm^2. The mean energy loss rate obtained from the Bethe-Bloch equation includes the δ electrons that can be ejected away from the main track of energy deposition. Depending on the sensitivity of the detector to those δ electrons (possibly exiting the detector), corrections have to be applied to the Bethe-Bloch formula.

The energy loss inside a medium is a stochastic process with a mean value given by the Bethe-Bloch equation. However, the ionization is not constant along the particles trajectory. For MIPs that have an energy that can be considered constant during their travel inside a TPC, the distribution of the deposited energy per unit length $\frac{\mathrm{d}E}{\mathrm{d}s}$ follows a Landau law convoluted with a Gaussian [71]. An example of such a distribution is displayed in Figure 2.5. The Most Probable Value (MPV) of the Landau distribution depends on the energy of the ionizing particle. We can see that that the convolution with a gaussian shifts the Most Probable Value (MPV) of the distribution. For instance, for cosmic muons in liquid Argon, the expected MPV of the distribution is $\frac{\mathrm{d}E}{\mathrm{d}s} = 1.62\,\mathrm{MeV/cm}$ [72].

This deposited energy leads to the ionization of the material atoms. Each material possess a characteristic ionization yield, that describes the required energy deposited in order to ionize the material and extract one electron from it. This ionisation yield is noted W_I ans the number of ionisation electron, N_e, produced by an energy deposit E is

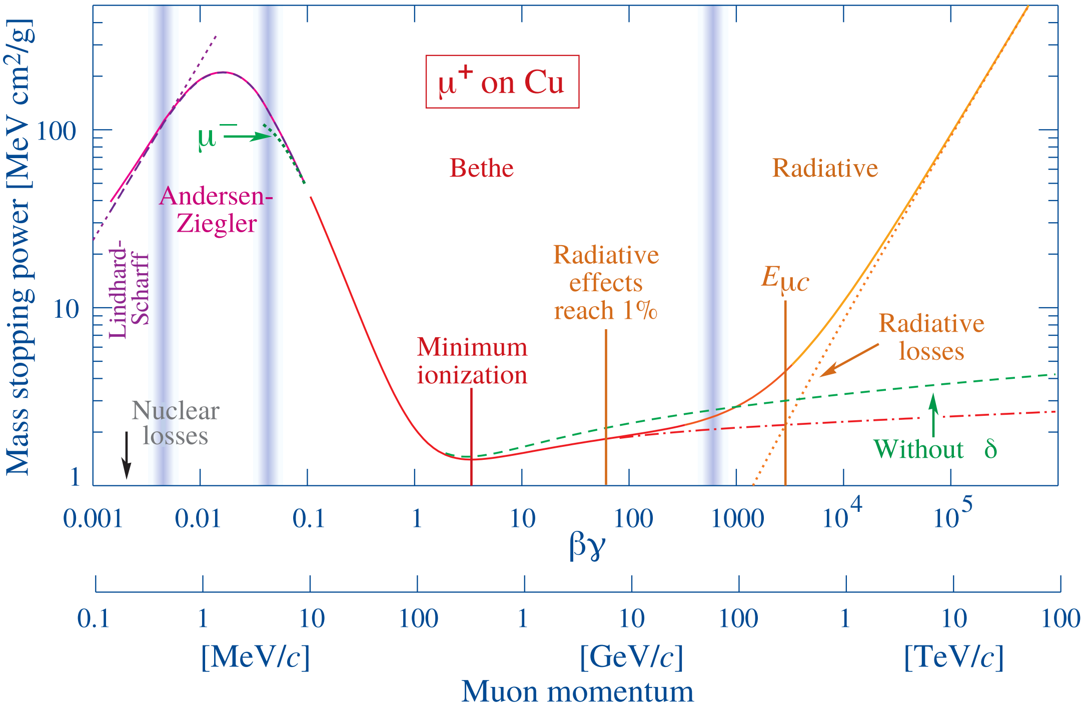

Figure 2.4: Mass stopping power for muons in copper as a function of $\beta\gamma$ (reproduced from [70]).

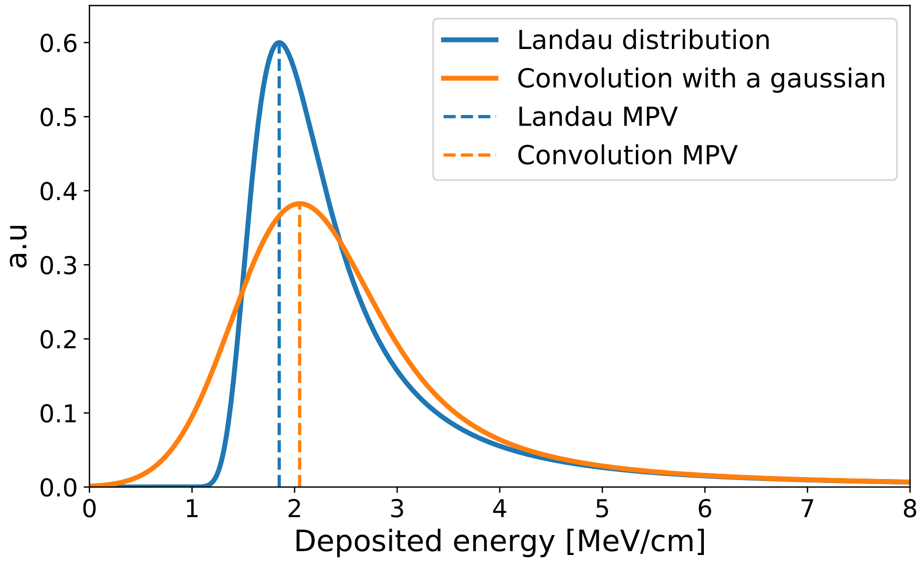

Figure 2.5: Example of a Landau distribution and its convolution to a gaussian.

$$N_e = \frac{E}{W_I} \tag{2.3}$$

W_I does not depend much on the material and, both for liquid and gas, stays in the range 15 eV to 40 eV meaning that the expected electron yield per deposited energy is 25 e^-/keV to 65 e^-/keV. We have $W_I = 23.6(3)$ eV [73] for liquid argon and a very similar value for pure gaseous argon. However, the ionisation yield can be modified by using gas mixtures by making use of Penning effect.

The Penning effect describes the possibility in a gas mixture for excited atoms or molecules A^* to deexcite and transfer its energy via a two-body collision to another atom or molecule B with a lower ionisation potential:

$$\mathrm{A}^* + \mathrm{B} \longrightarrow \mathrm{A} + \mathrm{B}^+ + \mathrm{e}^- \tag{2.4}$$

This process leads to the production of additional ionisation electrons from excited atoms or molecules instead of photo-emission or thermalisation. The Penning effect can therefore enhance the gas primary ionisation yield (and amplification as well) [74].

2.2.2 Recombination

Once the electrons are extracted from their nucleus by ionizing particle, a high density of positive ions lies close in space to a high density of electrons. Consequently, the electrons and ions can directly recombine if a sufficient electric potential is not applied in order to separate them as fast as possible. This effect is called recombination and, depends very strongly on the magnitude of the applied electric field but also partly on the track topology. Indeed, a ionization track aligned in the electric field direction will tend to increase the recombination effect as the produced electrons and ions will remain in contact for a longer time during their respective drift under the electric field. Several models have been developed in order to model the recombination effect by taking into account the local charge density and the electric field strength. These formula are most of the time phenomenological and are an adaptation of the Birks formula:

$$R = \frac{1}{1 + \frac{k}{\mathcal{E}}\frac{\mathrm{d}E}{\mathrm{d}x}} \tag{2.5}$$

where R denotes the fraction of remaining drifting charge after the effect of the recombination, $\mathcal{E}$ the local electric field strength, $\frac{\mathrm{d}E}{\mathrm{d}x}$ the rate of energy deposition and k a fitting parameter. This formula corrsponds

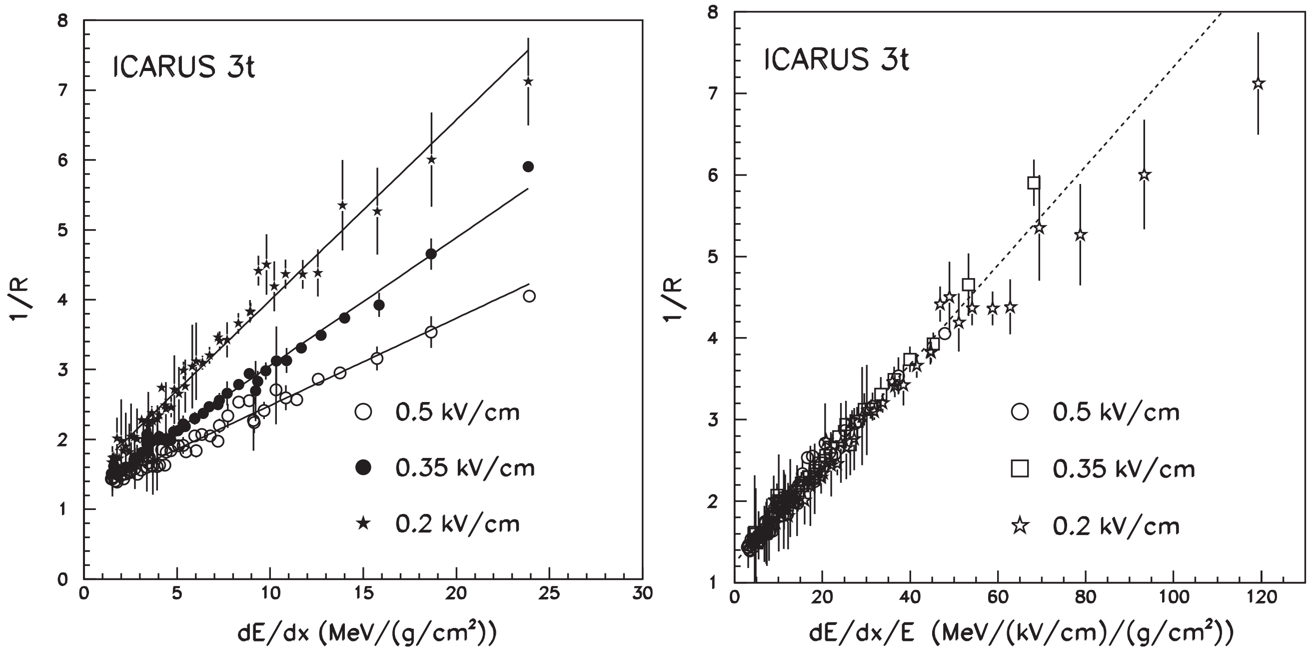

Figure 2.6: ICARUS recombination data. Birks fit of the inverse of the recombination factor vs. stopping power (left) and vs. stopping power divided by the electric field value (right) (reproduced from [75]).

to the Jaffé solution for the charge recombination within a column of ionized gas under the high drift field approximation. Recombination results obtained by the ICARUS collaboration in a liquid argon TPC are shown in Figure 2.6. For muon MIPs and a drift field of 500 V cm^{-1}, the measured recombination factor is for instance $R = 0.66$ meaning that a third of the electrons recombine.

2.2.3 Scintillation

The energy deposition of a charged particle produces scintillation in addition to ionization in liquid and gases. The scintillation yield that gives the number of scintillation photon per unit of deposited energy, W_{sc}, is in the range 15 eV to 70 eV for most materials. The typical light yield in LAr TPCs is of a few 1×10^4 photons/MeV [76]. The light production being isotropic, only a small fraction of the scintillation signal can reach light detectors eventually placed inside a TPC. As a consequence, the use of this primary scintillation for imaging or calorimetric measurement is challenging. However, in addition to the ionization signal, scintillation light also provides valuable information. Indeed, detection of scintillation light can provide a time reference for an event (t_0). The measurement of the scintillation light is therefore mostly useful for non accelerator-based experiments where the time reference cannot be acquired by other means and can be useful to reject background.

2.3 Charge drifting

In a TPC, the ionization electrons are drifted towards the electronic sensors of the detector allowing to measure the deposited energy and its position in the readout plane. The depth position is reconstructed from the electrons drift time allowing to fully recover the position of the energy deposition in 3D.

2.3.1 Field cage

A drift field can be provided by simply having a cathode at a potential lower than the anode creating an electric field inside the TPC volume. However, as the TPC dimensions increase, the field provided by two opposite conducting plate will be less and less homogenous, especially on the borders. In order to cope with this issue, the TPCs are encased inside a field cage that helps providing an homogenous drift field in the whole TPC volume. This field cage usually consist of metallic strips interconnected with high precision resistor creating a linear potential gradient, as this can be seen with the example of the XENON1T TPC shown in Figure 2.7.

The drift field has to be aligned with the magnetic field, if any, thus requiring a high mechanical precision and stability of the field cage. Moreover the handling of high voltages requires a high electrical stability. However, these requirements can enter in conflict with the necessity to use low radiation length materials for the field cage to limit energy loss of particles entering the TPC. In addition, it is necessary to limit the amount of insulating surfaces to avoid possible charging up effects that could modify the produced electric field. Indeed, the insulating surfaces can collect the different charges when exposed to electric fields leading to local modifications of the field.

2.3.2 Space charge effect

The ionization of the TPC medium creates electron/ion pairs that drift towards the anode/cathode of the TPC respectively. However the drift velocities of the electrons and ions in the medium differ. For liquid TPCs where the medium is dense, the respective drift velocities of electrons is typically 5 or 6 orders of magnitude larger than those of ions. In gaseous TPCs, the drift velocities of the electrons and ions differ too but by a smaller factor. Therefore, under a continuous injection of charges, as it is the case with cosmic-ray muons on Earth surface, for example, a large density of positively charged ions can build-up inside a TPC, most notably in non-gaseous TPCs. Nonetheless, this can also happen in gaseous TPCs because when large numbers of ions are produced

Figure 2.7: Picture of the XENON1T TPC fieldcage.

from multiplication in gas.

A simple unidimendional model of the effect of these charges on the TPC electric field can be easily developed. Given the large difference in the electrons and ions drift times, we can consider that the charge density in the TPC volume is mostly due to the positive ion. The continuity equation of the charge conservation is therefore:

$$\frac{\partial \rho^+}{\partial t} + \nabla \cdot \left(\rho^+ v^+\right) = K \tag{2.6}$$

where ρ^+ and v^+ designate the positive ion density and mean velocity while K is the charge density injection rate. The value of K depends directly on the amount of ionization made in the detector by crossing ionizing particles and on the electric field strength that drives the early electron/ion recombination. The stationary solution for which $\frac{\partial \rho^+}{\partial t} = 0$ is of particular interest as the system should converge to it after some time if we consider a constant charge density injection rate K. In reality, the space charge itself induces distortions of the electric field leading to a space dependant K, but this second order effect is not considered here.

Supposing an electric field produced by two parallel plates with a potential difference of V and a distance of L producing an electric field $E_0 = \frac{V}{L}$ directed along $+x$, the stationary solution becomes:

$$\frac{\mathrm{d}(\rho^+ v_x^+)}{\mathrm{d}x} = K \tag{2.7}$$

that can be solved, introducing the ion mobility $\mu^+ = \frac{v_x^+}{E_x}$, as:

$$\rho^+(x) = \frac{Kx}{\mu^+} E_x(x) \tag{2.8}$$

using the boundary condition $\rho^+(0) = 0$ as no positive ion accumulate at the anode.

Gauss' law can then be used to compute the resulting electric field:

$$\frac{\mathrm{d}E_x}{\mathrm{d}x} = \frac{\rho^+}{\varepsilon} = \frac{Kx}{\varepsilon \mu^+ E_x} \tag{2.9}$$

This can be directly solved as

$$E_x(x) = E_0 \sqrt{\frac{E_a}{E_0}^2 + \alpha^2 \left(\frac{x}{L}\right)^2} \tag{2.10}$$

introducing the electric field at the anode E_a that can be computed from the boundary condition $\int_0^L E_x \, \mathrm{d}x$, and the dimensionless parameter α defined as

$$\alpha = \frac{L}{E_0} \sqrt{\frac{K}{\varepsilon \mu^+}} \tag{2.11}$$

As shown in Figure 2.8, the field at the anode, E_a, is always lower than the nominal field E_0, while the field at the cathode, E_c, is always larger. A critical situation occurs for $\alpha > 2$, with a vanishing electric field at the anode. This case leads to the formation of an area with high positive ion density where ionization electrons witness almost total recombination, thus reducing the effective TPC active region.

In the case of a liquid argon detector operated at the surface and subject to cosmic rays, the charge density injection rate is approximately given by $K = 2 \times 10^{-10}\,\mathrm{C\,m^{-3}\,s^{-1}}$. Considering $L = 6\,\mathrm{m}$, $E_0 = 500\,\mathrm{V\,cm^{-1}}$, a dielectric constant of 1.504, and a ion monility $\mu^+ = 1.6 \times 10^{-7}\,\mathrm{m^2\,s^{-1}\,V^{-1}}$, the dimensionless parameter α equals 1.16. For such a value, Figure 2.8 shows that the field at the anode is reduced by 23 % and the field at the cathode increased by 39 % with respect to the nominal field value. Figure 2.9 shows more precisely the field evolution with depth. This shows that space charge effects have to be taken into account for liquid argon TPCs operated at the surface like the ProtoDUNE experiments.

The space charge effect can be an important issue for TPCs. Indeed, TPCs rely on the constant drift velocity and straight field lines in order to fully reconstruct the tracks in 3D. Any modification of the electric field, through space charge effect for example, modifies the drift of the electrons and requires corrections to be made in order

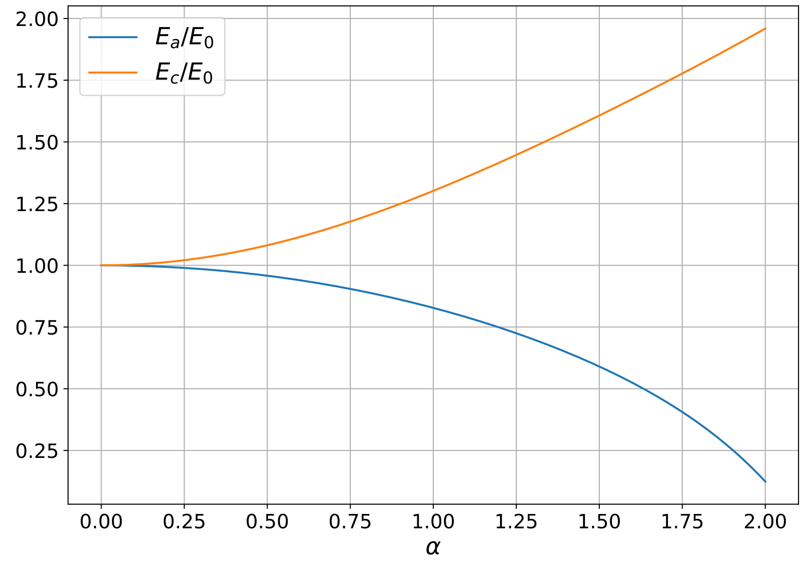

Figure 2.8: Normalized electric field at the anode and cathode as a function of the dimensionless parameter α. Computed using the approximations from [77].

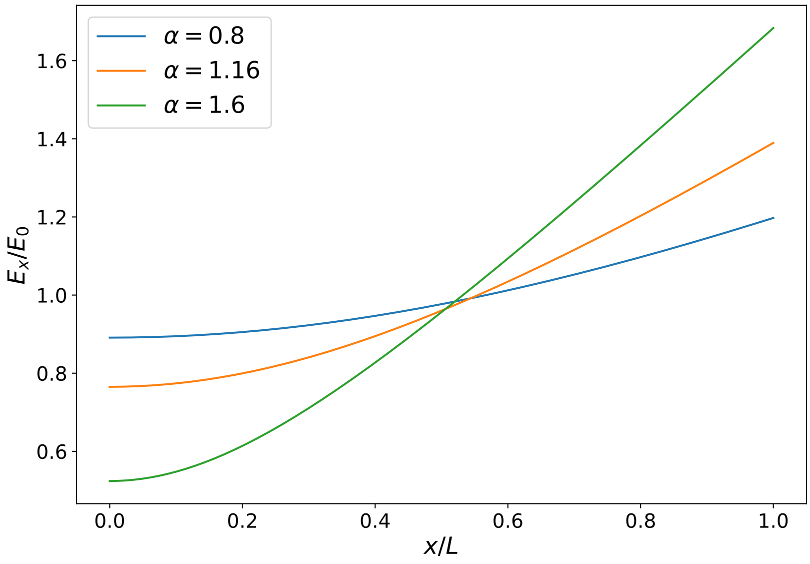

Figure 2.9: Electric field deviation with respect to the nominal field for different α values.

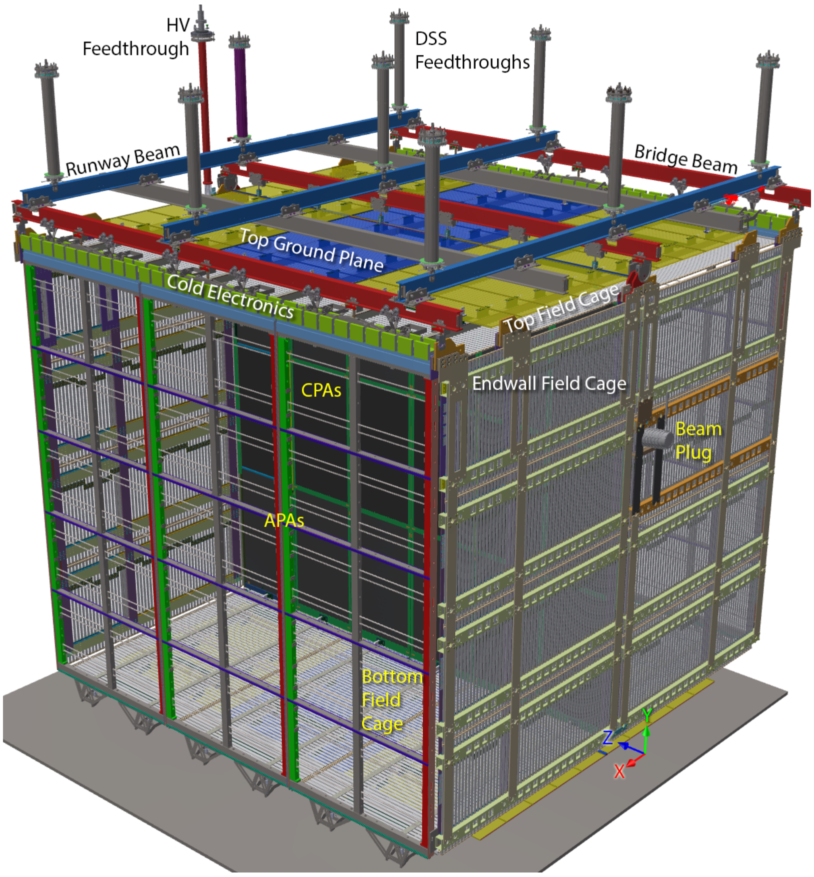

Figure 2.10: Schematic view of ProtoDUNE-SP.

to recover the true track trajectories. The modifications of the drift field with respect to the nominal field also impact the recombination effect and can therefore also shift the energy measurements made by the TPC.

The space charge effect has been measured by the ProtoDUNE-SinglePhase experiment of which a scheme is presented in Figure 2.10. Projections of reconstructed cosmic-ray tracks are shown in Figure 2.11. The tracks are choosen to cross the cathode (at $x = 0$). Without space charge effects, the track end points should be reconstructed on the TPC active volume boundaries that are respresented with dashed lines. We can see that the space charge effect distorts the tracks reconstructions. Figure 2.12 quantifies more specifically these distortions by showing the corrections to apply for tracks crossing different sides of the detector in order to recover the true tracks position. The distortions due to the space charge effect are shown to be as high as 40 cm which means that the space charge effect is of major importance when operating a liquid argon TPC at the surface. For underground experiments, the effects are smaller as the charge density injection rate is largely reduced. In the case of DUNE, the muon charge injection rate will become negligeable and the main charge injection is expected to come from the ^{39}Ar radioactivity with a natural argon activity around 1 Bq/kg.

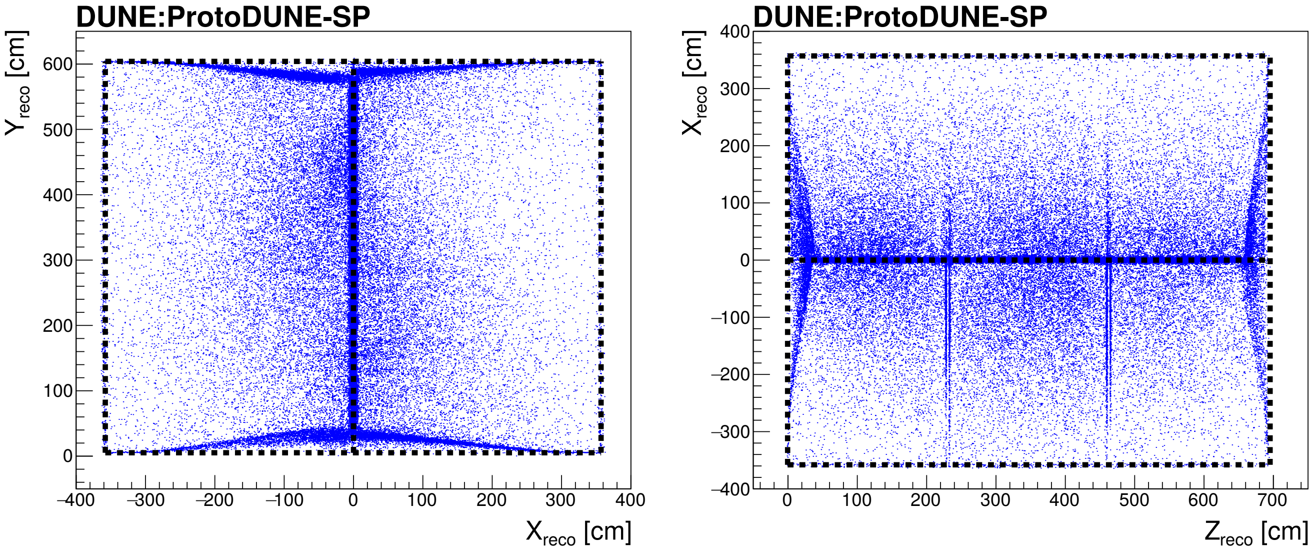

Figure 2.11: Projections of reconstructed cathode crossing cosmic-ray track end points in the xy plane (left) and zx plane (right) in ProtoDUNE-SP data with a drift along x (reproduced from [78]).

2.3.3 Electrons drift

Assuming a perfectly homogeneous drift field and no space charge effect, the drifting of the electrons can be described with an hydrodynamic approximation of the Boltzmann equations [79]:

$$\frac{\partial n_e}{\partial t} + v_d \frac{\partial n_e}{\partial z} - D_T \left(\frac{\partial^2 n_e}{\partial x^2} + \frac{\partial^2 n_e}{\partial y^2} \right) - D_L \frac{\partial^2 n_e}{\partial z^2} = -\eta v_d n_e \tag{2.12}$$

assuming a drift along the z direction. n_e designates the electron density, v_d the drift velocity, D_L and D_T the longitudinal and transverse diffusion coefficients respectively due to the scattering of the electrons in the medium during their drift, and η the attachment coefficient corresponding to the rate of attachment of the electrons on electronegative impurities in the TPC gas or liquid.

The various parameters of the drift, such as the drift velocity and the diffusion coefficients, can be numerically estimated with specific softwares, such as Magboltz, for each specific gas mixture. The drift parameters for some typical gas mixture used for TPCs are shown in Figure 2.13.

This drift equation can be easily solved when far enough from the boundaries, leading to:

$$n_e(x, y, z, t) = RN_e e^{-\eta v_d (t-t_0)} \times \frac{e^{-\frac{(x-x_0)^2 + (y-y0)^2}{4D_T(t-t_0)}} e^{-\frac{((z-z_0)+v_d(t-t_0))^2}{4D_L(t-t_0)}}}{4\pi(t-t_0)\sqrt{D_L D_T}} \tag{2.13}$$

where (x, y, z, t) correspond to the current position while (x_0, y_0, z_0, t_0) refer to the initial position and time

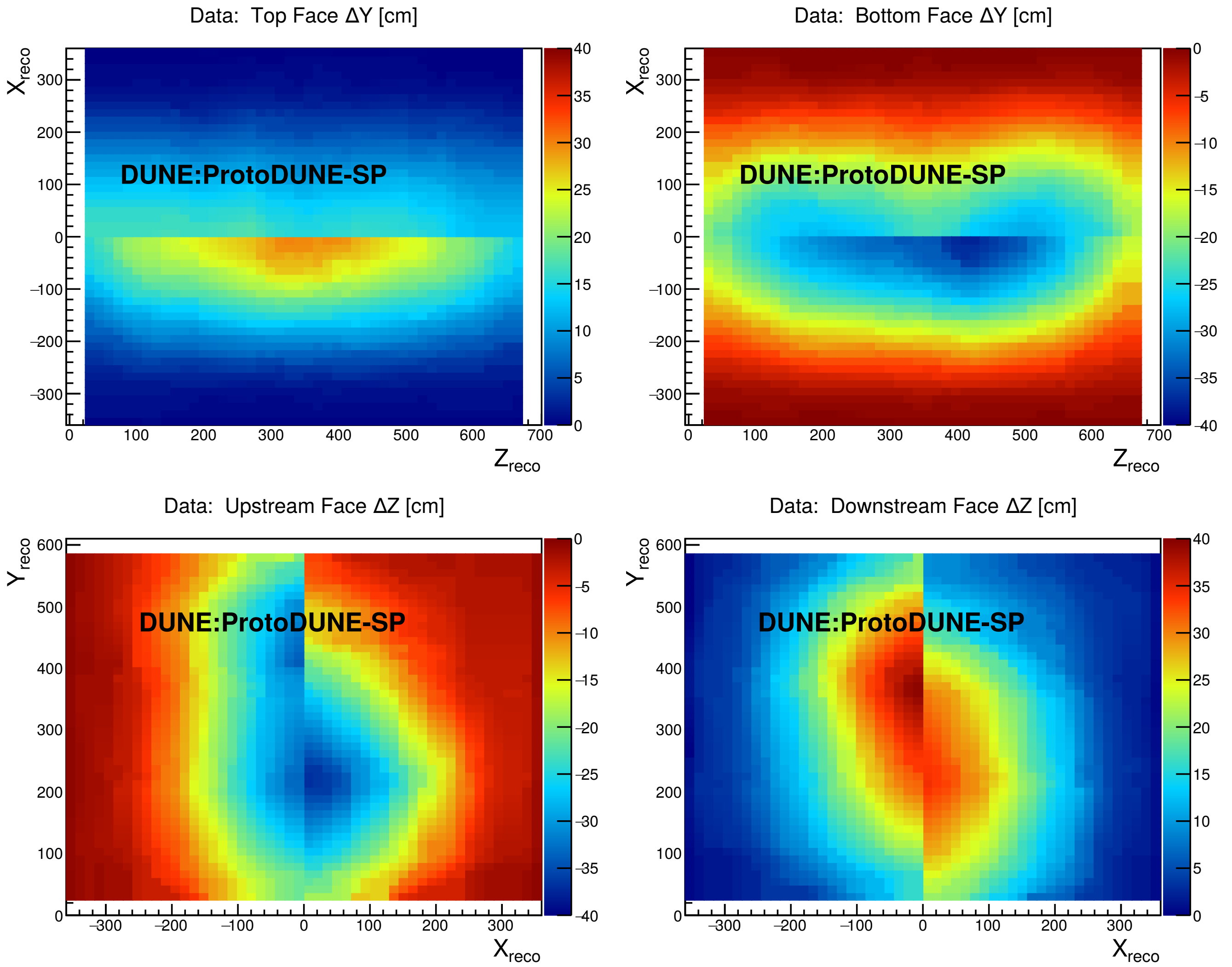

Figure 2.12: Spatial distortions to apply to the start/end point of a track passing through the given face of the TPC in ProtoDUNE-SP data to access its true position (reproduced from [78]).

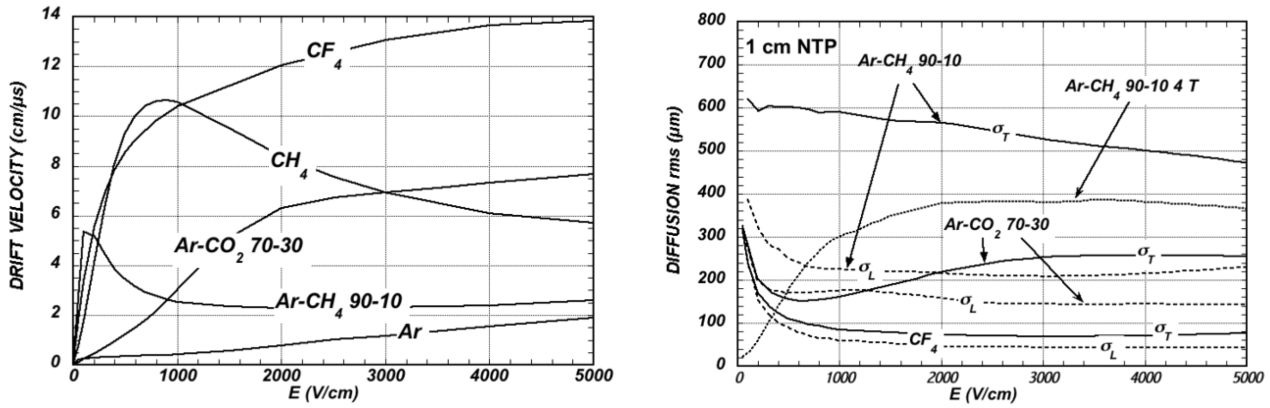

Figure 2.13: Electron drift velocity as a function of electric field in several gases (left), and longitudinal and transverse diffusions for 1 cm of drift (reproduced from [70]).

of the electron cloud. This solution corresponds to a gaussian electron cloud that broadens asymetrically in the longitudinal and transverse directions along the drift while losing charges to electronegative impurities.

The spread of the charge in space during the drift is due to the random motion of the electrons as they scatter into encountered atoms. The characteristic longitudinal and transversal spread depend on the drift distance z, with the following relation:

$$\sigma_{L,T} = D_{L,T}\sqrt{z} \tag{2.14}$$

An interesting phenomenon that was considered since the first introduction of the TPC in 1974, is the reduction of the transverse diffusion in the presence of a magnetic field parallel to the drift field. Indeed, this additional magnetic field, in addition to curving the charged particles to make their momentum measurable using spatial information, also constrains the movement of the electrons in the directions transverse to the drift field. As a consequence the diffusion effect is reduced and the spatial resolution is increased as the width of the electron clouds is limited. This reduction in the transverse diffusion is a function of the cyclotron frequency, $\omega = \frac{q_e}{m_e}B$:

$$D_T(B) = \frac{D_T(0)}{\sqrt{1+\omega^2\tau^2}} \tag{2.15}$$

where τ is the mean time between collisions and depends on the medium density and the electric field, and m_e and q_e are the electron mass and charge respectively. This effect can be seen in Magboltz simulations as shown in Figure 2.14. TPCs at atmospheric pressure manage to reach sub-mm diffusion over a drift of 1 m using a strong magnetic field.

2.3.4 Attachment

During their drift in the TPC, part of the electrons from the ionization cloud can attach to electronegative impurities present in the gas or liquid. This translates as a charge attenuation along the drift that can be described through the concept of electron lifetime τ. The electron lifetime represents the drift time for which the number of carriers has been reduced by a factor e and is linked to the attachment rate and drift velocity through:

$$\tau = \frac{1}{\eta v_d} \tag{2.16}$$

The fraction of remaining electrons after drifting over a distance z follows an exponential law as shown in

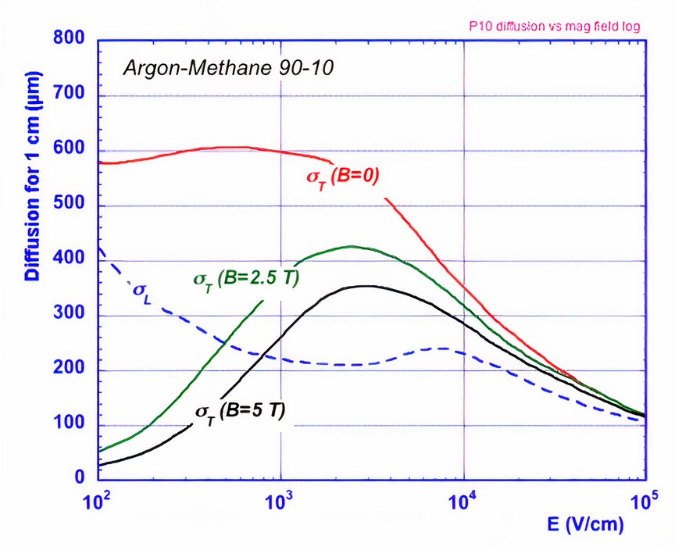

Figure 2.14: Evolution of the Ar-CH_4 diffusion coefficients with the drift field and magnetic field simulated with MagBoltz (reproduced from [80]).

Equation 2.13, and the attenuation factor is

$$\mathcal{A}(z) = e^{-\frac{v_d z}{\tau}} \tag{2.17}$$

The attachment rate of the electrons depends on the type of impurities. One of the contaminants with the highest attachment rate is O_2. The following two step process for the attachment of drifting electrons into O_2 impurities has been proposed [81]

$$\mathrm{e^-} + \mathrm{O_2} \longrightarrow \mathrm{O_2}^{-*} \tag{2.18}$$

$$\mathrm{O_2}^{-*} + \mathrm{X} \longrightarrow \mathrm{O_2}^{-} + \mathrm{X}^* \tag{2.19}$$

where the main gas consistuent X acts as a stabilizer for the dissipation of the captured electron kinetic energy.

The attachment rate also depends on the density inside the detector. Liquid TPCs are therefore more susceptible to the presence of impurities as their effect on the charge attenuation is much stronger. It was for example measured for liquid argon TPCs at a drift field of $\mathcal{E} = 500\,\mathrm{V\,cm^{-1}}$ that the relation between the electron lifetime and the O_2 concentration, $f_{\mathrm{O_2}}$ is the following [82]:

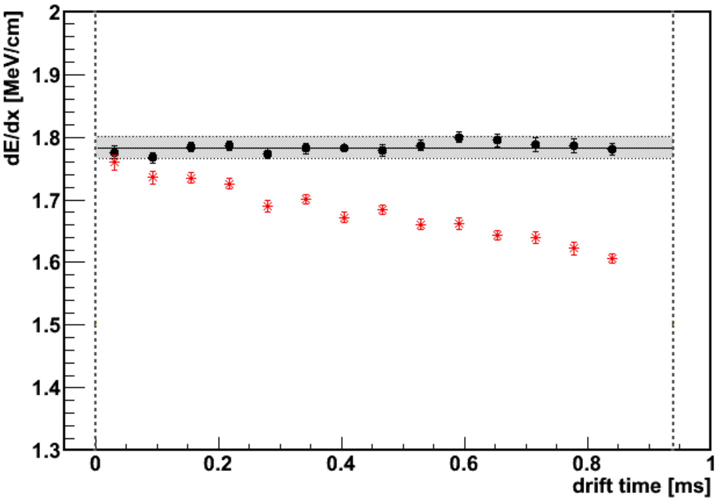

Figure 2.15: Mean energy loss for minimum ionizing particles in liquid argon as a function of drift time (red) and corrected after electron lifetime fitting (black) of 9 ms corresponding to an O_2 contamination around 30 ppt in ICARUS experiment (reproduced from [83]).

$$\tau = \frac{300\,\text{ms}}{f_{\mathrm{O}_2}[\text{ppt}]} \tag{2.20}$$

Consequently, any experiment involving a large liquid argon TPC needs to reach a sub-ppb level of O_2 contamination in order to obtain electron lifetimes larger than ms, necessary to drift electrons on a long distance (few meters) without too much charge attenuation. Figure 2.15 shows the attenuation witnessed in the ICARUS experiment that managed to purify its liquid argon up to around 30 ppt, given the observed electron lifetime.

For gaseous TPCs, the electron lifetime is typically smaller but has a large dependance with the gas pressure. It has been shown [84] for argon-based gaseous TPCs to be of the form:

$$\tau = \frac{1}{P^2[\text{bar}^2]}\,\frac{\tau_0[\text{ms}]}{f_{\mathrm{O}_2}[\text{ppm}]} \tag{2.21}$$

Note that similar expressions can be obtained for different contaminents. For a Ar/CH_4/i-C_4H_{10} (88/10/2) gas mixture and $E/P = 100\,\text{V}\,\text{cm}^{-1}\,\text{bar}^{-1}$, τ_0 has been measured to be 13.8(50) ms [84].

2.4 Charge detection

Several ways of detecting the charge signal in a TPC are possible. The detecting devices often operate by creating electron avalanches from the ionisation electrons in an amplification part of the detector. The avalanches have to be created with small size in order to not deteteriorate the spatial resolution. A wide range of multiplicators can be operated depending on the experiment requirements in terms of S/N ratio. For most of the TPCs existence, wire-based multiplication has been used in order to create the avalanches. Wires pitched by a few millimeters are set at a high voltage and allow to locally multiply the charges. However there are some limitations to this kind of detectors. First, the spatial resolution is limited by the possibility to assemble wire planes with small pitches between the wires. Then the wires have to remain perfectly tensioned and not to move and the disuniformity of the field around the wires induces $\vec{\mathbf{E}} \times \vec{\mathbf{B}}$ effect which deteriorates the spatial resolution. Moreover, the rate capabilities of MWPC are limited to a few kHZ/cm^2 because of the long ion drift time and induced space charge density which reduces the effective electric field.

Over the last two decades, the rise of Micro-Pattern Gas Detectors (MPGDs) as multiplication structures has been seen. This terms regroups all the amplification devices featuring either sub-millimetric holes, strips or gaps to conduct the avalanching process. A lot of these MPGDs make use of optimized industrial procedures allowing to drill or form micro structures with a size that can be below 100 µm over surfaces of multiple m^2.

The currently used MPGD detectors can be grouped in two main families: the detectors based on strip or hole structures and the detectors based on micromesh.

2.4.1 Micro-strip gas chamber (MSGC)

The first micro-structure gas detector, the Micro-Strip Gas Chamber (MSGC), was invented in 1988. It contains a set of small parallel metal strips (~ 10 µm) applied by photo-lithographic process onto a thin resistive support. The metal strips are alternatively connected as anodes and cathodes with a typical pitch of ~ 100 µm as shown in Figure 2.16. Applying a sufficient voltage to the electrodes leads to the multiplication and collection on the anodes of the nearby free electrons. The small distance between the anodes and cathodes allows for the fast collection of the positive ions on the cathode strips resulting in a fast signal rise time and removal of any space charge build-up.

Despite the promising performance improvements proposed by the MSGC with respect to the previous MWPC detectors, several issues can appear at high rates. For example, high charging-up of the substrate and destructive discharges can be witnessed. This issue of discharges is common to most MPGD designs. Indeed, when the total charge in the electron avalanche reaches the Raether limit of 1×10^7 to 1×10^8 electron ion pairs [86], a conductive path can be established between the cathode an anode leading to a breakdown. The large amount of released energy during this breakdown discharge can severely damage the detector as shown in Figure 2.16.

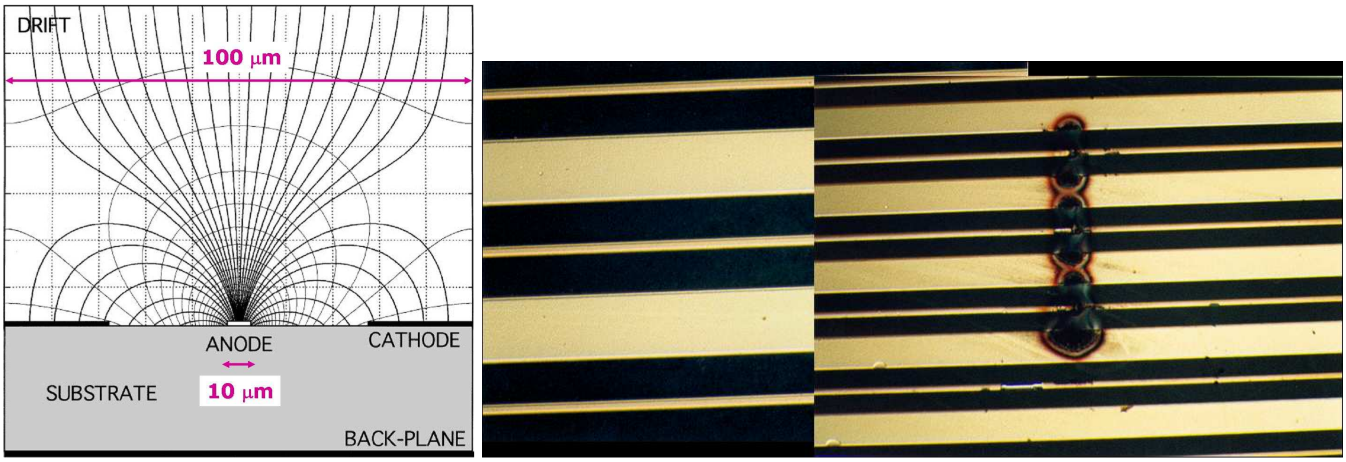

Figure 2.16: Scheme of equipotentials and field lines in a MSGC (left) and microscopic image of MSGC electrodes with damages due to discharges (reproduced from [85]).

Given the high fields and narrow gaps used in MSGC, the damages are often very destructive. In addition, the substrate used for the MSGCs production tends to accumulate the charges enhancing the electric field in some points and increasing the breakdown probability and the discharge energy.

2.4.2 Gas Electron Multiplier (GEM)

The Gas Electron Multiplier (GEM) was introduced in 1996 and consists of microscopic holes perforated into a thin copper-insulator-copper stack. The typical hole diameter lies between 25 μm and 150 μm with inter-hole distances between 50 μm and 200 μm. The GEM manufacturing process was developed at CERN and relies on chemical etching performed on both sides of the GEM to create the holes. The insulator that is sandwiched between two copper foils is usally made of polymer kapton. Applying a voltage across the two copper foils produces an electric field allowing for the multiplication of the electrons in each hole through an avalanching process. Several GEM foils can be stacked together at a short distance of typically 1 mm to 2 mm in order to distribute the amplification over multiple stages as shown in Figure 2.17. This technique allows to maintain high gains above 1×10^4 while reducing the electric field applied individually across each GEM, thus reducing the discharge rate. Contrary to the previous designs, the GEM only performs the amplification stage of the detector without any readout capabilities. A 2D anode kept at the ground potential has to be placed behind the GEM to collect the charges. In the case of GEMs, only the avalanche electrons contribute to the signal collected onto the anode, while the ions are mostly absorbed on the GEM electrodes. A Garfield/Magboltz electric and gaseous simulation of a GEM hole is presented in Figure 2.18 where we can see the avalanche phenomenon and the path

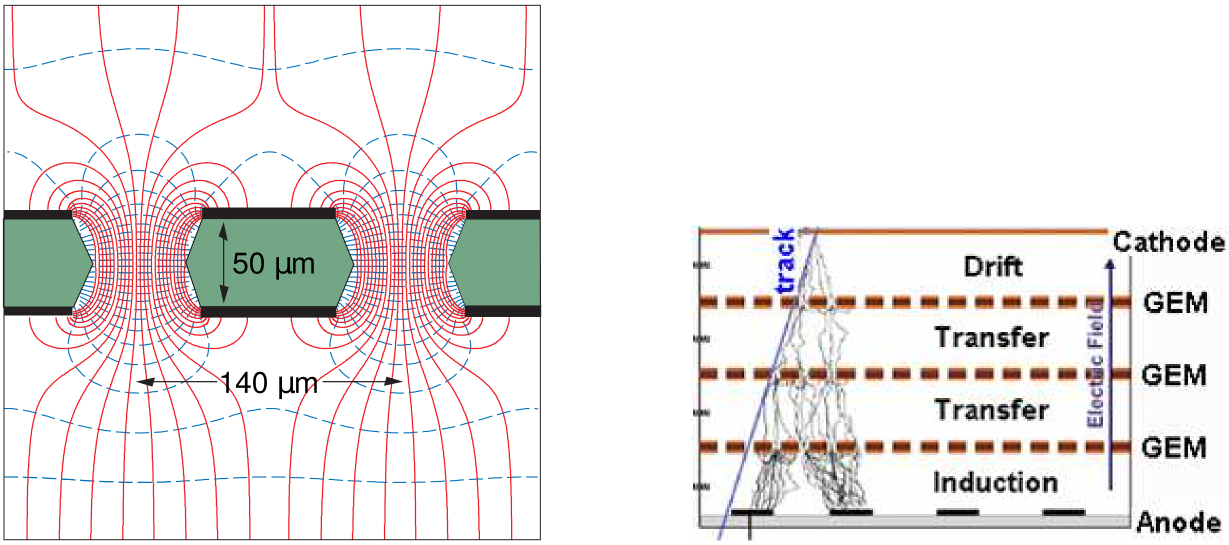

Figure 2.17: Schematic view of GEM holes with field lines (left) and schematic view of a triple-GEM detector (right) (reproduced from [85]).

of the electrons into the holes.

As electrons and ions get collected onto the copper anodes and the dielectric surfaces, the GEM experiences a charging-up effect during which the effective field produced across the GEM holes decreases with time before stabilizing. The magnitude of this charging-up effect and its characteristic time depend on the materials used and on the holes geometry.

2.4.3 Thick-GEM (THGEM)

Led by the success of the GEM technology, Thick-GEMs, sometime called Large Electron Multipliers (LEMs), are GEMs with a coarser hole structure using thicker plates of around 1 mm. They are produced by mechanically drilling 0.3 mm to 1 mm holes into a copper-insulator-copper stack while chemically etching their rims to limit chunks on the copper surface that would lead to electrical instabilities. Studies have been conducted in order to find the best operating configurations for these devices by mainly varying the hole size, the rim size and the hole spacing. It was shown that large rims allow for an increased stability of the detector, reducing the discharges and allowing to reach higher gains. However these larger rims also increase the charging-up that can severely reduce the field in the holes and impair the electrons collection or amplification. An example of this charging-up effect is presented in Figure 2.19. Passivation of specific THGEM parts to reduce the discharge rate also tend to lead to higher charging-up effects by introducing more dielectric material on the detector.

In Figure 2.20 are shown some LEM designs tested in [89] in the R&D leading to the dual-phase techmology

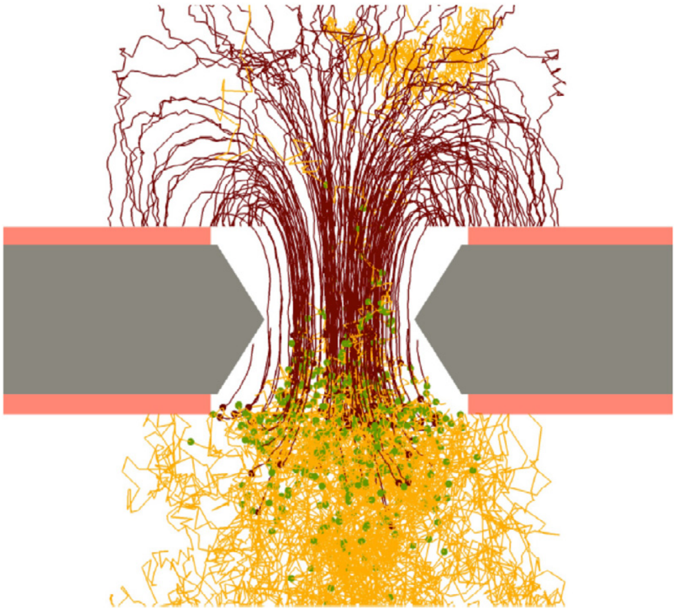

Figure 2.18: Garfield/Magboltz simulation of a GEM hole by the ALICE experiment (reproduced from [87]).

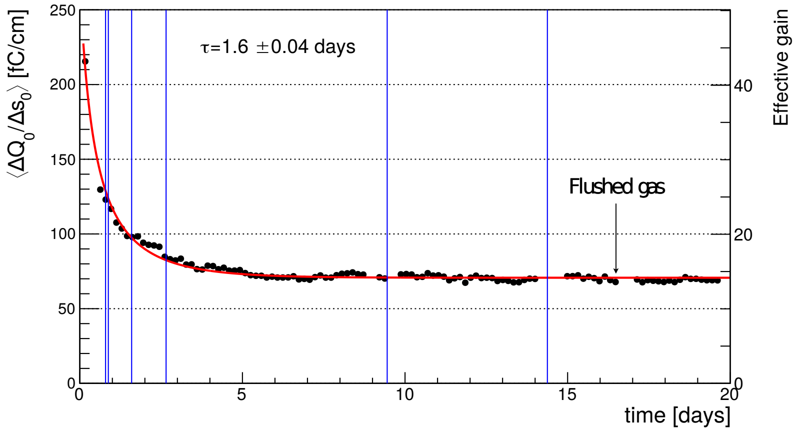

Figure 2.19: Charging-up of a LEM detector with an observed gain reduction with time that reaches a plateau (reproduced from [88]).

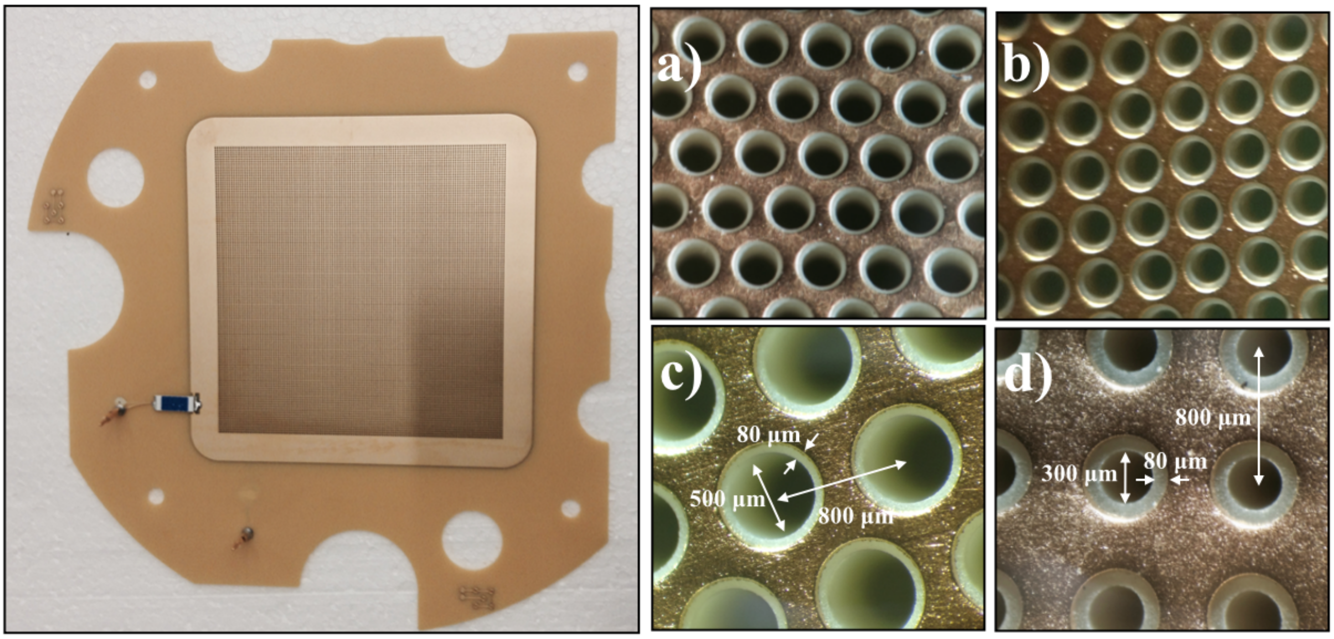

Figure 2.20: Picture of a 10 cm × 10 cm LEM tested in [89] (left). Microscopic views of different LEM designs (right): (a) hexagonal arrangement, (b) square arrangement, (c) and (d) different hole sizes.

while the associated measured gains as function of the applied electric field are reproduced in Figure 2.21. The largest tested PCB thickness of 1 mm and the hexagonal layout seem to perform the best. While decreasing the hole and rim size increases the obtained effective gain for a given applied field, the designs with larger holes and rims are able to reach the same gains at higher fields as they are more stable. The LEM design has to be chosen so as to be able to reach the desired gains while keeping sufficient operation stability.

2.4.4 Micro-mesh gaseous structure (MicroMegas)

The MicroMegas have also been introduced in 1996, and consist of a drift region of a few mm followed by an amplification region between a thin metal grid, called micromesh, and a readout electrode as shown in Figure 2.22. The micromesh is maintained at a fixed distance from the readout electrode by insulating pillars to ensure a constant amplification gap size. The ionization electrons are guided in the drift region through the micromesh holes to create avalanches in the amplification gap where a strong field of ~50 kV/cm to 70 kV/cm. Given the small opening of the micromesh and the small amplification gap, the size of the electron avalanche is of the order of 10 µm to 15 µm depending on the gap size, electric field and gas mixture. The small size of the electron avalanche allows reaching high spatial resolutions. As a single stage amplification detector, the MicroMegas also suffer from discharges created by heavily ionizing particles, but contrary to MSGCs these discharges are

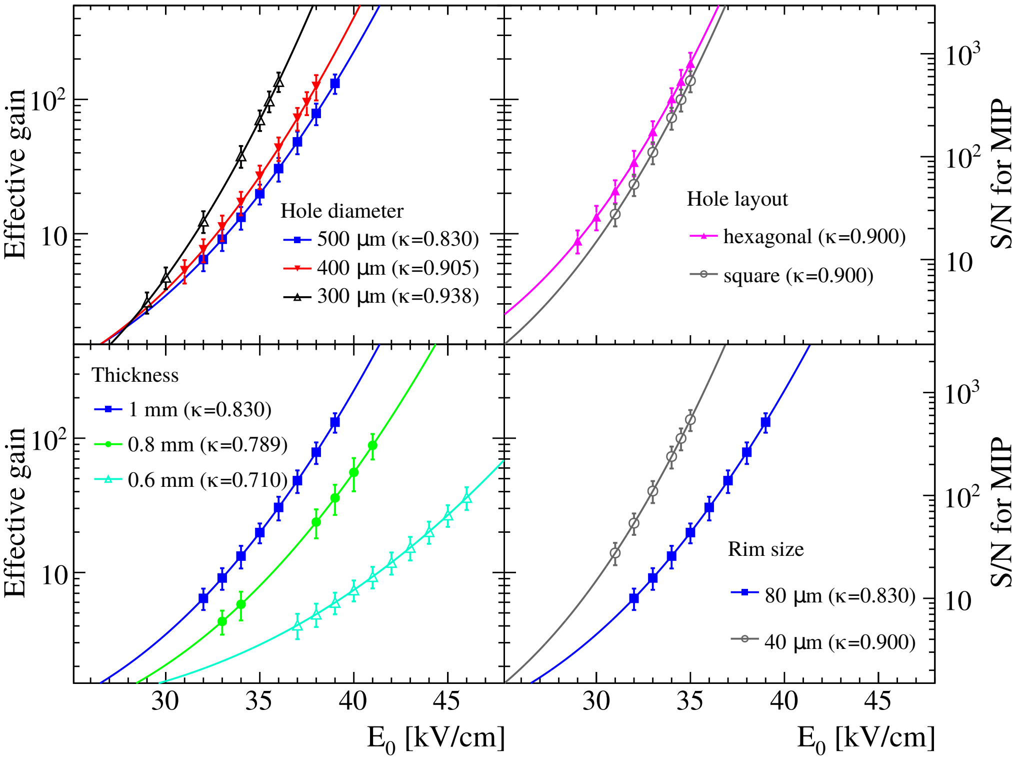

Figure 2.21: Comparison of the obtained gains for various LEM designs in pure argon vapor at 87 K as function of the applied electric field (from [89]).

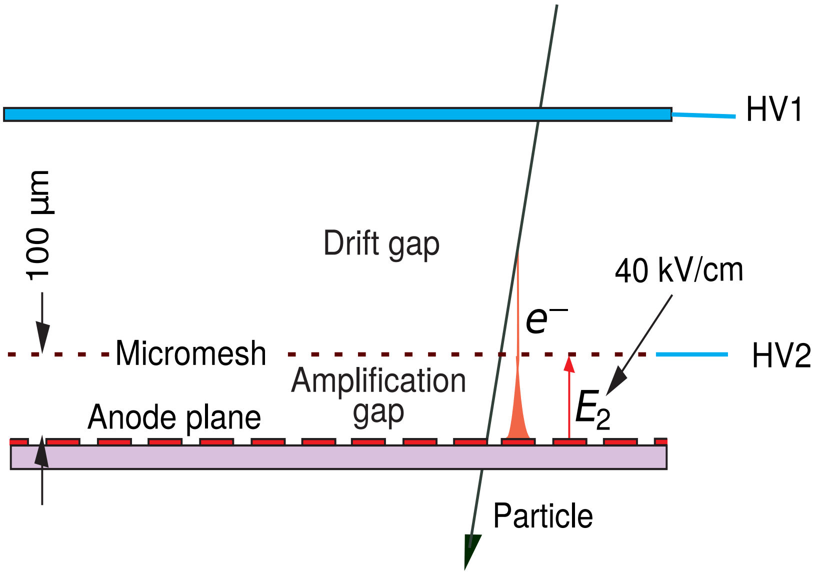

Figure 2.22: Scheme of a MicroMegas detector.

not destructive as the materials used allow for a better control of the electric field. The probability of having discharges can be reduced significantly with the choice of the gas mixture by introducing some quenchers for example.

This first MicroMegas design has since been improved with the development of Bulk MicroMegas that are all-in-one detectors with first prototypes produced by a collaboration between the Irfu and the CERN PCB workshop. This kind of one-piece detector is more robust, allows for the obtention of improved homogeneities and increases the production speed while reducing the cost. These Bulk MicroMegas are produced starting from a PCB with a thickness equal to the amplification gap size that is covered with a photo-imageable coverlay. A woven micromesh and a second layer of photosensitive polyamide film are then laminated on top. Finally, exposing the photosensitive films through the appropriate masks allows for the formation of the pillars supporting the micromesh. The Bulk MicroMegas make use of no frame or mechanics allowing for the optimisation of the active area. Bulk MicroMegas can typically reach gains of 1×10^4 independently of the employed gas mixture as shown in Figure 2.23 which displays gain curves for different gas mixtures.

2.4.5 Readout

Several different segmentations of the readout planes are possible depending on the targeted spatial resolutions or specific geometric considerations. Two main segmentation types exist:

- Pad or pixel anodes allowing to directly reconstruct inambiguously the 3D position of the track by combining

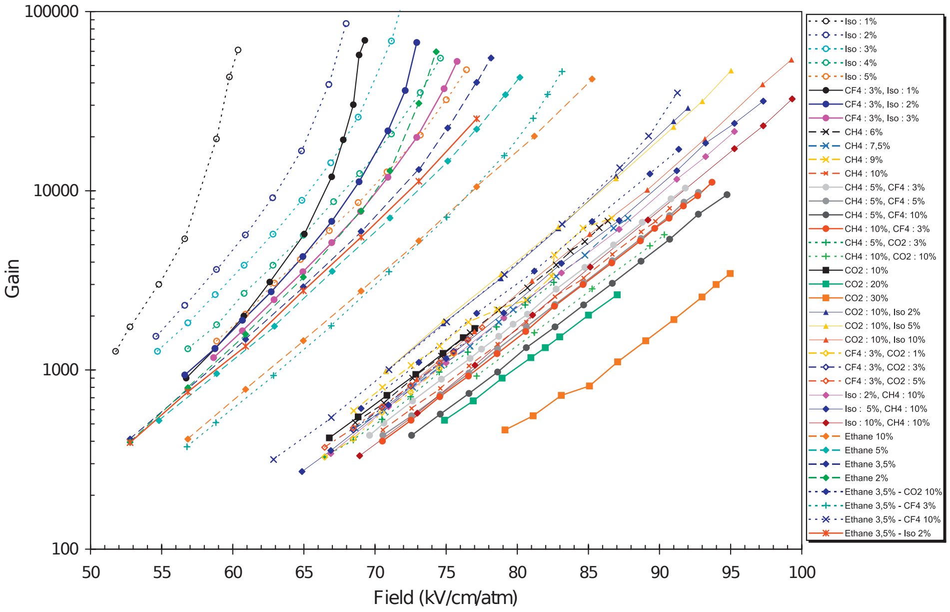

Figure 2.23: Measured gains in Bulk MicroMegas structures (50 μm gap) for different Argon based gas mixtures (reproduced from [90]).

the 2D information from the pad/pixel with the drift time.

- Segmented anodes in both the x and y directions with strips. The reconstruction is made in both the (x, z) and (y, z) planes and then matched on the reconstructed z position. This technique allows for finer segmentation that would be hardly feasible with pad detectors as the number of electronics channel would grow too fast. The reconstruction can however be more challenging.

The electronics is the second element of the readout and has to be chosen carefully as it will provide the third coordinate necessary to reconstruct the tracks in 3D through time measurements. One particulary succesful development of such an electronics is the AFTER chip developed for the T2K TPCs that has since been adopted for the charge readout of a number of other TPCs. The AFTER ASIC is protected against the micro-discharges that can occur in gas avalanche detectors. It can also adapt to several TPC conditions in terms of sensitivity, dynamic range and sampling time while having cross-talk levels between the channels below 0.1 %. It also can operate over a range of shaping times going from 100 ns to 2000 ns.

2.4.6 Calibration

Sevral calibrations can be conducted in order to infer most properties of the TPC. To calibrate the dE/dx response of the detector, it is possible to pulse the grid wires (or MicroMegas mesh) or use radioactive sources. The first method allows to inject a known signal that will be read by induction on the anode, the second method makes use of radioactive sources with a known spectrum of emission, both used to calibrate the detector response and measure the gain.

Actual tracks or cosmic ray events in the whole TPC volume can help detecting dead zones of the TPC or deriving the electron drift velocity in the different detector areas. Field inhomogeneities or misalignement can be assessed by measuring the distortions of the various tracks. Additionally, a laser calibration system can be added to the TPC design to help calibrating the field distortions and the electron drift velocity in the TPC volume. Laser beams are used either by generating tracks by a 2 photon ionization process either by extracting photoelectrons onto a metallic structure such as the TPC cathode. This allows for the emission of tracks or point-like interactions at specific location in the TPC.

Chapter 3

ProtoDUNE Dual-Phase

3.1 The ProtoDUNE Dual-Phase detector

Two multi-ton Liquid Argon TPCs (LArTPCs) were built and operated at CERN in the framework of the Neutrino Platform: a Dual-Phase TPC and a Single-Phase TPC. Such prototypes aim to demonstrate the technologies and engineering solutions proposed for the DUNE far detectors [91]. These two prototypes can be seen in Figure 3.1 with ProtoDUNE Single-Phase (PDSP) at the front and ProtoDUNE Dual-Phase (PDDP) in the back. ProtoDUNE Single-Phase commissioning started at the end of 2018, while PDDP's installation was completed during summer 2019. As a consequence, PDDP was only operated with data taking on cosmics while ProtoDUNE Single-Phase also took beam data with a charged particle beam (0.3 GeV to 7 GeV) provided by CERN.

The Dual-Phase concept and its advantages

The PDDP detector relies on the Argon Dual-Phase Time Projection Chamber design. The concept of this technology is presented in Figure 3.2. This Dual-Phase technology takes advantage of two Argon phases with a liquid phase topped by a gaseous phase. The liquid Argon is dense enough to serve as a target while the less dense gaseous phase allows multiplying the ionization electrons using avalanche effects to increase the detector's gain.

The working principle is the following:

1. The energy deposition inside the liquid Argon creates ionization electrons and scintillation.

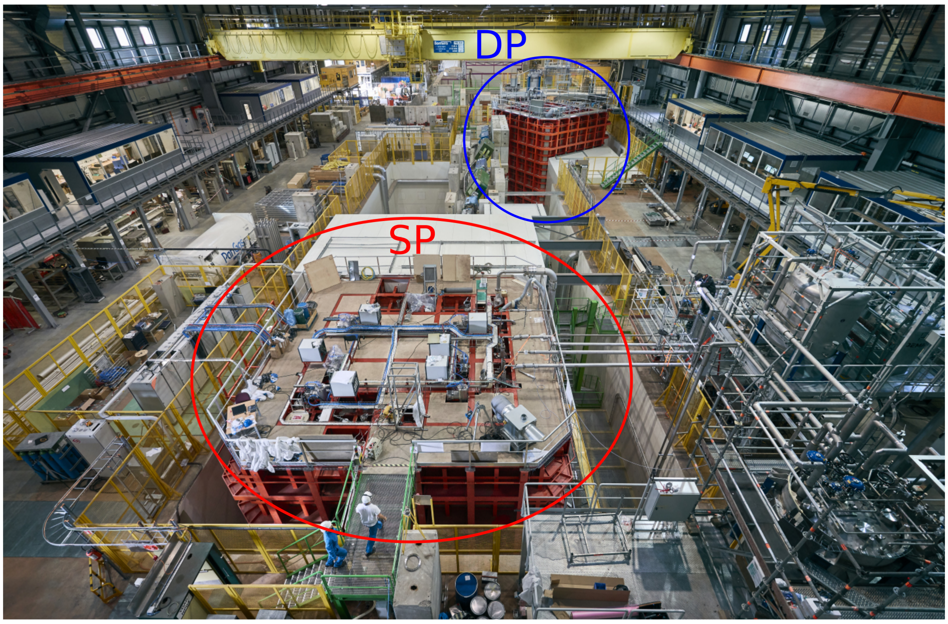

Figure 3.1: CERN neutrino platform with the two protoDUNE detectors.

2. (a) Part of the ionization electrons recombines with Ar nuclei emitting light detected by the Photo-Multipliers Tubes (PMT) at the bottom of the detector. This prompt signal can later be used as a trigger and starting time (t_0) for cosmic-induced muon tracks.

   (b) Most of the electrons are drifted towards the top of the detector by a strong drift field (~ 500 V cm^{-1}). Some electrons are absorbed by impurities such as O_2 during their drift.

3. Ionisation electrons that reach the top of the liquid phase are extracted to the gaseous phase thanks to a grid at a high potential (6 kV) located 0.5 cm below the interface, creating a large electric field.

4. The electrons extracted in the gaseous phase are multiplied via Townsend avalanches inside the Large Electron Multipliers (LEMs) holes, where they experience a large electric field (~ 30 kV cm^{-1}).

5. The electrons are collected by the anode strips, arranged in two orthogonal directions, creating an electrical signal that is then measured and digitized by the electronics.

The Dual-Phase design was proposed as a DUNE far detector because it implements some unique features and offers several advantages over the Single-Phase design.

- The charge amplification in the gas phase allows to tune the signal over noise ratio (S/N) and get a lower detection threshold. It also allows for designs with longer drift distances.

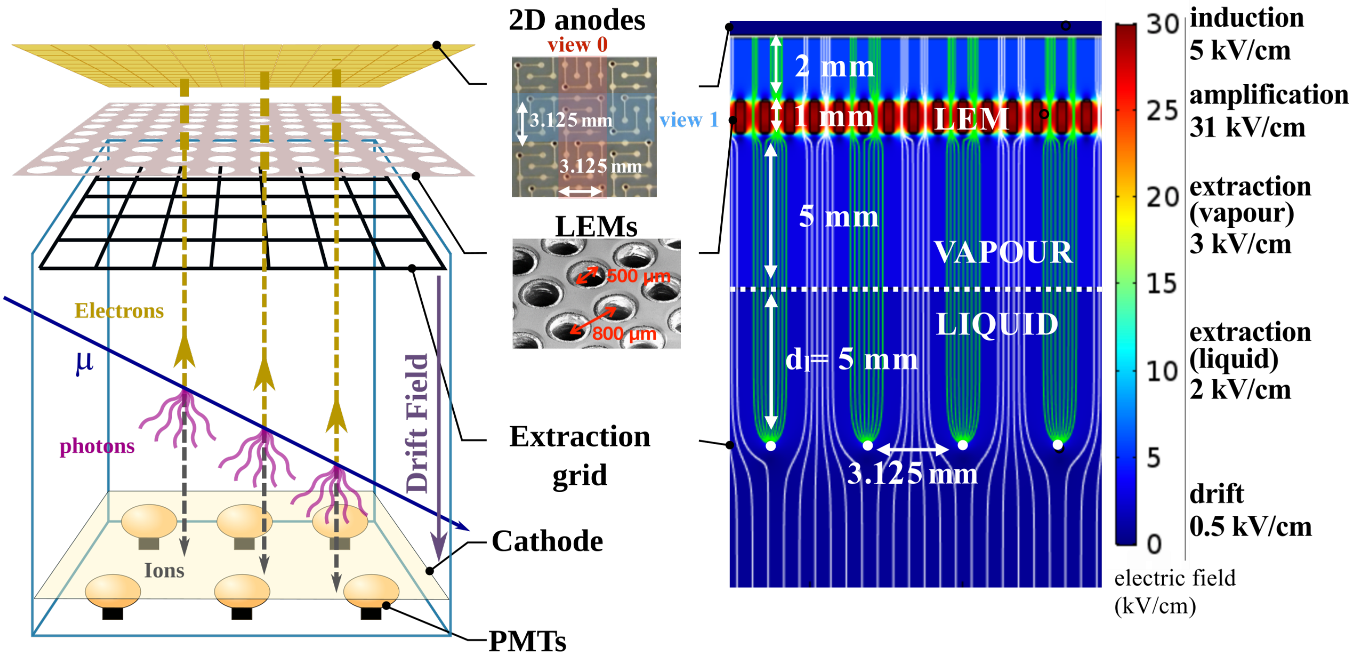

Figure 3.2: Scheme of a Dual-Phase Time Projection Chamber

- The absence of dead material inside the LAr drift volume contrary to the SP design that has a cathode and light sensors in the middle of the detector.
- Finer readout pitch (3.125 mm) alongside the two collection views.
- Fewer readout channels (153600 for DP versus 384000 for SP for a 10 kt module) reducing the costs, with two collection views instead of 3 induction views.
- Full accessibility and replaceability of the cold front-end electronics located at the top of the detector, contrary to the SP design, during the operations.
- The charge readout technology is less labor-intensive and less expensive. The Anode Plane Assemblies (APAs) used by the SP require a lot of person-power for their construction, and their installation is more costly.

The construction and operation of PDDP are mainly aimed at assessing the possibility to construct and operate a multi kiloton dual-phase liquid argon TPC in stable conditions. Several essential characteristics were also to be determined, such as the S/N ratio and the spatial and energy resolutions. PDDP had to demonstrate the possibility of reaching high purity to allow 12 m long charge drift (> 3 ms electron lifetime) and that the CRPs allowed reaching sufficient gain for the established physics program of DUNE (gain > 6). PDDP was operated from August 2019 to September 2020.

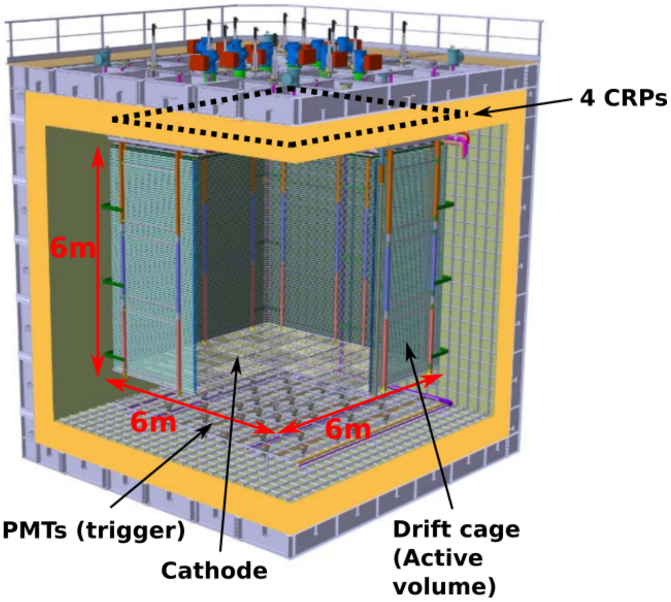

Figure 3.3: 3D modelization of PDDP

3.1.1 The ProtoDUNE Dual-Phase design

The ProtoDUNE Dual-Phase detector has an active volume of 6 m × 6 m × 6 m as shown in Figure 3.3, and is filled with 300 t of liquid argon. The detector is placed inside a cryostat that keeps a temperature gradient compatible with the dual-phase requirements. All the electronics and high voltage power supply pass through the roof of the detector, thus being accessible during the operations.

Cryogeny

The cryogenic operation of PDDP had two main goals:

- Maintaining stable temperature and pressure conditions inside the cryostat: the Argon has to be kept at a temperature of around 87 K and the pressure around 1045 mbar. This was achieved using an insulated membrane cryostat that limits the heat transfer from the exterior, and the active cooling of the recirculated liquid Argon.
- Purifying the liquid Argon to allow for a 6 m drift of the ionization electrons corresponding to a 3 ms electron lifetime. This was achieved by purifying the recirculated liquid Argon by specific cold filters [92] during the operations.

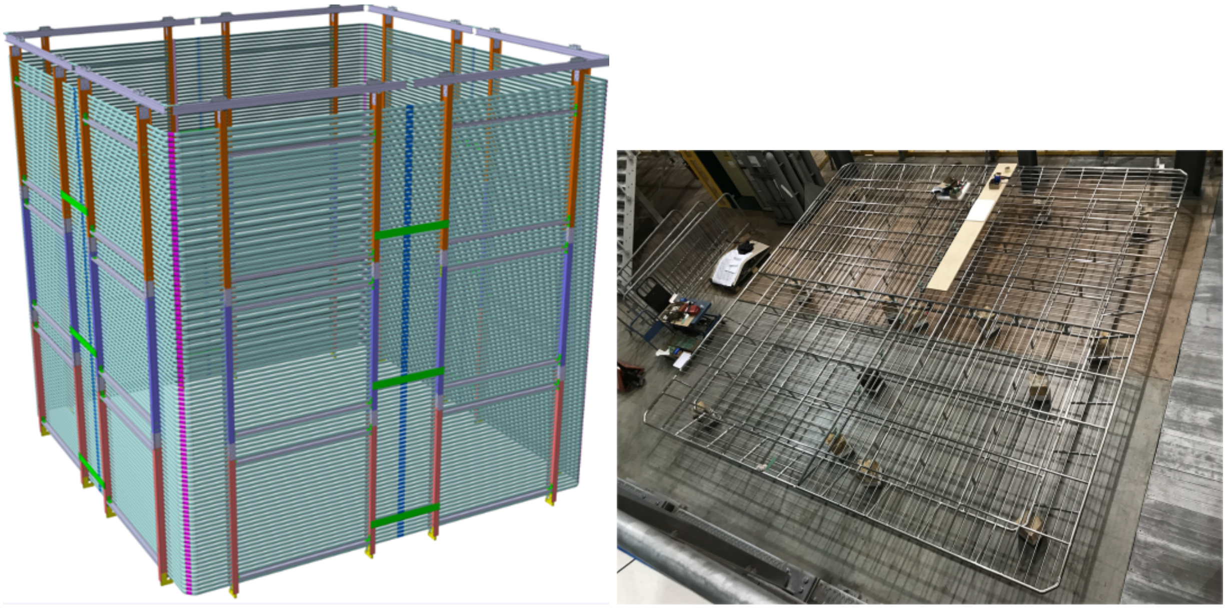

(a) 3D representation of the field cage

(b) Cathode assembling test

Figure 3.4: PDDP field cage and cathode

Drift field

A uniform vertical drift field at a nominal value of 500 V cm^{-1} is applied inside the detector. This field is obtained by applying a voltage up to ~ 300 kV to a cathode located at the bottom of the detector, 6 m below the charge readout system. The cathode is made of a stainless steel frame supporting a stainless steel grid-shaped structure. To guarantee the uniformity of the drift field, a field cage made of 98 aluminum equipotential rings with 6 cm spacing is installed inside the detector. Each ring of the field cage is linked with its neighbors by two voltage divider bridges. The field cage and cathode are shown in Figure 3.4. High voltage is brought to the cathode and the field cage rings from the top of the cryostat by a high voltage extender.

Charge readout

The charge readout is performed at the top of the detector by 4 Charge Readout Planes (CRPs) of 3 m × 3 m size. The CRPs are composed of 3 main elements:

- An extraction grid made of stainless steel entangled wires spaced with a pitch of 3.125 mm. A tension of 3 N m^{-1} is applied to the wires of the grid.
- Large Electrom Multipliers (LEMs) modules of 50 cm × 50 cm size (6×6 per CRP) that amplify the signal by generating electron avalanches. An exaple of a LEM used in PDDP is shown in Figure 3.6.

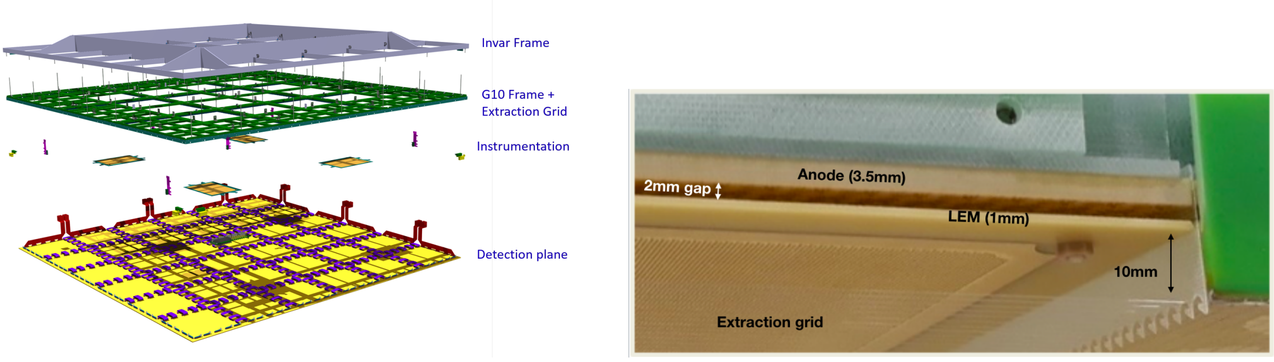

(a) Exploded view of a CRP

(b) Side view of a CRP

Figure 3.5: CRP layout

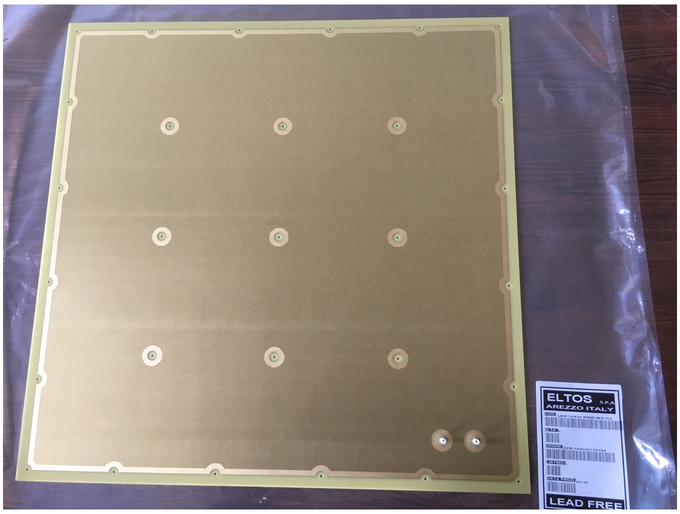

Figure 3.6: LEM used in ProtoDUNE Dual-Phase (CFR-35). The nine central holes are used to screw the LEM and anode together. The two bottom right pins are for high voltage connection.

- Anodes of 50 cm × 50 cm size that collect the charges of the avalanches. The anodes provide a 2D detection with 160 channels in each dimension spaced with a pitch of 3.125 mm. The channels of the anodes are chained together along lines and columns to obtain 2×960 channels for the readout of a CRP. The current design of the anodes, shown in Figure 3.7, is a compromise between the resolution on the charge measurement and the capacitance of the strips. This design is the result of a dedicated R&D [91].

In PDDP, only 2 CRPs were fully instrumented (CRP1 and CRP2). CRP4 is mounted with 4 50 cm × 50 cm anodes, without LEMs. All the other slots that are not instrumented with an anode are filled with grounded copper plates. This configuration can be seen in Figure 3.8.

All the bottom LEM electrodes and grids have dedicated power supplies to set their voltages individually. However, the power supply of the top LEM electrodes drives 6 LEMs simultaneously to reduce the number of

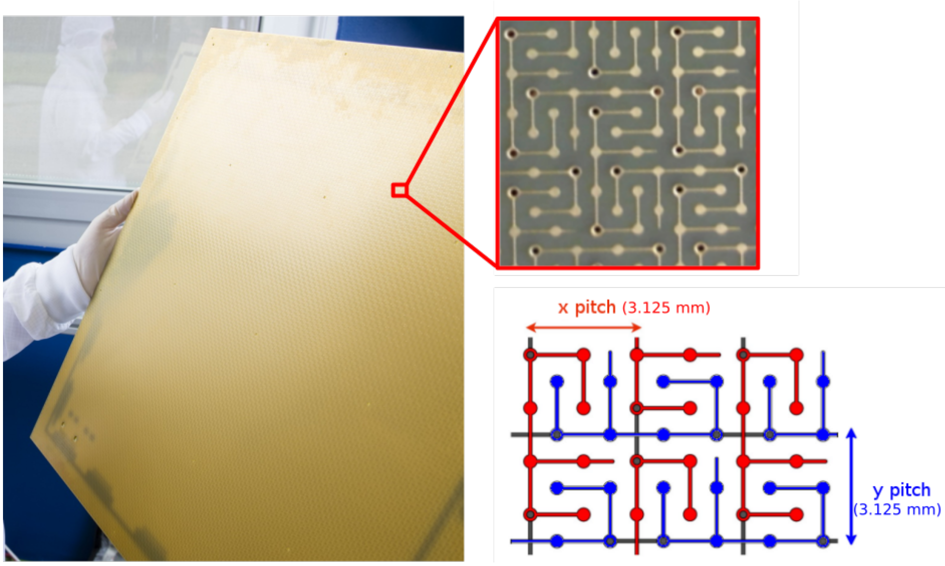

Figure 3.7: Anode used in ProtoDUNE Dual-Phase

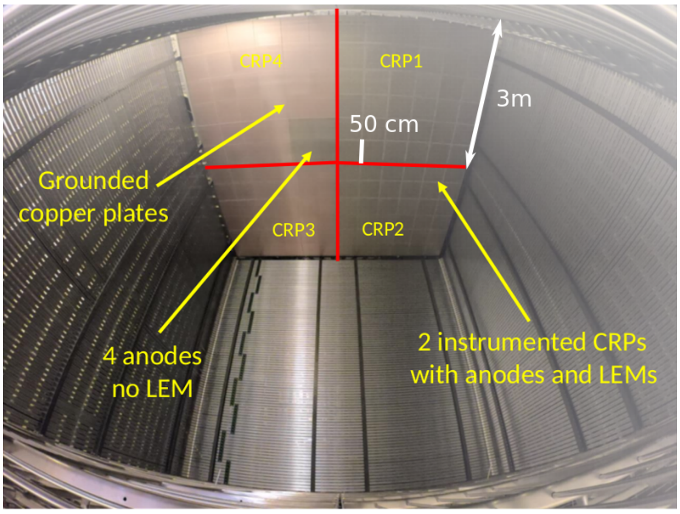

Figure 3.8: CRPs as seen from the inside of PDDP.

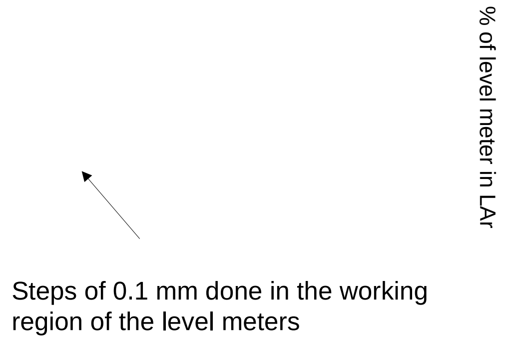

Figure 3.9: Impact on the level-meters measure of displacement steps of 0.1 mm of the CRPs

power supply modules. All the LEM electrodes, top and bottom, are connected in series to their power supply by 500 MΩ current-limiting resistors.

In addition to what is necessary for the charge extraction, amplification and readout, the CRPs have been instrumented with level-meters allowing to accurately determine the position of the CRP with respect to the LAr surface. Indeed, as the CRP must be partly immersed (the grid) in order to control the extraction field, it is crucial to monitor their position closely. The level-meters consist of parallel plate capacitors that measure their immersion depth as a capacity change. The level-meters are coupled with the motorized suspension system to adjust in real-time the immersion depth. The entire system (motors + level meters) allows adjusting the CRP to the liquid argon level with a precision of about 100 µm. As shown in Figure 3.9, displacement steps of 0.1 mm can be measured with the level-meters. The CRPs are also equipped with temperature sensors to monitor the temperature gradient inside the gas.

Photon detection system

The PDDP photon detection system [93] is composed of 36 8-inch cryogenic Hamamatsu photomultipliers (PMTs) positioned on the cryostat floor, below the cathode. In order to optimize the amount of light collected from cosmic rays, most of the PMTs are placed in the center of the TPC as can be seen in Figure 3.10. The roles of the photon detection in the DUNE far detector will be to:

- provide a trigger time t_0 for non-beam events
- enable the determination of the event absolute time for all the events from the prompt light signal allowing to reconstruct the depth of the charge signal by measurement of the drift time

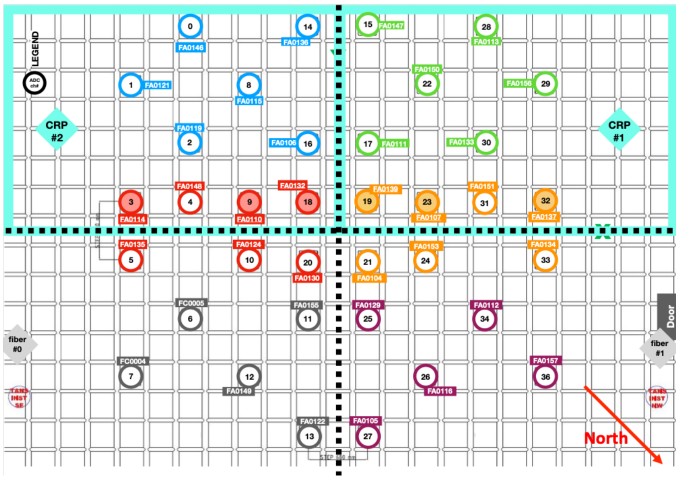

Figure 3.10: PDDP PMT layout

- perform additional calorimetric measurements

In the framework of PDDP that is located at the surface, the event rate, and thus light yield, is too strong for the PMTs to serve as trigger. Consequently, data are taken regularly with no external trigger as the acquisition window is way longer than the typical time between two muon tracks crossing the detector.

Purity monitors

Three purity monitors were installed inside PDDP [91]. Two short purity monitors with a length of 17 cm were installed at a corner of the TPC. One is located on the floor of the cryostat and another at the height of about 2.5 m. An additional long purity monitor with a length of 48 cm was installed next to the bottom short purity monitor. A picture of one short purity monitor taken during the installation is shown in Figure 3.11. These purity monitors were installed to closely monitor the purity of the LAr by measuring the electron lifetime inside the TPC. This measurement is made using the following process inside the purity monitors:

1. flashes from a Xe lamp produce photoelectrons on the purity monitor cathode.
2. electrons drift in the chamber under the influence of a drift field that can go up to 25 V cm^{-1}.
3. two Frisch grids placed in front of the anode and cathode sharpen the signal and shorten its duration.
4. the electron lifetime is then measured by analyzing the charge ratio between the cathode and the anode.

A sketch of a purity monitor can be found in Figure 3.12

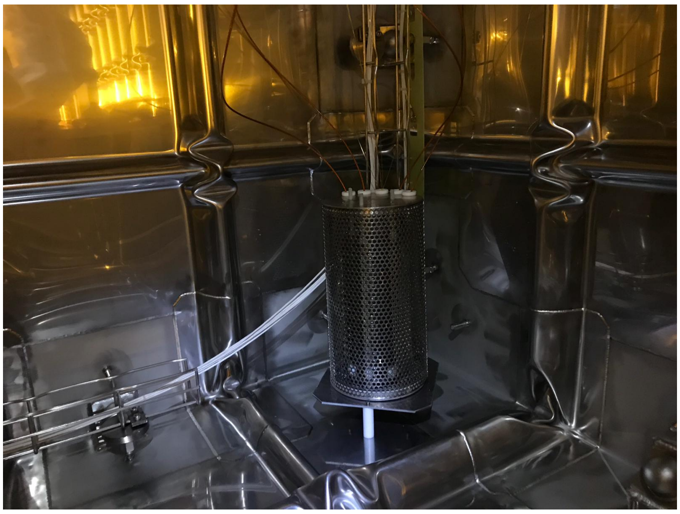

Figure 3.11: Short purity monitor during the installation

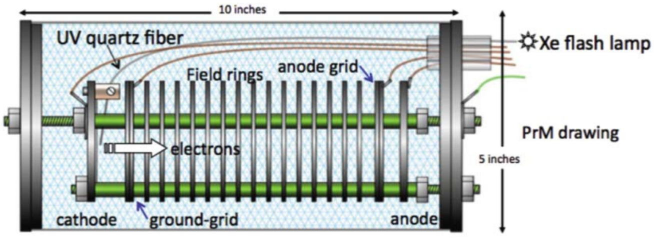

Figure 3.12: Sketch of an argon purity monitor used in PDDP

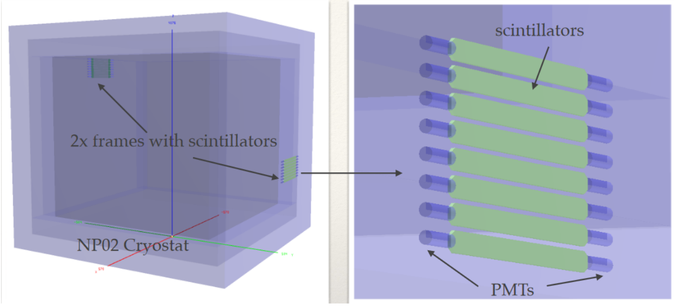

Figure 3.13: Position of the CRTs with respect to the PDDP cryostat

Additional elements

Cryogenic cameras were placed at different locations of the TPC to monitor the interior of the cryostat. Given that the cryostat is closed, LEDs were installed inside the cryostat to provide light for the cameras. An interlock was present to avoid the LEDs and the PMTs to be working at the same time. The multiple cameras allowed to monitor the liquid argon surface's stability and detect possible sparks inside the detector.

Temperature sensors were also placed at different depths along the field cage to monitor the status of the liquid Argon and to adapt the cryogenic operations in consequence.

Two Cosmic Ray Taggers (CRTs) were added to PDDP in November 2019. These two CRTs are each made of eight scintillator paddles covering an active area of 1 m^2. The CRTs are placed in such a way to detect tracks passing below the two fully instrumented CRPs. One is located near the LAr surface, while the other was placed at the bottom of the detector, as shown in Figure 3.13. These CRTs could provide a trigger used for some PMTs operations but were not used for CRP data taking.

3.1.2 Previous R&D

ProtoDUNE Dual-Phase design was the result of years of R&D on the Dual-Phase technology. The Dual-Phase technology was first proposed in 2004 [94]. A first prototype with a drift length of 21 cm and a volume of 3 L was tested in 2010 and the following years and set up the basis of collection and amplification technology [88]. This prototype allowed to measure the gain performances and the stability of such a detector [89], but at a small scale. Indeed, the challenge is to be able to reproduce the impressive performances obtained on 10 cm × 10 cm LEMs, instrumenting detectors with total surfaces scaled by a factor larger than 1000. The first large scale detector using this technology was the $3 \times 3 \times 1 \mathrm{m}^3$ detector operated by the WA105 collaboration [95] and shown in Figure 3.14. It was constructed and operated at CERN between 2016 and 2017 to assess the performances and

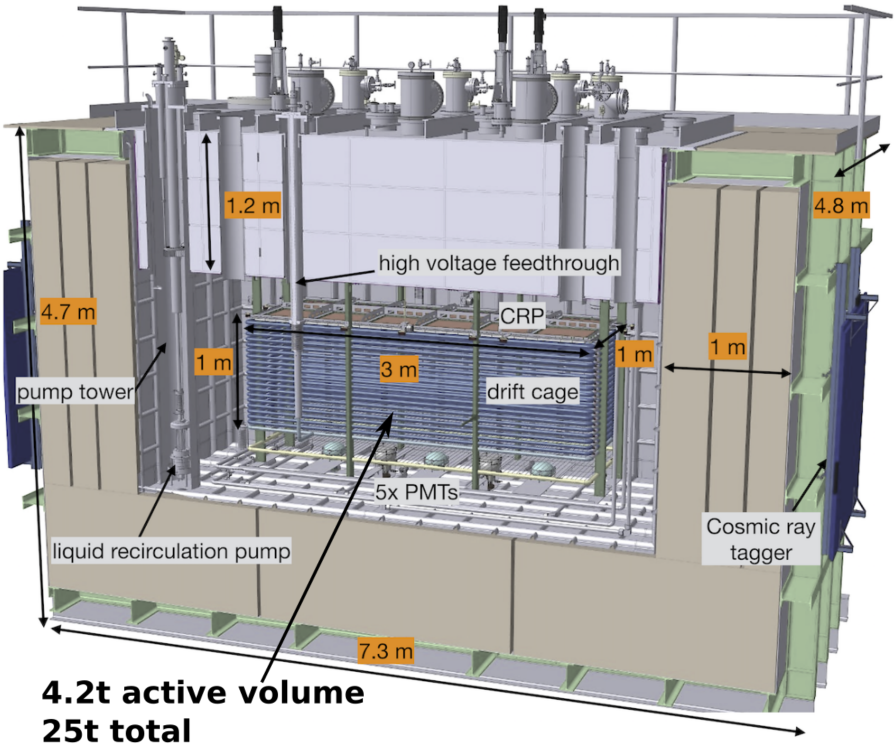

Figure 3.14: Scheme of the WA105 detector

check the stability of this novel technology. This prototype was filled with 4.2 t of LAr and was equipped with a single 3 m × 1 m CRP composed of 12 LEM-anode sandwiches for the charge readout. Most of the technical choices made for this demonstrator were kept identical for PDDP.

This prototype was able to observe cosmic tracks. An example of an electromagnetic shower is shown in Figure 3.15. However, some high voltage instabilities appeared during the operation of this detector. The manifestation of these instabilities were sparks involving the LEMs alone or the LEMs and the grid. These issues were mainly imputed to an insufficient tension of the grid wires and the LEM design was improved to further reduce the sparking rate.

In light of this previous large-scale prototype, improved designs have been developed for the LEMs and the CRP structure and integrated into PDDP. The CRP structure was stiffened by replacing the stainless steel frame with invar, less sensitive to temperature changes. The tensioning procedure of the grid was also improved to guarantee a regular spacing between the LEMs and the grid. These updated designs have been tested in a coldbox at CERN before the installation inside PDDP, as shown in Figure 3.16. It was shown during these coldbox tests that a CRP could be operated stably under PDDP HV conditions.

The LEM design was improved to cope with the need for sparking rate to be below 1 spark/CRP/hour due to

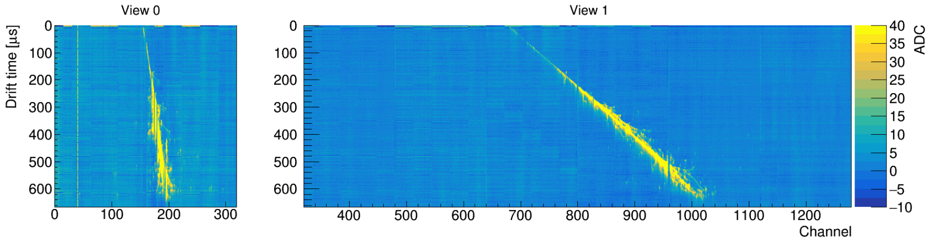

Figure 3.15: Electromagnetic shower as shown in the WA105 prototype. The amplification field was 29 kV cm^{-1}

Figure 3.16: Closing of the coldbox with a mounted CRP

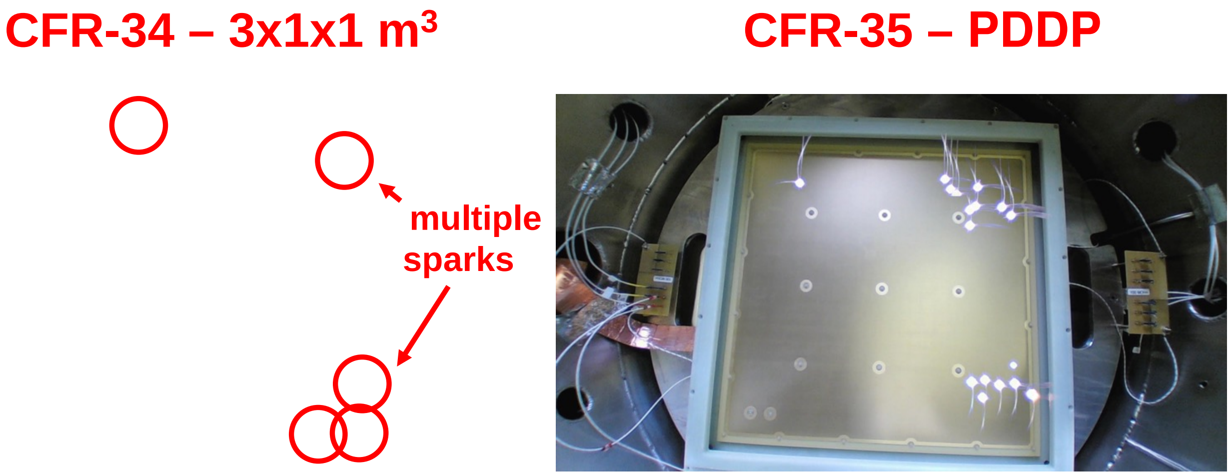

Figure 3.17: Accumulation of sparks on two different designs of LEMs during Saclay tests. For CFR-34, almost 50 % of the witnessed spark occurred on the LEM border. This is primarily reduced with the CFR-35 design.

Table 3.1: LEM design update

		LEM borders		Screw holes		HV connections	
LEM design	Active area	FR4	copper ring	FR4 ring ⌀	copper ring ⌀	FR4 ring ⌀	copper ring
CFR-34	96.2 %	2 mm	2 mm	4.2 mm	6 mm	10 mm	12 mm
CFR-35	85.8 %	10 mm	5 mm	10 mm	20 mm	10 mm	20 mm

the larger detector size. It has been found in tests at Saclay that most of the sparks occurred at the LEM border or near the screw holes for the design that was used for the $3 \times 1 \times 1\text{m}^3$ prototype (CFR-34). This can be seen in Figure 3.17 where most of the recorded sparks are indeed in these locations. In order to reduce the amount of sparks, an updated design (CFR-35) was developed. In this new design, the width of the copper-free border was increased from 2 mm to 10 mm at the edge of the LEM and from 4.2 mm to 10 mm around the screw holes. The copper guard ring diameter was also increased from 6 mm to 20 mm around the screw holes. The list of the changes can be found in Table 3.1. The two LEM designs can be seen in Figures 3.18 and 3.19. By making these changes, the active area of the LEMs has been reduced from 96 % to 86 %. Further R&D is still ongoing at Saclay to optimize the active area while keeping a low sparking rate consistent with what is necessary for the operation of a multi-kiloton detector.

3.2 Stability of the detector

Various stability issues arose during the commissioning of the detector leading to some difficulties in operating the detector.

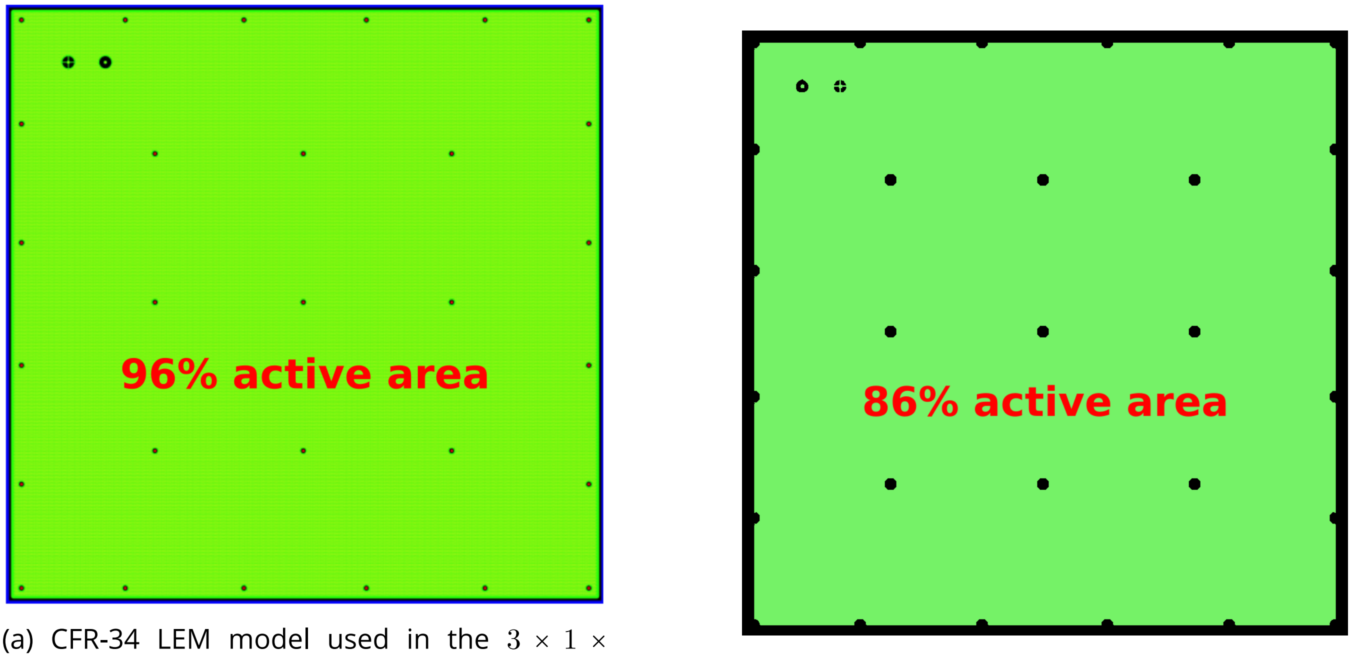

(a) CFR-34 LEM model used in the $3 \times 1 \times 1\mathrm{m}^3$prototype.

(b) CFR-35 LEM model with increased passivated areas used in the $6 \times 6 \times 6\mathrm{m}^3$ prototype.

Figure 3.18: CFR-34 and CFR-35 LEM designs

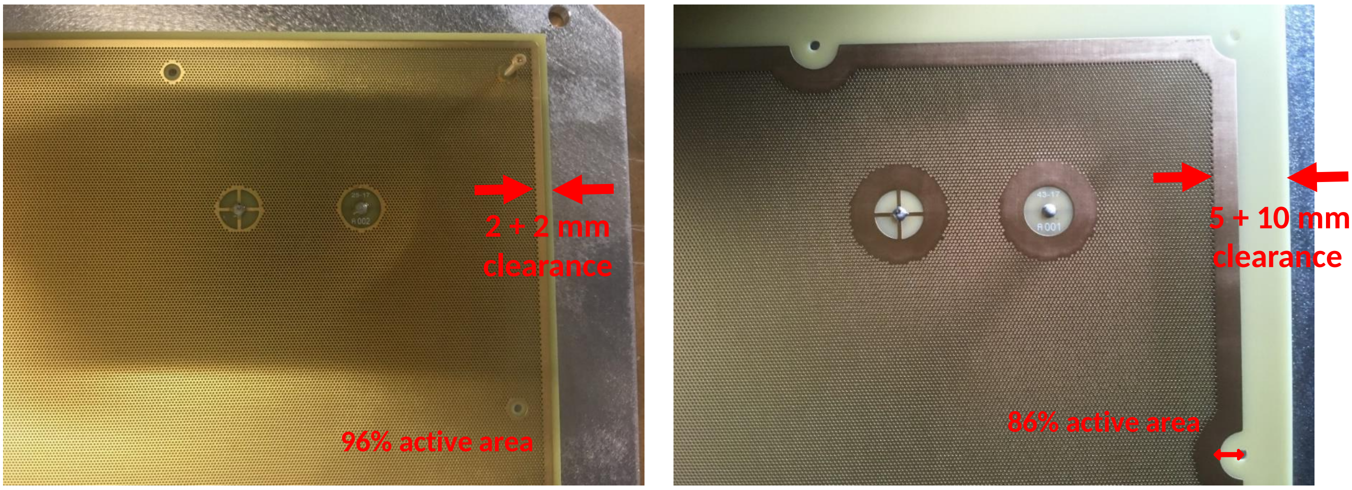

Figure 3.19: Comparison of LEM designs. CFR-34 ($3 \times 1 \times 1\mathrm{m}^3$) on left image and CFR-35 (PDDP) on right image.

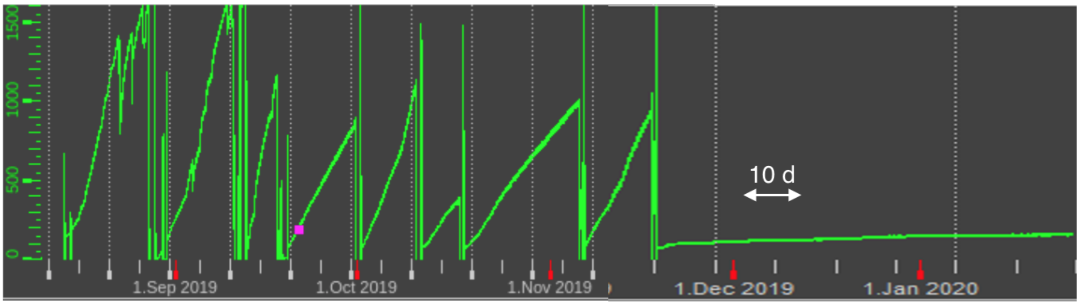

Figure 3.20: Evolution of the pressure across the cold filters with time

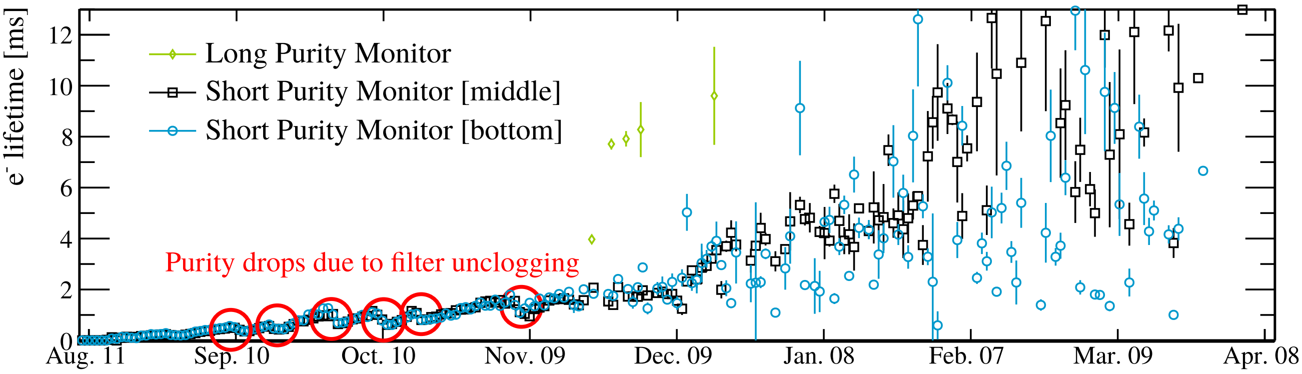

Figure 3.21: Drifting electron lifetime measured by the purity monitors

3.2.1 Argon purification

As explained previously, the liquid Argon is recirculated and passes through cold filters that remove the impurities. During the commissioning, a pressure build-up has been witnessed across the mechanical filters when starting the recirculation pump. These filters therefore necessitated a cleaning that was conducted after bypassing and opening the filtering components. It appeared that fibers had been choking these filters. Further studies indicated that the composition of these fibers was compatible with the cryostat insulation. This obstruction of the filters continued until November 2019, as shown in Figure 3.20. The bypassing and cleaning of these filters impacted the Argon purity by momentaneously stopping the purification and introducing impurities in the opening process.

Purity monitor runs were made each day with the two smaller purity monitors to get regular feedback on the purity of the Argon. The drifting electron lifetimes measured with these purity monitors can be seen in Figure 3.21. We can see the increase in electron lifetime with time on the data of the short purity monitors. Losses in purity caused by the openings of the purification system to unclog the filters can be seen. The two small purity monitors find very similar results all along the operations until the end of January, when they start

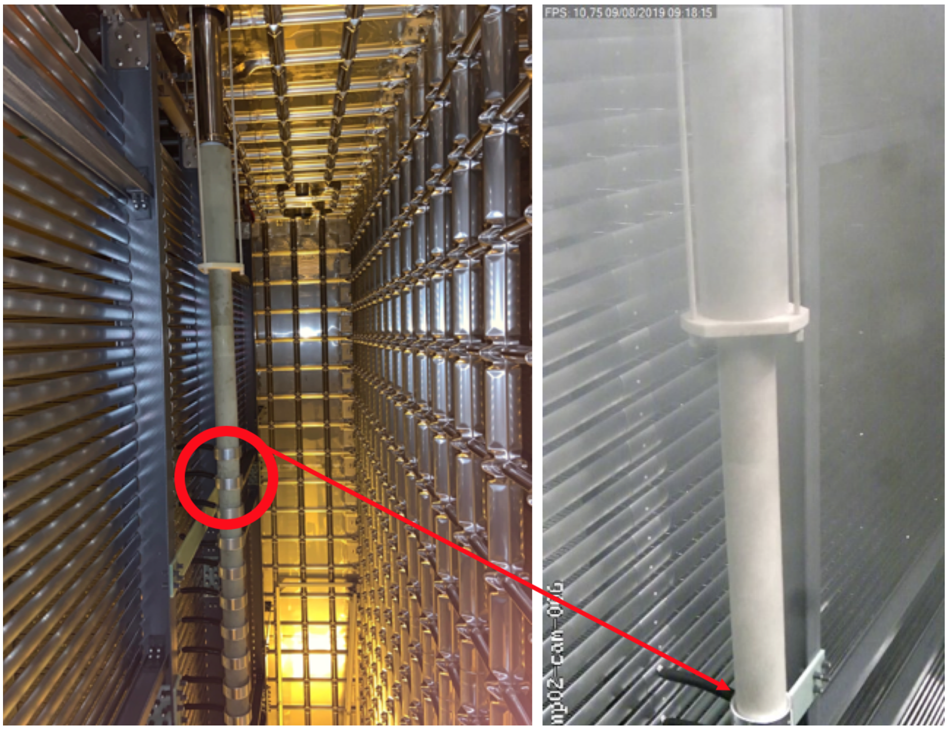

Figure 3.22: Location of the High Voltage Extender short.

to reach their precision limit. After January, the drift distance used by the two shorter purity monitors is too small to accurately measure lifetimes above 5 ms, hence the large dispersion of the measurements. On the other hand, a few measurements have been conducted using the long purity monitor, and these measurements are in apparent disagreement with the ones of the small purity monitors. The long purity monitor measured higher purities than the short purity monitors. Further investigations by the collaboration on this subject are required.

3.2.2 High Voltage extender short

During the commissioning of the High Voltage, an issue occurred. The voltage applied to the cathode through the HV extender was risen to 200 kV with 50 kV increments. Further increases in steps of 10 kV allowed to reach a voltage of 250 kV. However, after 15 minutes at 250 kV a current trip (> 500 µA) occurred that reset the voltage to 0 V. Subsequent attempts to raise the HV resulted in a very unstable current when the HV was set above 100 kV. The results pointed at a fault on the HV extender that experiences a short circuit of its inner conductor with a ring of the field cage. Further analysis and simulations concluded that the short circuit occurred at ring 24, leading to a drift field only being applied on the topmost 1.5 m of the TPC. The location of the short-circuit is displayed in Figure 3.22.

All the subsequent operations and data runs were realized in the presence of this high-voltage short. This

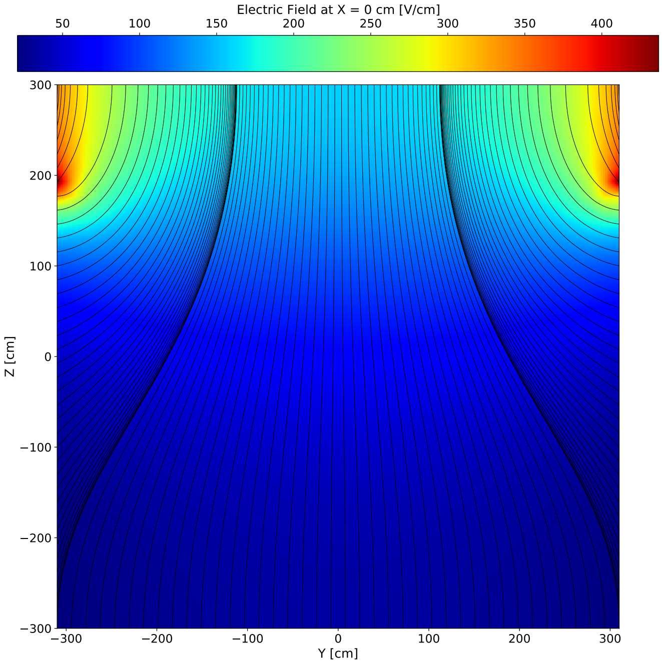

Figure 3.23: Vertical section of the drift field taking into account the extender short with the drift lines

failure of the high voltage extender largely impacted the magnitude and shape of the drift field that could be applied inside the TPC. Indeed, the created drift field only allows for drifting the ionization electrons produced on the top 150 cm of the TPC. This leads to the charge readout to be blind to around 75 % of the TPC. Moreover, the maximal high voltage that could be supplied was also limited. As a consequence, most of the runs were taken with 50 kV being applied by the HV supply leading to an average drift field strength of around 200 V cm^{-1}.

To deal at best with this field configuration for the analysis, the electric field in the drift volume was simulated using a Finite Element Model, however, not taking into account the space charge effects. The electric field map calculated with this simulation is shown in Figure 3.23 for 50 kV provided by the power supply. As can be seen, the field is very inhomogeneous, with a field near the surface that can change by a factor of 2 depending on location in the TPC. It will be necessary to take these inhomogeneities into account for the reconstruction.

After the first sequence of operations ranging from August 2019 to May 2020, an attempt to fix the high voltage extender was made. To do so, the cryostat was partially emptied to expose the faulty connection in the gas. The repair of the HV extender short was performed on June 17th by cutting some connections between the field cage and the extender. The cryostat was then refilled with LAr. Tests of the HV were performed in July to take data in August 2020 before emptying the cryostat in September. During these tests, it appeared that despite the operation conducted on the HV extender, a surface current was flowing on the extender from the first

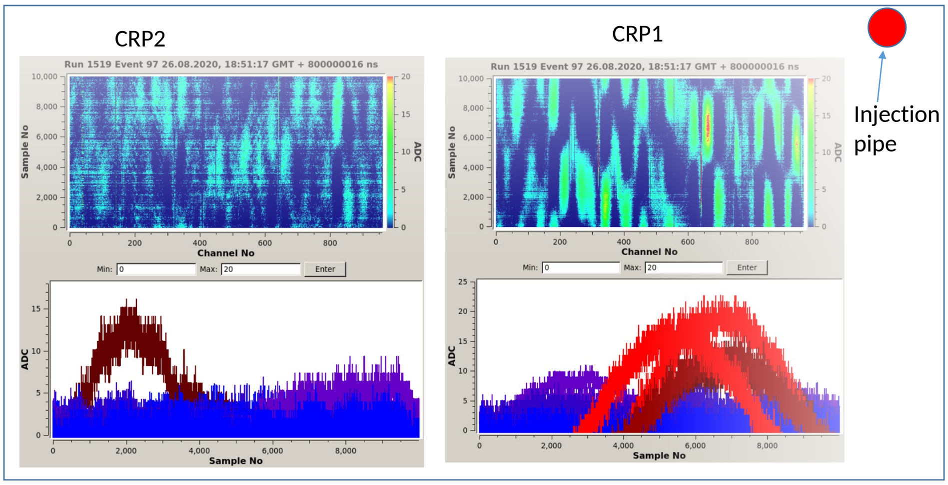

Figure 3.24: Signals measured by the electronics with the speaker at 250 Hz

ring down to the 4th ring, which was connected to the field cage. This current was creating a new short circuit path. This surface current was not continuous but appeared as sparks. As a consequence, this repair attempt did not allow to recover a uniform and constant drift field over 6 m.

3.2.3 Microphonic noise

A more considerable than expected noise was observed in the charge readout. This noise was correlated in space and time and looked like a propagated wave. It has been proposed that this noise could correspond to vibrations of the LEM-anode sandwich leading to induction fields that induce noise into the anode strips. The amplitude of this noise depends on the voltage of the LEM top electrode, indicating that this noise comes from capacitive coupling between the LEM top electrode and the anode. The typical frequencies of this effect corresponded to microphonic noise. Studies were conducted to find the excitation frequencies that could produce such an effect. Acoustic excitations were created by a 160 W speaker positioned externally on a gate valve flange close to the CRP1. The speaker was connected to a waveform generator producing sinusoidal signals at precise frequencies. During these tests, the LEM top voltage was set at the nominal value of 500 V. During these tests, a spectacular microphonic effect could be observed for excitation frequencies in the 240 Hz to 265 Hz range, as can be seen in Figures 3.24 and 3.25. The effect on the CRP1 is more substantial given the closer position of the injection pipe.

This effect could probably be mitigated with a redesign of the CRPs by reducing the possibility for the LEM top and anode to move with respect to one another. Some acoustic frequency dumpeners could be added in the links between the TPC roof and the CRPs to prevent acoustic oscillations from being transmitted to the system.

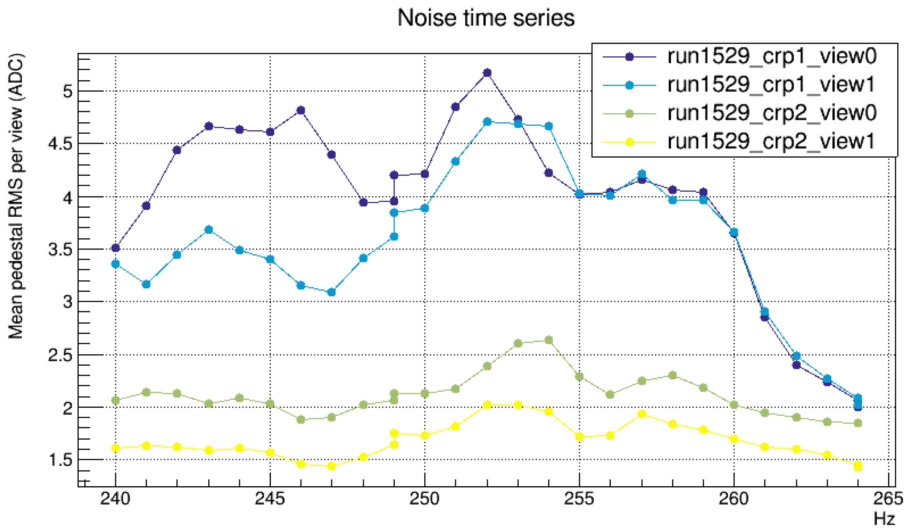

Figure 3.25: Evolution of the microphonic noise with frequency in the peak region

3.2.4 Liquid argon bubbling and mitigation strategies

After the detector filling, some LAr bubbling activity has been observed at its surface. These bubbles were located near the HV feedthrough and near the field cage. This phenomenon was detected thanks to the cameras installed inside the detector. The bubbling frequency has been measured at ~ 1 Hz. There exists a capacitance between the grid and the LEMs that corresponds to two capacitances in series: LEM/LAr-interface and LAr-interface/grid with media that have two different dielectric constants. The dielectric constant of the gaseous Argon, ε_g, is close to 1, while the dielectric constant of the liquid Argon is $\varepsilon_l = 1.5$. The capacity between the LEMs and the grid is then such that:

$$C = \frac{\varepsilon_g \varepsilon_l}{\varepsilon_l (L - d) + \varepsilon_g d} C_0 \tag{3.1}$$

with C_0 a constant that depends on the surfaces and geometries of the LEMs and the grid, L the distance between the LEMs and the grid that is equal to 1 cm and d the distance between the grid and the LAr-interface as it is shown in Figure 3.26. Consequently, when ripples affect the interface between the LEMs and the grid, d changes and the capacity between them is changed rapidly, modifying the capacitive coupling, thus creating currents and instabilities in the system. A ripple of 1 mm changes the capacity by 5 %.

This bubbling that appeared since the first commissioning operations prevented a stable operation of the CRPs, which require a steady Liquid-Gas interface. This issue was mitigated in the first phases of detector operations by performing pressure cycles to remove the bubbling temporarily. The pressure inside the cryostat

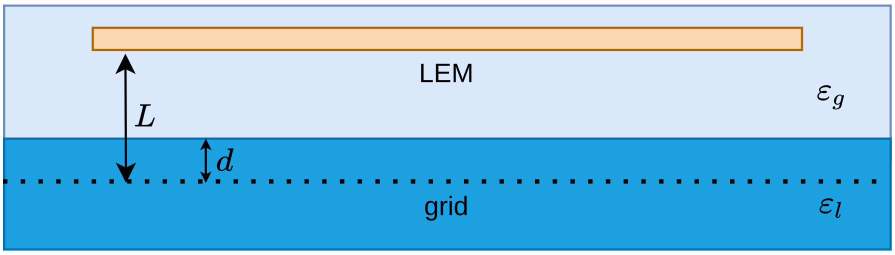

Figure 3.26: Scheme of the LEM-grid capacitive coupling

was increased by 35 mbar in the morning of each day to allow stable operations and data taking for the day. The pressure was then lowered back to its nominal value in the evening. These pressure cycles allowed suppressing the bubbling and operating the detector to assess the CRP performances. However, these pressure cycles introduced some instability in the cryogenic state, and it was sometimes necessary to wait for the recovery of the cryogenic system in a normal state during a day. The effects and origins of the bubbling are shown in Figure 3.27. Part of the bubbles come from the uppermost field cage profile (~ 10 cm below the liquid argon surface) where argon bubbles are trapped in a pocket made by the field cage profile. Argon bubbles come out at the clips that join two consecutive profiles.

In October 2019, further mitigation strategies were investigated. The liquid argon level was lowered, and a partial vacuum was made in the cryostat insulation to limit the heat exchanges with the exterior. With these new conditions, it has been found that applying a pressure bump, that is to say increasing the cryostat pressure by only 2 to 3 hours, allowed to remove the bubbling for around a week. This technique has then been used systematically during the following operation.

3.2.5 Analysis of sparks

During operations of the LEMs, some sparking can occur between the two faces of the LEM. These sparks are due to field instabilities and have been reported since the beginning of the operations of such devices [88]. When such discharges occur, the difference of potential applied to 2 faces of the LEM drops suddenly and, as a consequence, the gain of the LEM decreases drastically. Another side effect of such a discharge is the local removal of the charging-up effect in the LEM. Indeed, the charges accumulated locally in the PCB discharged during the spark, leading to a local de-charging that will introduce a gain inhomogeneity inside a given LEM for a short time, even after the full voltage recovery. As previously explained, several LEM designs implementing multiple improvements have been produced allowing to reach the target of 1 spark/LEM/CRP/hour, that is to

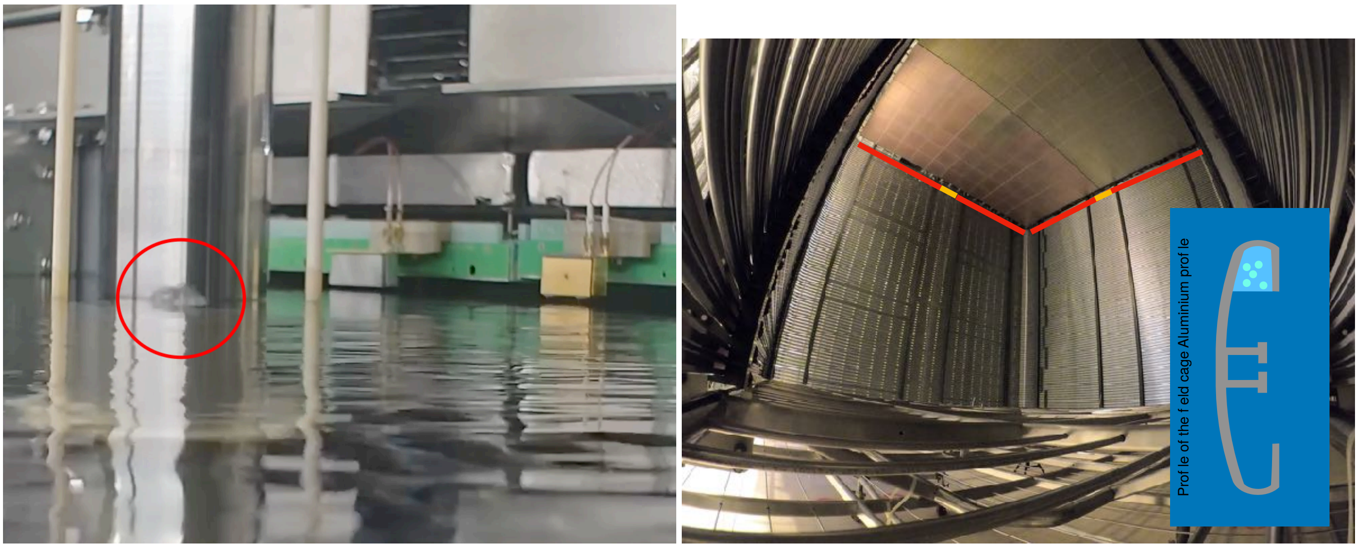

(a) Bubble from the High Voltage FeedThrough

(b) Clips releasing gas bubbles

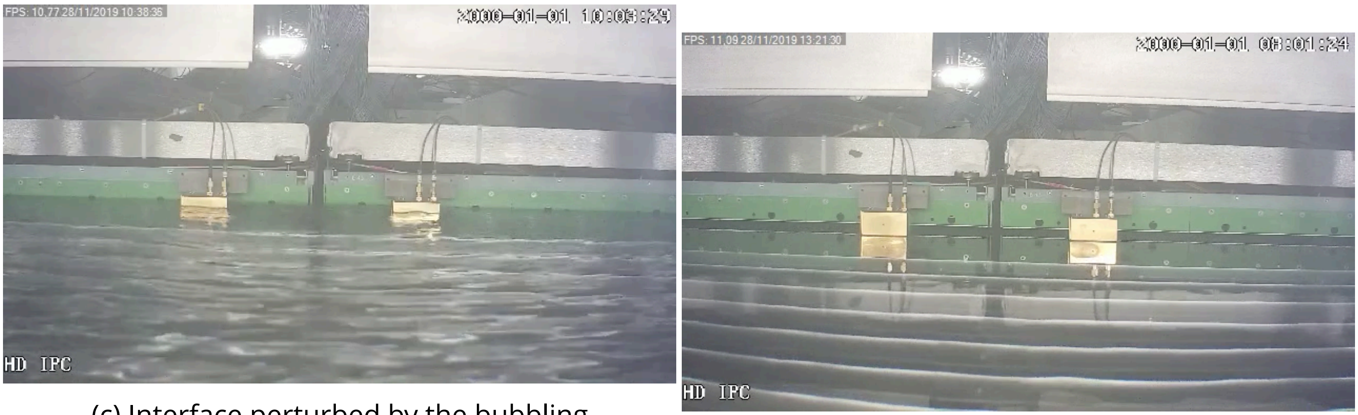

(c) Interface perturbed by the bubbling

.

(d) Steady surface during a pressure cycle

Figure 3.27: Bubbling in PDDP

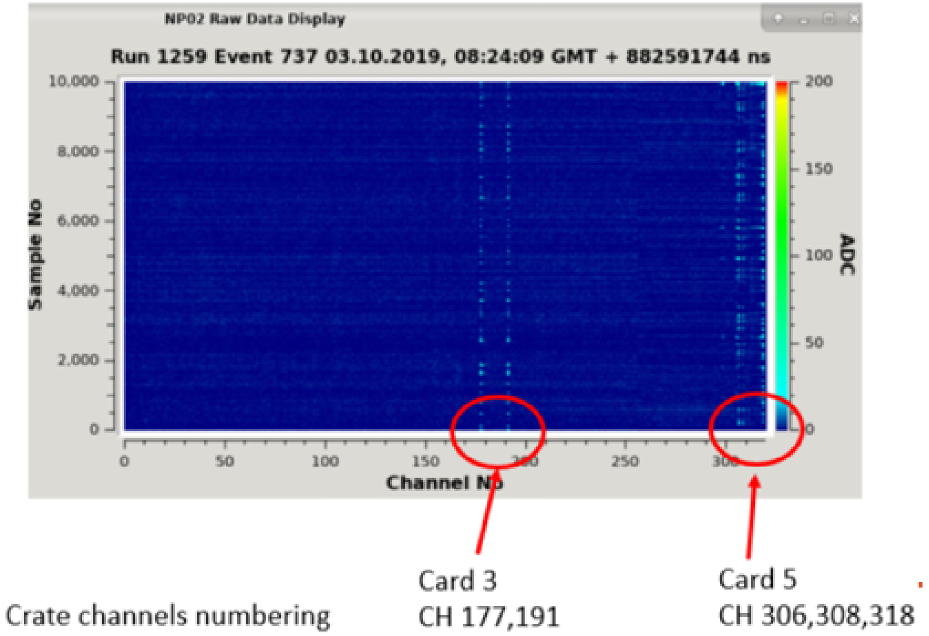

Figure 3.28: Apparition of high noise on some electronics channels after the occurrence of a grid spark.

say, one spark per LEM per 36h. This sparking activity is intrinsic to the LEMs: when applying a large enough difference of potential to a LEM (with no anode or extraction grid), some sparking events are expected, but the improved design mentioned in Section 3.1.2 and tested in the cold-box allowed to reach a spark rate low enough for stable detector operation. However, additional sparks have been observed, such as discharges of a grid on a LEM or even discharge of the grid directly onto an anode, as witnessed during the PDDP operations. During the PDDP operations, the most prejudicial impact of sparks was the damage of some electronic channels due to sparks that occurred directly from the grid to the anodes. The electronics was developed, introducing sufficient protection using transient voltage suppressor diodes that were carefully chosen to withstand the energy from possible sparks from the LEMs. The possibility of sparks coming directly from the extraction grids that are at a higher potential wasn't considered as the grids are supposed to remain immerged in stable cryogenic conditions. The introduced protections are then not sufficient and thus such discharges damaged the electronics. This can be seen in Figure 3.28 where electronics channels display a noisy behavior after the occurrence of a grid spark. Consequently, the electrical stability of the CRPs had to be obtained and strictly monitored during the data acquisition to limit as much as possible any damage to the electronics.

At least part of the sparks was due to surface instabilities of the LAr-GAr interface. Indeed, a direct correlation between the bubbling and the sparking activities of both the LEMs and the grids was found. An example is shown

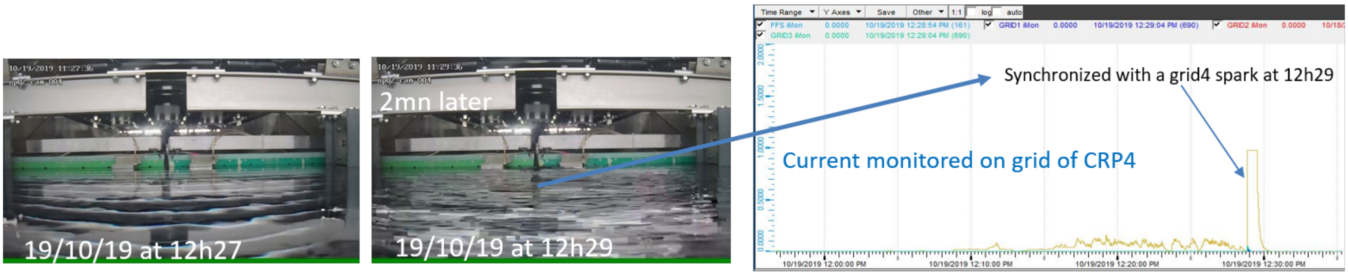

Figure 3.29: Coincidence of bubble appearance together with a grid spark

in Figure 3.29 where a spark on the grid of the CRP4 occurred in coincidence with the appearance of bubbles in-between the CRP3 and CRP4.

To monitor regularly the stability of the LEMs and all the charge readout components of the detector, I wrote a program fetching slow control data to publish a daily report on the sparking of the LEMs and grids. The program condenses the information to be discussed in the daily operation meetings. An example of such a summary is presented in Figure 3.30.

Method used to detect the sparks from Slow Control data

. The PDDP Slow Control (SC) provided crucial information on the state of all the systems. For what concerns the CRPs, the voltage of each LEM and grid could be directly controlled from the SC. The current and voltage values delivered by all the power supplies were stored in a database. What is considered as a spark is a sudden discharge of a high voltage element onto an element with a lower voltage. This can happen between the two faces of the LEMs that have a difference of potential around 3 kV in operations. During a spark, the power supply's OverCurrent flag (OvC) is triggered, and the voltage drops instantaneously.

When a spark occurs, the voltage is raised back by the SC to its nominal value at a given pace. However, if the instability persists, multiple sparks can occur during this rise. After a certain amount of consecutive sparks occurring in a small time window on a LEM, an inverse exponential rise is applied to the voltage to recover the nominal voltage at a slower pace. These behaviors are displayed in Figure 3.31.

It is possible to detect all the sparks that happened in the system by looking at the SC data for overcurrent or large voltage drops. Coherent sparking events across the different LEMs/grids could be found by searching for sparks that occurred simultaneously or in a close time window. For the spark analysis, the sparking events are classified into different categories:

- LEM-only sparks that can involve one or multiple LEMs.

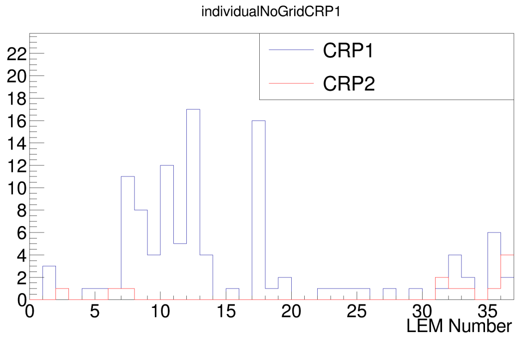

(a) Number of individual LEM sparks not associated with a grid spark for 24 h for each LEM

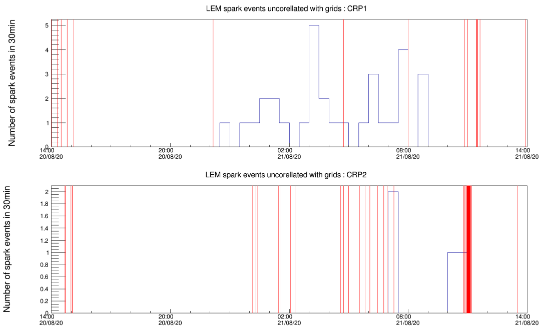

(b) Time distribution of the LEM only sparks with the grid sparks in red

.

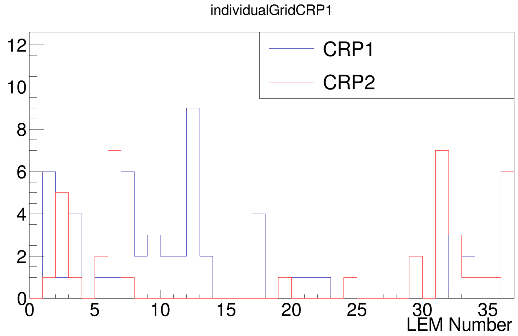

(c) Number of sparks associated with a grid spark for 24 h for each LEM

Figure 3.30: Daily sparking activity summary made available on the ELOG

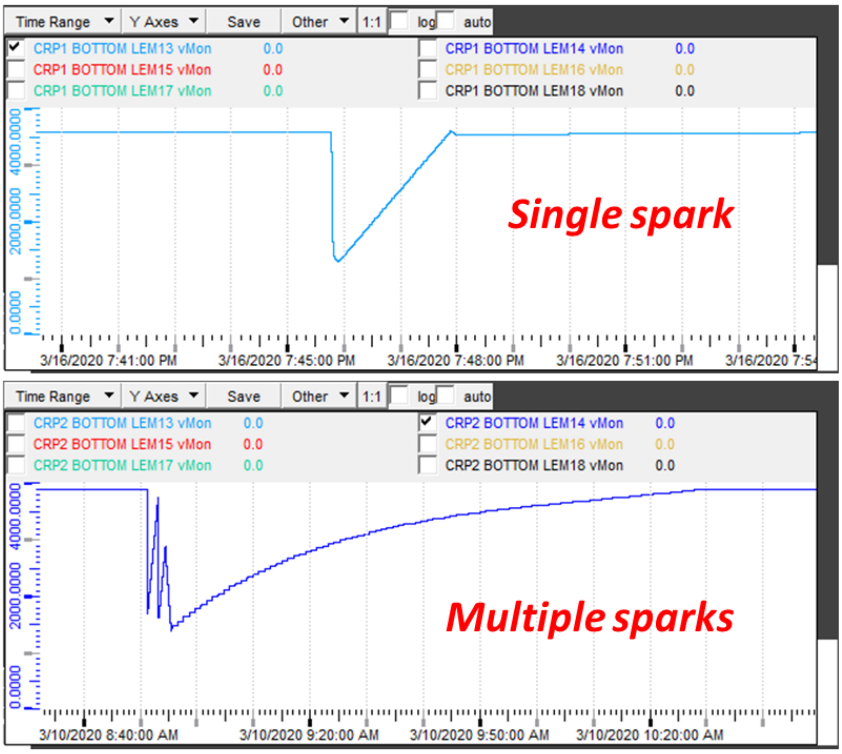

Figure 3.31: LEM voltage recovery after a spark

- Grid-only spark when a grid spark with no spark on the LEMs.
- Grid and LEMs coherent sparks.

Distinctive categories are made because the sources of the sparks are likely to be different. Indeed, for the sparks that involve both the LEMs and the grids, the main culprit probably is the LAr surface instability. In contrast, sparks involving only single LEMs are more likely to be instabilities inherent to the LEM design.

A spark analysis program fetching the data from the SC has been used to conduct extensive studies of the charge readout system instabilities.

Sparking rate analysis

Stability studies of the charge readout system have been conducted since the beginning of the operations to understand the witnessed instabilities. I will hereafter focus on the analysis of the specific stability studies that were carried out over the course of several months, between January and May 2020 and in August 2020, to investigate the CRP electrical stability. The studies aimed at disentangling intrinsic sparking from the LEMs from the capacitive coupling between the LEMs and the grids. The LAr surface conditions were kept as constant as possible during these stability studies by proceeding to pressure bumps when necessary.

This series of long-term HV stability tests were designed to determine a regime of operation of the detector that would minimize the sparking rates from all sources. To do so, various configurations have been studied varying the following parameters:

- drift field ON or OFF
- extraction field ON or OFF (grids at the LEM bottom potential or at an extraction potential respectively)
- different values of the current limiting resistors connecting the power supply to the bottom electrode of the LEMs (500 MΩ, 10 MΩ, no resistor)

The tests made by changing the current limiting resistors aimed at changing the RC value of the grid + LEM circuit to mitigate the rapid changes of capacitive coupling between the LEMs and the grids, which are induced by the presence of ripples on the LAr surface. To keep the LEMs sparking rate around the target value of 1 spark per CRP per hour without extraction field, the maximum operation high voltage is ΔV = 2.9 kV. More significant sparking rates can be observed under these same conditions when the extraction field is activated. In order tp evaluate the impact of the LEMs amplification voltage on the sparking rates, the LEMs of the CRP1 were operated at ΔV_{CRP1} = 2.4 kV while those of the CRP2 were operated at ΔV_{CRP2} = 2.9 kV.

All these tests were conducted with the front-end electronics blades unplugged from the cold flange to avoid any damage being made to the readout electronics due to grid sparks. The obtained results are reproduced in the Tables 3.2 to 3.5 reproduced below from [96], where "ON - OFF" corresponds to the difference between the sparking rate in the cathode ON situation and in the cathode OFF configuration. Most of the data sets acquired for these measurements have been taken with ~ 100 h in each configuration to reach sufficient statistical precision.

Tables 3.2 and 3.3 display the results obtained for the grid sparking rates. The numbers correspond to the addition of single grid sparks (only the grid of the considered CRP) and common grid sparks (simultaneous sparking of multiple grids).

Tables 3.4 and 3.5 display the results of a similar sparking analysis conducted for the LEMs.

Table 3.2: Grid sparking rates per hour for various configurations for CRP 1.

	Extraction	Cathode	R = 0	R = 10 MΩ	R = 500 MΩ
CRP1	ON	ON	0.63 ± 0.08	0.37 ± 0.06	0.50 ± 0.06
		OFF	0.26 ± 0.05	0.24 ± 0.03	0.20 ± 0.05 — 0.16 ± 0.04
		ON - OFF	0.37 ± 0.09	0.13 ± 0.07	— 0.34 ± 0.07
	OFF	ON			0.00 ± 0.00
		OFF			
		ON-OFF			

Table 3.3: Grid sparking rates per hour for various configurations for CRP 2.

	Extraction	Cathode	R = 0	R = 10 MΩ	R = 500 MΩ
CRP2	ON	ON		0.47 ± 0.06	0.89 ± 0.15
		OFF		0.39 ± 0.07	0.86 ± 0.18
		ON - OFF		0.08 ± 0.09	0.03 ± 0.24
	OFF	ON		0.00 ± 0.00	0.02 ± 0.02
		OFF		0.00 ± 0.00	0.00 ± 0.00
		ON-OFF		0.00 ± 0.00	0.02 ± 0.02

Several conclusions have been drawn from these tests. The grid sparking rate is observed to be 0.2-0.9 sparks per hour when the extraction field is switched on. However, when the extraction field is OFF, the results are consistent with the absence of any grid sparking activity even in the presence of ripples on the LAr surface. This result was reproduced in all the configurations and is independent of the ΔV value across the LEMs, the value

Table 3.4: LEMs sparking rates per hour normalised to a full CRP for various configurations for CRP 1.

	Extraction	Cathode	R = 0	R = 10 MΩ	R = 500 MΩ
CRP1	ON	ON	1.4 ± 0.2	2.9 ± 0.3	1.45 ± 0.16
		OFF	1.9 ± 0.2	2.6 ± 0.2	1.0 ± 0.2 — 0.34 ± 0.08
		ON - OFF	-0.5 ± 0.3	0.3 ± 0.3	1.11 ± 0.18
	OFF	ON			
		OFF			0.34 ± 0.11
		ON - OFF			

Table 3.5: LEMs sparking rates per hour normalised to a full CRP for various configurations for CRP 2.

	Extraction	Cathode	R = 0	R = 10 MΩ	R = 500 MΩ
CRP2	ON	ON		5.9 ± 0.5	4.7 ± 0.6
		OFF		6.2 ± 0.6	3.9 ± 0.7
		ON - OFF		-0.3 ± 0.8	0.8 ± 0.9
	OFF	ON		0.60 ± 0.17	5.4 ± 0.5
		OFF		0.00 ± 0.00 — 0.28 ± 0.16	0.9 ± 0.2
		ON - OFF		0.60 ± 0.17 — 0.32 ± 0.23	4.4 ± 0.6

of the current limiting resistors, and the presence or not of a drift field. Consequently, the onset of grid sparks with extraction field is attributed to the coupling between the LEMs and the grid, given that they only appear when there is a difference of potential between the LEMs and the grid.

For what concerns the LEMs sparking rates, it can be seen that larger ΔV applied across the LEMs lead to higher sparking rates as the rates are larger for CRP2. It also appears that the value of the current limiting resistors plays a role in the sparking rates. Reducing the value of this resistor, or removing it, tends to reduce the sparking rates. This demonstrates that some sparking activity is linked with the capacitive effects in the detector.

For both the grid and LEM sparks, the presence or not of the extraction field has no impact on the measured rates. There is no evidence for a contribution to the LEM or grid sparking rates from ionization produced in the drift region.

Given that part of the sparking activity is directly linked with the instabilities of the LAr surface, introducing rapid changes in the RC value of the grid + LEM system, a capacitive box was built at Saclay. This capacitive box aimed at introducing a large enough capacity in-between the LEMs and the grid to suppress the variations of the RC value of the system due to surface instabilities. However, no improvement in the sparking rates could be observed when testing this box for a short duration. Moreover, this additional capacity led to increased

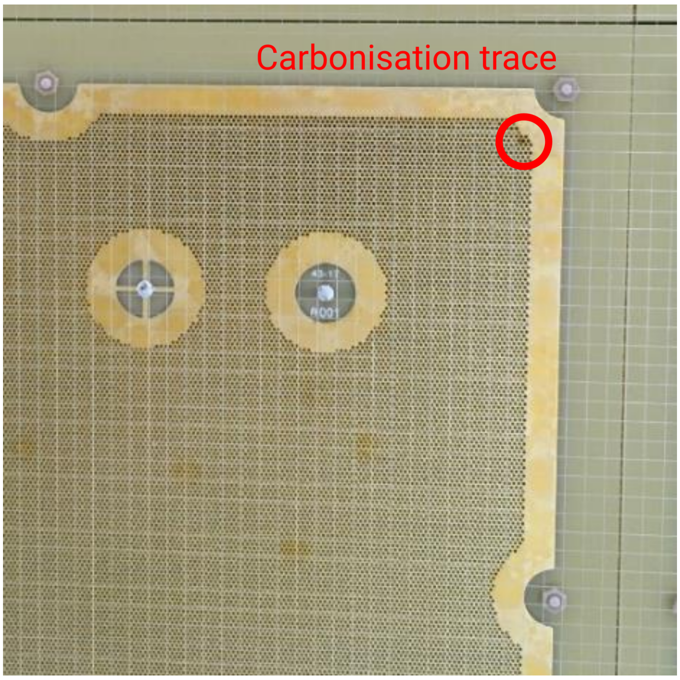

Figure 3.32: Traces of carbonization on a LEM that underwent sparking activity

difficulties in raising the voltages of the grids and LEMs, given that the two systems were now coupled with 36 10 nF capacitors in parallel (1 capacitor for each LEM) that introduces long time constants in the system.

LEM aging

The numerous sparks that occurred across the operations damaged some of the LEMs partly. Indeed, a spark may damage the LEM materials inducing carbonization, given the large amount of energy released. This carbonization, shown in Figure 3.32, decreases the local voltage required to find a conductive path and to produce further sparks. Consequently, the voltage that the LEM can withstand decreases with time. The number of LEMs that had to be kept at a voltage lower than the nominal voltage increased with time, as shown in Figure 3.33. The sudden changes displayed in this Figure are linked to the different operation phases (stability tests, data taking with higher amplification fields) that induce different stresses of the LEMs.

Comparing with Saclay's results

During prototyping and tests at Saclay and in the coldbox, LEMs were not sparking as much as witnessed during the protoDUNE operation. There are two significant differences between the test conditions and the PDDP conditions. The first one concerns the capacitive effects due to the ripples on the LAr surface that are only present for PDDP. Indeed, in the tests at Saclay, the LEMs are only tested in a single gaseous phase without any

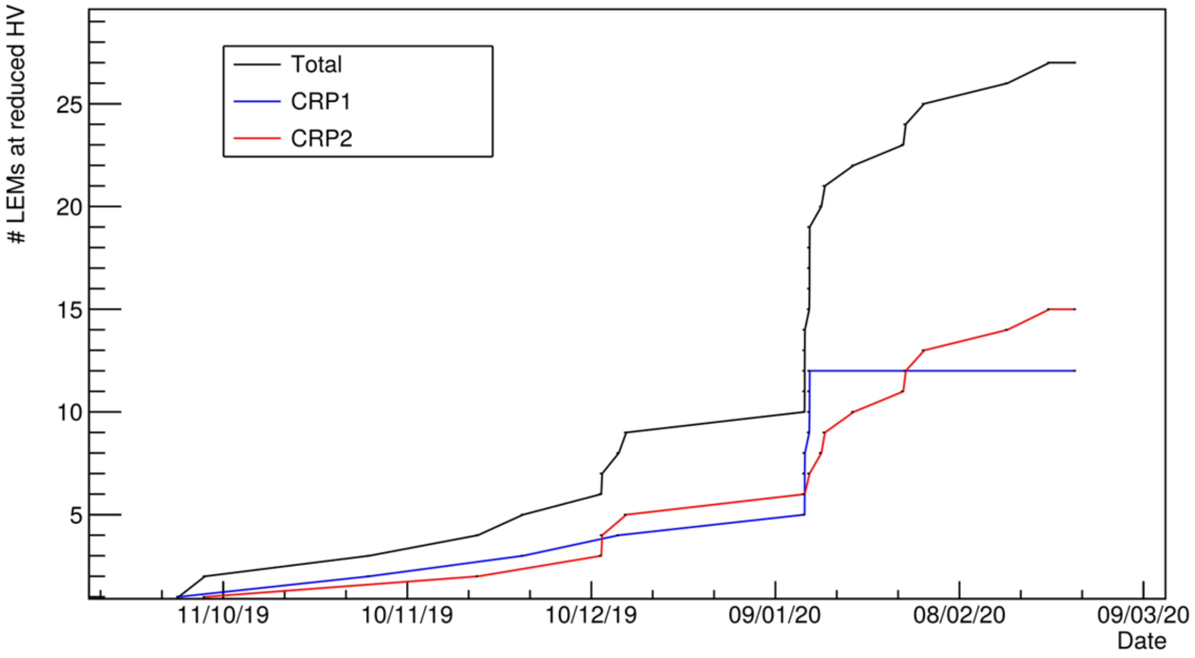

Figure 3.33: Number of LEMs kept at a voltage lower than the nominal value of 2.9 kV

LAr interface. Consequently, there is no extraction grid with a very high potential close to the LEM bottom and no capacitive coupling effect. In the coldbox, however, a complete CRP was tested in dual-phase configuration and showed no instability such as observed in PDDP. In this coldbox, the interface between LAr and GAr was perfectly flat with no perturbation, implying no sharp variation in the capacitive coupling between the LEMs and the grid. These observations point towards the importance of the disturbed LAr surface in the instabilities that occurred. A second difference between the various configurations is the GAr purity. The use of high purity Argon can increase the instabilities in a micropattern detector with respect to a less-pure gas as impurities cannot act as quenchers anymore. Both at Saclay and in the coldbox, the purity wasn't controlled. At Saclay, Argon 6.0 bottles are used, and there was no system purification. In the case of the coldbox, the detector was open with the gaseous Argon coming directly from the evaporation of the liquid Argon, and thus the purity was lower than what was then reached in PDDP. Conversely, in PDDP, the purity was thoroughly controlled to lower the attenuation and allow signals from a long drift distance to be detected.

To study the eventuality of an effect of purity on the LEM stability, the test setup at Saclay has been updated to be able to purify the gaseous Argon to a level of a few ppb. Studies are currently ongoing in order to determine the effect of purity on the LEM stability.

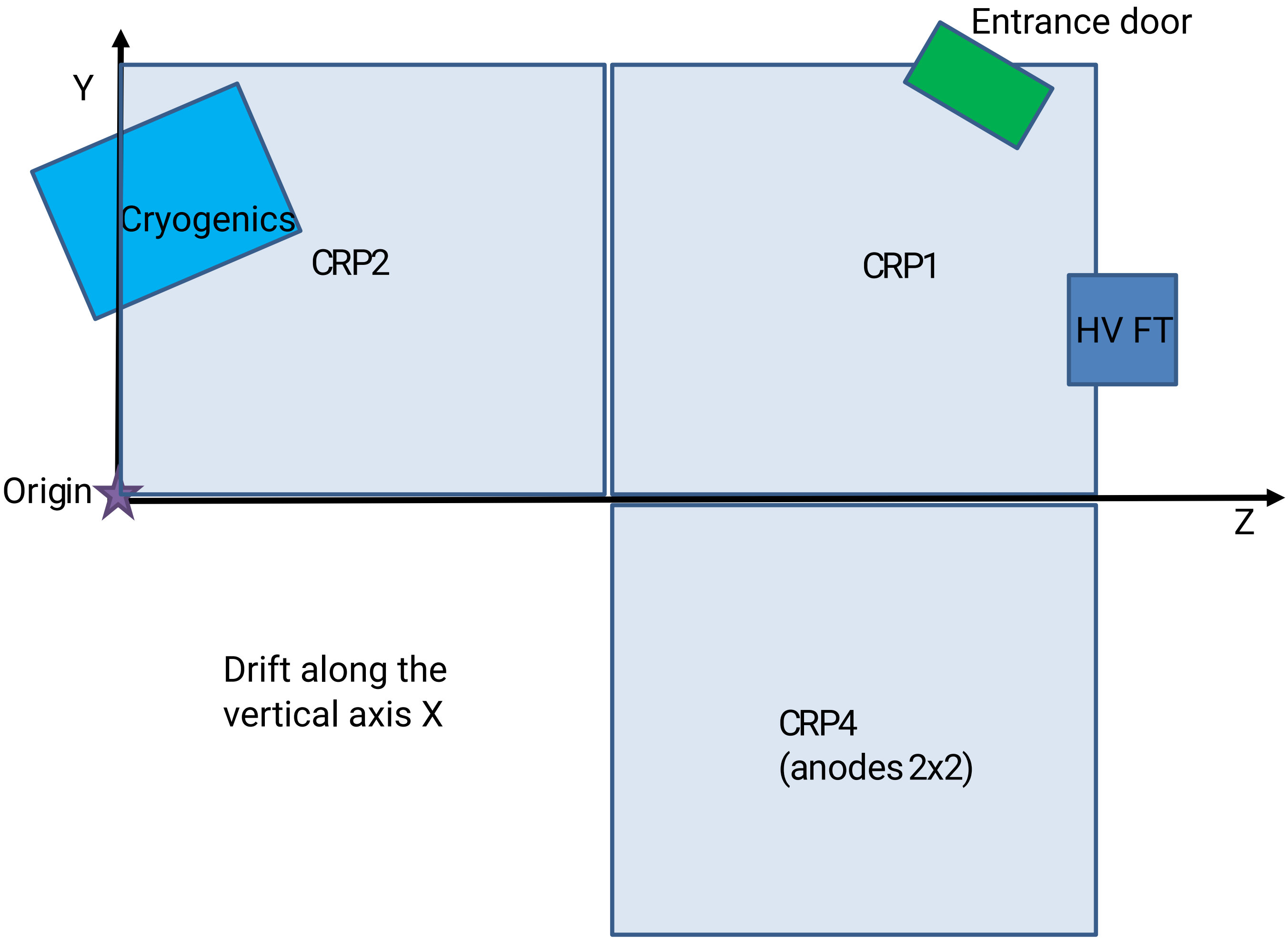

Figure 3.34: Definition of the axes used for the PDDP analysis.

3.3 Characterization of detector response

3.3.1 Reconstruction framework

The data acquired from the PDDP runs are processed with LArSoft (Liquid Argon Software) [97]. LarSoft is a framework written in C++ that aims at being used for any reconstruction or simulation of liquid Argon TPCs data. This software results from a collaboration between liquid-argon neutrino experiments such as ICARUS, DUNE, or MicroBoone. There exists a DUNE specific LArSoft repository called *dunetpc* that is the reference software for simulation and reconstruction of DUNE far detector events.

The reconstruction of an event in LArSoft is made in multiple steps, as presented below. The used axis parametrization is displayed in Figure 3.34.

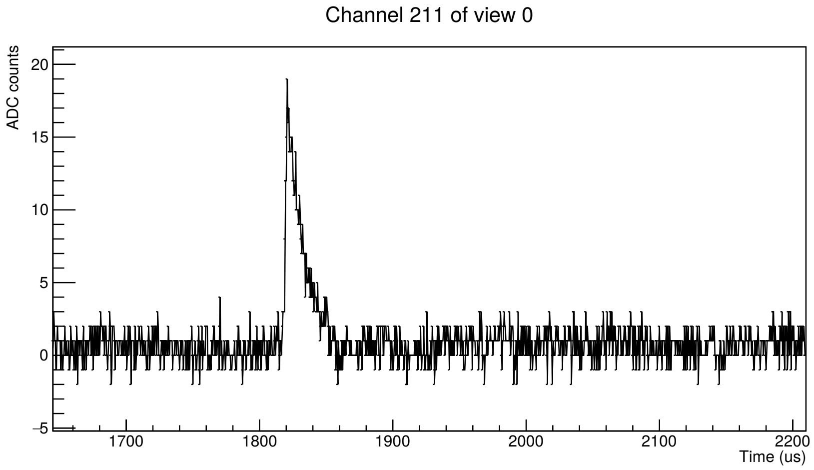

Figure 3.35: Example of a PDDP channel showing the recorded ADC counts as a function of time.

Electronics signal

The starting point of the data analysis is the electronic signals from the detector. In the case of the charge signal in PDDP, the charge that is collected on the two views of the anodes (View 0 along the Y direction and View 1 along the Z direction) is digitized by Analog-to-Digital Converters (ADCs). The charge signal is sampled with a rate of 2.5 MHz meaning that one tick corresponds to 400 ns. PDDP events last 4 ms (10 000 ticks). This event duration has been chosen to match the time of 6 m drift of electrons at nominal drift field of 500 V m^{-1}. A typical PDDP electronic signal featuring a hit is shown in Figure 3.35.

Electronic noise

The collected data are composed of the signal that we want to extract but also contain electronic noise that comes from multiple sources. Three primary sources of noise were present in PDDP data:

- Inherent electronic noise with an average level of ~ 0.7 ADC
- Coherent noise: environmental noise induced on slow control cables with a level of ~ 1.5 ADC
- Microphonic noise caused by external acoustic waves creating a movement between the LEM top electrode (@ 500 V) and the anode, inducing a signal on the anode by induction as explained in Section 3.2.3. This effect leads to a noise of 4 ADC to 5 ADC.

The noise inherent to the electronic can be dealt with using a low-pass filter given that it is a high-frequency noise. The coherent noise can be suppressed by subtracting the mean of all the channels that are on the same

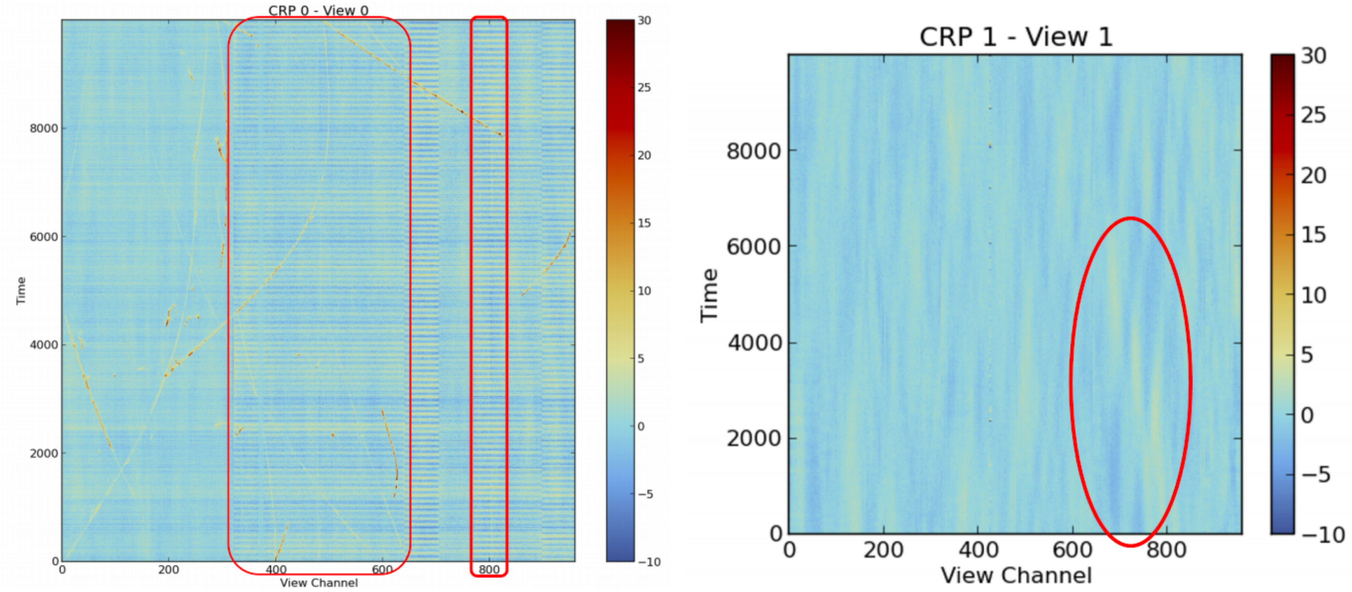

(a) Coherent noise (b) Microphonic noise

Figure 3.36: Representations of an event with ADC counts as a function of time for all the channels, displaying coherent and microphonic noise patterns.

electronic card, given that it is coherent among those channels. However, the microphonic noise is harder to remove given that it has a low frequency and impacts multiple channels but not coherently in space and time: it behaves like a wave propagating on the channels. This noise can be mostly removed by filtering the low frequency components of the signal. The impact of these noises on the obtained data is shown in Figure 3.36.

Hit detection

After reducing the noise from the electronic signal, LArSoft uses a hit detection algorithm (named *DPRawHit* in the case of dual-phase). The algorithm detects, for each channel, the region of interest where the number of ADC counts exceeds a given threshold. Then the detected pulses in the regions of interest are merged together when close in time and are fitted with a theoretical formula describing the pulse shape as a function of time. The fit function used is the following :

$$f(t) = A\frac{e^{\frac{t-B}{C}}}{1+e^{\frac{t-D}{E}}} \tag{3.2}$$

where A, B, C, D and E are the fit parameters and t the time. An example of a pulse fitted with this function can be found in Figure 3.37. The fittedt B and D parameters are identical as the electronics peaking time is of the same order of magnitude as the sampling rate.

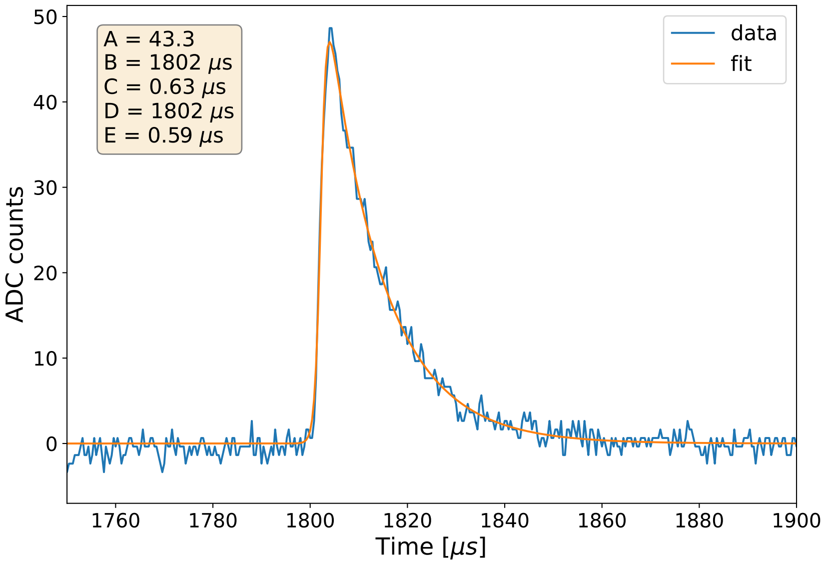

Figure 3.37: Example of a pulse fitted with Equation 3.2.

Once the pulse is fitted, its time at maximum and total integrated charge can be determined and used for the event reconstruction. The channel on which the hit is detected gives some information on the location of the energy deposit in Y or Z direction for view 0 or 1, respectively. The time of the hit is used to reconstruct the depth (X coordinate) with respect to the trigger signal, the drift velocity of the electrons being known. When the prompt light signal is used as a trigger, the reconstructed depth with respect to the trigger signal is directly the correct depth. However, all the PDDP runs have been acquired in continuous data taking without trigger despite installing CRTs at some point in the operations. The CRTs triggering has only been used for some studies of the light readout. We have no reference starting point in time for the time measurement of the charge readout. Consequently, the depth reconstructed by LArSoft is unknown, and specific attention will have to be made in the track selection to cope with this.

Trajectory reconstruction with Pandora

Pandora is a multi-algorithm reconstruction software used by the DUNE experiment in the LArSoft framework. The trajectory reconstruction performed by Pandora for dual-phase event reconstruction consists of two main steps:

- Clustering the hits in each view to merge together hits linked to the same particle. This leads to the formation of 2D clusters in the time/view-direction plane.

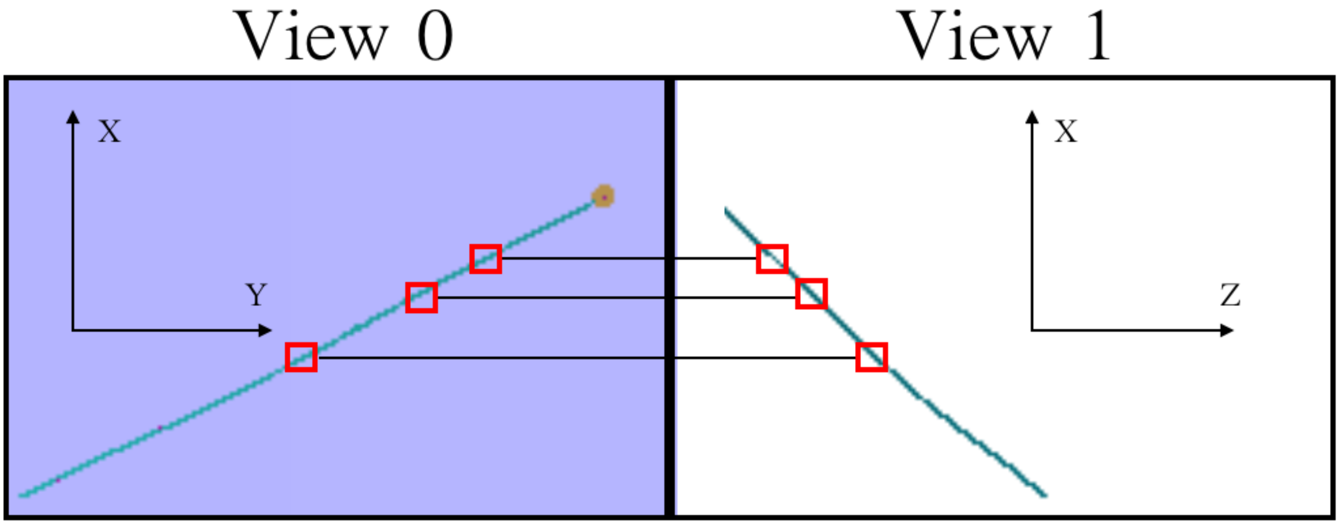

Figure 3.38: Example of view matching where clustered hits from the two views are matched together given their time of arrival on the anode

- View matching where 2D clusters from separate views are matched together to reconstruct 3D tracks. Time is used to match the 2D clusters together is the time that is common to both views. An example of the view matching step is shown in Figure 3.38.

Once all these reconstruction steps are done, most of the tracks of the events have been detected and can be used for calibrations and analysis. The global reconstruction efficency for cosmic-generated tracks has been estimated with simulations to be 76 % [98]. A typical event reconstructed by LarSoft is displayed in Figure 3.39.

3.3.2 Distorted electric field due to HV extender short

Due to the HV extender short, all the data have been collected using a distorted drift field. The short on the 24^{th} ring of the field cage leads to the high voltage being applied only until a drift distance of around 150 cm. Moreover, this voltage is only applied to the rings of the field cage without cathode at this location, leading to a drift field strongly distorted on the borders of the TPC with respect to its center. The distorted drift field has been simulated with COMSOL by the collaboration. The simulation results can be seen in Figure 3.40 where we can see the strong inhomogeneity of the drift field. The field strength ranges from 160V/cm to 320V/cm, depending on the location inside the TPC. This distorted field has to be taken into account in the reconstruction because it impacts the following physical phenomena as explained in Chapter 2:

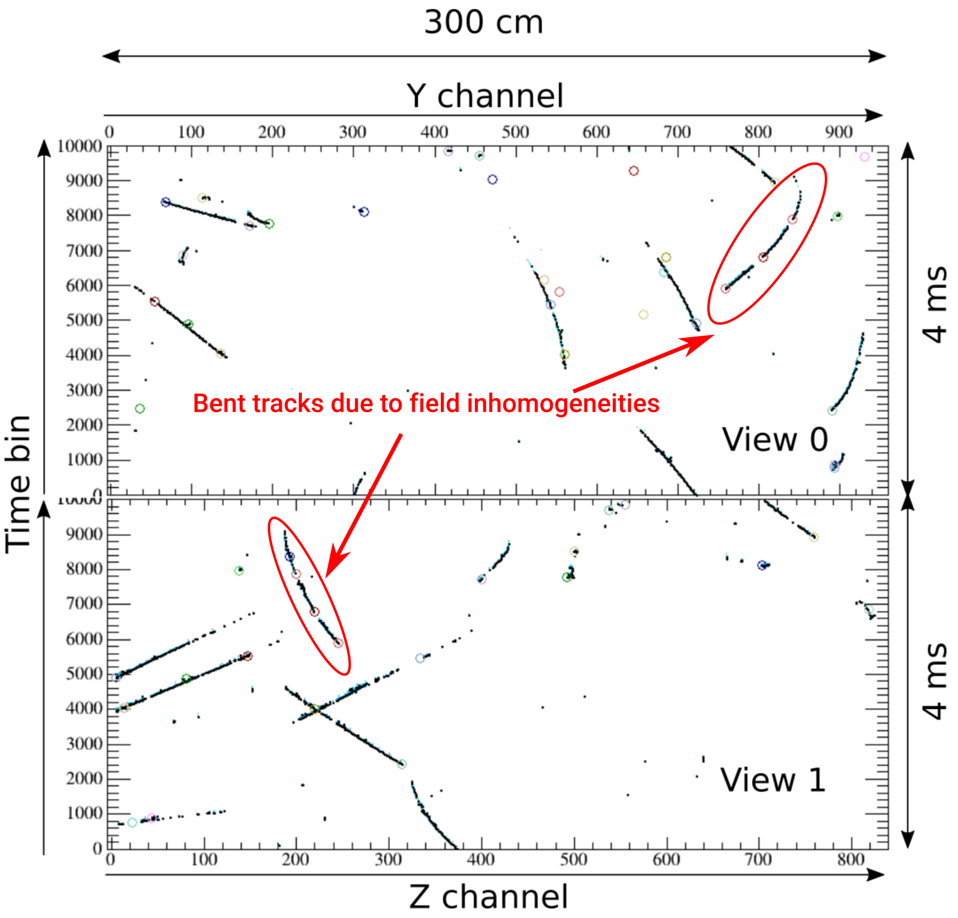

Figure 3.39: Example of an event reconstructed with LArSoft
.

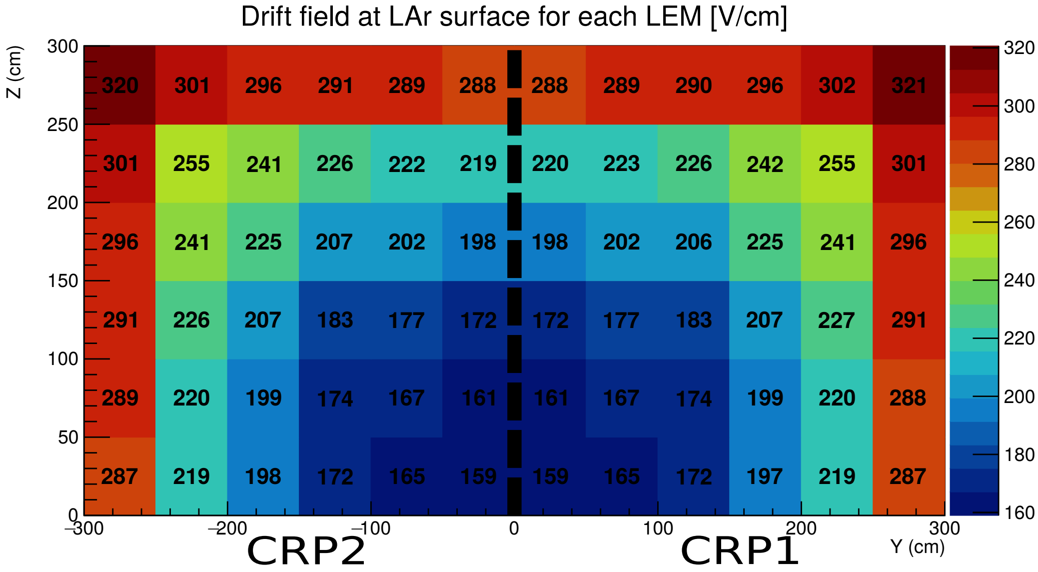

Figure 3.40: Simulated drift field at the surface of the LAr

- The drift velocity directly depends on the field with the following law [99]:

$$v(E,T) = [P_1(T-T_0)+1]\left[P_3 E \ln\left(1+\frac{P_4}{E}+P_5 E^{P_6}\right)\right]+P_2(T-T_0) \tag{3.3}$$

  parameterized by $P_1, ..., P_6$ obtained by a fit to Icarus data. This is the reason why, muon tracks that should be straight, appear as bent in the LArSoft reconstruction, as can be seen in Figure 3.39.

- The recombination of the ionization electrons follows Birk's law which has a dependency on the strength of the drift field:

$$R = \frac{A}{1+\frac{\lambda}{\mathcal{E}}\frac{\mathrm{d}E}{\mathrm{d}x}} \tag{3.4}$$

- The attachment rate of the electrons to the Argon impurities also depends on the strength of the drift field

All of these phenomena have to be taken into account in the analysis by correcting the recombination and the drift velocity as a function of the distance from the anode of the energy deposit.

3.3.3 Available charge data

The available data with the detector operating in stable conditions is limited by the multiple issues presented before: HV extender short, surface instability, sparking higher than expected. The available cosmics runs are

run	date	nominal LEM voltage [kV]	Vcathode [kV]	Number of events
1262	2019-10-03	2.9	50	33377
1263	2019-10-03	3.0	50	18424
1267	2019-10-03	3.1	50	4505
1294	2019-10-04	3.2	50	29314
1323	2019-11-21	3.1	50	11464
1327	2019-11-21	3.0	50	11966
1337	2019-11-22	3.2	50	12063
1387	2020-01-13	3.1	50	4258
1401	2020-01-14	2.5	50	24378
1405	2020-01-14	2.7	50	18049
1407	2020-01-14	2.9	50	25497
1415	2020-01-14	3.0	50	4824
1410	2020-01-14	2.9	70	11889
1411	2020-01-14	2.9	90	11769

Table 3.6: List of cosmics runs used for the analysis.

listed in Table 3.6. Four main groups of runs are taken, each lasting 1 or 2 days. The total cumulated time of cosmics data acquired is around 15 min (221477 events of 4 ms duration). These are relatively low statistics given the total time of operations. Moreover, as explained before, the LEM aging enhanced by the difficult run conditions (GRID sparks and surface instability) has led to an increasing number of LEMs not being able to withstand a nominal voltage. The latest data have fewer and fewer LEMs at sufficient voltage to amplify enough the charges to get readable signals on the anode.

3.3.4 Electronics calibration

For PDDP, no systematic calibration of the electronics channels has been conducted despite a dedicated system identical to the one present in the $3 \times 1 \times 1\text{m}^3$ prototype [95]. This system injects pulses on groups of 32 strips for each view, allowing to calibrate the response of the electronics. Indeed, given the capacitance to ground of $\sim$ 160 pF of the strips, the two views do not have the same capacitive load, thus modifying the amplitude of the measured signals. The cables used to connect the anodes to the electronics also introduce some capacitance that impacts the charge measurement. As a consequence, the calibration conducted for the $3 \times 1 \times 1\text{m}^3$ prototype, led to a calibration constant in fC × tick/ADC that was 20 % smaller for the view with a length of 3 m with respect to the 1 m view. This constant is used to convert the pulse integral into a charge deposited on an anode strip.

For PDDP, this calibration wasn't conducted, and all the analyses rely on the calibration constant measured on the naked electronics without any input impedance: 89 fC × tick/ADC. This means that all the gains measured

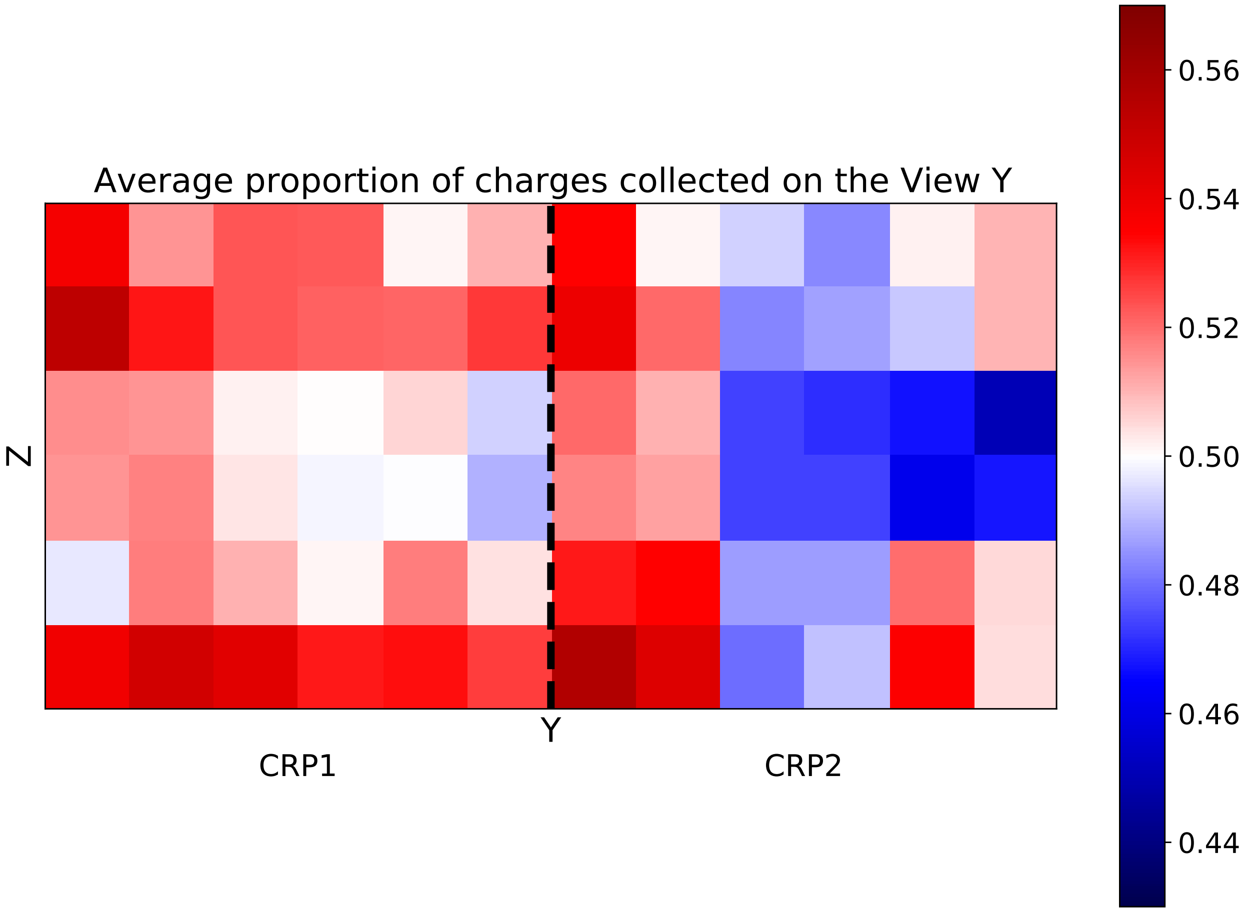

Figure 3.41: Average over all the runs of the charge fraction going to the View Y

do not consider the effects of the input impedance of the electronics. Furthermore, consistent behavior of all the electronics channels is assumed, which is an approximation. This lack of calibration can be seen by looking, for each reconstructed hit, at the charge ratio between the two charge readout views. Figure 3.41 shows an average of the ratio going to the View along Y for each LEM over all the runs. Whereas with calibrated electronics, this ratio should be close to 0.5, we can see clear deviations from this equal share ratio, even forming some patterns. Indeed, some lines or columns of LEMs clearly display inhomogeneous behaviors of the electronics.

3.4 Muon tracks analysis

3.4.1 Track selection

As explained previously, PDDP data have been acquired without trigger: charge data were acquired regularly in windows of 400 ms. The reconstruction allows to recover 2D hits in the YZ plane. For 3D hits, a reference starting time is needed. Given that we are acquiring data from cosmics muons, we know that they are either entering the TPC by the side or by the top of the detector. Discarding all the reconstructed tracks that start too close to a border of the TPC allows to only keep the muon tracks passing through the anode towards the bottom of the TPC. Similarly, all the tracks that start in time too close to the beginning of the acquisition window are discarded. Indeed, these tracks could have been entering the TPC before the start of the data acquisition window. Given this information, we can match, for each track, the first hit in time with an ionization at the surface of the LAr (at a depth of 0 cm). Having this reference and then using the hit time in combination with the drift velocity allows us to fully reconstruct the tracks in 3D. The Pandora reconstruction software used by LArSoft has some difficulties reconstructing the tracks that cross multiple LEMs. Indeed, there is a dead area at the border of all the LEMs with no amplification and no possibility for the electrons to pass through. Thus the reconstructed tracks are cut at the transition between 2 LEMs. This implies that some tracks could be mistakenly considered as two different tracks, both starting at the surface of the LAr, whereas one of them has a starting time that doesn't correspond to the LAr surface. Therefore I discard from the analysis all the tracks that start on a LEM border since they are likely to be a cut track. Figure 3.42 shows the two cuts that are applied at the start of the track for them to be considered by the analysis: the tracks signal must start at least 200 μs after t_0 and must begin at least at 6.25 cm from any TPC border. This last cut corresponds to excluding 40 over 960 electronics channels on each view. The misreconstruction of the tracks over the LEM gaps can be clearly seen, with track bits from the same track that Pandora does not merge together. This excess of tracks starting close to the LEM borders can be seen from a statistical perspective by looking at the distribution of the distances between the starting point of the reconstructed tracks and the closest LEM border. In theory, the entry points of the tracks should be spread uniformly across the CRP planes and, more specifically, on each LEM. For this uniform case, the expected probability for the track's starting point to be at a distance between a and b of the closest border of the LEM (that is a square of side length $L = 50$ cm) can be computed and is equal to

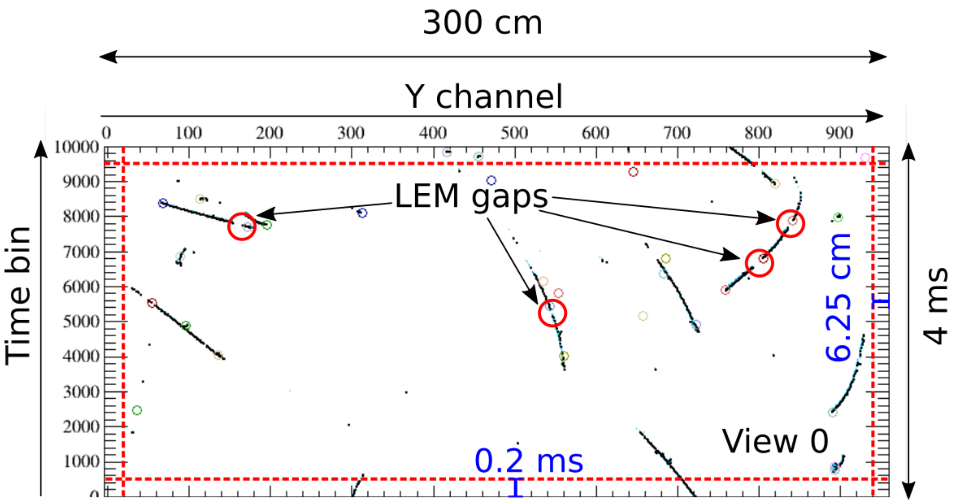

Figure 3.42: Cuts applied to track selection

.

$$\mathcal{P}\left(a \leq d \leq b\right) = \frac{4}{L^2}(b-a)(L-b-a) \tag{3.5}$$

In reality, given the passive area on the LEM borders, tracks are not detected at a distance from the border inferior to 1.5 cm. This effect is taken into account in Figure 3.43 where this theoretical distribution is compared with the actual distribution of the distance to the closest LEM border obtained from the reconstruction. We can indeed see a low number of events very close to the LEM border (below 1.5 cm). Consequently, many tracks start just after these passive areas since we accumulate all the tracks that start earlier but in an inactive region. This peaking effect is more spread out in the actual data than in the computed distribution because the effects at the border of the LEMs are more complicated than just a LEM transparency going from 0 to 1. The second apparent effect that we can witness is a lack of reconstructed tracks that start between 3.5 cm and 10 cm from the LEM border. This lack of event can be explained by an excess of tracks starting too close to the LEM borders due to the mentioned issues of the reconstruction software to stitch the different track bits together over LEM borders crosses. To prevent these misreconstructed tracks from biasing the analysis, all the reconstructed tracks that start less than 3.5 cm away from the closest LEM border are removed from the study. This cut represents a significant loss of around 35 % of the reconstructed tracks. Part of them correspond to a unique real track that was cut in the reconstruction.

When analyzing the tracks, we want to ensure that all the tracks have been obtained with the same amplification voltage across the LEMs. However, as previously explained in Section 3.2.5, two phenomena can lead to some data not being acquired with the nominal amplification voltage:

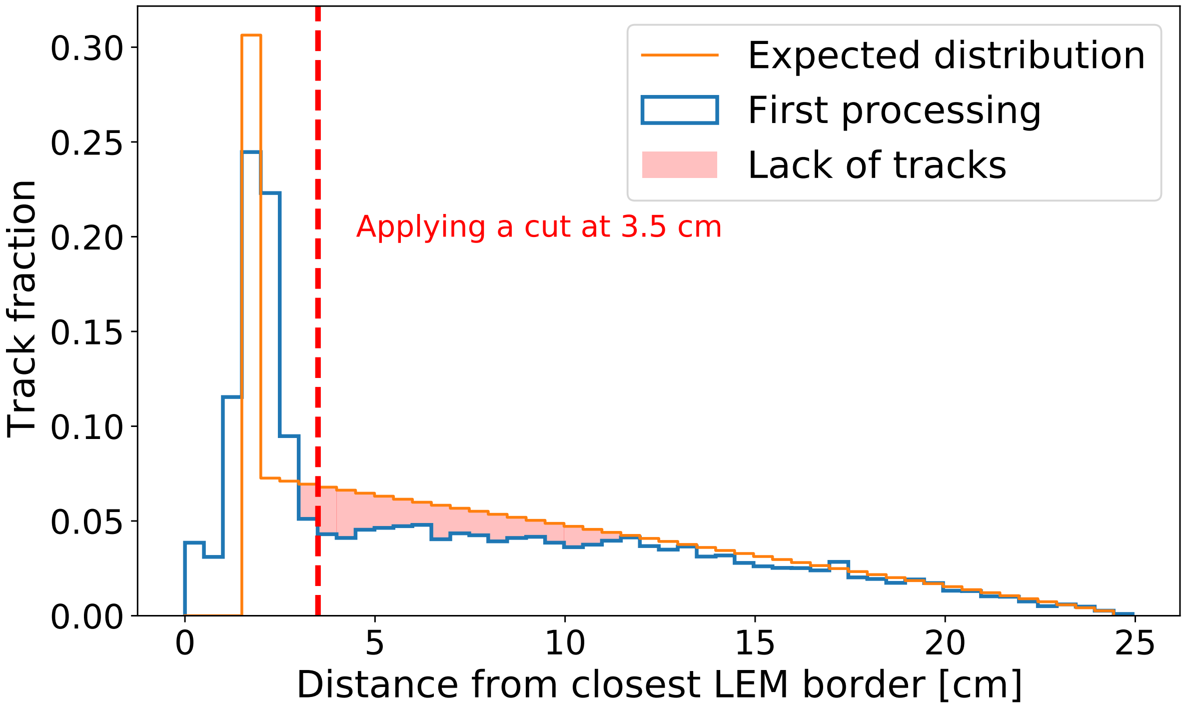

Figure 3.43: Distribution of track start distance to the closest LEM border. A cut will be applied given the excess of tracks starting close to the borders.

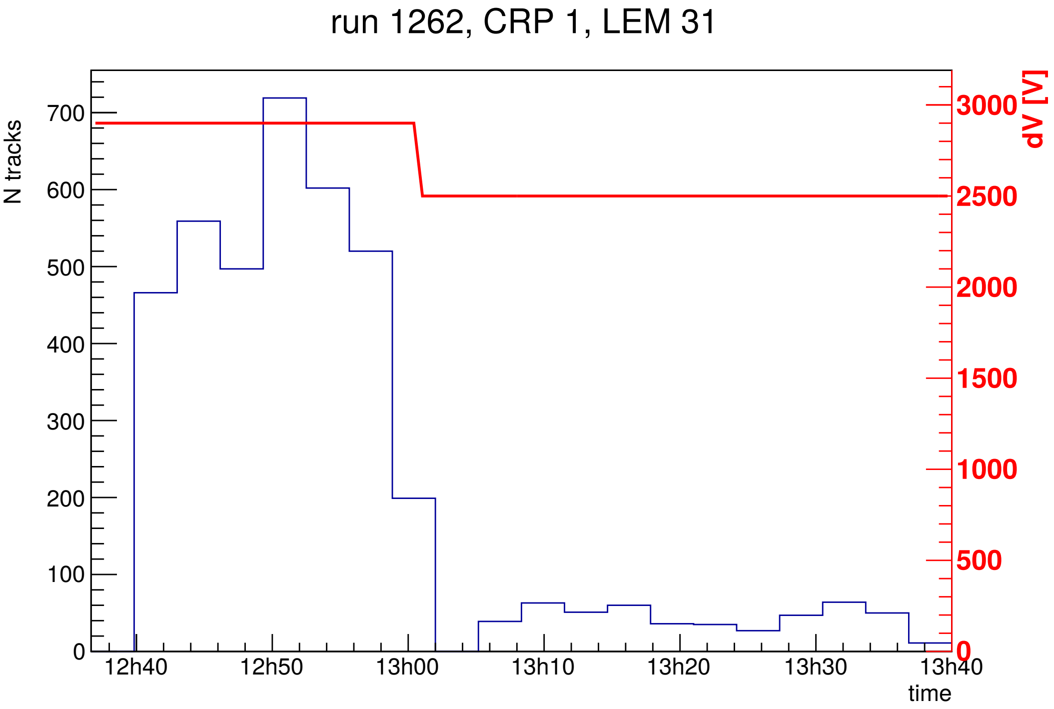

Figure 3.44: Example of the effect of a LEM voltage drop on the number of recorded tracks

- If the LEM under which the track passes is not set at the nominal voltage because it can no longer withstand the necessary difference of potential.

- If the LEM is recovering from a spark and its voltage is temporarily lower than the nominal voltage during the recovery duration (around 2 min).

I discard the tracks reconstructed under LEMs that are not at the nominal voltage by fetching all the data from the slow-control to precisely know each LEM's voltage during the various runs. These precautions are necessary to ensure that the physical quantities that are going to be measured are not biased by some LEMs that are not at their nominal voltage either for the whole run or just sporadically because of a spark. The effect of a voltage drop on the number of reconstructed tracks below a LEM can be seen in Figure 3.44, where the voltage across the LEM drops from 2.9 kV to 2.5 kV. It can clearly be seen that the amount of reconstructed tracks below this LEM drops significantly when the amplification becomes lower. Consequently, all the tracks that pass below this LEM after the voltage drop cannot be considered for the analysis.

3.4.2 Electron lifetime estimation

The electron lifetime inside the liquid Argon can be estimated using the cosmics data and compared to the results of purity monitors. As mentioned before, three purity monitors are installed inside PDDP: 2 with short drift and 1 with long drift, and their results are in tension. Estimating the drifting electrons lifetime allows for an independant measurement on a longer drift distance and is necessary to conduct any gain analysis of the CRPs. Indeed, knowing the electron lifetime is crucial to correct attachment effects and thus to convert the collected charge on the anode into an energy deposit made by a particle at a given depth. The signal attenuation with depth has to be estimated to assess the electron lifetime from the charge data. Indeed, impurities will capture the electrons during their drift, and the measured signal will be attenuated. The attenuation follows an exponential low as explained in Chapter 2, given by:

$$Q(t) = Q_0 e^{-t/\tau} \tag{3.6}$$

with τ the electron lifetime. The depth of the deposited energy can be linked to the time of arrival of the electrons at the anode with respect to the start of the track (that corresponds to the LAr surface) using the drift velocity. In the case of a constant drift velocity, we simply have:

$$t = \frac{x}{v_{\text{drift}}} \tag{3.7}$$

But for our analysis, the drit field is inhomogeneous and so is the drift velocity thus we have:

$$t = \int_0^x \frac{1}{v_{\text{drift}}(x, y, z)} \mathrm{d}x \tag{3.8}$$

To estimate the electron lifetime for a given run, we first select the tracks according to the selection procedure explained previously. For each track, the X and Y positions along the track are known from the hit position. The TPC volume is discretized in depth bins of 3 cm as shown in Figure 3.45. For each segment, the segment length (ds) is computed from the track angles. The measured charge on the anode (dq) has to be corrected by the recombination that depends on the local drift field at the ionization location. The apparent (not corrected by the electron lifetime) $\frac{\mathrm{d}q}{\mathrm{d}s}$ of the segment distributions for all the depth bins can be seen in Figure 3.46 for different depths and at two different periods. We can clearly see that the $\frac{\mathrm{d}q}{\mathrm{d}s}$ distributions shift to lower values when the depth is increasing. It can also be seen that this decrease is much larger for the October run than for the January run. This corresponds to the fact that the purity was larger in January. To obtain the charge

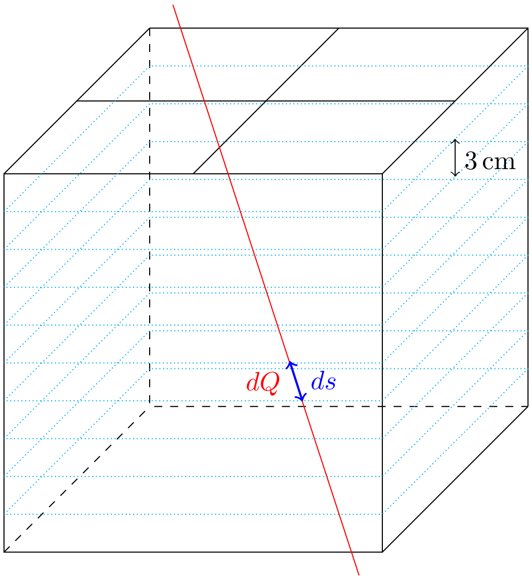

Figure 3.45: Computing the electron lifetime

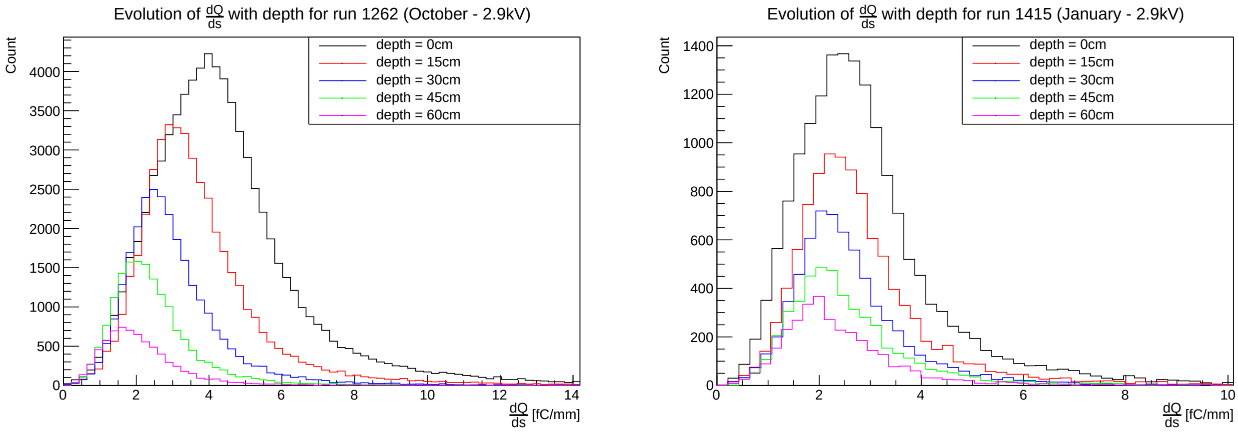

(a) October

(b) January

Figure 3.46: Signal attenuation with depth

evolution with depth, the $\frac{dq}{ds}$ distributions are fitted with the convolution of a Landau and a Gaussian function to retrieve their MPV (Most Probable Value). An example of $\frac{dq}{ds}$ fit has been conducted is presented in Figure 3.47. The fitted MPVs can then be plotted as a function of the depth. The MPVs versus depth follow the exponential law of Eq. 3.6. Figure 3.48 shows the exponential fit for three runs at different periods. It can be seen that the electron lifetime is increasing with time as the liquid Argon is purified. The computed error only comes from the fit error and does not include any uncertainty coming from the modeling of the drift field, for example. We can see that this fit error is larger for larger electron lifetimes. This is because the larger the electron lifetime, the smaller the exponential decrease that becomes harder to measure correctly.

The drift field corrections play an essential role in the evaluation of the electron lifetime by affecting both

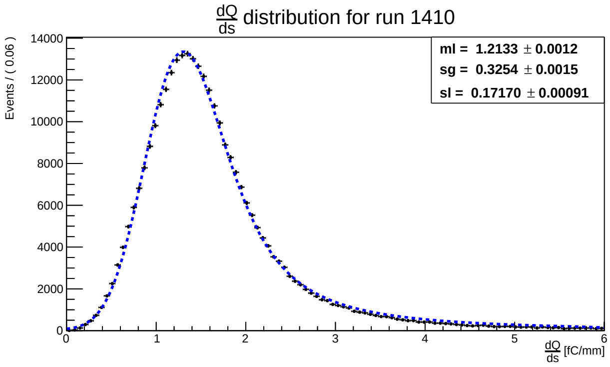

Figure 3.47: Fitted $\frac{\mathrm{d}q}{\mathrm{d}s}$ distribution for a whole CRP

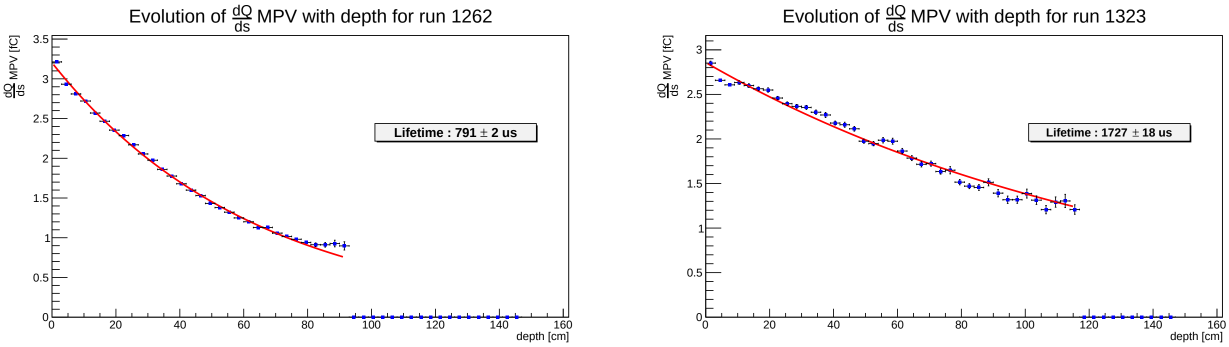

(a) October

(b) November

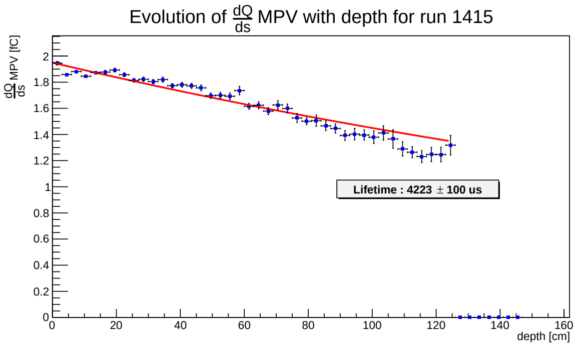

(c) January

Figure 3.48: Measured electron lifetimes with tracks

the estimated depth, due to the drift velocity dependency on the drift field, and the evaluation of the deposited charge because of the relation between the recombination and the drift field. To ensure that field inhomogeneities induce no bias on electron lifetime measurement, we can check the uniformity of the electron lifetime estimation with the (X, Y) position on the TPC anode. Indeed, the purity is supposed to be homogeneous inside the TPC, so the measured electron lifetime should be the same in all the XY areas of the TPC, whereas, as discussed previously, the drift field largely depends on the position inside the TPC. The TPC is divided into three regions corresponding to an increasing drift field: the center of the TPC, the middle part, and the border. This division can be seen in Figure 3.49 with the average drift field at the LAr surface of the associated LEMs. The electron lifetime analysis has been reproduced by separating the results for the three different zones, and the results are presented in Figure 3.50. A summary of all the measurements made in the different areas for all the runs is presented in Figure 3.51 and Table 3.7. We can see that for most of the measurements, the estimations in the various areas are in agreement within 3 σ of the overall measurement. This demonstrates that the drift field effects are taken into account correctly for most of the runs. However, we can see that some results, more especially for the LEMs at the borders where the field inhomogeneity is the largest, differ by more than $3\,\sigma$ from the overall obtained value. Some smaller uncorrected effects could affect the obtained results, such as the dependency of the attachment rate of the electrons with the drift field as it has already been reported by [100], the attachment rate between the drifting electrons and the impurities inside the LAr, such as O_2, depends on the drift field. The change in the attachment rate will depend on the type of impurities. For O_2, the attachment rate decreases when the drift field is higher, leading to a positive bias on the measured electron lifetimes. For the field inhomogeneities present in PDDP, the difference in the attachment rate to O_2 could vary from $0\,\%$ to $10\,\%$ depending on the measurements [100] [101]. Another possibility that can explain the variations in the measurements is an imperfect estimation of the drift field inhomogeneities. We only rely on simulations to estimate the drift field in the TPC volume taking into account the HV extender short. This simulation might not be entirely accurate. Finally, a last hypothesis could be a non-uniform distribution of the impurities inside the LAr volume. Given the unexpected configuration of the drift field due to the short, and the modest amount of available data, it is complicated to obtain better precisions on the estimation of the electron lifetime using muon tracks.

The electron lifetime estimations made with the charged tracks can be compared with the measurements made by the purity monitors. The analysis results are shown in Figure 3.52 where we can see good agreement with the measurements made with the small purity monitors. Consequently, it seems that the measurements

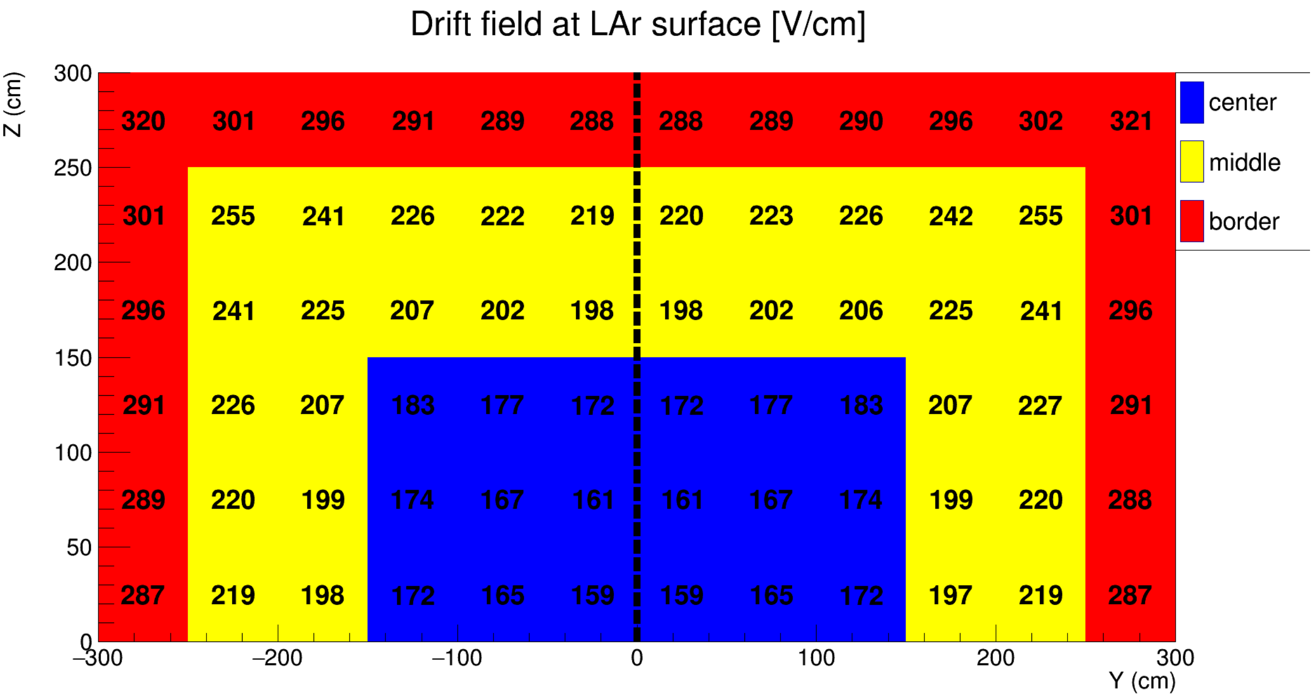

Figure 3.49: Mean drift field in V cm^{-1} at the LAr surface for all the LEMs

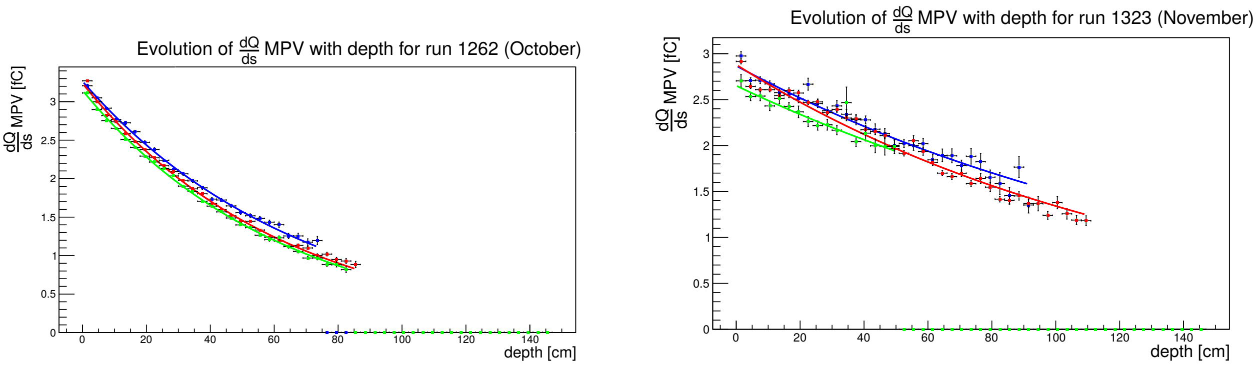

(a) October

(b) November

Figure 3.50: Signal attenuation with depth

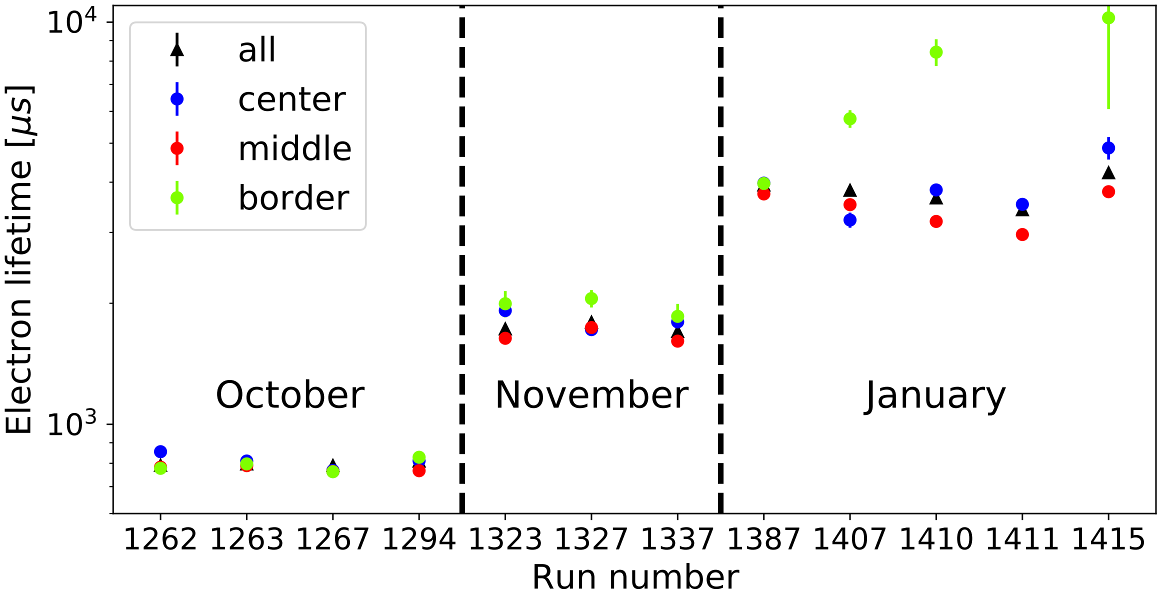

Figure 3.51: Comparison of the purity measurements in the different zones for all the runs

Table 3.7: Summary of all the electron lifetime estimations. The differences are reported with respect to the lifetime measured with all the LEMs and the computed σ only accounts for the statistical error.

.

		All LEMs	Center			Middle			Borde	
Month	Run	lifetime	lifetime	% diff	Nb σ diff	lifetime	% diff	Nb σ diff	lifetime	%
October	1262	791 ± 2	855 ± 7	8.1	7.1	782 ± 3	-1.1	1.8	777 ± 4	
October	1263	797 ± 3	811 ± 8	1.8	1.3	789 ± 5	-1.0	1.0	797 ± 6	
October	1267	790 ± 8	768 ± 24	-2.8	0.7	763 ± 12	-3.4	1.4	762 ± 22	
October	1294	810 ± 3	811 ± 6	0.1	0.1	767 ± 4	-5.3	6.1	828 ± 8	
November	1323	1727 ± 18	1918 ± 54	11.1	2.7	1637 ± 21	-5.2	2.3	1995 ± 150	1
November	1327	1795 ± 25	1720 ± 62	-4.2	0.9	1741 ± 29	-3.0	1.0	2055 ± 102	1
November	1337	1701 ± 15	1798 ± 27	5.7	2.3	1610 ± 17	-5.3	2.8	1856 ± 137	
January	1387	3936 ± 82	3978 ± 133	1.1	0.2	3740 ± 101	-5.0	1.1	3970 ± 112	
January	1407	3819 ± 58	3221 ± 139	-15.7	3.0	3517 ± 62	-7.9	2.5	5751 ± 290	5
January	1410	3656 ± 36	3826 ± 68	4.6	1.6	3195 ± 37	-12.6	6.3	8423 ± 646	13
January	1411	3417 ± 31	3523 ± 51	3.1	1.3	2964 ± 33	-13.3	7.1	63270 ± 46072	175
January	1415	4223 ± 100	4866 ± 313	15.2	1.6	3788 ± 102	-10.3	2.2	10251 ± 4172	14

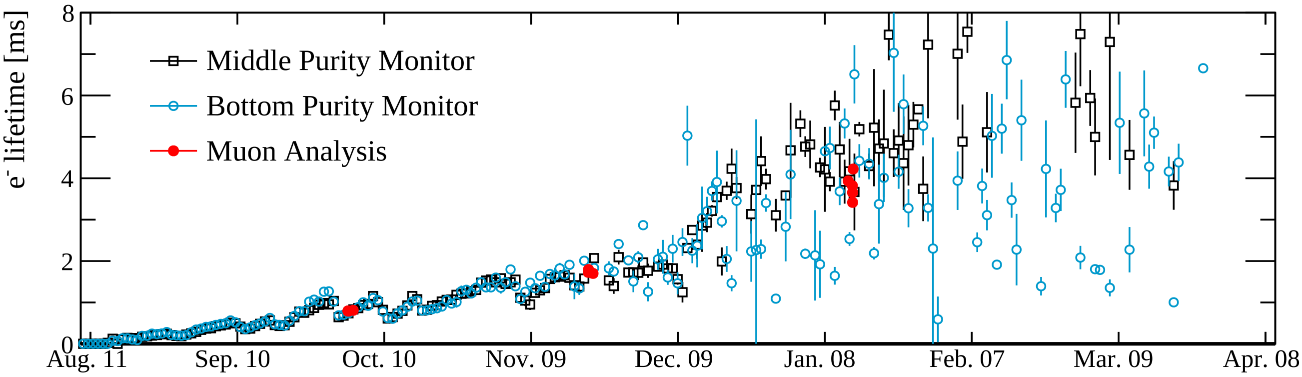

Figure 3.52: Electron attenuation measurements made with charge data overlayed with short purity monitors measurements

.

made by the long purity monitor are probably inaccurate.

3.4.3 Gain estimation

The possibility to reach high purity (>3 ms electron lifetime) has been demonstrated. It is also necessary to demonstrate that the CRPs allow reaching sufficient gain for the established physics program of DUNE (gain > 6). Using the available charge data, I measured the gain of the LEMs for different voltages and estimated the gain variations across the different LEMs.

The effective gain of the CRP assembly is composed of several parameters:

$$G = \epsilon_{\text{extr}} \times G_{\text{LEM}} \times \epsilon_{\text{coll}} \tag{3.9}$$

where ϵ_{extr} is the extraction efficiency driven by the extraction field, ϵ_{coll} is the collection efficiency on the anode and G_{LEM} is the gain due to the LEM amplification.

The gain of the whole CRP can be estimated by comparing the measured $\frac{\mathrm{d}q}{\mathrm{d}s}$ with the expected $\frac{\mathrm{d}E}{\mathrm{d}x}$ distribution for MIP particles inside the liquid Argon and in the conditions of PDDP. To perform this analysis, I proceed similarly to the electron lifetime analysis. For each track under a given LEM, I compute the locally deposited energy, dq, and the length of the track, ds, correcting for all the effects such as recombination, attenuation (given the previously computed lifetime), and local drift velocity. This allows to compute a $\frac{\mathrm{d}q}{\mathrm{d}s}$ distribution below each LEM that is equal to $\frac{\mathrm{d}q}{\mathrm{d}s} = G\left.\frac{\mathrm{d}q}{\mathrm{d}s}\right|_{\text{ref}}$ with $\left.\frac{\mathrm{d}q}{\mathrm{d}s}\right|_{\text{ref}}$ computed from the $\frac{\mathrm{d}E}{\mathrm{d}x}$ value for muon of 1.62 MeV/cm and including the corrections of all the detector effects such as ionisation yield and recombination effect. Given all these parameters, the reference quantity of charge per unit length expected to be measured on the anodes is $\left.\frac{\mathrm{d}q}{\mathrm{d}s}\right|_{\text{ref}} = 0.8\,\text{fC/cm}$ for the reference drift field. The drift field distortions are already taken into account in the $\frac{\mathrm{d}q}{\mathrm{d}s}$ calculation and the results are normalized with respect to the nominal drift field so as to remain with: $G = \frac{\mathrm{d}q}{\mathrm{d}s} / \left.\frac{\mathrm{d}q}{\mathrm{d}s}\right|_{\text{ref}}$.

Checking the various corrections

The CRP gains for each LEM are estimated with and without the recombination correction. Applying this correction should improve the homogeneity of the gains across the LEMs, and there should be no dependency of the gain with the mean drift field below the LEM. Figure 3.53 shows these gains as a function of the mean drift field at the LAr surface below each LEM with and without the recombination correction due to the drift field inhomogeneities. We can see that without this correction, there is a dependency between the drift field below the LEM and the measured gain. There is a correlation factor of 0.58 between the electric field value and the measured charge. Once the differences in recombination due to the drift field inhomogeneities are accounted for, the correlation between the measured gain and the simulated drift field is reduced to 0.05, showing that the drift field correction based on the simulated drift field is reliable. Moreover, it can be seen in Figure 3.54that the spread in the gain values is reduced after the application of the corrections. The $\frac{\sigma}{\mu}$ value is reduced from $10\,\%$ to $8\,\%$.

I then studied the evolution of the measured gain with the depth of the considered tracks. If all the corrections due to the inhomogeneous drift field and the electron lifetime are correctly made, the estimated $\frac{\mathrm{d}E}{\mathrm{d}x}$ distributions should not depend on the depth. Figure 3.55 shows boxplots of the LEM gains for each run for three different depth ranges. The stacked distributions are also shown in Figure 3.56. On the boxplots, the lower and upper hinges correspond to the first and third quartiles of the distributions. The upper/lower whisker extends from the hinge to the largest/smallest value no further than $1.5\times$IQR from the hinge (where IQR is the inter-quartile range, or distance between the first and third quartiles). Data beyond the end of the whiskers are called "outlying" points and are plotted individually. The lines in the boxes show the medians of the distributions. We can see in this Figure that for the runs in October (labeled as 12xx runs), the measured gains tend to increase when we use data from higher depths. This would indicate that the estimated electron lifetime is underestimated (given that it seems we overcorrect for the signal attenuation with depth). However, this apparent dependency remains below the intrinsic gain spread among the different LEMs. The same kind of behavior appears on November

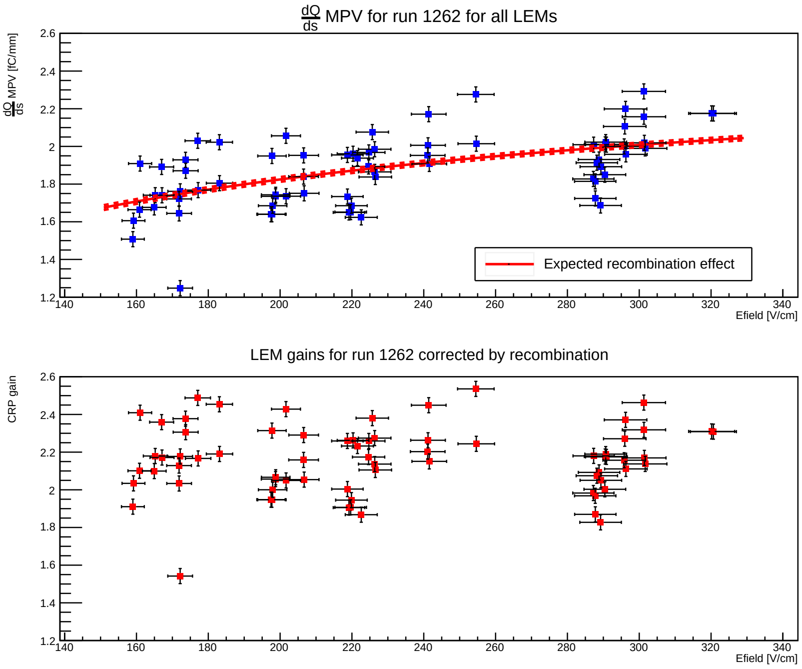

Figure 3.53: Computed gains for each LEMs of a run before and after taking into account the variations in recombination effects due to the inhomogeneous drift field

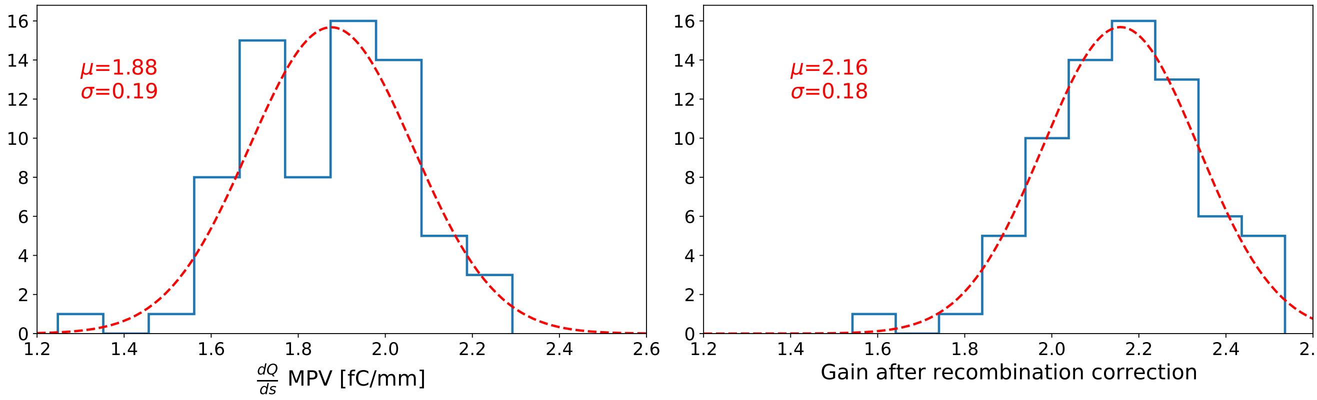

Figure 3.54: Comparison of the dispersion between LEMs before and after recombination corrections

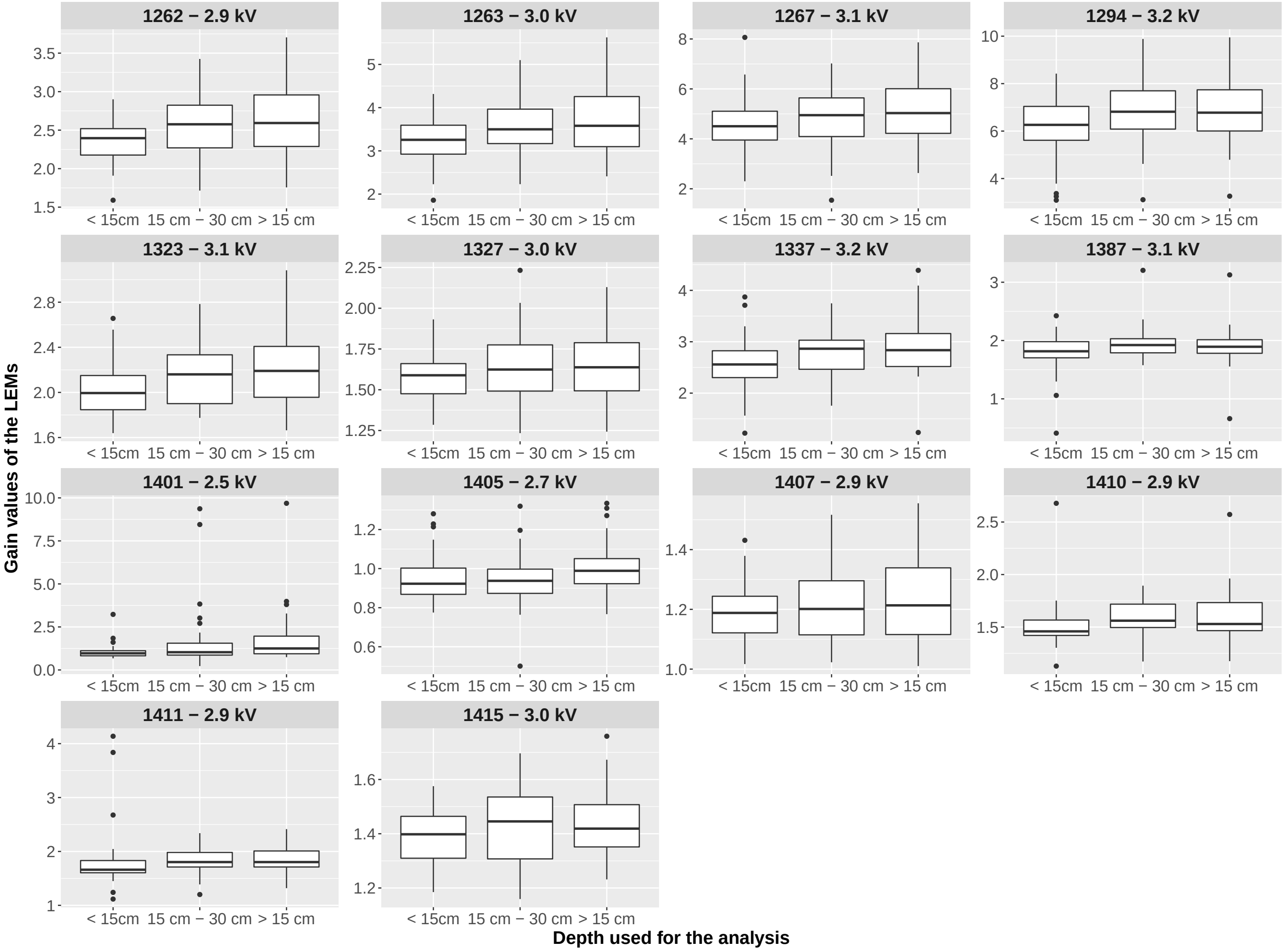

Figure 3.55: Evolution of the measured gains for different depths of analysis

(labeled as 13xx runs) and January (labeled as 14xx) runs, although it is less clear, possibly because of higher purities. Another way to quantify this effect is to aggregate all the runs and consider for each LEM the ratio between the gains measured with data of different depths. This is what is done in Figure 3.57 where the average of the ratios is larger than 1. However, this bias remains smaller than the standard deviation of the distribution. These results indicate that the evolution of the drift field with depth might be slightly different from what we simulate, even if the resulting bias is smaller than our precision. To avoid any bias, all gain studies presented below have only been realized using data with a depth < 15 cm because these data are less sensitive to errors on the drift field simulation or electron lifetime estimations.

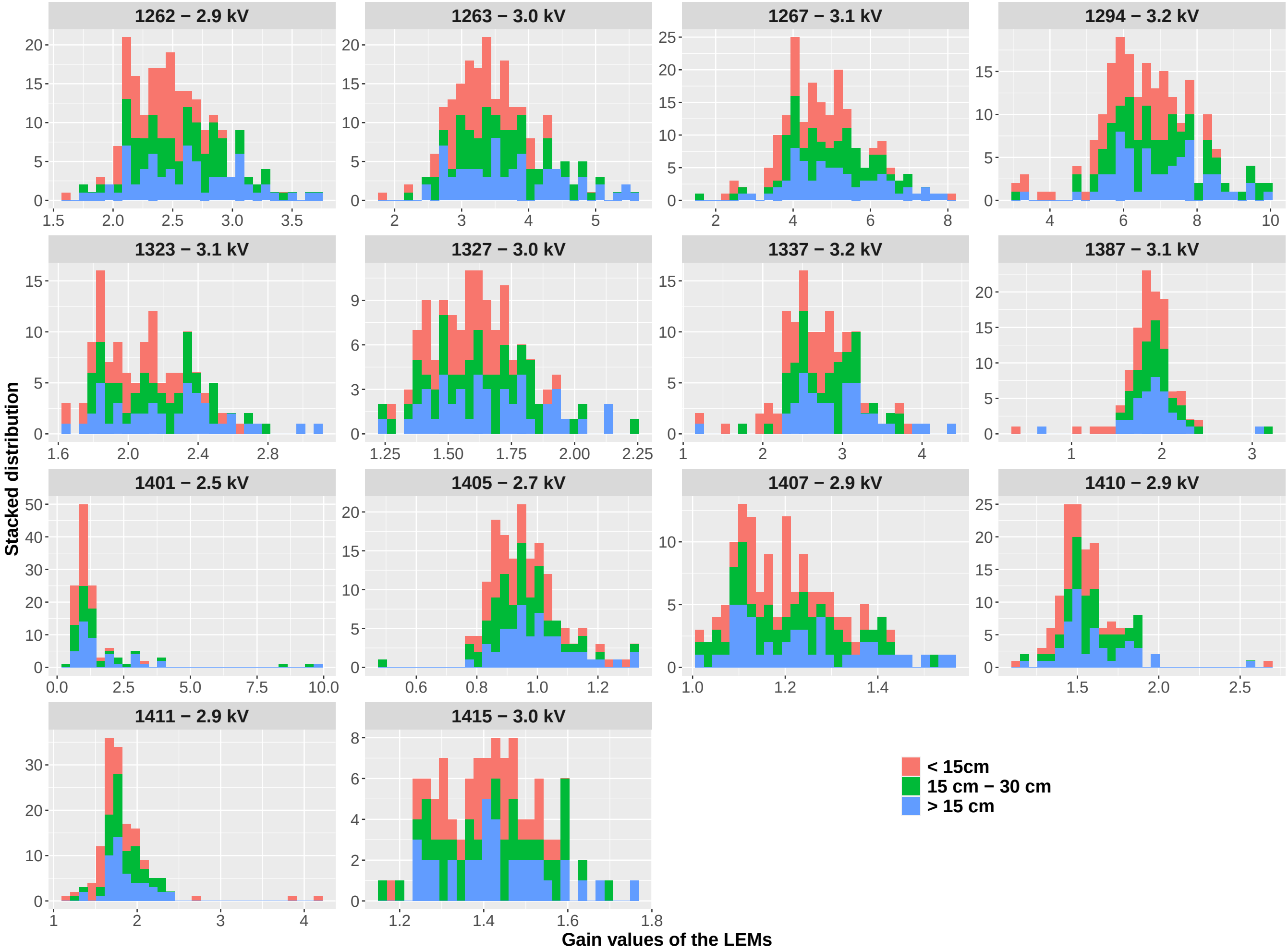

Figure 3.56: Evolution of the measured gains for different depths of analysis as stacked distributions

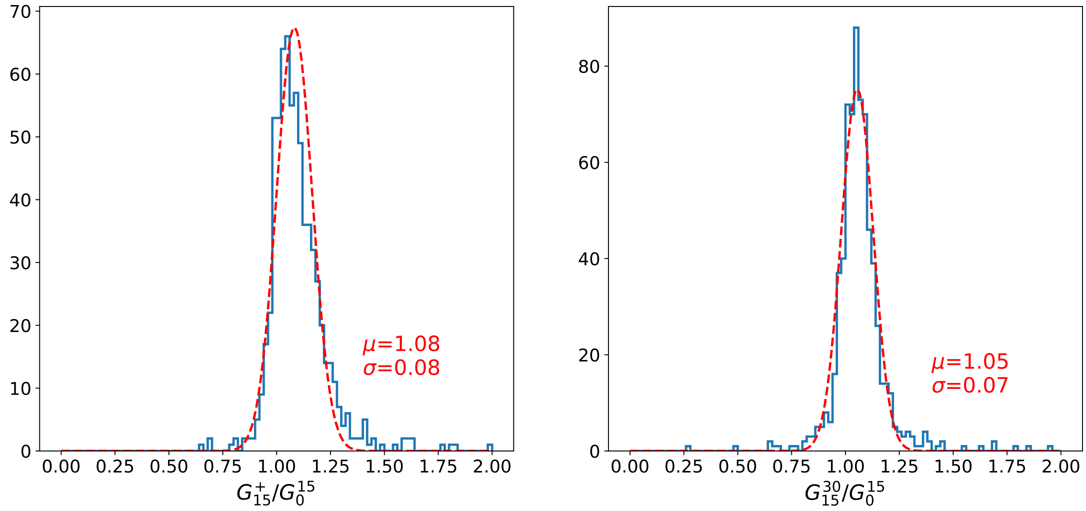

Figure 3.57: Ratio of the gain measurements with data at different depths. G_a^b designates the gain obtained using data at reconstructed depths between a and b cm.

Results

The gains have been estimated using the previously explained method for all the available runs. The measured CRP assembly gains for all the LEMs at the nominal voltage during the run are given for three runs in Figure 3.58. The expected gains reached by LEMs as a function of pressure, temperature, and voltage are well-known thanks to the R&D studies. We expect to retrieve the same gain curves for the operations of PDDP. The gains computed for all the active LEMs have been averaged for each run and studied as a function of the voltage supplied to the LEMs. These measurements are reported in Figure 3.59. For a given set of runs taken at the same date, the gain rises with voltage as expected. The charging-up effect, described in Section 2.3, that reduces the gain of the LEMs with the time of operations is noticeable. Finally, we can notice that the gain measurements made with the runs of January, so after charging-up, display an unexpected behavior with respect to the previous R&D studies. Indeed, the obtained gains are a factor ~ 2 lower than predicted. Note, however, that we cannot fully conclude without an electronics calibration, as this factor of 2 could come from this absence of calibration. This electronics calibration was conducted for the $3 \times 1 \times 1\mathrm{m}^3$ prototype [102] and led to digital integral to charge conversion factors up to 40 % smaller than the conversion factor used for PDDP.

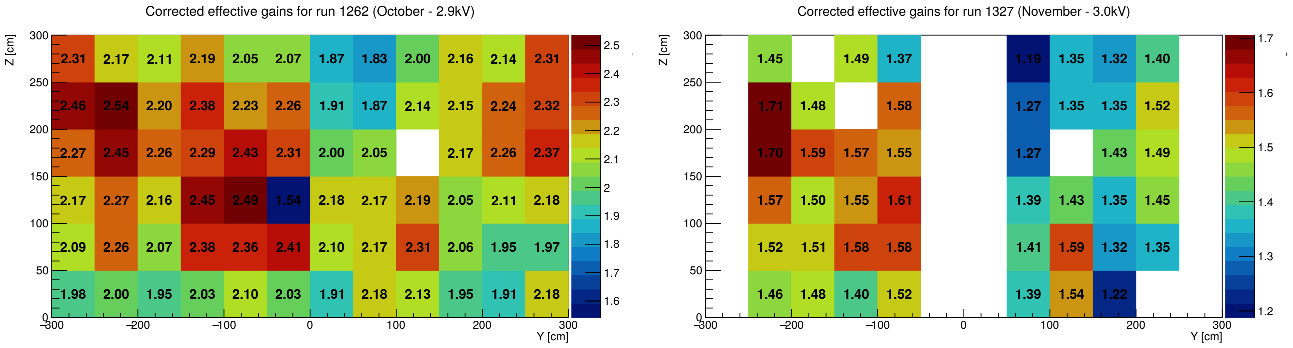

(a) October

(b) November

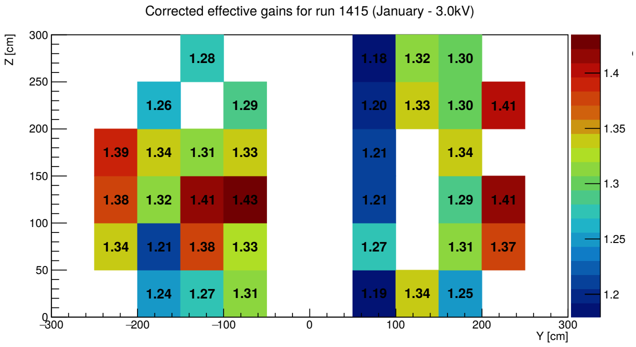

(c) January

Figure 3.58: Measured CRP gains for each LEM for three different runs

3.4.4 Gain inhomogeneities

As shown before, relatively large gain inhomogeneities are visible among the LEMs. We remind here that the LEM gain can be parametrized by:

$$G = C \exp\left(A\rho d e^{-\frac{B\rho d}{V}}\right) \tag{3.10}$$

with A, B, and C fitted constants, ρ the gas density, d the LEM thickness, and V the voltage applied.

The factors that can influence the LEMs gain inside the detector are the temperature, the gas pressure, and the LEMs thickness. Indeed the temperature and pressure impact the gas density, and the temperature gradient between the LEMs inside the detector could lead to gain inhomogeneities. Concerning the thickness, the applied voltage being constant for all the LEMs, thickness differences lead to electric field differences that induce gain inhomogeneities. We expect a decrease in the gain for increased thicknesses, given that a larger thickness implies a smaller multiplication field.

The thickness of most of the LEMs installed in PDDP have been measured on 24 points for each 10 cm×10 cm square of the LEMs [103]. The thickness measurement of the central 10 cm × 10 cm square of the LEMs was

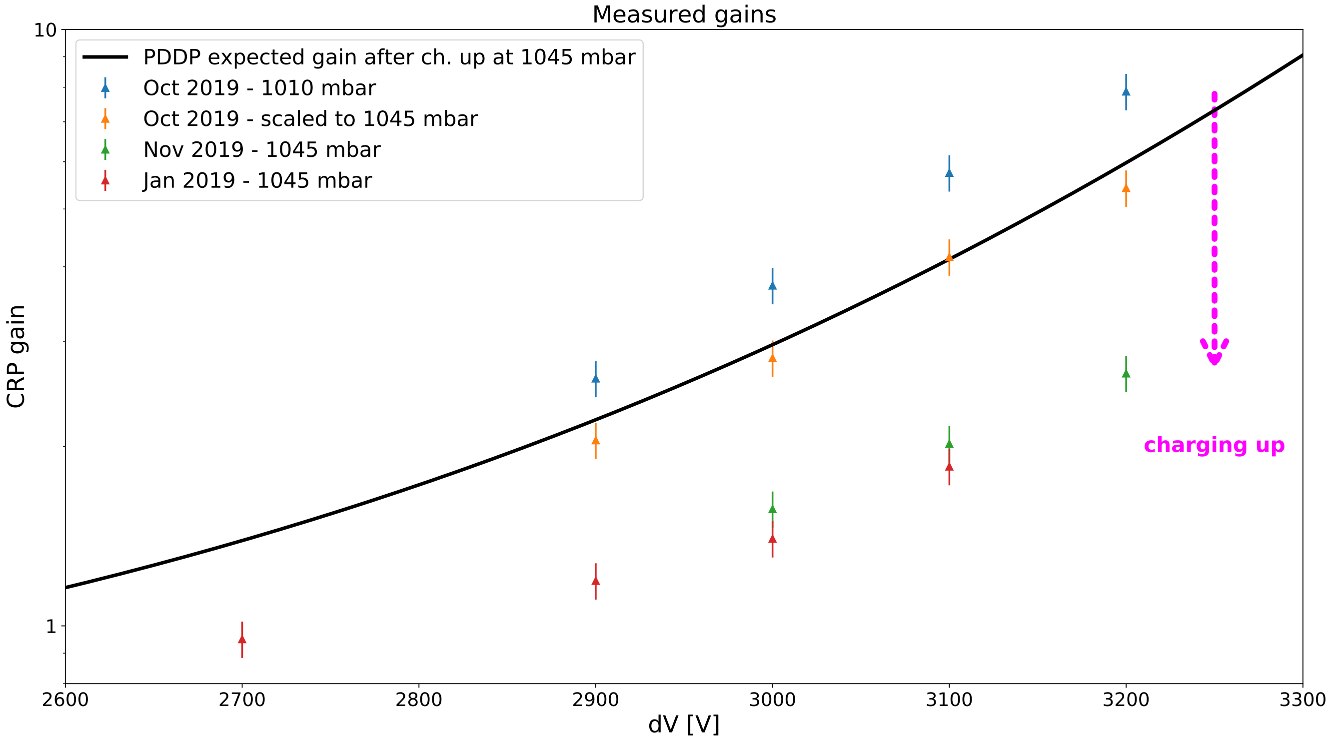

Figure 3.59: Gain curve as a function of LEMs voltage

not made; thus, its thickness is taken as the mean of the surrounding squares. The distribution of the thickness measurements is presented in Figure 3.60. We can see that the average value of the measurements is close to the specification of a LEM thickness of 1100 µm. However, there exists a spread in these thicknesses across the LEMs and inside the same LEM with a standard deviation of 16 µm. The thickness map of the LEMs installed in PDDP can be found in Figure 3.61. The evolution of the gain for the different thicknesses is presented in Figure 3.62. We can see that for the available LEM measurements, we expect to see gain inhomogeneities that can go up to ±20 %.

To study the impact of the thickness on the measured gain in the data, I repeat the above gain study by measuring the $\frac{\mathrm{d}q}{\mathrm{d}s}$ value for each track. The $\frac{\mathrm{d}q}{\mathrm{d}s}$ distribution can then be plotted as a function of the thickness by considering the thickness of the 10 cm × 10 cm square area under which the particle deposited energy. The results are shown in Figure 3.63 for the runs that provide a sufficient amount of data. It can be seen through the Pearson correlation coefficient that there is a negative correlation between the thickness and the gain, as expected. The p-value is always highly significant. The distributions are fitted using Equation 3.10 fixing all the parameters but C. The fit results are reported in Table 3.8, where it can be seen that the fitted constant C varies across the runs. The decrease of C with time is expected given the LEM charging-up process. However, there are also variations

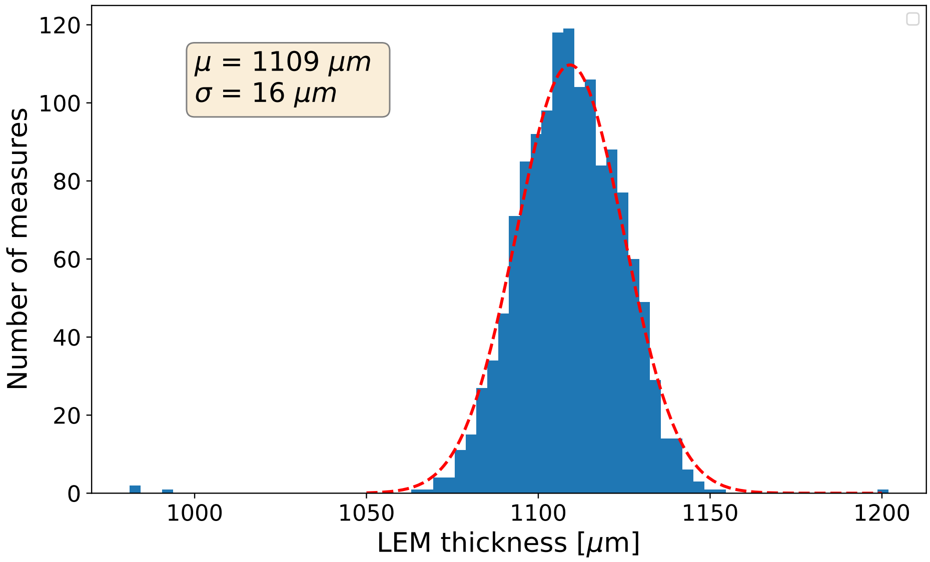

Figure 3.60: Distribution of the thickness measurements conducted on the PDDP LEMs

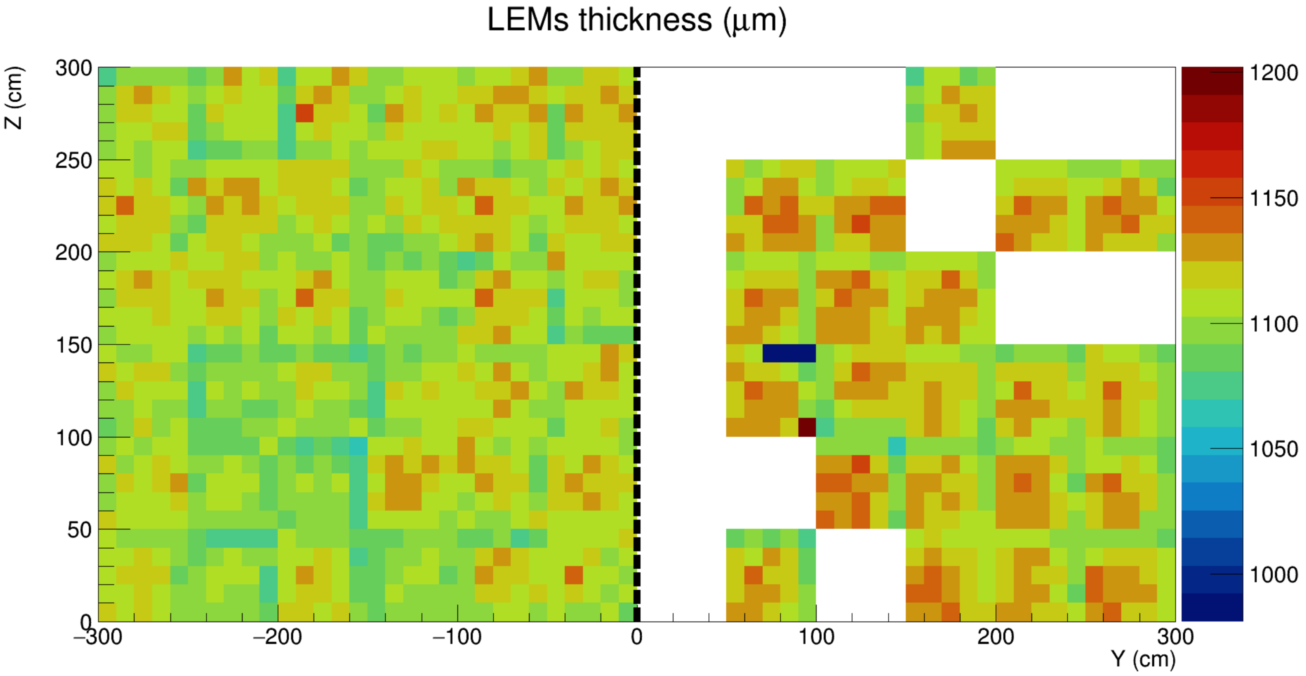

Figure 3.61: Thickness map of the PDDP LEMs

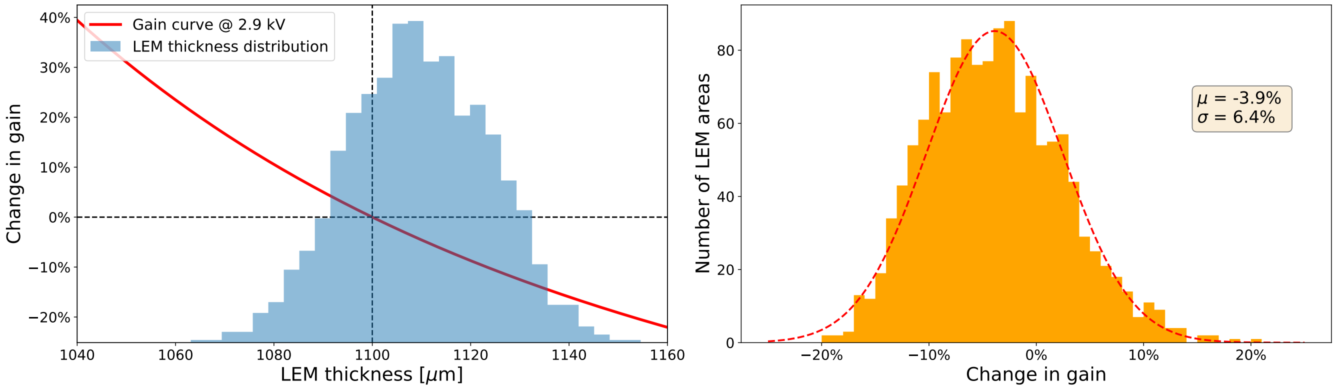

Figure 3.62: Impact of the thickness inhomogeneities on the gain with respect to the nominal thickness of 1100 μm for a voltage of 2.9 kV

Table 3.8: Result of the gain fit as a function of LEM thickness

Month	Run	Fitted C
October	1262	2.33
October	1263	2.52
October	1294	3.12
November	1323	1.36
November	1327	1.28
November	1337	1.36
January	1401	1.27
January	1405	1.09
January	1407	1.18

across the runs taken on the same day. These intra-day variations should not be present as the amplification field should be the only varying parameter. This shows that the fit is probably not significant. This can be confirmed by looking at the residuals shown in Figure 3.64 for which a positive correlation coefficient, higher in absolute value than the initial one, is found. This demonstrates that, despite witnessing a slight negative correlation of the gain with the thickness, the gain dependency with respect to the thickness does not seem to correspond to what is expected. We are probably dominated, for this study, by uncertainties larger than the effect of the LEM thickness on the gain, such as the inhomogeneous drift field.

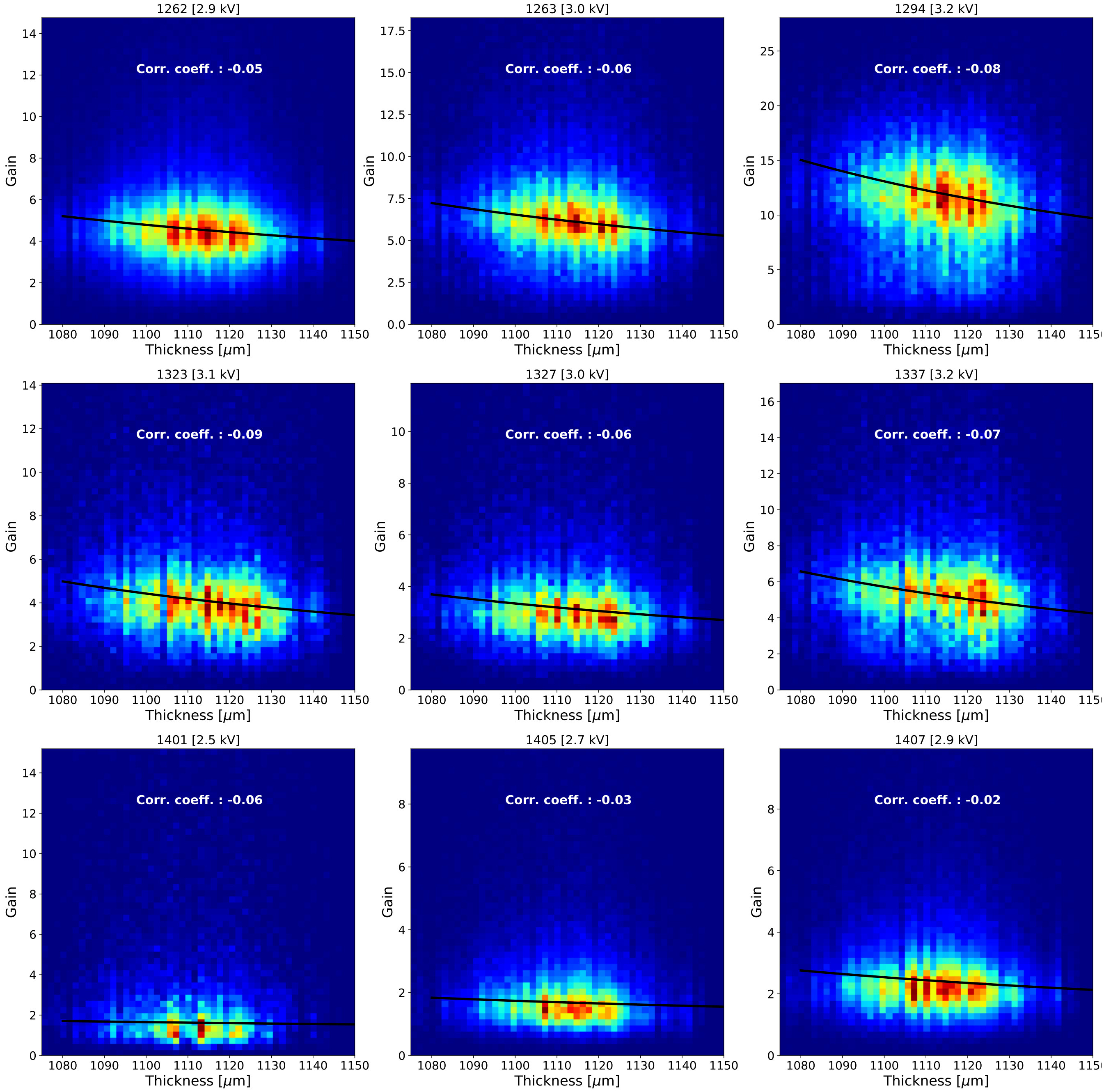

Figure 3.63: Distributions of the measured $\frac{\mathrm{d}q}{\mathrm{d}s}$ of the tracks translated as gains. The Pearson correlation coefficient is given for each run. The gain is fitted as a function of the thickness, in black, using the Equation 3.10fixing all the parameters but C.

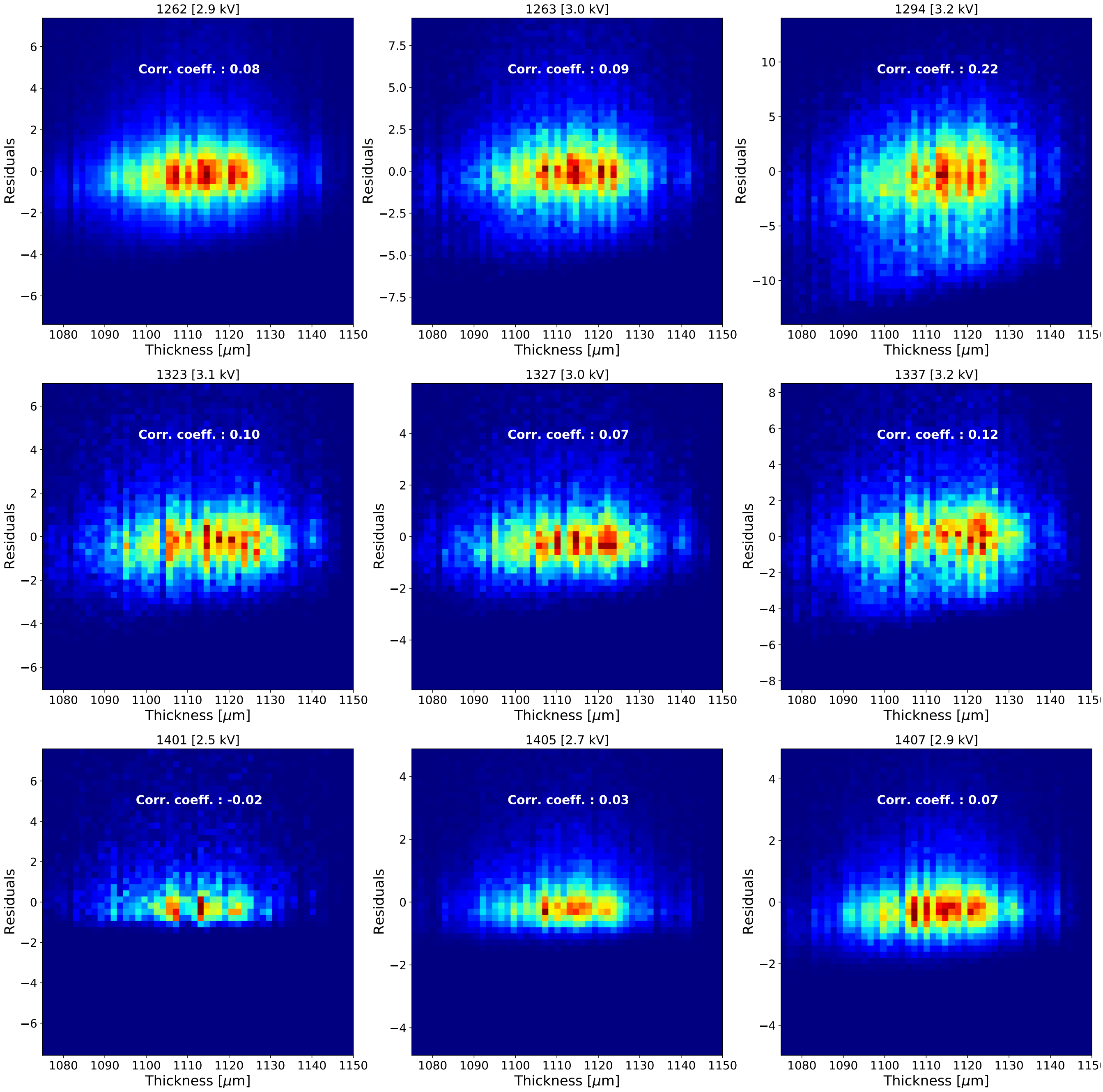

Figure 3.64: Residuals of the measured gain distributions as a function of the thickness after fitting.

3.4.5 Cathode field scan

Some specific runs were taken in which the cathode voltage was varied. Modifying the cathode voltage changes the drift field affecting the recombination, the attenuation, and the drift velocity. When the drift field is increased, the drift velocity increases, and the attenuation due to impurities is reduced. The recombination is also reduced at higher fields. Consequently, rising the cathode field should increase the measured signals on the anode. Three different cathode voltages were used for this study (50 kV, 70 kV and 90 kV) with the LEM voltage kept constant at 2.9 kV.

A gain analysis was performed on these runs in the same way as for the other runs. However, the change in drift field was not accounted for in the analysis to see the effects of this modified drift field on the results: any excess in the measured gain will be due to the change in the drift field. The gain was estimated for each LEM (without the drift field correction) for these additional runs, and then the ratios of the gains of each LEM between the different cathode fields are computed, as shown in Figure 3.65. It can be seen that increasing the cathode voltage from 50 kV to 70 kV (90 kV) increases the recovered signal by a factor 1.12 (1.21). The evolution of the signal collected on the anodes as a function of the cathode voltage is expected to follow Birk's law that guides the recombination ratio as a function of the drift field (if we neglect the lower attenuation).

The gain ratio depends on the drift field (supposing identical deposited energies), following:

$$\frac{R(\alpha E)}{R(E)} = \frac{E+k}{E+\frac{k}{\alpha}} \tag{3.11}$$

where E is the drift field, α the ratio between the cathode voltages and k a parameter. In the case of PDDP, where the drift field is inhomogeneous because of the short, this dependence with the drift field has to be considered.

We can see in Figure 3.67 these ratios with the expected evolution from Birk's law with the parameters fitted by ICARUS [75] ($k = 75.45$ for MIPs in LAr). There is a difference between the measurements and what is expected from Birk's law. The measured median value of the ratio with respect to the 50 kV run is 4 % higher than expected for the 70 kV run and 7 % larger for the 90 kV run. This discrepancy can also be seen in Figure 3.68 where we look at the evolution of the measured gain (before recombination correction) with respect to the drift field at the surface for each LEM. The runs at higher cathode voltages give access to measurements at higher drift fields. The measurements don't match what is expected from Birk's law using the ICARUS parameters, especially for higher fields. The measured dependency of the recombination on the drift field is higher than

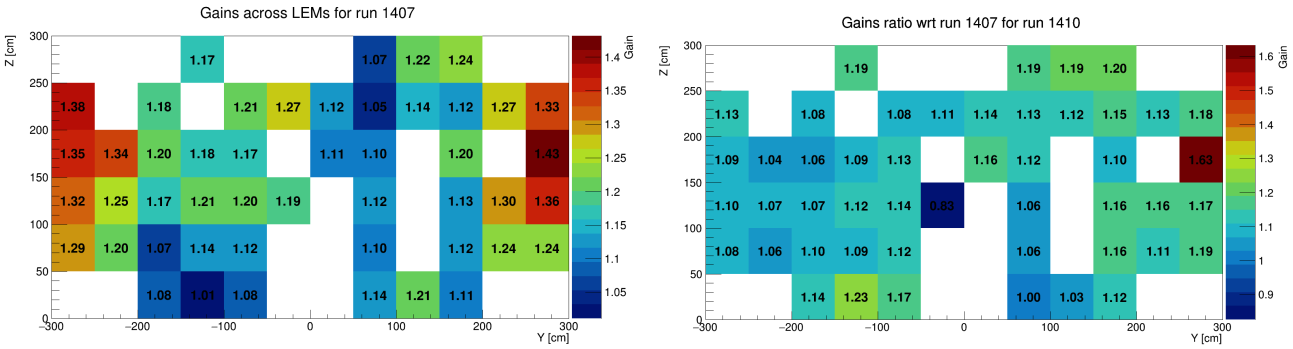

(a) 50 kV

(b) 70 kV

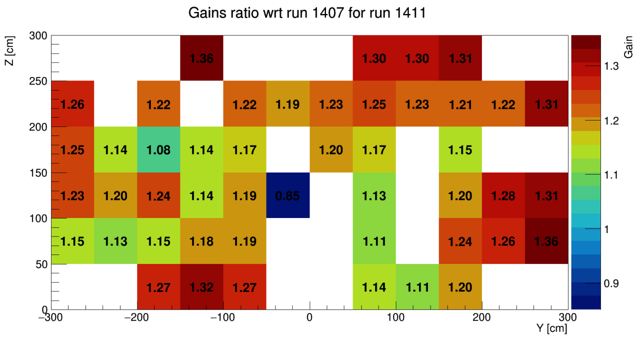

(c) 90 kV

Figure 3.65: Measured LEM gains for cathode field scan

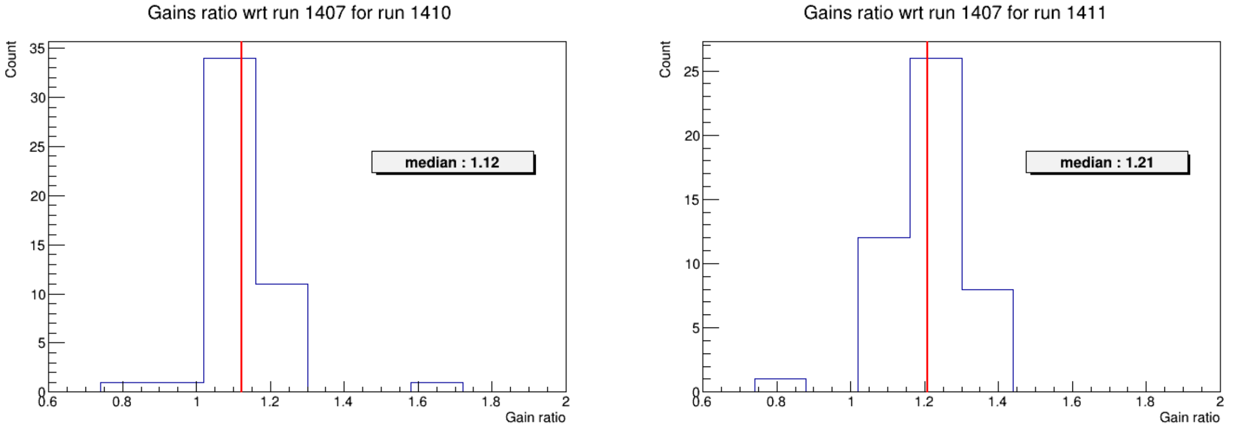

(a) 70 kV vs 50 kV

(b) 90 kV vs 50 kV

Figure 3.66: Measured LEM gains ratio for different cathode fields

.

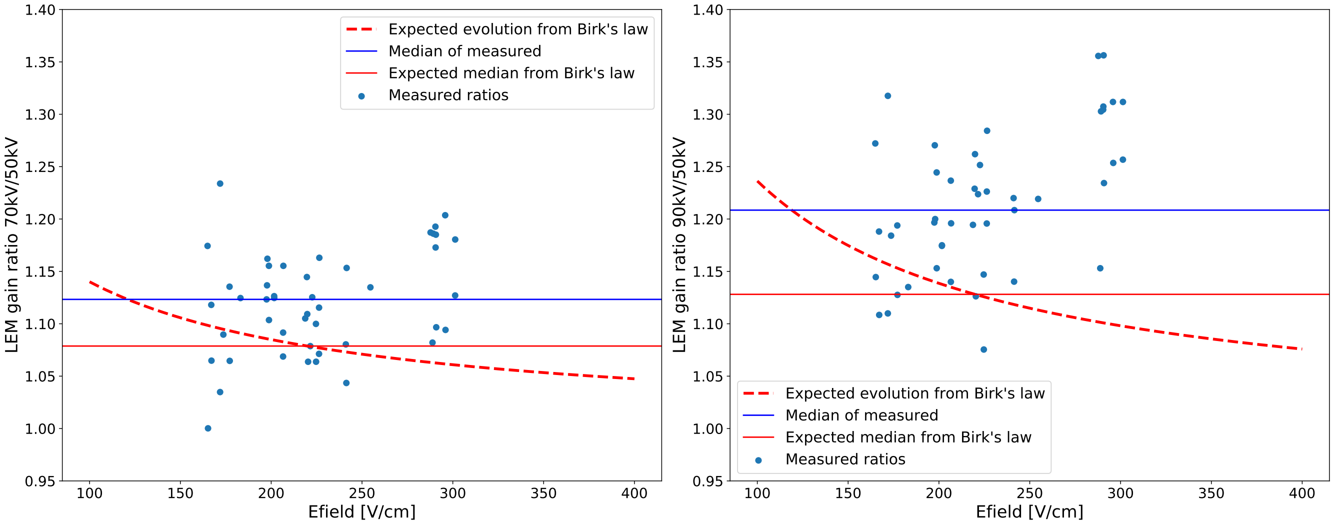

Figure 3.67: Comparisons of the measured gain ratios with respect to the expected values from Birk's law.

expected. This could be due to the space-charge effect that is not taken into account in the simulated drift field, and that can affect the magnitude of the drift field. Moreover, the field map is supposed in this study to scale with the cathode voltage, whereas the reality might differ.

3.5 Conclusion

ProtoDUNE Dual-Phase was built to demonstrate that the dual-phase technology could be used for a DUNE far detector. It was necessary to prove the possibility for stable operations of the detector and check that the requirements in terms of argon purity and CRP gains could be reached. In addition, it aimed at testing the technical solutions proposed for the high-voltage supply and the cryostat. However, several issues did not allow to demonstrate the possibility to operate a dual-phase detector of such size stably. The short on the High Voltage extender showed the necessity to improve the current design to be able to provide a high voltage of 600 kV down 12 m, as it would be required for a DUNE far detector. Furthermore, this impossibility to operate PDDP with a homogenous field in the whole TPC volume was very prejudicial to the further data analysis. It made it impossible to measure ionization beyond 1.2 m of drift. A second technical issue was the instability of the LAr-GAr interface, mainly due to the appearance of bubbles at the interface. This bubbling had a significant impact on the CRPs stability. Some temporary workarounds have been found to obtain a relatively stable interface for a specific period of time, allowing to take some data. However, the available quantity of data remains quite low. The

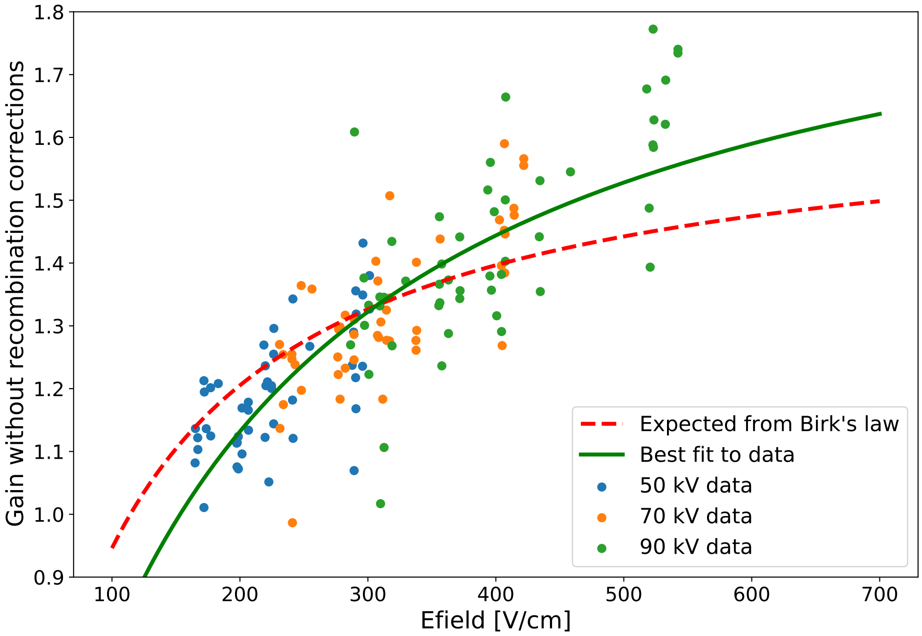

Figure 3.68: Evolution of the gain as a function of the drift field with all the cathode runs data.

LEMs have only been able to display a number of sparks below 1 spark/CRP/hour for amplification fields less or equal than 2.9 kV, thus not allowing to reach gains of 6 or more. The LEMs had, however, previously proved the possibility to reach higher amplification fields with high stability in the coldbox, thus pointing towards the unstable cryogenic conditions of PDDP as the main cause for the LEMs increased instability.

The available data allowed conducting several analyses. However, no electronics calibration has been made available, which complicates the interpretation of the results. The track analysis allowed to measure the electron lifetime in the TPC. The measurements were perfectly consistent with those of the short drift purity monitors indicating that the results obtained with the long drift purity monitor are flawed. This electron lifetime analysis also allows concluding that the implementation of the drift field simulation, after the HV extender short, allows obtaining meaningful results in the different areas of the TPC. It seems, nonetheless, that the simulation or its implementation in the analysis could be partly imperfect given that we measure, for some runs, electron lifetimes with up to 10 % differences in the different areas of the TPC. A gain analysis of the CRPs showed that gain inhomogeneities were present across the LEMs. These gain inhomogeneities can be qualitatively explained with thickness variations across and inside the LEMs. However, the available data are too few to precisely recover the expected variation of the measured gains with the thickness. Moreover, some other parameters, such as the temperature gradient inside the gas, could also impact the measured gains. Finally, the evolution of the estimated gains with the voltages allows obtaining the gain curves of the CRPs. After charging-up, that was clearly witnessed with the evolution of the gain curve with time. The maximum obtained CRP gain was below 2, which is a factor of 2 below the expected value coming from several measurements made at ETHz or Saclay. Most of the effects that could explain a discrepancy have been investigated, such as purity or recombination effects. However, even though some measurements cannot be precisely explained by what is expected from the physical processes involved, mainly because of the difficulty to control some parameters such as the drift field that is largely affected by the HV extender short, none of the considered effects could explain this factor of 2 discrepancy. The only effect left to explain these results is the electronics calibration that is not available. More data with anode only are being taken in 2022 to investigate this.

During the operations, the possibility for stable operations of such a detector could not be demonstrated. Consequently, the decision was made to move from the Dual-Phase design to a new Vertical Drift detector that could, in theory, be operated with fewer stability issues at the cost of removing the amplification stage of PDDP. This new design proposes to operate in a single phase setup, similarly to what is done in PDSP, but using PCB printed anodes placed horizontally instead of planes of wires installed horizontally. This design allows to leverage the development made on the anodes for PDDP to propose a vertical drift detector, less expensive than the typical horizontal drift single phase LAr detector. However several new challenges come along with this new technology, such as the necessity for very high argon purity and a cathode in the middle of the detector to compensate for the absence of amplification, or the development of new anodes with additional induction views. The PDDP cryostat will be reused in order to demonstrate the performances of this new design.

Chapter 4

An inner tracker proposal for the SAND near detector of DUNE

4.1 The SAND near detector of DUNE

SAND (System for on-Axis near detector) will be the only detector of the DUNE ND complex to stay permanently on the neutrino beam axis. This will allow SAND to perform beam monitoring with the aim of providing feedback about any change in the beam on a weekly timescale. SAND will continuously monitor the rate, spectrum and profile of the neutrino beam by measuring the event topology of the neutrino interactions. SAND will thus be also capable of serving DUNE as standard near detector (as in NOνA or T2K), enabling the extrapolation of the neutrino flux at the far detectors and the constrain of systematics from nuclear effects to improve the precision of the final oscillation analysis. The oscillation parameters are measured by comparing the oscillated neutrino and antineutrino spectra for the ν_e and ν_μ flavors at the far detector complex with the corresponding unoscillated spectra at the near detector complex. near detectors measure both the flux and the neutrino cross-sections which can then be extrapolated to the far detector using the flux and the neutrino interaction models. Given that these items, as well as the oscillation probability, are energy dependent, as emphasised in Figure 4.1, it is necessary to have the best possible resolution in the reconstructed neutrino energy. Moreover, it can be of main interest to be able to measure the flux on samples with low cross-section uncertainties in order to decorrelate the flux and cross-section measurements. We herafter describe a design proposition for the SAND detector that adresses these requirements. A neutrino energy resolution below 10 % is achivied thanks to a fully active highly granular

$$N^{\text{ND}}_{\nu_\alpha}(E_\nu) = \overset{\text{Flux}}{\boxed{\Phi^{\text{ND}}_{\nu_\alpha}(E_\nu)}} \times \overset{\text{Cross-section}}{\boxed{\epsilon^{\text{ND}}(E_\nu)}} \times \overset{\text{Detector effects}}{\boxed{\sigma^{\text{ND}}_{\nu_\alpha}(E_\nu)}}$$

$$N^{\text{FD}}_{\nu_\beta}(E_\nu) = \boxed{\Phi^{\text{FD}}_{\nu_\beta}(E_\nu)} \times \mathcal{P}_{\nu_\alpha \to \nu_\beta}(E_\nu) \times \boxed{\epsilon^{\text{FD}}(E_\nu)} \times \boxed{\sigma^{\text{FD}}_{\nu_\beta}(E_\nu)}$$

Figure 4.1: Formulas giving the expected number of unoscillated and oscillated neutinos at the near and far detectors.

target with a low momentum threshold on protons and neutrons and TPCs using an innovative MicroMegas technology. Furthermore, the neutron and proton detection capabilities of the active target allow the selection of a data subset with reduced nuclear effects. Here we will focus on the neutron detection capabilities, which are new and which are a unique features of SAND in the whole DUNE ND and FD complex.

4.1.1 Neutrino beam spectrum monitoring

The main objectives of the DUNE experiment are to assess the neutrino mass hierarchy, measure the θ_{23} and Δm^2_{23} parameters of the PMNS matrix, and the CP violating phase δ_{CP}, possibly discovering the CP-violation in the lepton sector. To achieve these goals, DUNE will use an on-axis neutrino beam with a wide energy range, as shown in Figure 4.2, covering two oscillation maxima. The neutrino spectrum produced by the accelerator facility can change over time. Despite the beamline monitoring systems, some changes in the beamline elements can remain undetected, as already experienced in previous experiments such as MINOS and NOνA located on the NUMI beam. In this specific case, the MINOS near detector allowed to detect unexpected changes in the beam spectrum and to take them into account, as exemplified in Figure 4.3.

It should be noted that off-axis detectors tend to be less sensitive to the spectrum changes as they can only observe a narrow energy band, thus the importance of SAND being on-axis. In the context of DUNE, the DUNE-PRISM method is expected to predict the oscillated neutrino spectrum at the far detectors by linearly combining spectra measured at various off-axis position at the near detector complex. By moving off-axis, the detectors become less sensitive to the spectrum changes and, as a consequence, it is critical to have a detector continuously monitoring the on-axis spectrum. Moreover, the "PRISM" approach is particularly affected by time-dependant instabilities of the neutrino spectrum, which need then to be detected and corrected for.

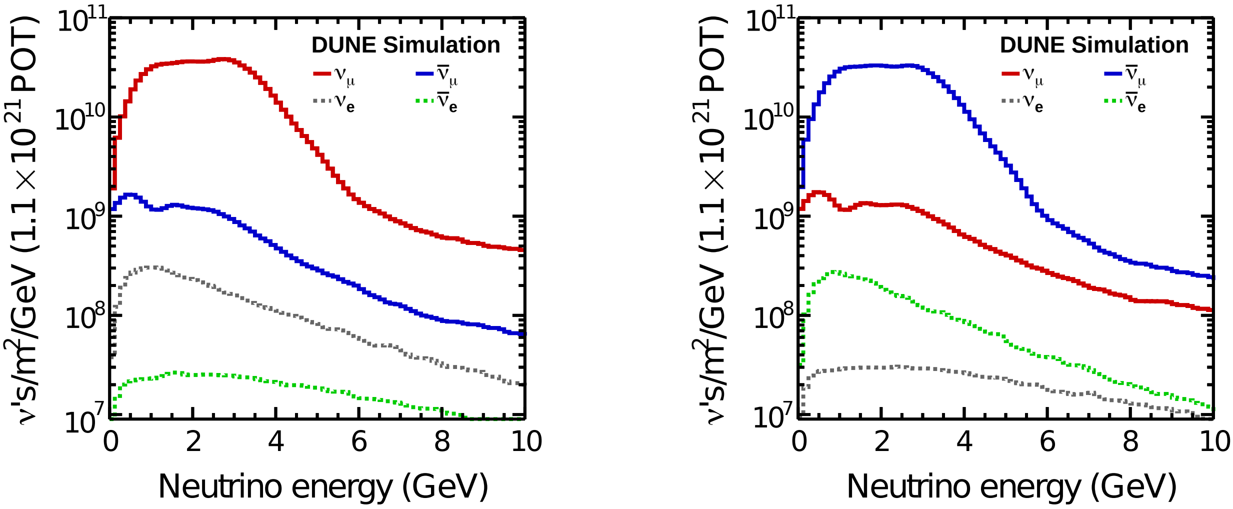

Figure 4.2: Neutrino fluxes at the far detector for neutrino-enhanced beam (left) and antineutrino-enhanced beam (right).

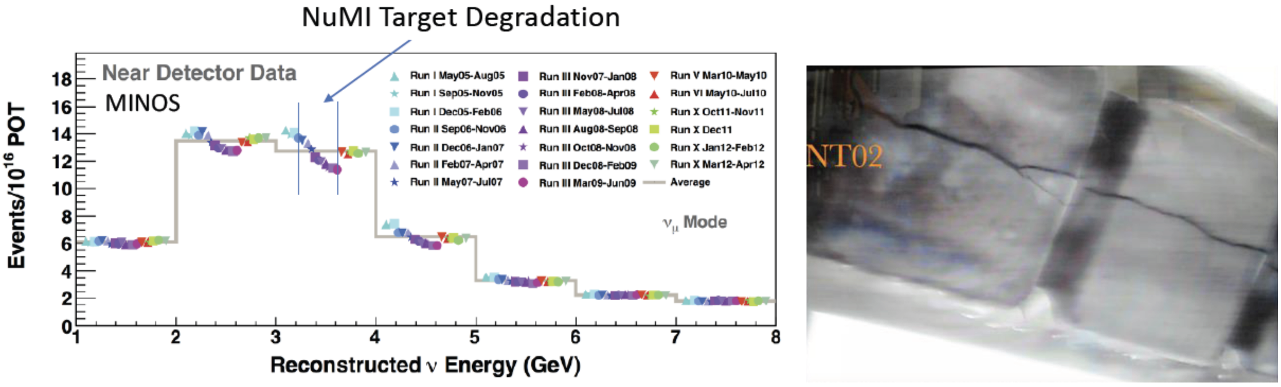

Figure 4.3: Neutrino spectrum changes in the NUMI beam detected by the MINOS near detector (left) due to a target damage (right)

4.1.2 Proposed design

The SAND detector will be composed of a magnet and an electromagnetic calorimeter (ECal) repurposed from the KLOE detector, which is a cylindrical detector previously used to study ϕ meson production at the DAϕNE collider at the INFN LNF laboratory in Frascati (Italy) The superconducting coil of the KLOE magnet provides a 0.6 T magnetic field and it surrounds the ECal which is a lead-scintillating-fiber sampling calorimeter [104]. The ECal has a readout spatial granularity of 1.3 cm and a weight of 100 t. The energy and time resolutions of the calorimeter were evaluated for the KLOE experiment and were found to be:

- Energy resolution: $\sigma/E = 5\,\%/\sqrt{\mathrm{E(GeV)}}$
- Time resolution: $\sigma/E = 54\,\mathrm{ps}/\sqrt{\mathrm{E(GeV)}}$

SAND will be instrumented with an inner tracker inside the ECal. The 3DST+TPC group proposed a design for the inner tracker composed of the 3DST (3D Scintillating Tracker), acting as an active target, surrounded on the top, bottom and downstream sides by TPCs that measure the momentum and charge of the outgoing particles. This design is illustrated in Figure 4.4. This design is based on technologies that have been developed for the upgrade of the ND280 near detector of T2K. The proposed 3DST and TPCs designs for SAND are based on the superFGD and High-Angle TPCs designs, respectively, that will be installed in ND280 for the detector upgrade. These detectors are under thorough test and characterization before their installation in the ND280 upgrade. Their measured performances are therefore been used to tune a realistic simulation of the SAND 3DST+TPCs design.

4.2 The technology of 3D scintillating detector

4.2.1 Motivations for a new technology

Numerous particle physics experiments in high energy physics make use of detectors based on plastic scintillator technology. This kind of technology allows to obtain good timing resolutions (below 1 ns) and to accurately measure the deposited energy. Recent neutrino experiments like MINOS [105], Minerva [106] and ND280 [107] have all been relying on plastic scintillator material. The rise of this kind of technology is certainly due to the progress made in industrial processing (production, shaping, drilling) of scintillating materials and in wavelength

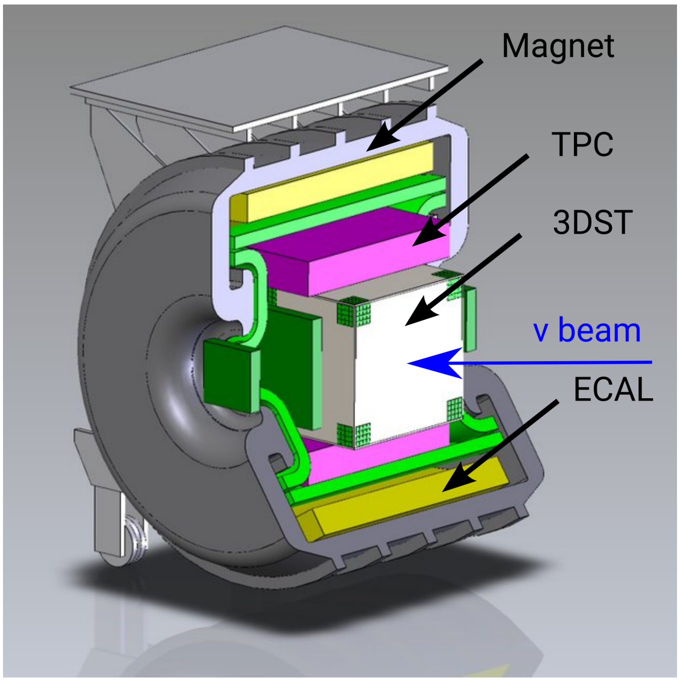

Figure 4.4: Illustration of the SAND detector instrumented with 3DST+TPC as inner tracker.

shifting fibers technology allowing any kind of geometry. This technology also benefitted from the improvement and cost decrease of the Silicon PhotoMultipliers (SiPM) detectors that are used for the readout.

In ND280 previous Fine Grained Detectors [107] these detectors have been arranged in bars disposed orthogonally to the beam direction. This geometrical setup has the disavantages of having direction-dependant acceptances and resolutions, given that particles traveling along the bar cannot be tracked. Furthermore, a particle needs to travel several bars in order for its track to be reconstructed and its momentum to be measured. For protons that have large $\frac{\mathrm{d}E}{\mathrm{d}x}$ values, this means that there is a large momentum threshold for their reconstruction. In order to overcome this limitation, the idea of a 3D highly granular detector arose [108]. The new design consists of assembling 3D cubes with a granularity of ~ $1\,\mathrm{cm}^3$, allowing to detect very localised energy deposits. The finer detector granularity allows to improve the tracking resolution and to lower the tracking threshold. Moreover, this kind of detector can serve as a fully active target covering a full solid angle of 4π allowing to reconstruct all the particules produced in the neutrino interaction independently of their direction and to calorimetrically measure the energy of those with very low momentum (below tracking threshold). The issue of such a high granularity is that it leads to the use of a high number of readout electronics channels. Typically, for a cubic detector with a side of N cubes, the number of electronics channels scales as N^3. A way to mitigate this problem consists in reading out the scintillation signals of the cubes in each of the three directions by having fibers passing through all lines and columns of elementary cubes. This solution leads to a number of electronics channels that only scales with N^2, with the drawback of some ambiguity in the reconstruction of the location of the energy deposits which can be solved with advanced tracking algorithms. The 3D information is reconstructed from the individual unidimensional fibers by looking at coinciding signals in-between the fibers from different views. In order to allow for this approach, the elementary cubes of the detectors are optically isolated from one-another by a reflective coating.

Simulations [109] and test beam studies [110] have also revealed that such a detector, thanks to its high granularity, could allow to detect the neutrons emitted from the neutrino interaction vertex. Neutrons produce very localised energy deposits and their energy can be evaluated by measuring both the neutrons travel distance and the time-of-flight between the interaction vertex and the energy deposit, thus inferring the neutrons velocity.

This ability to detect neutrons could largely improve the measurement of the incoming neutrino energy as demonstrated in [109]. Indeed, the neutrons take away a non-negligible part of the energy deposited by the neutrinos in their interactions as shown on Figure 4.5 for DUNE beam simulations. The neutrino/antineutrino charged current interactions can be separated into 4 different components.

QES Quasi-Elastic interactions were a $\nu/\bar{\nu}$ gives a p/n and a lepton after interacting with a nucleus.

RES Resonent interactions where a pion is produced in the final state through a Δ resonance excitation.

COH Coherent Scattering where an additional pion is produced in the final state through coherent interaction with the nucleus.

DIS Deep inelastic scattering where several hadrons are produced. This occurs when the energy transfered to the nucleus is high enough and leads to busy events with many outgoing tracks.

The energy carried by the neutrons is larger for anti-neutrinos as their charged-current interactions convert a proton to a neutron, often providing it sufficient kinetic energy to exit the nucleus, with an average of around 18 $\%$ for $\bar{\nu}$ QES interactions. This energy share can also be large for ν: of the order of 15 $\%$ for DIS interactions. The 90 $\%$ upper limits show that this energy share can be much higher for part of the events. As evident in Figure 4.6, the energy fraction carried out by primary neutrons is larger for lower energies, and thus very important to reconstruct, in order to improve the resolution on the measurement of the incoming neutrino energy, most notably for quasi-elastic and resonant interactions.

Previous experiments like NOνA were unable to directly detect the neutrons and measure their kinematics, thus they had to rely on specific nuclear models in order to evaluate the fraction of energy which goes to

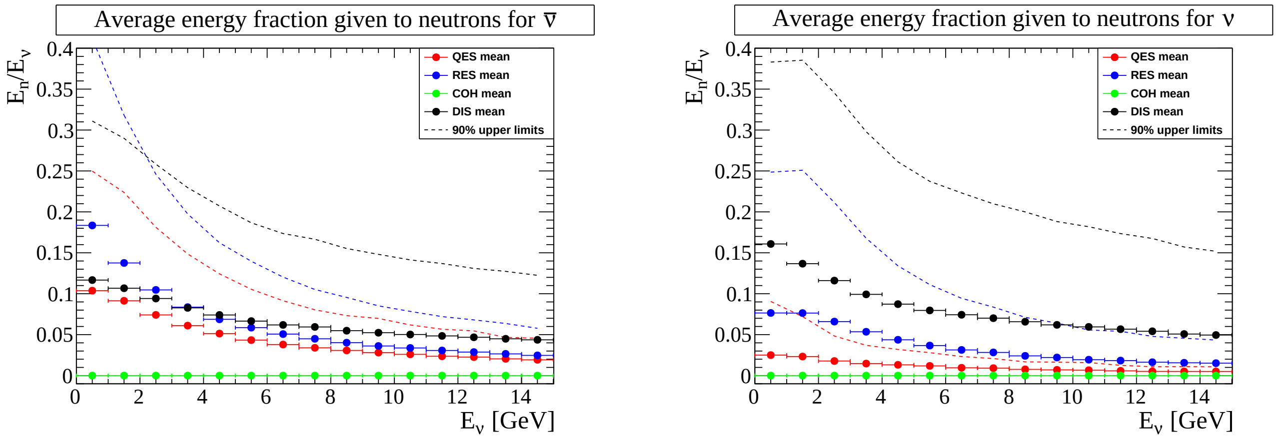

(a) Anti-neutrino interactions

(b) Neutrino interactions

Figure 4.5: Energy fraction given to the primary neutrons as a function of the interaction process.

(invisible) neutrons to correctly reconstruct the neutrino energy. Using these models introduces uncertainties that constitute a large contribution to the systematic error on the neutrino oscillation measurements. Figure 4.7 shows the example of the NOνA experiment in which a large disagreement is found between the prediction from the neutrino interaction model (default GENIE model) and the visible hadronic energy. Part of this disagreement comes from the neutron model and the neutron uncertainty constitutes the second larger systematic error in the measurement of the neutrino disappearance oscillation parameters by NOνA, as shown in Figure 4.8. The neutron detection capabilities of the 3DST detector would allow a reduction of this systematic uncertainty that will become necessary as we tend towards higher precision measurements of neutrino oscillations. It has already been shown in [111] that the reconstruction of the missing energy of the neutrino interactions, partly carried out by neutrons, will play a crucial role in the measurement of the CP violating phase for the next-generation of long-baseline experiments. An underestimation of 20 % of the missing energy was shown to intoduce a sizeable bias in the extracted δ_{CP} value while a 30 % underestimation would exclude the true δ_{CP} value with a confidence level between 2 σ and 3 σ, as shown in Figure 4.9. Considering these studies, the DUNE collaboration is investigating the possibility of performing neutron cross-section measurements in ProtoDUNE-SP [112], and thus neutron detection in LAr TPCs.

In the case of DUNE, the final oscillation measurement will come from linear combinations of neutrino spectra measured at different off-axis positions by the PRISM method. Using this linear combination in order to reproduce the oscillated spectra measured at the far detectors should minimize the systematic uncertainties due to the nuclear effects on the neutrino energy reconstruction. However, even in the very optimistic case

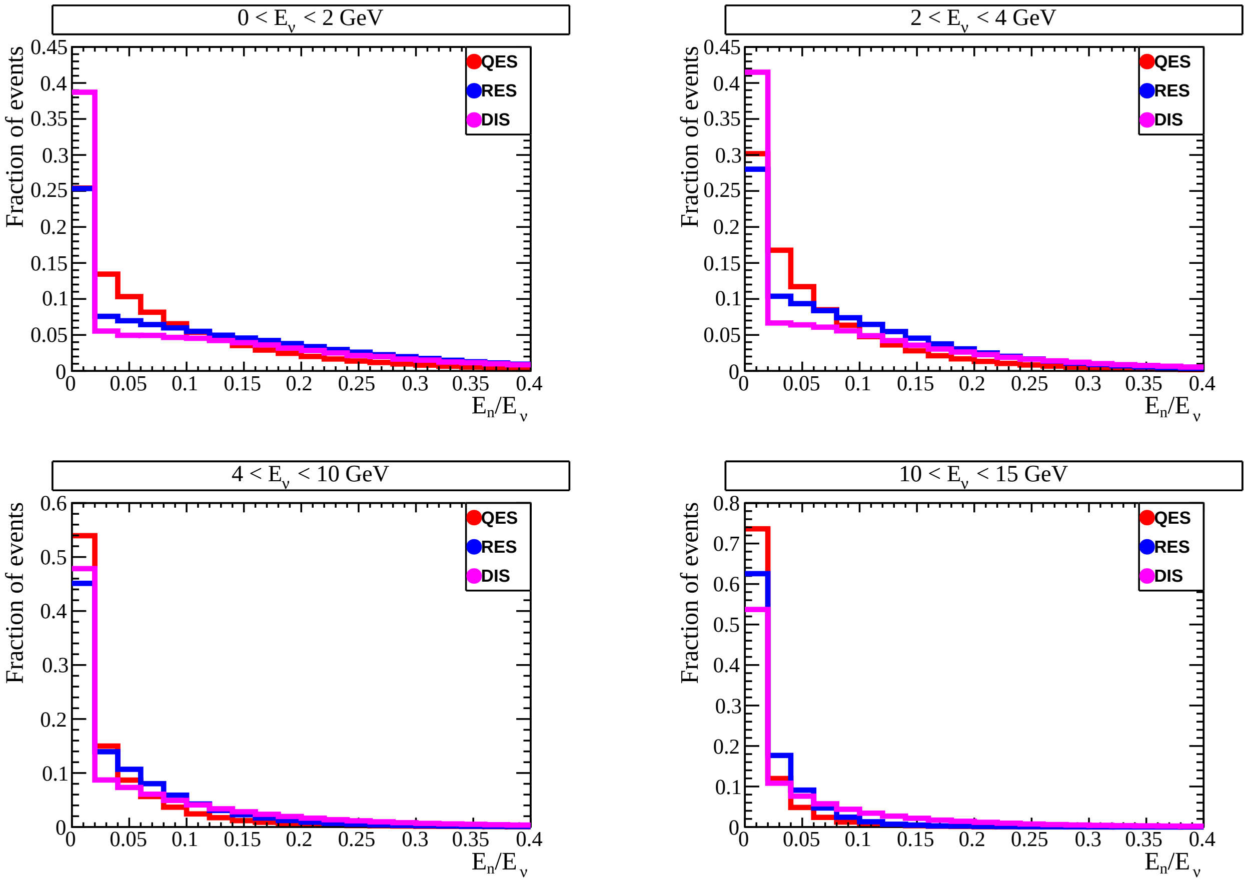

Figure 4.6: Distributions of the energy fraction given to neutrons as function of the interaction process for different energy ranges for anti-neutrinos.

in which this methods allows cancelling completely the systematics uncertainties due to nuclear effects, it will remain crucial to provide the best resolution in neutrino energy reconstruction so as to maximize the sensitivity on the oscillation measurement. It is therefore important, even in PRISM method, to avoid large uncertainties on neutrons energy reconstruction thanks to precise measurements of the fraction of neutrino energy going to neutrons.

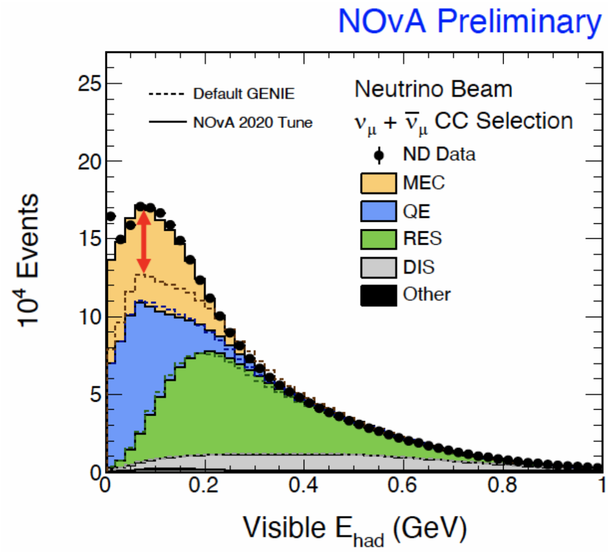

Figure 4.7: Visible hadronic energy measured by NOνA experiment. (reproduced from [113])

4.2.2 superFGD and 3DST designs

During my thesis I studied the performance of the 3DST to detect neutrons through simulations. This detector has a design inherited from the superFGD detector that will be installed in the ND280 near detector of T2K, as part of the ND280 upgrade. The plan was to leverage the already acquired and future experience working on the superFGD, in order to design a very similar detector for SAND. The designs of superFGD and 3DST are further described below.

superFGD

The ND280 near detector of T2K is an off-axis detector that helps constraining flux and ν-nucleus interaction systematic uncertainties in order to perform an oscillation analysis combining the near detector data and the oscillated data at the SuperKamiokande far detector. The ND280 upgrade aims at improving the performances of the detector that will be used for the next T2K data taking and future HyperKamiokande experiment [114,

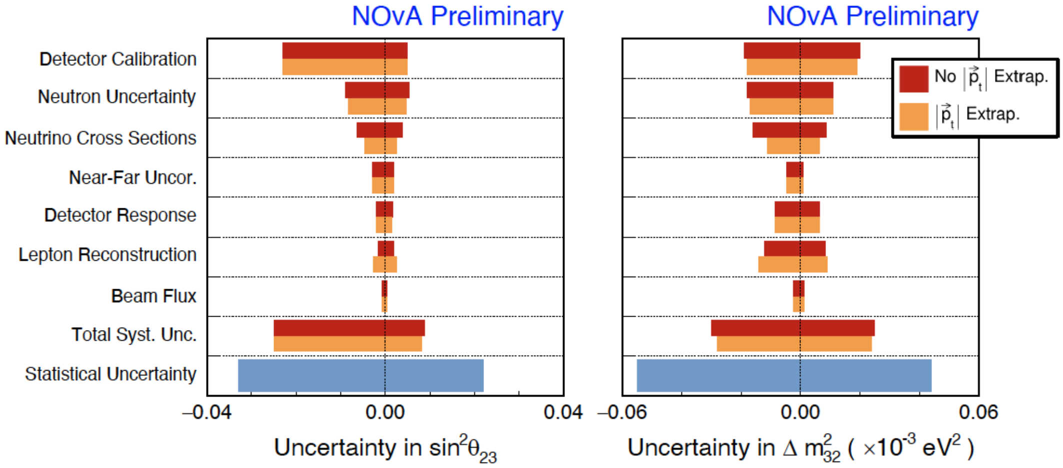

Figure 4.8: Breakdown of the total error on neutrino oscillation parameters for NOνA experiment. (reproduced from [113])

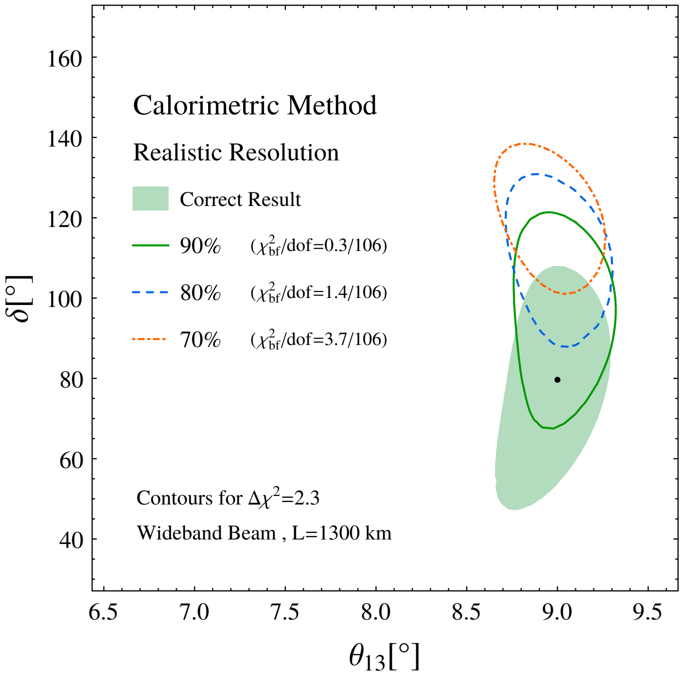

Figure 4.9: Effect on an underestimation of the missing energy in the calorimetric energy reconstruction on confidence regions in the (θ_{13}, δ) plane. The contours are given for 90 %, 70 % and 50 % of the missing energy accounted for. (reproduced from [111])

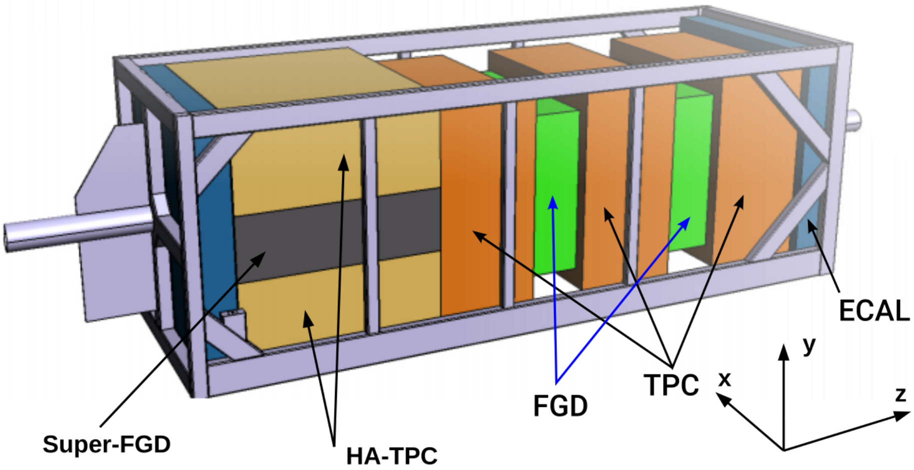

Figure 4.10: ND280 upgrade design. The superFGD and High Angle TPCs are added in replacement to P0D detector, a π^0 detector. The downstream part of the detector composed of FGDs, TPCs and ECal is kept as before the upgrade.

115].

The ongoing upgrade of the ND280 near detector of T2K [116] will feature a 3D scintillating detector, superFGD. The ND280 upgrade design is displayed in Figure 4.10. The whole ND280 detector is located inside a magnet providing a magnetic field of 0.2 T allowing to curve the charge particles and enabling the measurement of their momentum. The superFGD will be a 2 m×1.8 m×0.6 m 3D scintillating detector constituted of approximately 2 millions of scintillating cubes. the superFGD will be surrounded by two High-Angle TPCs which will allow to track and measure precisely the momentum of the high-angle charged particles escaping from superFGD, as it is done downstream by the already installed vertical TPCs. The superFGD detector will act both as a target and as a 3D tracker.

3DST

The 3DST detector is a 2.4 m × 2.16 m × 1.92 m 3D scintillating detector that was proposed in combination with TPCs in order to serve as tracker for the SAND near detector of DUNE. The size is driven by the available space inside the KLOE ECal.

Scintillator cubes

The plastic scintillator cubes that will compose the superFGD will be of size 1 cm × 1 cm × 1 cm whereas the proposition for 3DST was to have 1.5 cm side cubes. The cube size was chosen by considering the simulations studies of the physics performances but also the feasibility and the cost of the detector. The choice of a larger

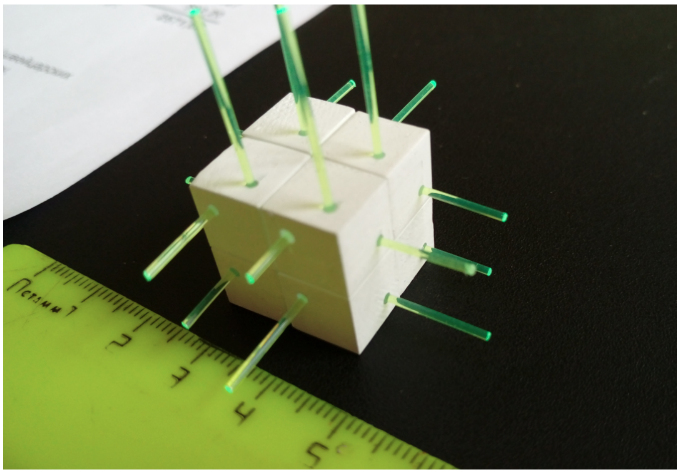

Figure 4.11: Picture of an assembly of 4 scintillating cubes with wavelength shifting fibers

cube size for 3DST was due to the higher peak energy of the DUNE beam that led to the production of higher energy particules after the neutrino interaction. This higher energy particles travel further inside the detector allowing for a larger cube size without significatively reducing the tracking capabilities of the detector, while considerably reducing the number of electronics channels. The cubes are pierced with three orthogonal holes of 1.5 mm diameter in each direction, which are used in order to fit the traversing wavelength shifting fibers as shown in Figure 4.11. The scintillator cubes are made of polystyrene doped with 1.5 % paraterphenyl (PTP) and 0.01 % of POPOP. The optical isolation of all the cubes is obtained by covering them with 50 µm thick reflector. For now, the cubes are produced using injection molding but studies are being conducted to investigate the possibility of using 3D printing techniques for an entire layer of cubes.

Light readout

The cubes are assembled together using fishing line that are passed inside the holes devoluted to the WLS (Wavelength-Shifting) fibers, in order to correctly align all the cubes, as displayed in Figure 4.12. Once all the cubes are correctly arranged and their holes aligned, the fishing lines are replaced by the WLS fibers that are driven through the cube holes.

In order to collect and transport the light of the scintillating cubes, 1 mm diameter plastic WLS fibers are used. These fibers absorb the scintillation light from the cubes and re-emit lower-wavelength photons that travel inside the fiber by undergoing total internal reflections.

The light collected by the WLS fibers is carried toward 3 readout planes (one for each direction) where the photons are detected by Multi Pixel Photon Counters (MPPCs).

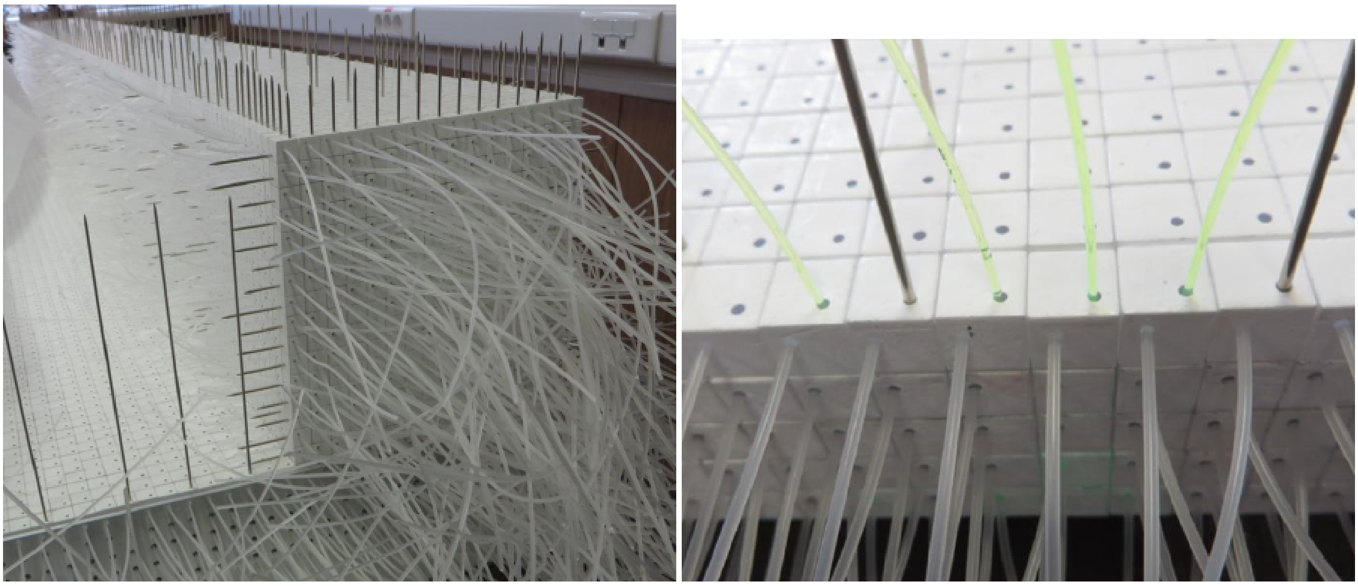

Figure 4.12: Partially assembled module of the T2K ND280 superFGD using fishing lines

Table 4.1: Specifications of the S13360-1325PE MPPC.

Item	Specification
Effective photosensitive area	$1.3\,\mathrm{mm} \times 1.3\,\mathrm{mm}$
Pixel Pitch	$25\,\mu\mathrm{m}$
Number of pixels	2668 pixels
Fill factor	$47\,\%$
Package type	Surface mount
Breackdown voltage	$53(5)\,\mathrm{V}$
Peak sensitivity wavelength	$450\,\mathrm{nm}$
Photo detection efficiency	$25\,\%$
Gain	7.0×10^5
Dark Count	$70\,\mathrm{kcps}$
Crosstalk probability	$1\,\%$

MPPC and electronics

The MPPC is a photosensor that detects the light channeled by the fibers. MPPCs have been successfully used in all the plastic scintillator detectors of the current near detectors of T2K [**a**]nd are also being used for the superFGD of the T2K near detector upgrade. For the latter and for the 3DST, MPPCs of type S13360-1325PE, produced by Hamamatsu Photonics K. K. have been chosen. Its specifications are reported in Table 4.1.

The MPPC sensitive area is $1.3\,\mathrm{mm} \times 1.3\,\mathrm{mm}$, which is designed to match the $1\,\mathrm{mm}$ diameter WLS fiber.

The base design for the electronics alo takes advantage of the development conducted for the T2K superFGD. The superFGD electronics are centered around the CITIROC [117] readout chip providing $1.25\,\mathrm{ns}$ time bins. For

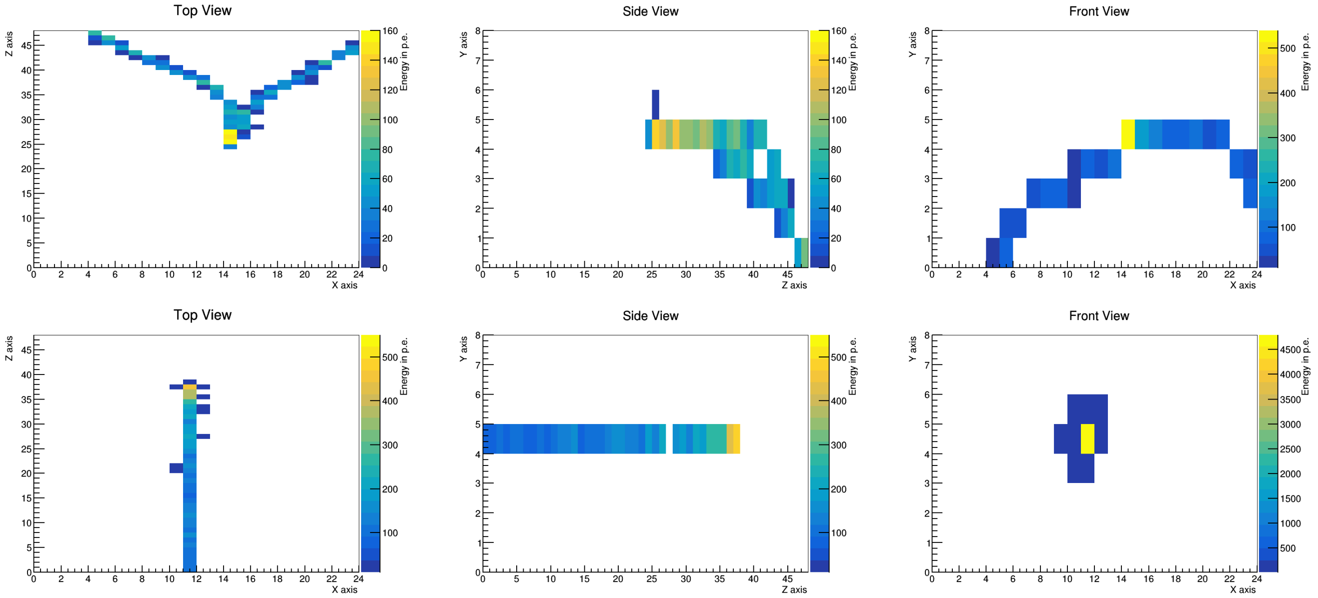

Figure 4.13: Event displays showing a photon conversion (top) and a stopping proton (bottom) from data collected at the 2018 test beams at CERN

SAND, an alternate chip to the CITIROC is considered: the KLauS [118] chip developed at Heidelberg. KLauS has been developed for the CALICE Analog Hadron Calorimeter with several key features useful for DUNE. The time binnin is better than one nanosecond allowing for a better neutron time-of-flight reconstruction, and the power comsumption is lower.

4.2.3 Test beam performances

Several test beams were conducted on prototypes aiming to assess the performance of this technology. Charged-beam tests were conducted at CERN. Additional neutron beam tests have been conducted at Los Alamos National Laboratory (LANL) in order to evaluate the neutron detection capabilities of such detector.

The charged-beam tests allowed to demonstrate the performance of the future superFGD detector in the framework of the near detector physics at the ND280 detector complex. Event displays from these tests are reproduced in Figure 4.13. These charged beam tests also allowed to caracterize various parameters of the detector such as the light yield, the cube cross-talk and the timing resolution [119].

The test beams at LANL used a pulsed neutron beam with a sub-centimetric collimation. This allowed to send neutron bunches in a single cube enabling therefore to measure the neutrons energy by ToF. Figure 4.14 shows the neutron beam spot as detected by the prototype. A publication of these beam test results is foreseen in the near future.

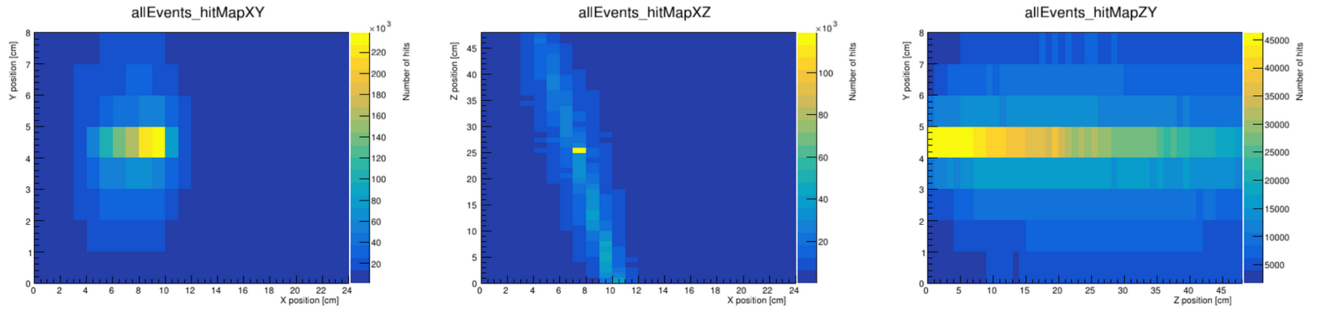

Figure 4.14: Beam spot in the superFGD prototype at LANL. The detector was rotated by 10 degrees along the vertical coordinate

4.3 The technology of resistive MicroMegas TPC

4.3.1 Motivations

Based on the successful experience coming from ND280, TPCs were proposed to be part of the inner tracker design of SAND. Moreover, the TPCs for SAND were proposed to include the innovative MicroMegas resistive technology, Encapsulated Resistive Anode MicroMegas (ERAM), that will be used for the new HA-TPCs of the upgrade of the ND280 detector.

As shown in Figure 4.10, ND280 is already instrumentd with vertical TPCs. The ND280 TPCs have been performing very stably and reliabily across the eleven years of running of the detector. Moreover, the ND280 TPCs have proven to be crucial for the measurement of particles produced by neutrino interactions at ND280.

The idea of using resistive MicroMegas as TPCs readout has been studied for a decade in the framework of the ILC R&D and the CEA-IRFU group is the main developper of the ERAM system for the ND280 upgrade. The proposed design for SAND includes 3 TPCs located above, below and downstream the 3DST, as it can be seen in Figure 4.15. The top and bottom TPCs have dimensions of 3.3 m × 0.57 m × 1.41 m while the downstream TPC is proposed to have a size of 3.3 m × 3 m × 0.77 m. The TPCs are separated in the middle by a cathode to drift the charge at the closest TPC endcap instrumented with ERAM modules. Eight ERAM modules of 36×32 (1 cm × 1 cm) pads are necessary to instrument the 2 readout planes of the top and bottom TPCs while the downstream TPC requires 28 ERAM modules. The proposed drift length of ~ 165 cm is longer than that of the HA TPCs for ND280 upgrade (1 m). The longer drift introduces additional challenges related with the uniformity of the drift field on such a distance and deal with the increased charge diffusion along the drift.

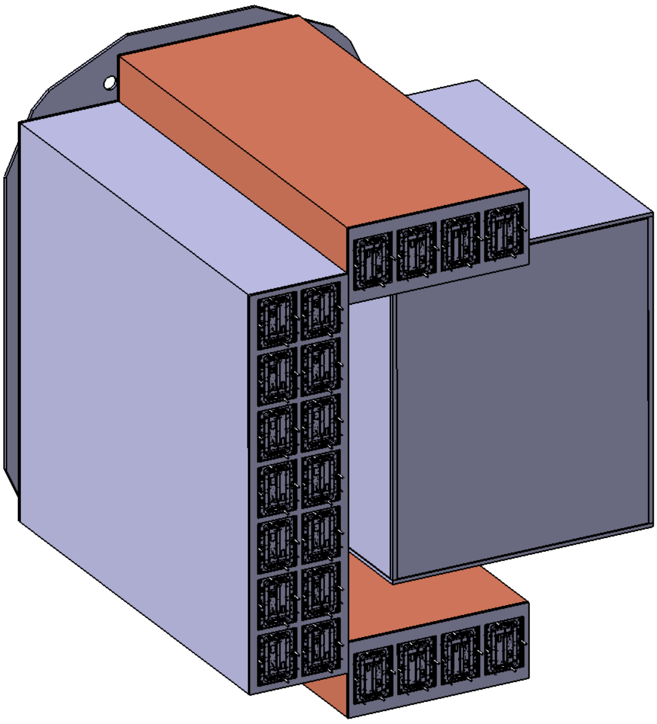

Figure 4.15: Schematic view of the 3DST detector surrounded by the 3 TPCs.

4.3.2 Encapsulated Resistive Anode MicroMegas (ERAM)

The currently used MicroMegas technology, named bulk-MicroMegas, was invented in 2004 by a collaboration between the CERN/EPDF-EF Printed Circuit Board (PCB) workshop and CEA-IRFU. The working principle of these detectors is presented in Figure 4.16 (left). A mesh is maintained by pillars above a pad-segmented anode. Applying a large difference of potential between the anode and the mesh allows to create an amplification gap in which the electrons are multiplied inducing an avalanche, thus increasing the gain of the detector and, ultimately, the signal/noise ratio. The electron avalanche produced in the gap is relatively narrow, given the small gap of 100 µm. Therefore, the avalanche size is in most of the cases restricted to a single pad enabling a spatial resolution equal to the pad dimension. When the avalanches are spread on multiple pads, as this happens when the charge is deposited near a boundary between two pads or for large drift distances because of diffusion, the obtained spatial resolution is improved given that the charge information from the two pads can be combined. In the ERAM technology, it has been proposed to arficially spread the charge on multiple pads to improve the spatial resolution of the detector. In the case of the ERAM detectors, this is performed by addind a Diamond-Like Carbon (DLC) foil on an insulator that is glued to the anode as shown in Figure 4.16 (right). The DLC foil has a resistive beahavior that internally spreads the charge while the glue allows to create a capacitance between

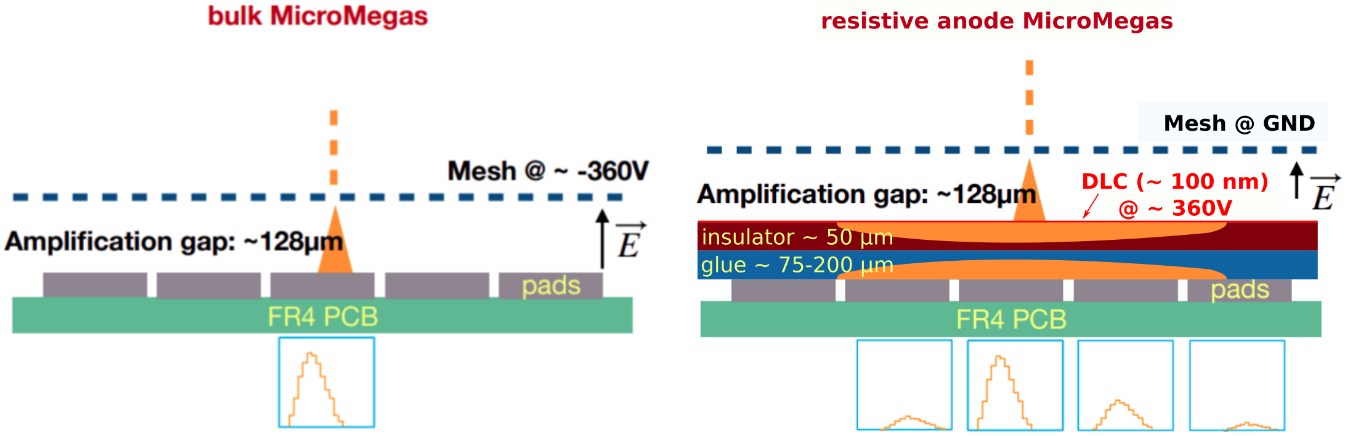

Figure 4.16: Comparative schemes of a bulk-MicroMegas (left) and a resistive bulk-MicroMegas (right)

the DLC foil and the anode pads. Therefore, the electron cloud created in the amplification gap deposits the charge on the DLC foil which spread the charge, and, by capacitive coupling, a signal is induced on the anode pads. By spreading the charge on multiple pads, this technology allows to improve the spatial resolution on the energy deposition while keeping the same pad size and thus the same number of electronics channels. This charge spreading phenomenon has been described in [120]. Furthermore, this addition of a resistive layer reduces the amount of sparks and their intensity.

The width and time of the charge spreading onto the anode pads is controlled by the RC time constant with R coming from the DLC foil resistivity and C from the glue physical properties and thickness. The shaping time of the electronics, t, has also a role on the charge spreading. The charge spreads uniformly in all the directions with a gaussian behavior with standard deviation:

$$\sigma_r = \sqrt{\frac{2t}{RC}} \quad \begin{cases} t \approx \text{shaping time (few 100 ns)} \\ RC_{[\text{ns/mm}^2]} = \frac{180 R_{[\text{M}\Omega/\blacksquare]}}{\frac{d_{[\mu\text{m}]}}{175}} \end{cases} \tag{4.1}$$

The charge spreading can therefore be precisely tuned to the adequate width by adjusting both the resistivity of the DLC foil and the glue thickness.

4.3.3 Prototype tests

In the framework of the ND280 upgrade, ERAM prototypes have been produced since the end of 2017 and several tests have been performed in order to prove the possibility to operate with this new technology and to assess its

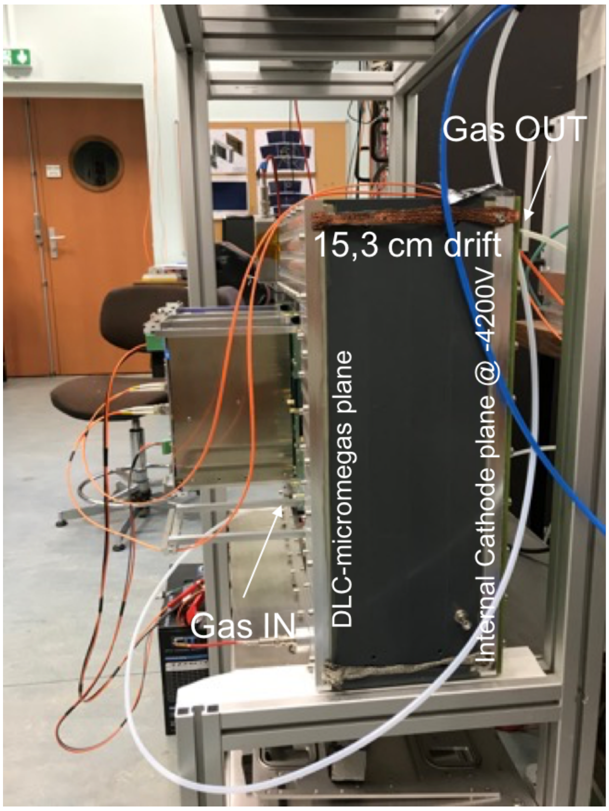

Figure 4.17: Saclay mini-TPC in comics test bench.

performances. The prototypes have been thoroughly tested in various conditions among which CERN test beam [121], DESY test beam [122], pad-by-pad caracterization with X-rays test bench and cosmics measurement with a mini-TPC of 15 cm drift length shown in Figure 4.17, both at Saclay.

All these tests performed on the ERAM prototypes, allowed the ERAM global design to be validated. Moreover, the charge spreading was also characterized, the uniformity of the resistivity controlled and a measurement of the spatial resolution has been extracted from the collected data.

Charge spreading characterisation

As explained previously, the ERAM technology allows for the spreading of the deposited charge onto multiple neighbooring pads. Figure 4.18 shows waveforms corresponding to this charge spreading. We can see that the pad which was initially hit (the leading pad) has the highest signal and appears first in time, while, after some delay, the charge spreads in the neighbooring pads which display delayed waveforms of smaller amplitudes.

The charge spreading was characterized in multiple ways on the different prototypes. The pad multiplicity per cluster and the fraction of charge in the pad with the largest signal are for example shown in Figure 4.19.

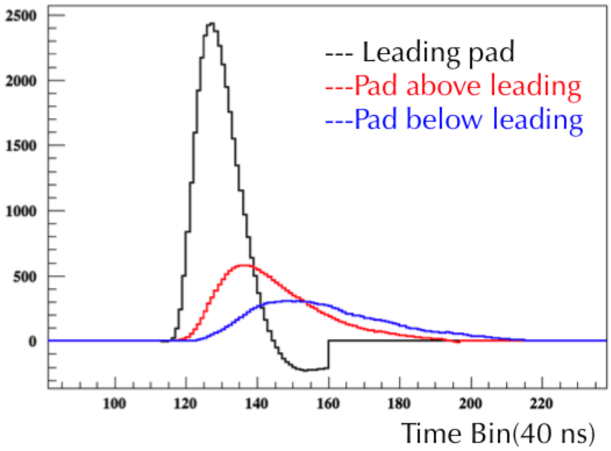

Figure 4.18: Signal waveforms in the three pads of a given cluster at 200 ns shaping time. (reproduced from [122])

RC maps of the detectors were also obtained analyzing the charge spreading behavior around each pad as shown in Figure 4.20.

Spatial resolution

The extensive tests realized on the prototypes also allowed to evaluate the spatial resolution that could be obtained with these new generation of MicroMegas. Indeed, the spatial resolution is a crucial characteristics, as it drives directly the momentum resolution that can be obtained on charged particles crossing the TPC. Some results are reproduced in Figures 4.21 and 4.22 where it can be seen that in all the tested configurations, the obtained spatial resolution is below 600 μm. Morerover, in the cases where the tracks are parallel to either the pad lines or columns, the spatial resolution can be as good as 200 μs. Improvements of the fitting procedure in order to improve further the spatial resolution in the diagonal cases are ongoing.

4.4 Simulation framework

4.4.1 Simulation softwares

Full hit-level simulation and event reconstruction have been developed for the 3DST and TPCs. In addition, a parametric hit level simulation is used for ECal in order to simulate the response of the full SAND detector to the DUNE beam.

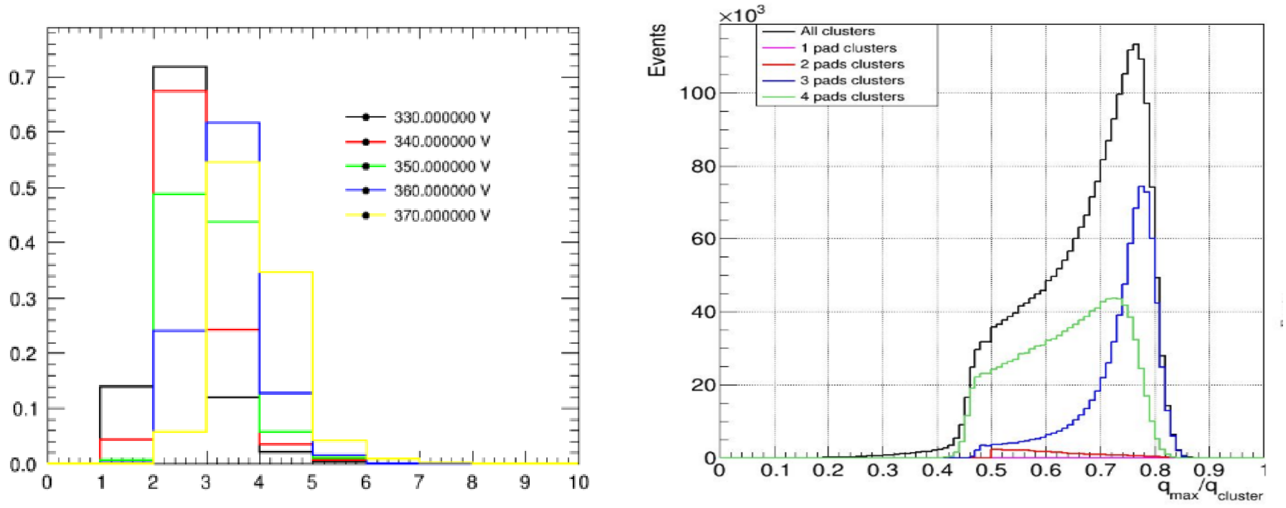

Figure 4.19: Number of pads in the cluster for different high voltages (left) and fraction of the cluster charge which is collected in the pad with the largest signal (right). (reproduced from [122])

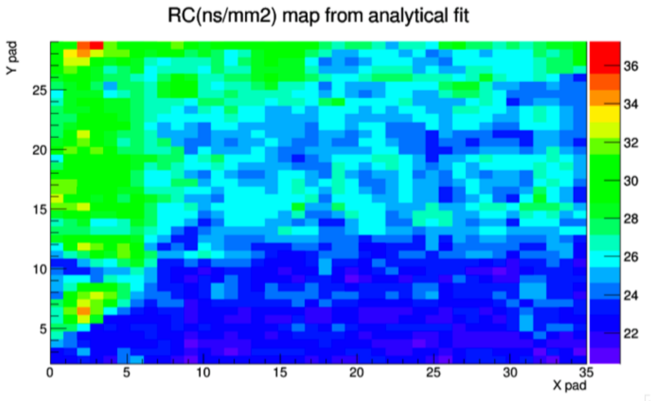

Figure 4.20: RC map obtained with cosmics data

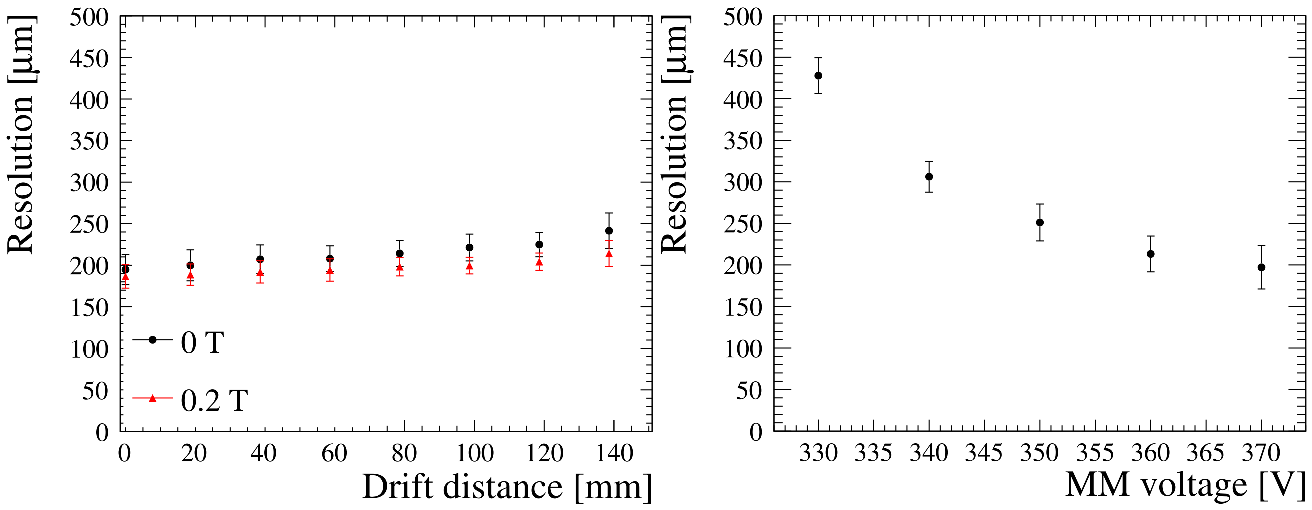

Figure 4.21: Measured spatial resolution with respect to the drift distance (left) and the MicroMegas voltage (right) for tracks parallel to the MicroMegas plane. (reproduced from [122])

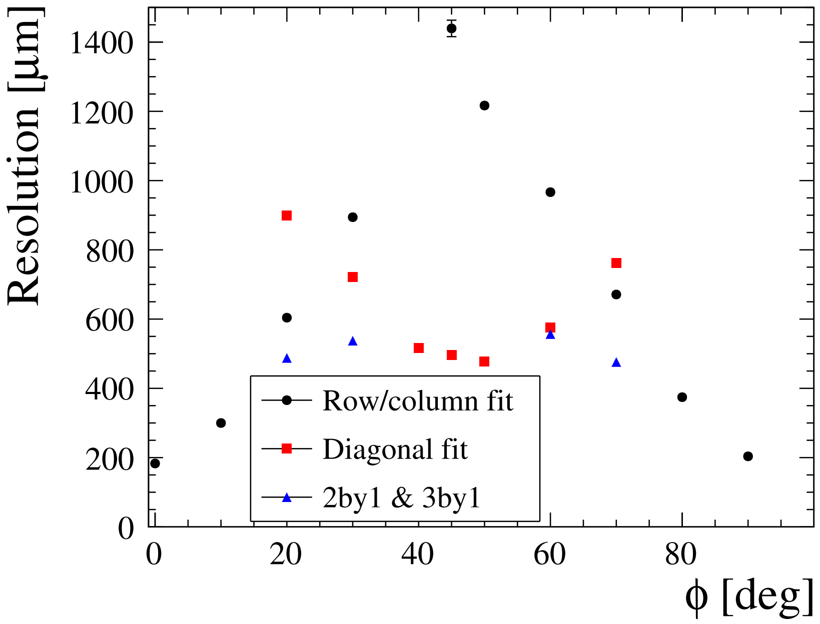

Figure 4.22: Measured spatial resolution as a function of the track angle in the MicroMegas plane for different cluster definitions. (reproduced from [122])

The following steps are applied in order to obtain a fully reconstructed simulation of neutrino interactions inside the 3DST + TPC inner tracker.

- The DUNE Reverse Horn Current (RHC) or Forward Horn Current (FHC) flux is used as neutrino source.
- The GENIE generator is used to model the interaction of neutrinos inside the detector.
- The final state particles are propagated inside the detector from the interaction vertex using GEANT4.
- The simulation of the detector response is implemented for the 3DST and the TPC.
- Finally, a full event reconstruction of the detector is performed by a dedicated software inspired by the superFGD one. For 3DST, the tracks are first reconstructed in 2D planes by using the information from 2 set of orthogonal fibers, before being merged together in order to obtain 3D reconstructed objects. Reconstructed objects are separated into clusers and tracks depending on their length: objects spreading over more than 3 cubes are considered as tracks while the others are clusters. For each object, its position, time and energy deposition are reconstructed. The reconstruction is similar for the TPCs. The track information on the anode plane is reconstructed and is combined with the time information to reconstruct 3D tracks.

4.4.2 3DST simulation

The simulation model used for the 3DST has been tuned to the test beam done at CERN for superFGD [119]. During this test beam, a cube size of 1 cm has been used. To simulate other cube sizes, the light yield is adjusted based on an empirical model matched to the behavior of the T2K FGD detectors [123]. The energy deposition is translated to photons entering the fibers, which are then transported to photosensors. For these simulations, the fibers are assumed to be read out on one end, and the far end is supposed to have no reflectivity. The transportation simulation includes the scintillation emission time, the WLS fiber shifting time, the light propagation in the fiber and the spread of the light as it exits the fiber. The signal produced by the photosensors is simulated assuming an idealized MPPC which does not include saturation effects. The simulation does not include dark noise, gain and timing jitter. The current from the photosensors is digitized assuming a miltihit ADC/TDC with a 2.5 photo-electron threshold, a gain of 4 counts per photo-electron, a time count of 500 ps, and a 50 ns integration time.

4.4.3 TPC simulation

I developed the simulation model used for the TPCs, based on the prototype measurements described in the Sub-section 4.3.3. ERAMs with 1 cm side pads are assumed by default but different pad sizes are also studied. The drift velocity is taken as 78 mm μs^{-1}, the same as for ND280 High-Angle TPCs [116], as the gas will be the same. The charge spreading in the ERAMs are described using a Gaussian distribution with a width matched to the behavior measured in test beams. The energy deposition along the tracks are translated into down-sampled distribution of drifting electrons which are transported to the sensors. The drift includes the longitudinal dispersion of $\sigma_L = 290\,\mu\mathrm{m}/\sqrt{\mathrm{cm}}$ [124], shown in Figure 4.23, while the transversal dispersion is in first approximation neglected with respect to the charge spreading effect (the transverse dispersion can be extrapolated from [124] to a magnetic field of 0.6 T, giving $\sigma_T = 113\,\mu\mathrm{m}/\sqrt{\mathrm{cm}}$ corresponding to a maximum longitudinal spread of 1.4 mm). The charge arriving at each ERAM pad is integrated assuming a 200 ns integration window. Hits are generated by returning the average arrival time and the sum of the charge in the integration window for each pad.

Figure 4.24 shows the example of a simulated spill (10 μs) on an anode plane of the downstream TPC.

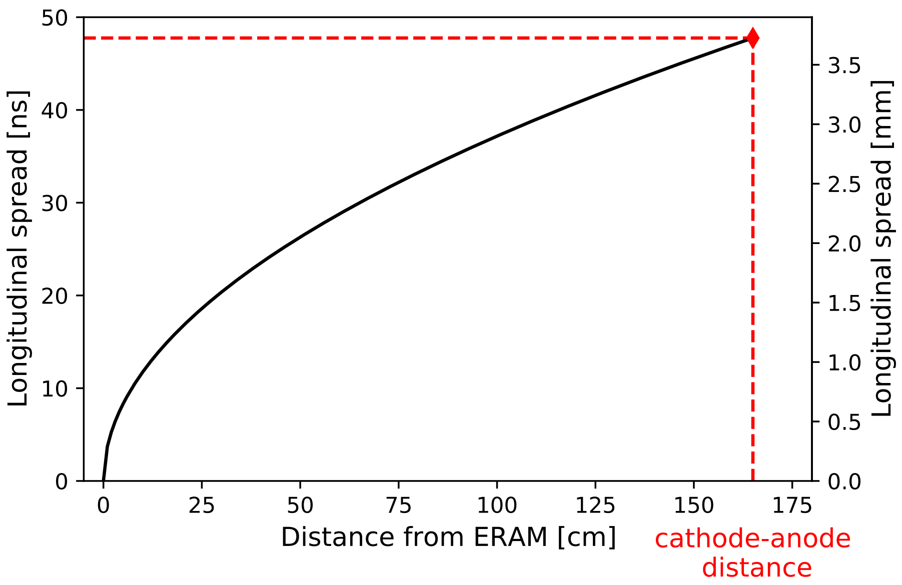

Figure 4.23: Longitudinal spread of the electron cloud in the TPC as function of the drift distance

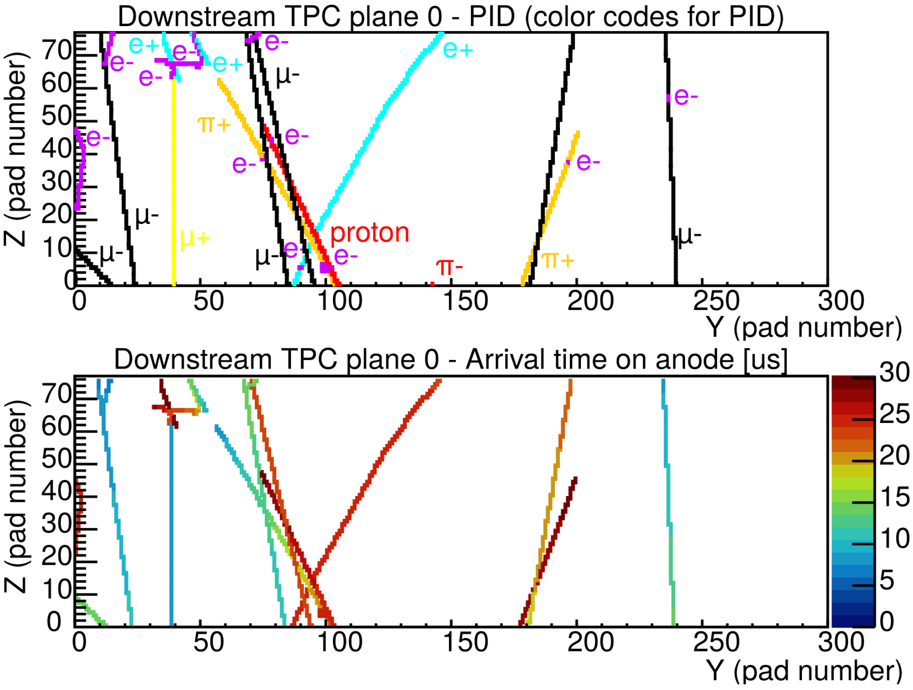

Figure 4.24: Event display of a simulated spill on an anode plate of the downstream TPC.

4.4.4 Reconstruction

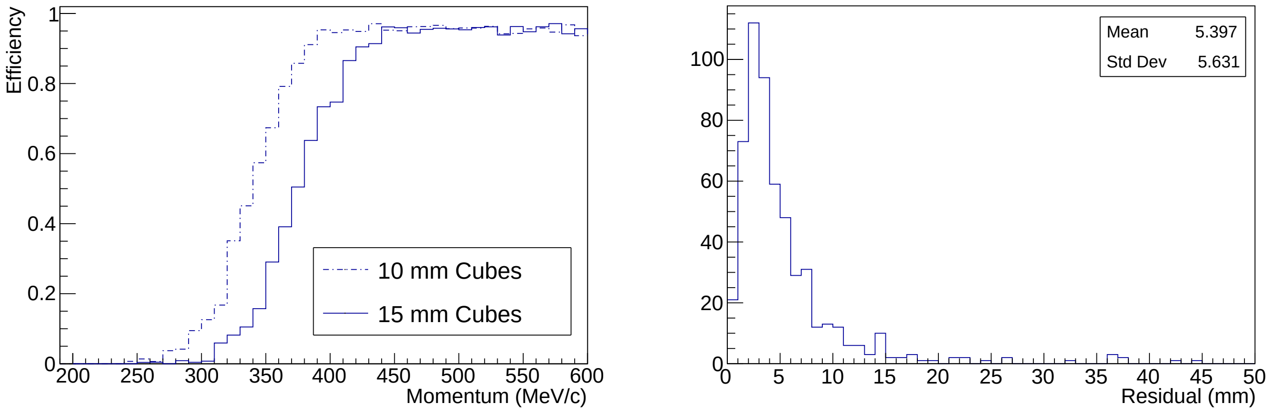

Figure 4.25: Left: Efficiency for proton track reconstruction as a function of momentum for both 10 mm (dashed line) and 15 mm (solid line) cubes. Right: vertex resolution for multi-track RHC neutrino interactions with 15 mm cubes.

A preliminary event reconstruction has been developed for both the 3DST and the TPC. For the 3DST, the reconstruction includes pattern recognition to find tracks, track fitting, determination of the track position and direction (including the sense of the direction using timing), particle identification using energy loss along the track, and vertex reconstruction. The TPC reconstruction focuses on pattern recognition to determine the efficiency of finding tracks in complex events. Final track fitting in the TPC is not done, and we assume the fitting resolutions demonstrated in [121] and presented in Figures 4.21 and 4.22.

The performance of the 3DST event reconstruction has been evaluated at a range of proposed cube sizes. The efficiency to reconstruct muon tracks longer than 15 cm in multi-track events is found to be insensitive to the cube size with the track finding efficiency being greater than 99 % for all directions. The primary effect of cube size is to raise the momentum threshold for short particle tracks as the reconstruction requires that reconstructed objects contain a minimum of 4 cubes before being fit as a candidate track. Shorter objects remain as a cluster of hits. Figure 4.25 (left) shows the efficiency to reconstruct protons as a track in multi track events as a function of proton momentum for 10 mm cubes (dashed line) and for 15 mm cubes (solid line). The proton 50 % threshold for 10 mm cubes is approximately 340 MeV/c increasing to approximately 370 MeV/c for 15 mm cubes.

Figure 4.25 (right) shows the reconstructed vertex resolution for multi-track RHC neutrino interactions occurring inside the 3DST. For single tracks the vertex position is based on the start of the track. The overall vertex resolution is determined by the ability to determine the track fitting parameters and the granularity of the

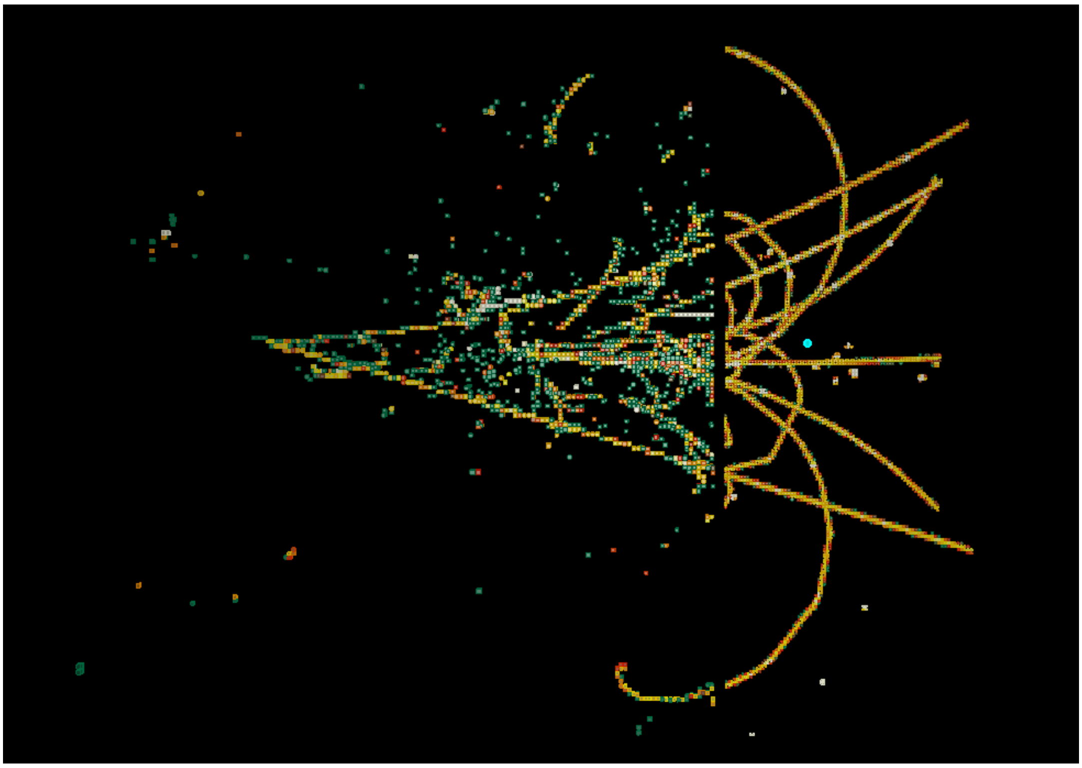

Figure 4.26: Reconstruction of a simulated event inside 3DST and the downstream TPC

detector limits the overall position resolution to be approximately equal to the cube size.

An example of a fully reconstructed event is shown in Figure 4.26. The interaction occurs inside the 3DST and the reconstructed cube hits are displayed. The reconstructed tracks in the downstream TPC are also shown.

4.5 Accordance of the design with DUNE beam

The baseline design of the 3 proposed TPCs for SAND is based on what has been proposed for the upgrade of the ND280 near detector of T2K. However, the neutrino flux and energy spectrum will be different for the DUNE experiment with respect to what is used in the T2K experiment. As a consequence, it is necessary to optimize the details of the design, such as the readout granularity, to cope with the DUNE neutrino beam. In this context, I have studied the TPC occupancy and the angular acceptance provided for neutrino interaction events in 3DST with DUNE beam.

Table 4.2: Fraction of $\bar{\nu}$ interactions in 3DST

Process	Fraction of events
COH	1.88 %
QES	30.85 %
RES	25.39 %
DIS	41.88 %

4.5.1 DUNE beam

The DUNE beam will feature a power of 1.07 MW with a number of protons on target of 1.47×10^{21} per year. The peak of the neutrino energy will be around 2 to 3 GeV. However, high energy neutrinos and anti-neutrinos with an energy above 10 GeV will also be produced as can be seen in Figure 4.27.

Contrary to T2K, the quasi-elastic (QES) channel will not be the dominant channel of interaction for the neutrinos in DUNE given the higher energy spectrum of the produced neutrinos. As it can be seen in Table 4.2, the main interaction channel in 3DST is DIS.

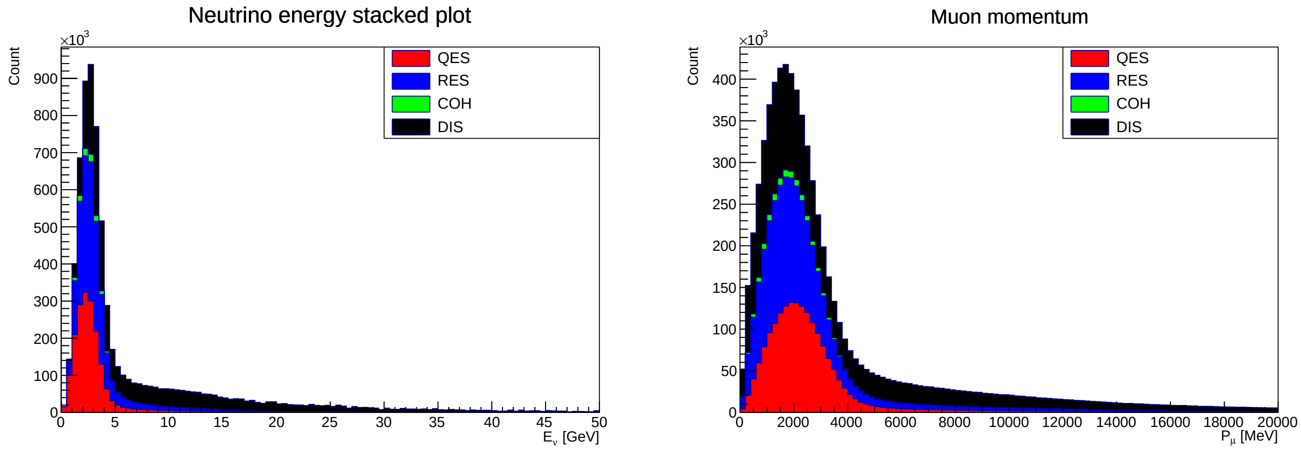

(a) Anti-neutrino energy stacked spectrum for each interaction

(b) Muon momentum stacked spectrum for each interaction

Figure 4.27: Stacked plots showing the kinematics associated with DUNE beam

4.5.2 TPC occupancy

An increased rate is expected in SAND with respect to what is observed in ND280 given the higher beam power of DUNE and the larger total mass of the detector. Moreover the wide neutrino energy range with neutrino energies up to 20 GeV will lead to an increased number of DIS interactions that produce more busy events, thus

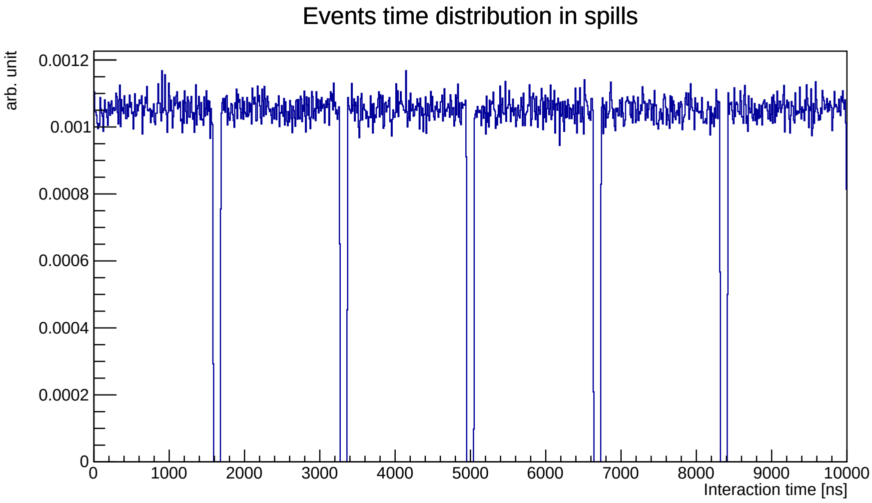

Figure 4.28: Simulated events time distribution with DUNE beam characteristics.

increasing the TPC occupancy. As a consequence, the occupancy of the TPCs is expected to be larger than for ND280, especially for the downstream TPC. I realized a study of the TPC occupancy using simulated data in order to make sure that the amount of overlaps of different tracks in the TPC is acceptable. Indeed, the presence of too many overlaps between tracks could affect the reconstruction capabilities of the TPCs. Moreover, two signals overlapping in time, in the same pad, lead to a loss of information that can affect both the $\frac{\mathrm{d}E}{\mathrm{d}x}$ and spatial resolutions.

Events are simulated according to the LBNF beam design with spills of 10 µs, composed of six bunches, themselves separated by 100 ns as it can be seen in Figure 4.28. The number of neutrino interactions occuring in the whole detector (including 3DST, ECal and magnet yoke) per spill is shown in Figure 4.29, with the number of events with tracks in each of the TPCs. As expected, the downstream TPC will have more tracks to detect than the two other TPCs. For each spill, the TPCs are expected to detect tracks from multiple interactions that can overlap in space and time. Moreover multiple tracks can be detected by a TPC for a single event. The number of tracks expected in each TPC, per event, is shown in Figure 4.30 (not displaying the events with no track).

The number of overlaps between tracks is mainly affected by the pad size, the charge spreading distance and the time separation capabilities between two hits. This time separation capability is a parameter that encompasses both the electronics peaking time and the charge spreading time. Figure 4.31 shows the fraction of events containing tracks with an overlapping fraction of pads greater than a given value, using different detector configurations by varying the pad size, the time window to consider an overlap (proxy for electronics shaping time) and the charge spreading. We can see that in the worst case scenario, about $1\,\%$ (1 ‰) of events have

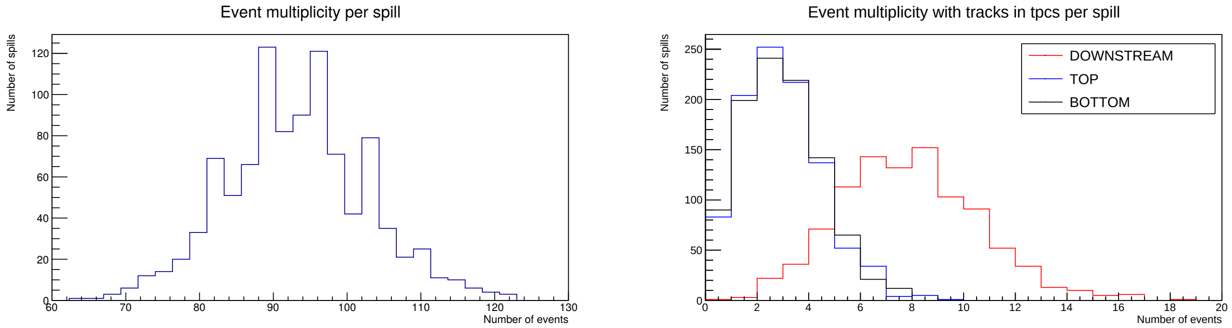

Figure 4.29: Number of interactions in the full detector volume per spill (left) and number of these events with tracks in the TPCs (right).

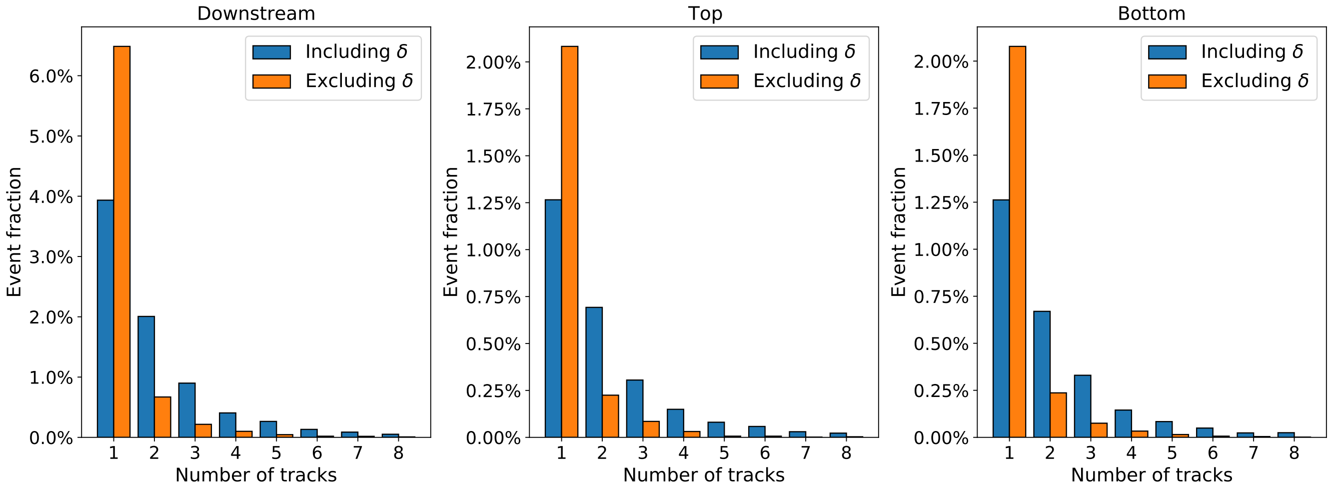

Figure 4.30: Number of tracks in each event for the different TPCs, considering or not the delta electron tracks are separate tracks.

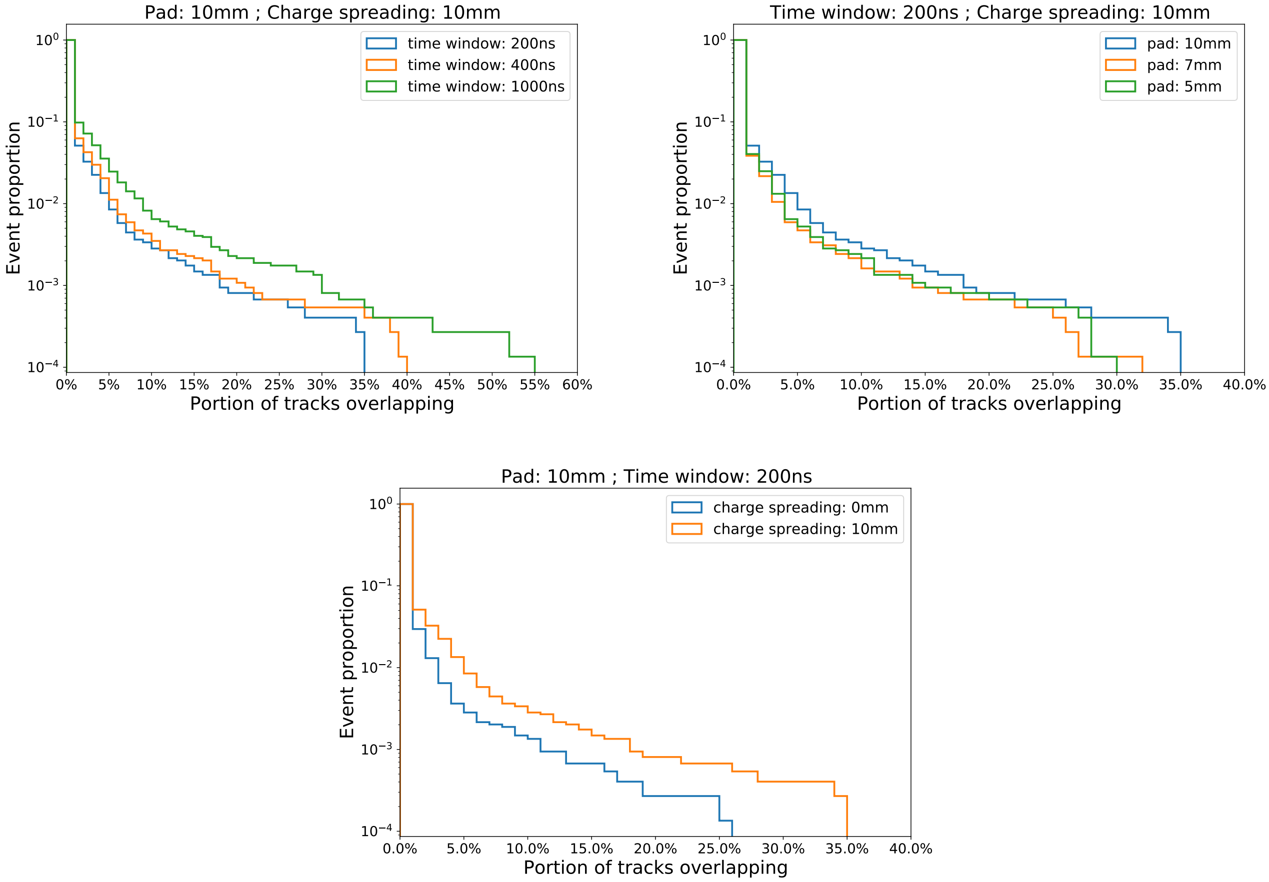

Figure 4.31: Inverse cumulative distribution of the event proportion containing tracks with a given overlapping percentage. Only events with at least 1 track in a TPC are included.

tracks with an overlap of 5 % (20 %) of their pads or more. Some of these overlaps can in principle be recovered with a careful analysis of the waveform signals and in some cases the overlap happens just on the sub-leading pad (collecting only the charge spread) while the leading pad is usable. Assuming the worst-case scenario, when all the overlapping pads are leading pads and not usable, a loss of 5 % (20 %) of the hits would correspond on average to a relative worsening of the resolution of 3% (10%), assuming a simple dependence on the square root of the number of track pads. For instance, for a base momentum resolution of 2 %, it would lead to 1 % (1 ‰) of events with a 2.05 % (2.2 %) momentum resolution. The impact on pattern recognition is more difficult to estimate in an approximated way but considering a number of pads of about 70-80 in the track direction, a loss of 5 % (20 %) of the hits should not be problematic. Therefore, the resistive MicroMegas technology can be applied to the TPCs of SAND, with the considered parameters.

4.5.3 Angular acceptance

The TPCs have to be sized and arranged around the 3DST so as to detect the maximum number of particules exiting the 3DST or the ECal. To do so, the angular coverage provided by the TPCs is evaluated in Figure 4.32. The portion of tracks crossing the TPCs is shown as a function of the polar angle θ between the beam axis and the tracks. The coverage for tracks produced in interactions in 3DST and for muons produced in interactions in ECal are shown separately and the proportion of contained tracks, respectively in 3DST and ECal, are also included. The overall coverage for ECal is about 50 %, where the loss is mainly due to interactions in the downstream part of ECal (while the efficiency for forward-going upstream interactions is around 80 %, similarly to the 3DST coverage). The crucial role of the downstream TPC is evident. In particular, in this study if a track pass by the downstream TPC, it is not considered for the top/bottom TPCs. One can also note that the efficiency for the bottom TPC is larger than for the top TPC, this is due to the slight downward tilt of the neutrino beam. These results allow to validate the proposed design for the ECal + 3DST + TPCs for what concerns the acceptances.

4.6 TPC performances

In order to monitor the DUNE beam variations over a weekly timescale, SAND is required to be able to reconstruct the muon momentum in charged-current events with a resolution below 10 % at 5 GeV and below 5 % at 1 GeV [63]. We hereafter study the TPC performances to ensure that they meet these requirements.

4.6.1 Momentum resolution

I evaluated the resolution capabilities of the proposed TPC concerning muon tracks produced in 3DST ν interactions.

The following notations are used in the following (also shown in Figure 4.33):

- z is the beam, x is the horizontal axis and y the vertical one;
- P and E are the initial momentum and energy of the particle at the interaction vertex;
- $\tilde{P}$ and $\tilde{E}$ are the momentum and energy of the particle when it exits the 3DST active volume;
- $\hat{P}$ and $\hat{E}$ are the momentum and energy of the particle when it enters the TPC active volume.

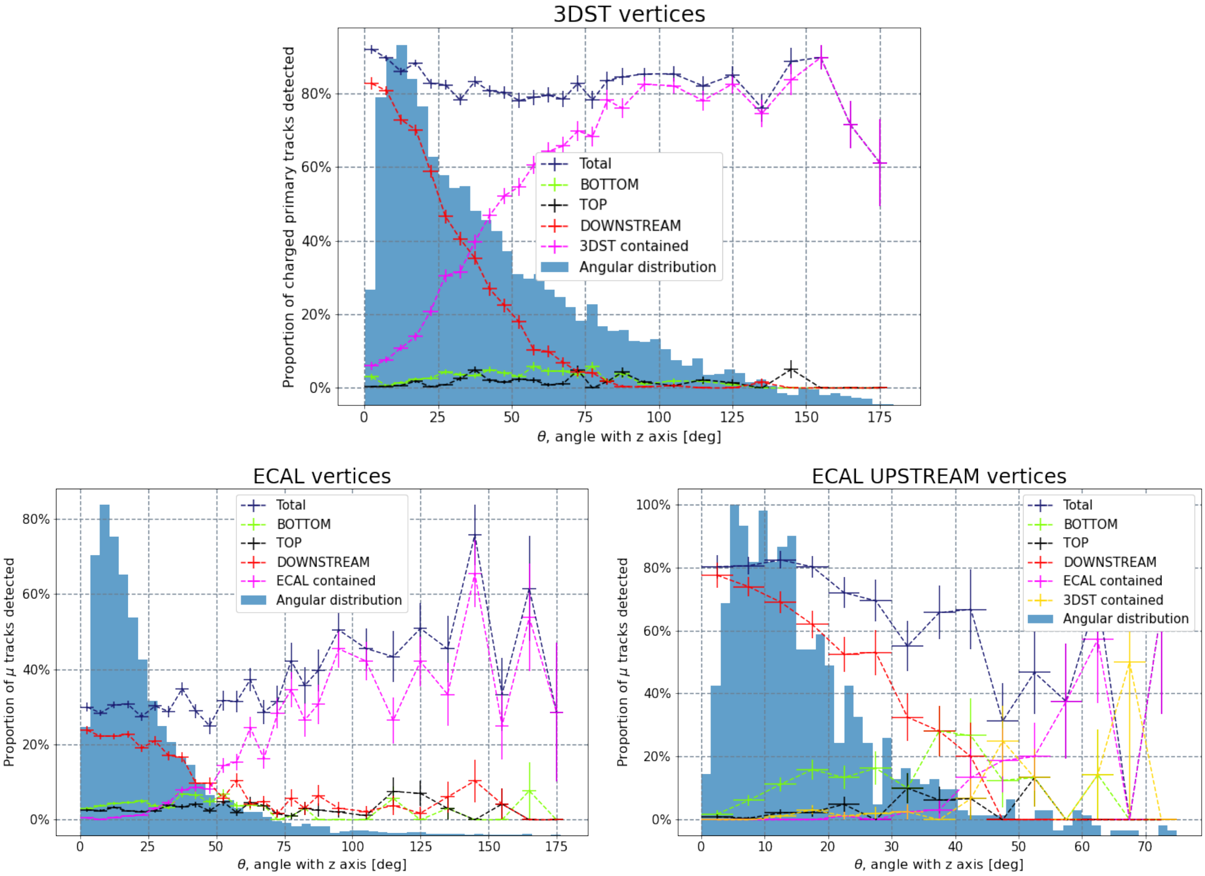

Figure 4.32: Angular coverage of the 3 TPCs for tracks produced in 3DST ν interactions (top), in all ECal ν interactions (bottom left) and upstream ECal ν interactions (bottom right). The tracks contained in 3DST and ECal are also included.

The TPC is able to reconstruct $\hat{P_T}$ from the curvature of the track under the magnetic field and $\hat{\Psi}$, the angle of the track with repect to the X axis, from the timing information. Based on these information, the TPC itself is able to reconstruct $\hat{P} = \frac{\hat{P_T}}{\sin\hat{\Psi}}$. The initial momentum of the particle can then be estimated by measuring the energy deposited inside the 3DST and considering the dead material between 3DST and TPC.

The following reconstruction steps are assumed in order to determine the resolution on the charged particles depositing energy inside a TPC:

- $\hat{P_T}$ is reconstructed in the TPC with a resolution $\sigma_{\hat{P_T}}$
- $\hat{\Psi}$ is reconstructed in the TPC with a resolution $\sigma_{\hat{\Psi}}$
- $\hat{P}$ is computed as $\hat{P} = \frac{\hat{P_T}}{\sin\hat{\Psi}}$
- The energy lost in the dead material between the active volumes of the detectors $\Delta P_{\text{mat}} = \tilde{P} - \hat{P}$ cannot be measured but is known on average. However, the uncertainty in the energy lost can be estimated from the Bethe-Bloch equation [125] and this effect is added as a resolution effect on $\tilde{P}$:

$$\sigma^2_{\tilde{P}} = \sigma^2_{\hat{P}} + \sigma^2_{\text{mat}} \tag{4.2}$$

- The energy deposited inside the 3DST E_{3DST} is measured with a resolution $\sigma_{E_{\text{3DST}}}$
- The initial particle momentum is finally computed as

$$P = \sqrt{E^2_{\text{3DST}} + \tilde{P}^2 + 2E_{\text{3DST}}\sqrt{\tilde{P}^2 + m^2}} \tag{4.3}$$

  with m the mass of the particle.

In order to propagate the various uncertainties on the measured parameters to the final reconstructed momentum, the following formula is used:

$$\sigma_P = \sqrt{\left(\frac{\partial P}{\partial E_{\text{3DST}}}\right)^2 \sigma^2_{E_{\text{3DST}}} + \left(\frac{\partial P}{\partial \hat{P_T}}\right)^2 \sigma^2_{\hat{P_T}} + \left(\frac{\partial P}{\partial \hat{\Psi}}\right)^2 \sigma^2_{\hat{\Psi}} + \left(\frac{\partial P}{\partial P_{\text{mat}}}\right)^2 \sigma^2_{P_{\text{mat}}}} \tag{4.4}$$

Computing the propagation of the various measurement uncertainties, we end up with the following formula for the relative uncertainty on the initial momentum of the particle:

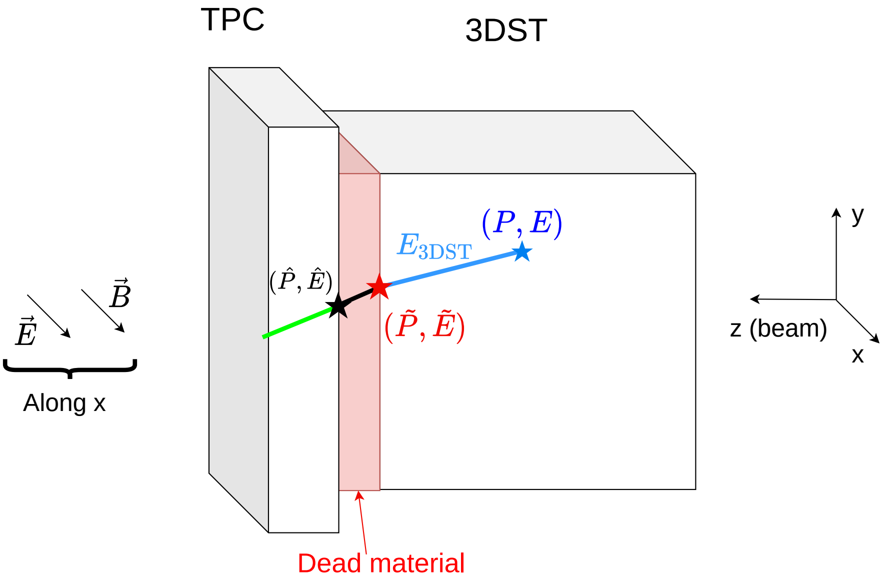

Figure 4.33: Sketch of the variables used to estimate the muon resolution

$$\begin{aligned}\left(\frac{\sigma_P}{P}\right)^2 &= \left(\frac{E E_{\mathrm{3DST}}}{P^2}\right)^2\left(\frac{\sigma_{E_{\mathrm{3DST}}}}{E_{\mathrm{3DST}}}\right)^2 && \textbf{3DST energy term}\\ &+\left(\frac{\tilde{P}\hat{P}}{P}\frac{E}{E-E_{\mathrm{3DST}}}\right)^2\left(\frac{\sigma_{\tilde{P_T}}}{\tilde{P_T}}\right)^2 && \textbf{TPC transverse momentum term}\\ &+\left(\frac{\tilde{P}\hat{P}}{P}\frac{E}{E-E_{\mathrm{3DST}}}\right)^2\left(\sigma_{\hat{\Psi}}\cot\hat{\Psi}\right)^2 && \textbf{TPC angle measurement term}\\ &+\left(\frac{\tilde{P}\hat{P}}{P}\frac{E}{E-E_{\mathrm{3DST}}}\right)^2\left(\frac{\sigma_{P_{\mathrm{mat}}}}{\hat{P}}\right)^2 && \textbf{dead material energy loss}\end{aligned} \tag{4.5}$$

TPC resolution

The resolution on the transverse momentum of the particle measured in the TPC, $\frac{\sigma_{\hat{P_T}}}{\hat{P_T}}$, is estimated from the following formula [126]:

$$\frac{\sigma_{\hat{P_T}}}{\hat{P_T}} = \frac{\hat{P_T}}{0.3BL^2}\sqrt{\frac{720}{N+4}}.\sigma_{r\phi} \tag{4.6}$$

where L is the track length in cm, N the number of leading pads activated by the track, B the magnetic field (0.6 T in SAND) and $\sigma_{r\phi}$ the spatial resolution of the detector.

$\sigma_{r\phi}$ has been estimated during the different test beams of the resistive MM technology [121]. I used these

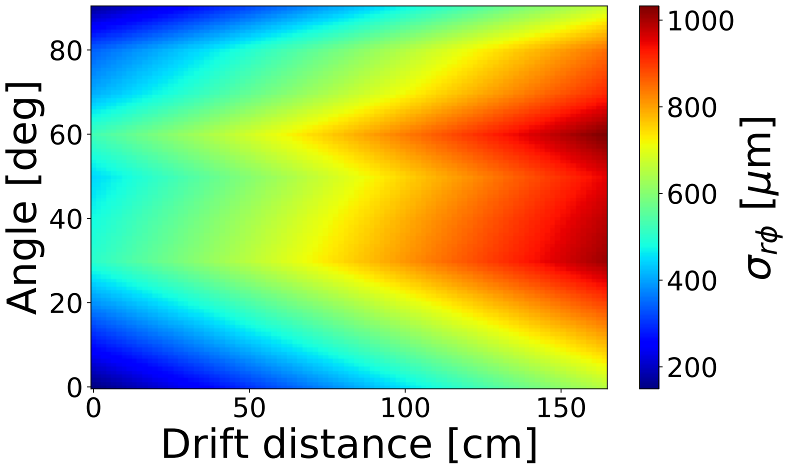

Figure 4.34: $\sigma_{r\phi}$ map computed from test beam data

test data in order to compute a $\sigma_{r\phi}$ map as a function of the average drift distance and the track angle in the anode plane. The resulting map is shown in Figure 4.34. It can be seen that the spatial resolution increases with the drift distance. Moreover, the resolution is the smallest for tracks that are parallel to the pads lines or columns, as the reconstruction of the charge spreading is then easier. This map assumes that the impact of the drift distance is the same for all the track angles, however recent DESY results show that the spatial resolution for diagonal tracks merely depends of the drift distance with 600 µm being the overall maximal spatial resolution. As a consequence, the study presented here relies on a pessimistic estimation of the TPC spatial resolution.

This resolution is computed track-by-track, with the relevant parameters taken into account for each track. Due to geometrical acceptance considerations, more tracks produced in 3DST ν interactions are close to the cathode at the center of the TPC than to an anode plane, as can be seen in Figure 4.35. These high drift distances lead to an average spatial resolution of 643 µm.

An additional resolution effect coming from the multiple scattering of the charged particle the gas atoms inside the TPC is taken into account. This effect, despite having a relatively small impact on the particle trajectory, has to be taken into account since the measured deviation due to the magnetic field can be relatively small too (below 1 cm for 2 GeV tracks crossing the downstream TPC with a low angle relative to the beam). The formula that estimates this contribution is the following:

$$\left.\frac{\sigma_{\hat{P_T}}}{\hat{P_T}}\right|^{\mathrm{MS}} = 0.045\frac{1}{B\sqrt{LX_0}} \tag{4.7}$$

where X_0 is the radiation length of the TPC gas, B the magnitude of the magnetic field and L the track

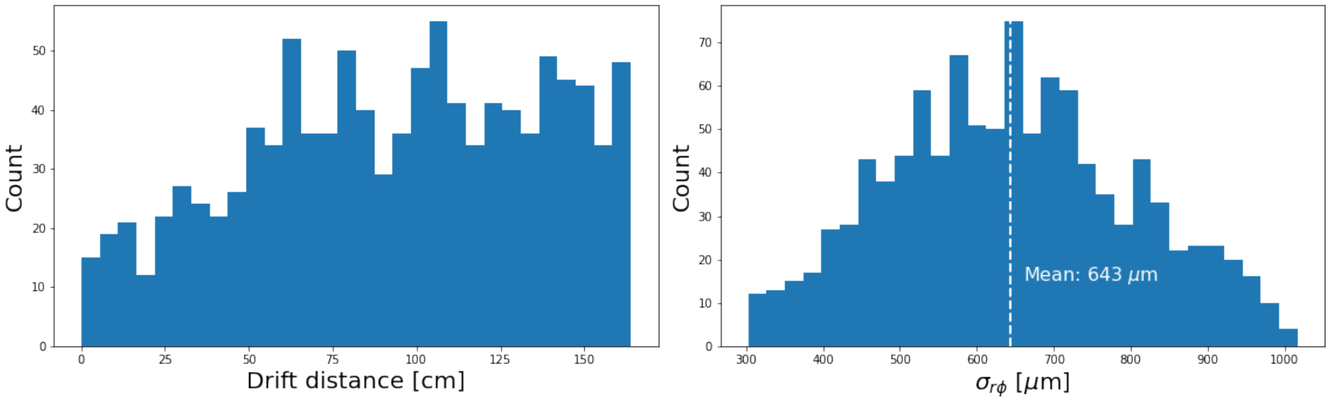

Figure 4.35: Distribution of the mean drift distances of the muon tracks (left) and distribution of the resulting spatial resolution on the anodes (right).

length. X_0 is taken as the radiation length of gaseous Argon at atmospheric pressure [125]: $X_0 = 117.6\,\text{m}$. With $B = 0.6\,\text{T}$ and a typical track length of $L = 80\,\text{cm}$, this effects accounts for:

$$\frac{\sigma_{\hat{P_T}}}{\hat{P_T}}\Bigg|^{\text{MS}} = 0.7\,\% \tag{4.8}$$

Taking into account these elements, the final resolution on the transverse momentum of the particles measured in the TPC is:

$$\left(\frac{\sigma_{\hat{P_T}}}{\hat{P_T}}\right)^2 = \left(\frac{\sigma_{\hat{P_T}}}{\hat{P_T}}\Bigg|^{\text{Measure}}\right)^2 + \left(\frac{\sigma_{\hat{P_T}}}{\hat{P_T}}\Bigg|^{\text{MS}}\right)^2 \tag{4.9}$$

The obtained transverse momentum resolution of the downstream TPC for the tracks from simulated 3DST ν and $\bar{\nu}$ interactions are shown in Figure 4.36. The obtained resolution is dominated by multiple scattering at low transverse momentum (notice that the multiple scattering in the dead material upstream of the TPC is not included yet at this stage) while spatial resolution dominates at higher transverse momentum. The intrinsic resolution of the TPC on the transverse momentum is better than $2\,\%$ at $1\,\text{GeV}$.

TPC angular resolution

In order to fully determine the momentum of the particles that enter the TPC, it is necessary to measure the angle of this particle with respect to the anode planes. This angle can be measured from the drift time of the electrons inside the TPC along the particle track. More precisely, the angle is estimated by measuring the drift time difference between the entrance and the exit of the TPC. The following two main parameters introduce an

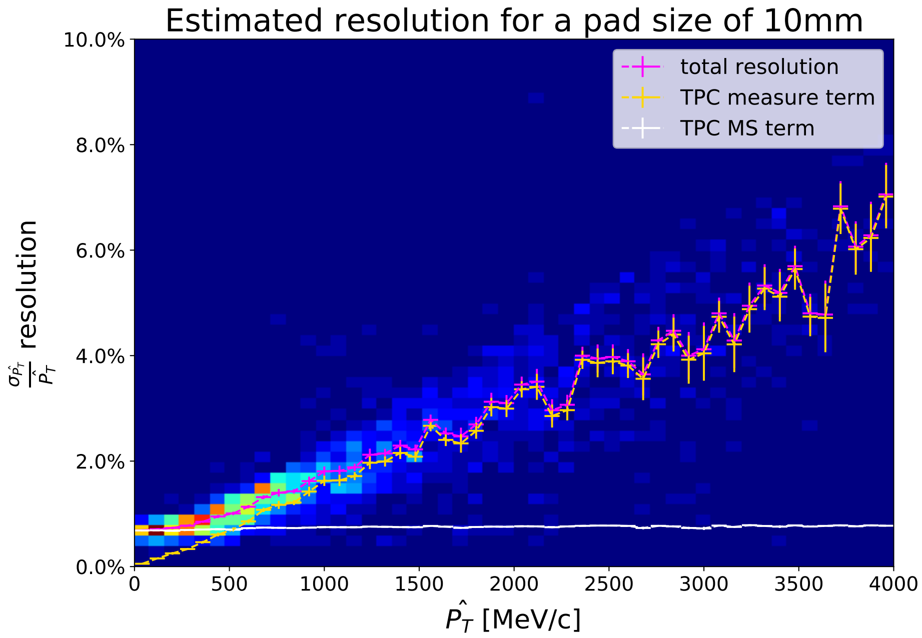

Figure 4.36: Estimated transverse momentum resolution of the downstream TPC for charged primary particles from 3DST ν and $\bar{\nu}$ interactions.

uncertainty on the measurement of this difference in drift time.

- The longitudinal spread of the electron cloud during the drift. For the TPC gas, the longitudinal spread is $\sigma_L = 0.29\,\mathrm{mm}/\sqrt{\mathrm{cm}}$ and the drift velocity is $v_d = 78\,\mathrm{mm}\,\mu\mathrm{s}^{-1}$ (see Figure 4.23).
- The time resolution of the readout electronics, $\sigma_t = 40\,\mathrm{ns}$ (a sampling rate of 25 MHz is used in ND280 [127]).

Considering a track passing through the TPC with differences between the exit and entrance coordinates of (dx, dy, dz), the total length of the track is $L = \sqrt{dx^2 + dy^2 + dz^2}$ while the length of the track image on the anode plane is $l = \sqrt{dy^2 + dz^2}$. The angle to be measured is then:

$$\hat{\Psi} = \arctan\frac{l}{dx} \tag{4.10}$$

and the uncertainty on the measurement of this angle is:

$$\sigma_{\hat{\Psi}}^2 = \left(\frac{dx}{L^2}\right)^2 \sigma_l^2 + \left(\frac{l}{L^2}\right)^2 \sigma_{dx}^2 \tag{4.11}$$

where

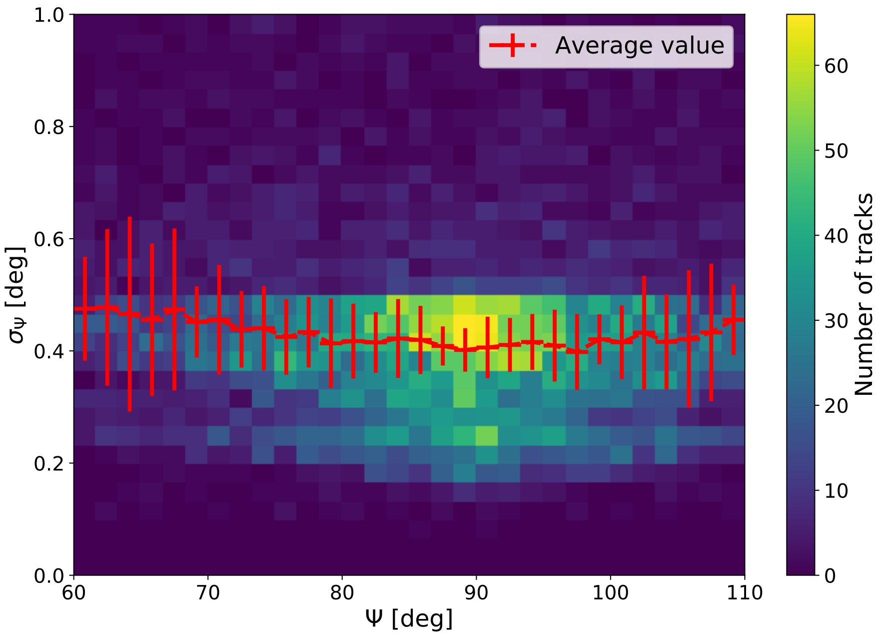

Figure 4.37: Estimated TPC angular resolution for simulated tracks

- σ_l is the resolution on the track length on the pad plane. This resolution is estimated to be equal to the pad size, 10 mm
- σ_{dx} is the resolution on the difference of drift distances. It is estimated from the longitudinal spread as $\sigma_{dx} = \sigma_L \times \sqrt{d_{\text{drift}}} + \sigma_{dt} \times v_{\text{drift}}$, with d_{drift} being the mean drift distance of the electrons.

$\sigma_{\hat{\Psi}}$ has been computed for all the simulated tracks and the results are presented in Figure 4.37. It can be seen that the angular resolution is below 0.5° for most of the tracks.

3DST energy loss

The resolution measurement of the deposited energy in the 3DST detector have been estimated from the test beam data [119]. A conservative estimation of $\frac{\sigma_{E_{\text{3DST}}}}{E_{\text{3DST}}} = 2\%$ is considered for this study.

Energy lost in the dead material

The energy that is lost by the particle in the material in-between the TPC and 3DST active areas can be estimated from the Bethe-Bloch formula, knowing the material composition and thickness of the dead material. The Bethe-Bloch formula also provides the typical fluctuations in the energy loss in the material and this value

Table 4.3: Energy loss fluctuations parameters

Variable name	Symbol	Value
Atomic number	Z	26
Mass number	A	56
Charge number	z	1
Mass per unit area [$\mathrm{g\,cm^{-2}}$]	x	7.83
$4\pi N_A r_e^2 m_e c^2$ [$\mathrm{mol^{-1}\,cm^2}$]	K	0.307

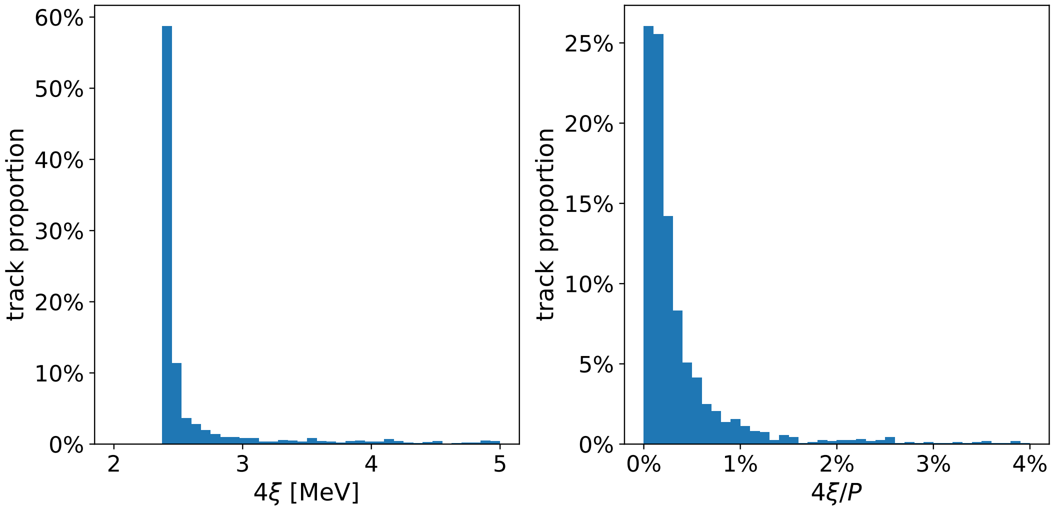

Figure 4.38: Uncertainty on the energy lost in the dead material (left) with the corresponding resolution effect (right).

is used as an uncertainty on the estimation of the energy deposited in this dead material [125]. The Full Width at Half Maximum (FWHM) is estimated to be 4ξ with

$$\xi = \frac{K}{2}\frac{Z}{A}\frac{x}{\beta^2}z^2 \tag{4.12}$$

The equation parameters are given in Table 4.3.

The obtained distribution of the FWHM values for the simulated tracks is shown in Figure 4.38. The typical uncertainty is around 2.5 MeV leading to a resolution effect around 0.25 % for most tracks but that can reach 1 % or more for the less energetic particles.

Results

The spreading and resolution effects described above are computed for each simulated track passing through a TPC and combined according to Equation 4.5. The final estimated resolutions for the simulated tracks, coming

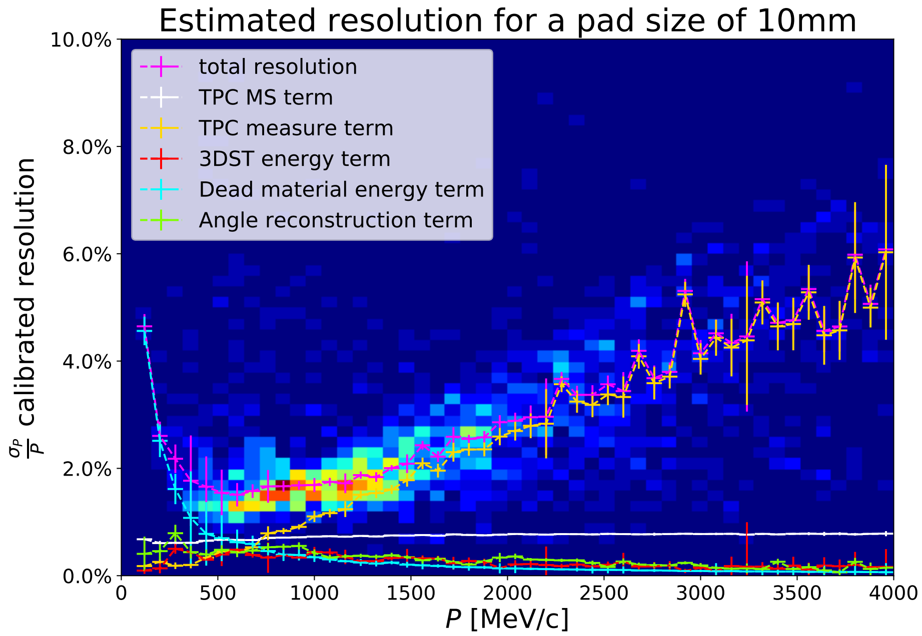

Figure 4.39: Estimated momentum resolution of charged primary particles from ν and $\bar{\nu}$ interactions

from neutrino or antineutrino interactions in the 3DST, are shown in Figure 4.39. The total resolution distribution and its mean value for each particle momentum is shown. The mean values of the different components of the resolution are also given. It can be noticed that the resolution for 1 GeV particles is slightly below 2 %, and can be extrapolated below 10 % at 5 GeV, thus matching the requirements for the SAND detector. As expected, for low momentum particles, below 500 MeV, the uncertainty on the energy lost in the dead material by multiple scattering dominates. For higher energy particles, the resolution is dominated by the curvature measurement.

The expected resolutions for different pad sizes have also been computed in order to quantify the gain in momentum resolution with smaller pads. The results are presented in Figure 4.40 : as expected, decreasing the pad size allows to increase the momentum resolution. This improvement increases with the particle momentum: for example 5 mm pads would allow to reach close to 2 % momentum resolution for 2 GeV particles. Increasing the pad granularity is always expected to improve the momentum resolution but the final choice of the pad size has to be a balance between the physics requirements and the detector cost.

4.6.2 $\vec{\mathrm{E}} \times \vec{\mathrm{B}}$ effect

The magnetic field produced by electromagnets is not homogenous. These magnetic field inhomogeneities, depending on their amplitude, can affect the momentum measurement capabilities of the TPCs. In the case of

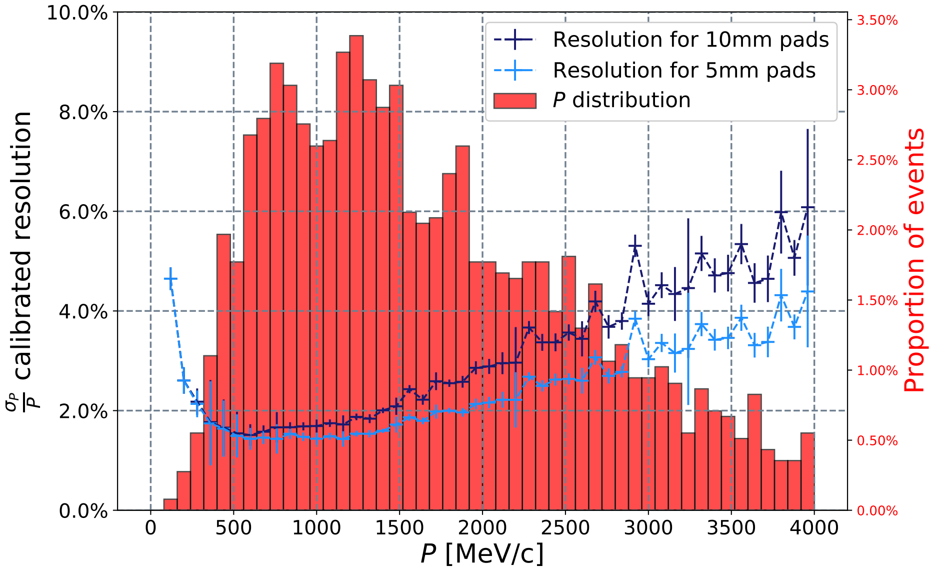

Figure 4.40: Estimated momentum resolution of the TPC on charged primary particles from ν and $\bar{\nu}$ interactions for different pad sizes

the KLOE magnet, its field has been previously mapped [128] showing relatively large inhomogeneities in the whole volume, as shown in Figure 4.41. The main deviations from the nominal field value occur at the borders of the magnet. The TPCs proposed for SAND would be partially placed close to the border of the magnet, as shown in Figure 4.42, thus experiencing an inhomogenous magnet field as displayed in Figures 4.43 and 4.44. We use for the field description cylindrical coordinates of axis x. The radial component of the magnetic field can reach 400 G in the TPC which is more than 6 % of the nominal axial field value of 0.6 T. This inhomogenous magnetic field impacts

- the curvature of the charged particled traveling inside the TPC (but also any other detector part)

- the drift of the electrons inside the TPC, most notably for magnetic field components orthogonal to the drift field

I quantified from the available magnetic field map the impact of this field inhomogeneity on the momentum resolution of the TPC using simulated tracks.

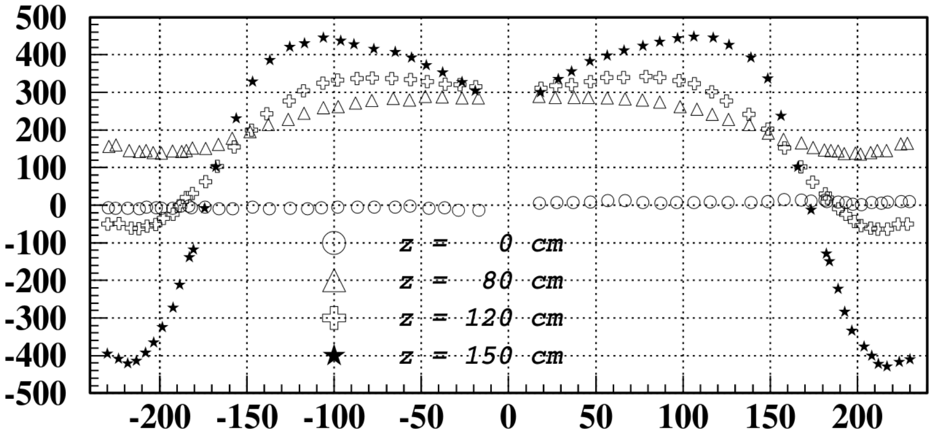

Br(Gauss) vs R(cm) at phi = 10

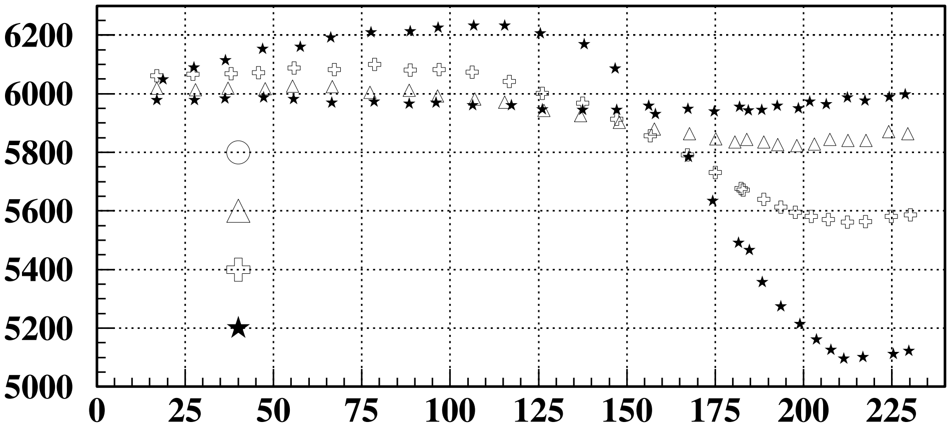

Bz(Gauss) vs R(cm) at phi = 10

Figure 4.41: Radial and axial components of the KLOE magnetic field in the KLOE cylindrical coordinate system around the Z (R, ϕ, Z), where Z would correspond to x axis in the DUNE SAND coordinate system. (reproduced from DellAgnello1999)

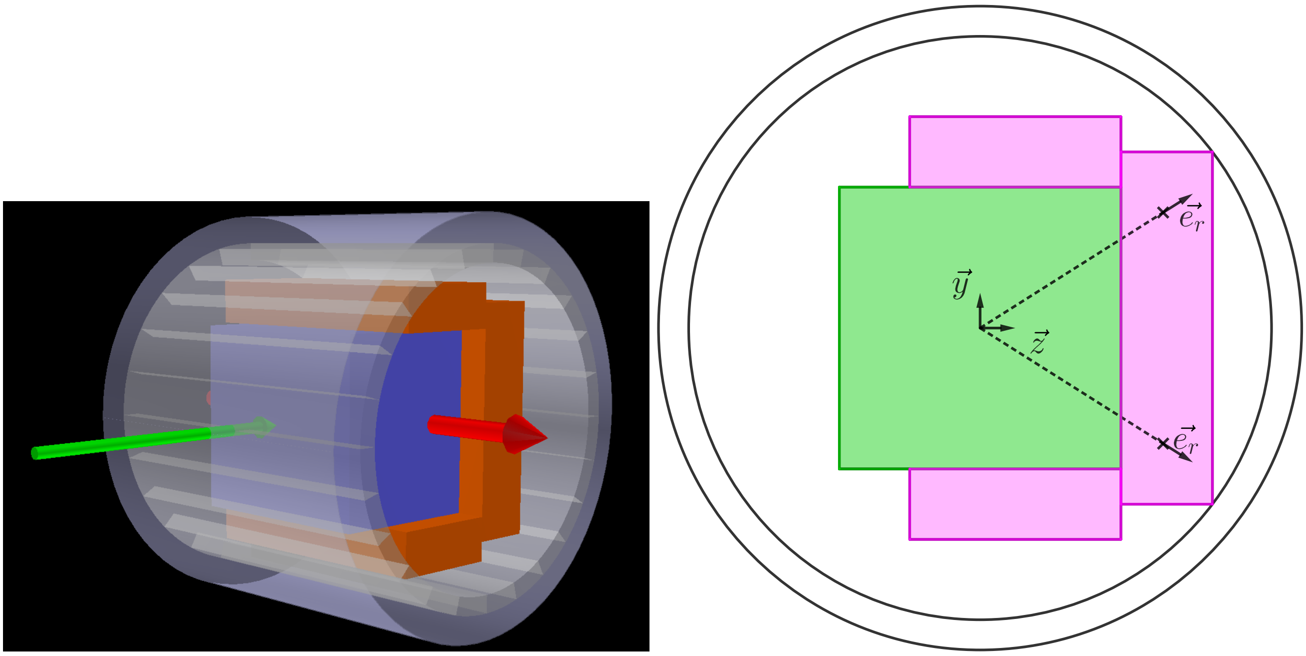

Figure 4.42: Scheme of the SAND solenoid magnetic axis orthogonal to the neutrino beam (left) and scheme cut of SAND at a constant x (right).

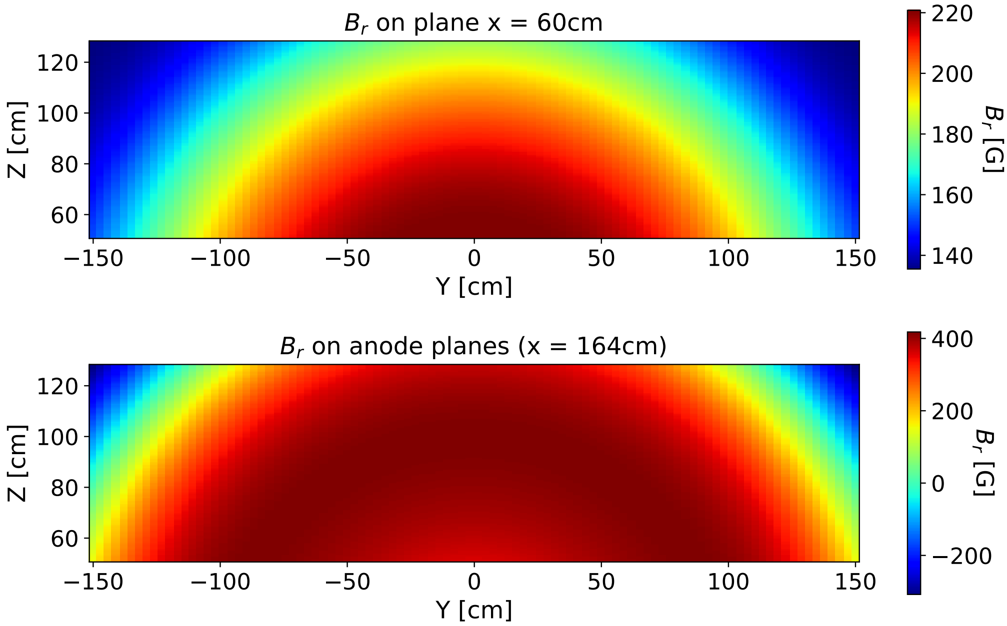

Figure 4.43: Radial component of the magnetic field in planes parallel to the ERAMs

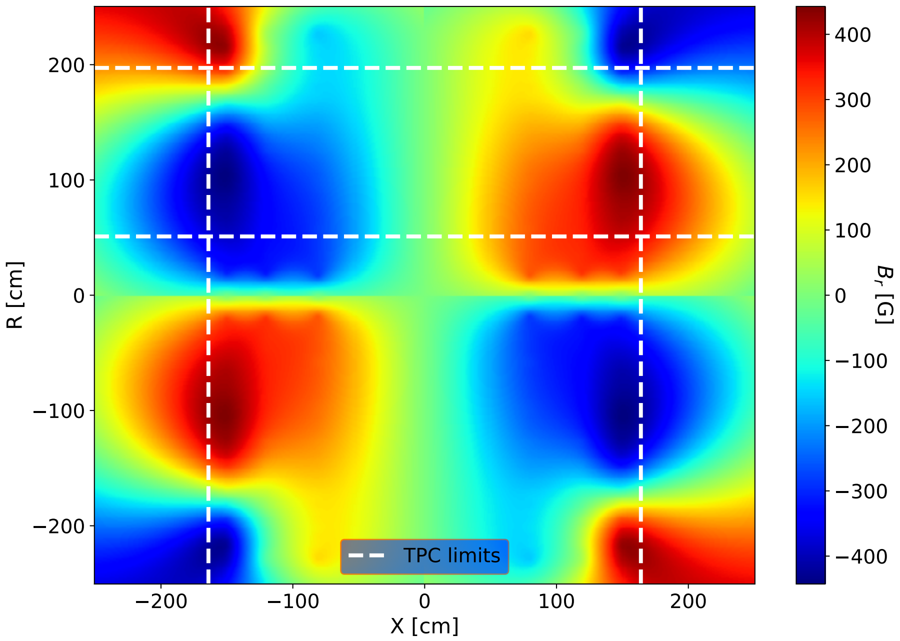

Figure 4.44: Radial component of the magnetic field.

Simulation of the magnetic field effect

The electrons drifting in the TPC, under the influence of both an electric and a magnetic field, have trajectories that follow the Langevin equation given here for a negatively charged particle such as an electron:

$$\vec{\mathbf{v}}_{\mathbf{D}} = \frac{\mu}{1+(\omega\tau)^2}\left(\vec{\mathbf{E}} - \omega\tau\frac{\vec{\mathbf{E}}\times\vec{\mathbf{B}}}{\left\|\vec{\mathbf{B}}\right\|} + (\omega\tau)^2\frac{\vec{\mathbf{B}}\left(\vec{\mathbf{E}}\cdot\vec{\mathbf{B}}\right)}{\vec{\mathbf{B}}^2}\right) \tag{4.13}$$

where all the relevant variables are defined in Table 4.4. This equation shows that when the drift field and the magnetic field are not aligned, because of magnetic field inhomogeneities in magnitude or direction, the drift of the electrons is no longer along the electric field ($\vec{\mathbf{E}}$) direction and the electron trajectory has a component in the $\vec{\mathbf{E}}\times\vec{\mathbf{B}}$ and $\vec{\mathbf{B}}$ directions. As a consequence, the image of the track collected on the anode planes will no longer be the orthogonal projection of the track but will feature some distortions.

To simulate the complete effect of the magnetic field on the drift of the electrons inside the TPC, I started by interpolating the available data from the KLOE collaboration in order to obtain a magnetic field map for the whole TPC volume. The final position of the electrons on the anode planes is computed by numerically integrating the Langevin equation using the Runge-Kutta 4 method. The chosen integration step is of 0.1 µs ~ 0.8 cm. The position of the drifted electrons on the anode plane is unique and only depends on their starting position

Table 4.4: Parameters used in Equation 4.13

Variable name	Symbol	Value
electron charge quantum	e	1.6×10^{-19} C
electron mass	m	9.11×10^{-31} kg
mean drift time between two collisions	τ	
electric field norm	E	$275\,\mathrm{V\,m^{-1}}$
magnetic field norm	B	0.6 T (nominal)
electron mobility	$\mu = \frac{e\tau}{m}$	$2.85\,\mathrm{m^2V^{-1}s^{-1}}$
cyclotron frequency	$\omega = \frac{eB}{m}$	105 GHz

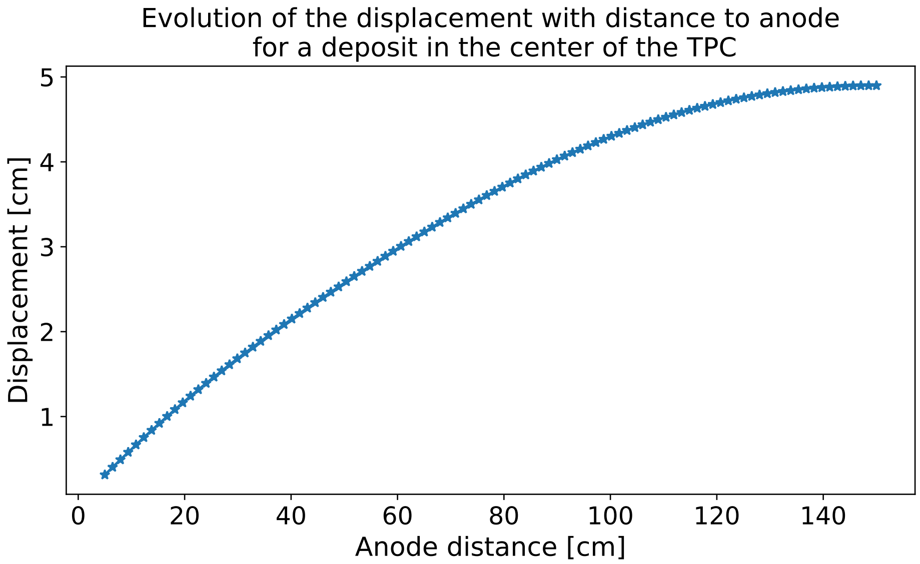

Figure 4.45: Evolution of the electron cloud displacement on the anode as a function of the drift distance for an energy deposit made in the center of the TPC.

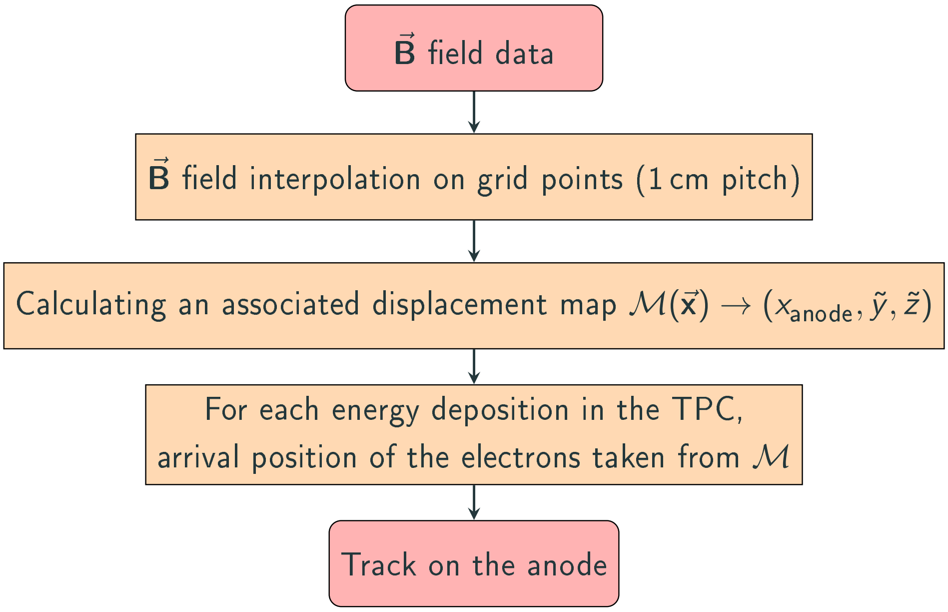

Figure 4.46: Simulation process of the magnetic field effects.

(ionization location) inside the TPC (neglecting the electron cloud transversal spread that will be taken into account later). Figure 4.45 gives an example of the displacement of an electron with respect to its drift as its drift distance increases.

Given the unique correspondance between a starting position in the TPC and an arrival point on the anode, it is possible to map each TPC voxel (3D equivalent of a pixel, here a 1 cm^3 cube) to a drift endpoint onto an anode:

$$\mathcal{M}(x,y,z) = (x_{\text{anode}}, \tilde{y}, \tilde{z}) \tag{4.14}$$

where $\mathcal{M}$ is the mapping that transports an electron produced in (x,y,z) onto the anode plane at the location $(\tilde{y},\tilde{z})$. Note that in the absence of magnetic field, or at least absence of any radial component of the magnetic field, the mapping $\mathcal{M}$ is simply the projection of the ionisation location onto the anode: $\mathcal{M}(x,y,z) = (x_{\text{anode}}, y, z)$. This map is computed with a 1 cm pitch in every direction inside the TPC. Then, we can replace the simple projection onto the anode that was done in the previous simulation by the newly computed transportation map and, by interpolating it, compute the image of the track on the anode for each energy deposition simulated inside the TPC. This process is summarized in Figure 4.46.

From the transportation maps, it is possible to get a first idea of the impact of the magnetic field inhomogeneity by looking at the displacement of the electron cloud on the anode. This displacement is defined as the distance between the arrival position of the charge on the anode and the simple ($B_r = 0$) projection of it on the anode:

$$d = \sqrt{(\tilde{y} - y)^2 + (\tilde{z} - z)^2} \tag{4.15}$$

The displacement map under the KLOE magnetic field, as a function of the drift distance and Z, for a fixed value of Y ($Y = 0$) is produced in Figure 4.47. We can see that the displacement values are symetric around $X = 0$ as this is the location of the cathode. Moreover, the displacement values are the largest for energy depositions close to the cathode as the drift distance is then larger, leading to an accumulation of $\vec{\mathbf{E}} \times \vec{\mathbf{B}}$ over a longer drift distance. The displacement on the anode can reach values larger than 4 cm. The displacement direction can be visualized more prcisely in Figure 4.48 where we can see that the displacement direction is not homogeneous in the YZ plan. In the case of SAND, this effect is clearly non-negligible. However, these displacements of the tracks are not themselves an issue if they can be precisely corrected for in the reconstruction.

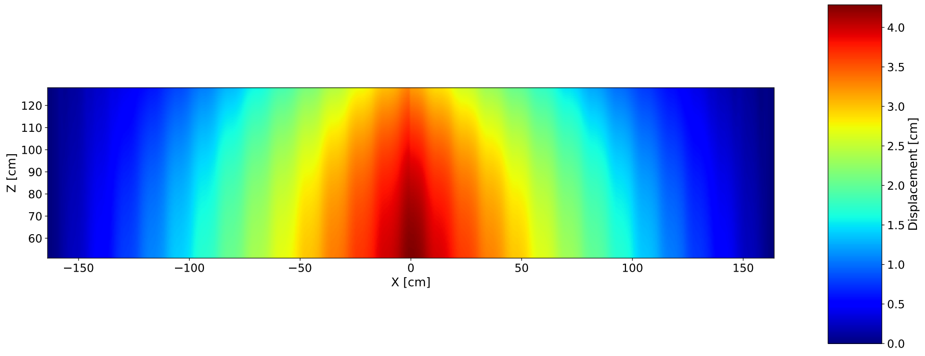

Figure 4.47: Displacement on the anode as function of Z and X at a fixed $Y = 0$. The cathode is located at $X = 0$.

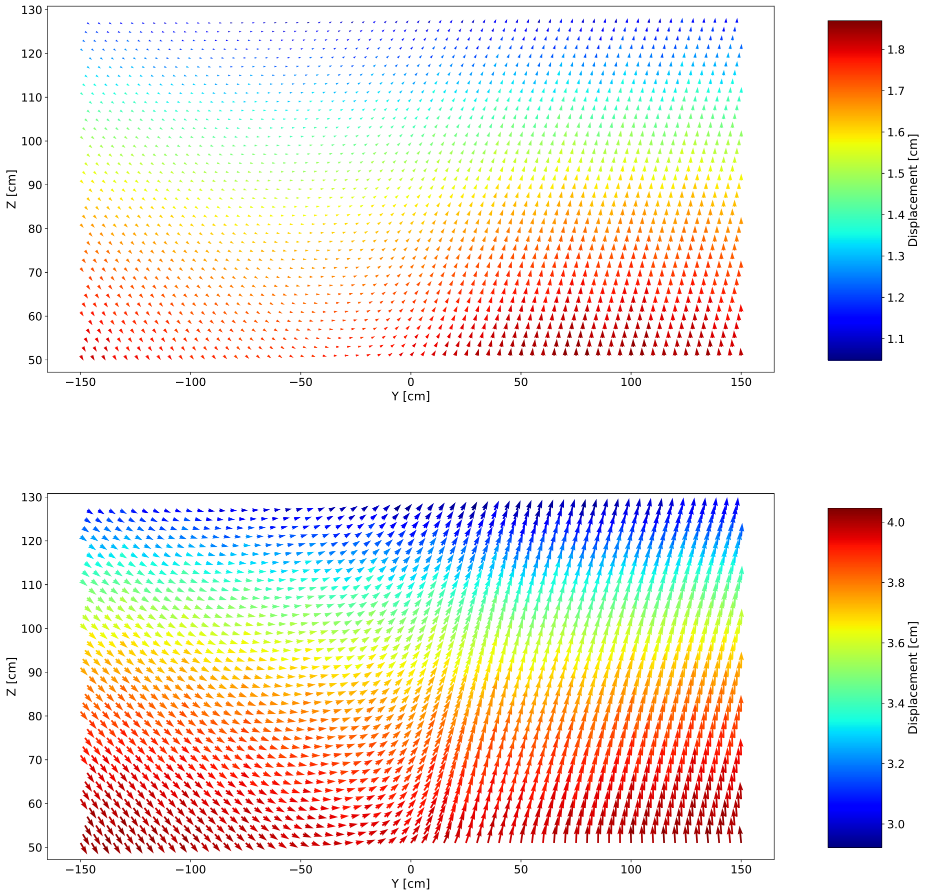

Figure 4.48: Displacement maps represented with arrows for $X = 90\,\mathrm{cm}$ (top) and $X = 10\,\mathrm{cm}$ (bottom). The base of the arrow is the expected position on the anode for $B_r = 0$ and its tip is the actual position with SAND magnetic field.

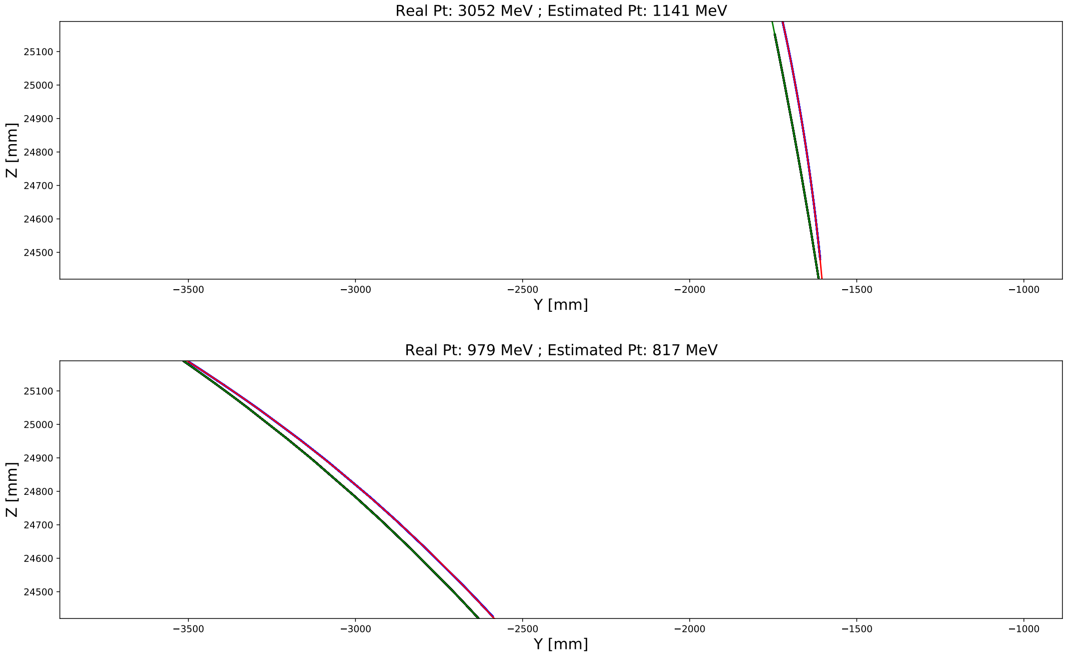

Figure 4.49: Anode images for simulated tracks with no radial component of the magnetic field (black) fitted with a circle (green), and images of the tracks with the radial component of the magnetic field (blue) fitted with a circle (red).

Reconstruction

The impact of this non-zero radial component of the magnetic field on the tracks projection can be seen in Figure 4.49. The tracks are displaced on the anode but not uniformly. As a consequence, an attempt to directly fit these tracks with a circular fit leads to totally erroneous estimations of the particle transverse momentum. Therefore, it is necessary to integrate the knowledge of the field distortion in the reconstruction of the particles momenta.

A more elaborated fit has to be conducted in order to recover the correct particle momentum. A particle trajectory inside the TPC describes an helix that can be uniquely defined by five parameters:

- its transverse momentum P_T, which will drive its curvature.
- its entrance point in the TPC, $\vec{\mathbf{x}}_\mathbf{0}$
- its angle with respect to the anode planes, Ψ
- its angle inside the anode plane, θ
- its charge sign, ε

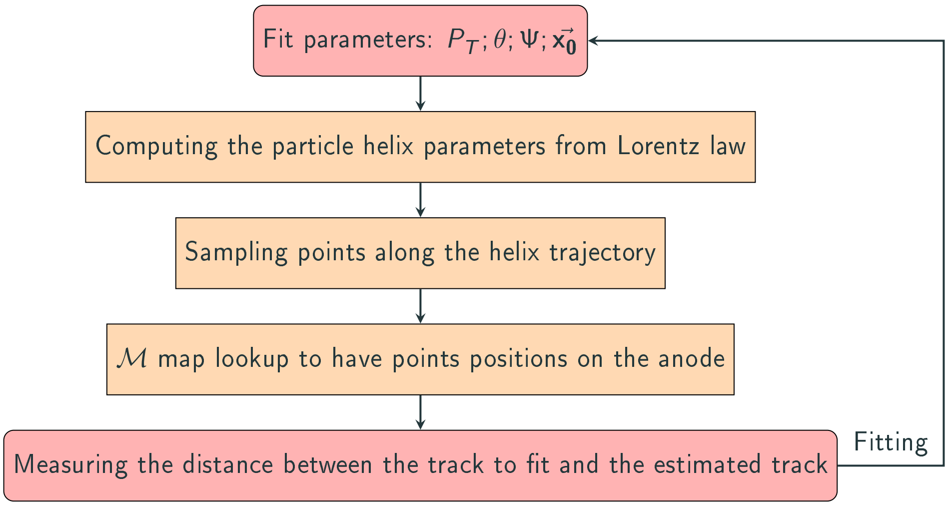

Figure 4.50: Fitting process of the magnetic field effects.

Therefore, I developed a fit that takes as input these parameters, compute the associated helicoidal trajectory, sample points along this trajectory, compute the projection on the anode, given the precomputed transportation map, and finally compute the distance between the detected track and the projection. This process is represented in Figure 4.50. The objective is to minimize the distance between the estimated track from a given set of parameters and the tracks detected on the anode plane by varying such parameters. Well constrained first guesses can be obtained for θ, Ψ and $\vec{x_0}$ by the 3DST detector from which the track is exiting before entering the TPC. Initial guesses on P_T and ε can be obtained by making an initial circular fit of the anode track.

To test this fitting procedure, tracks with the same P_T, Ψ and θ distributions as tracks expected to enter the downstream TPC in SAND are simulated. The projections on the TPC anodes of these tracks are computed, according to the electric and magnetic fields. Such tracks are then reconstructed with the fit according to the previous procedure and by supposing a perfect knowledge of the magnetic field. In this case, this method converges towards the right kinematic parameters of the tracks as shown in Figure 4.51.

It is unrealistic to assume a perfect knowledge of the fields inside the TPCs, but it is nonetheless possible to measure in-situ or through calibration methods the magnetic field in the TPC volume at a certain precision. The KLOE experiment reported that they were able to map the magnetic field of the magneted with a precision of 3 G. Thus, we can consider that it will be possible to know the magnetic field in the TPC volume with a similar precision of 3 G for SAND. In order to simulate this uncertainty on the field map, a random value following a gaussian with a σ_B width is added to the KLOE measurement points used for the field interpolation in the whole volume. This modified map is then used to simulate the drift, while the original map is used for the reconstruction. This process is reapeated multiple times with the same tracks but different generated maps in

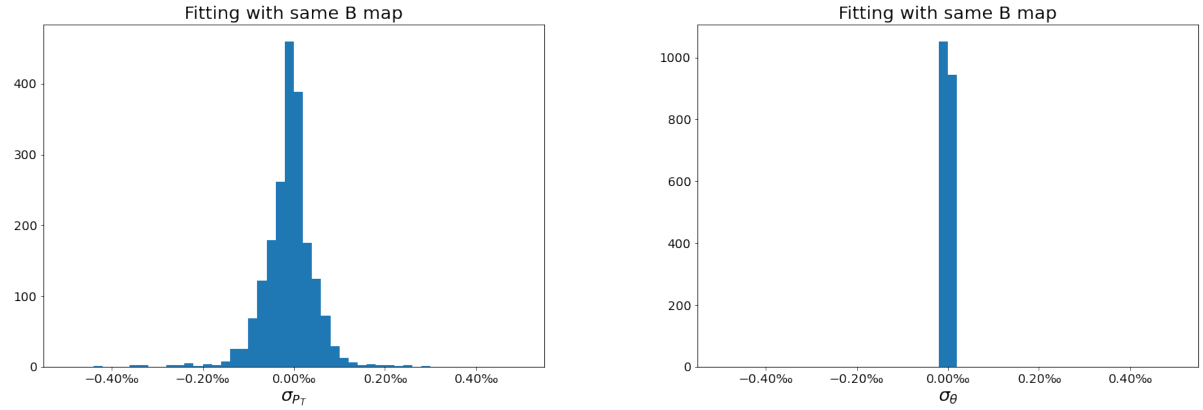

Figure 4.51: Results of the Asimov fit of the tracks parameters assuming that the magnetic field is perfectly known.

order to average the results on a set of differently distorted field maps. The obtained resolutions after the track fit are presented in Figure 4.52. Note that for this exercise, a perfect spatial resolution of the TPC is assumed. We can see that an uncertainty on the magnetic field map of 3 G (1 G) introduces a non negligeable uncertainty of 1.2 % RMS (0.9 % RMS) on the transverse momentum measurement of the particles. Moreover, the error distributions have large tails because of the regions with large magnetic field inhomogeneities that introduce large distortions.

The ERAMs spatial resolution is finally added by sampling each TPC trace with one position measurement per pad. The resolution spread is then applied, orthogonally to the track direction, to these exact measurement points according to the spatial resolution as a function of the track angle and drift distance determined during beam tests and previously shown in Figure 4.34. The results obtained including this TPC spatial resolution are shown in Figures 4.53 and 4.54. We can see that, even after considering the TPC spatial resolution, the impact of the magnetic field uncertainty on the transverse momentum resolution is still noticeable with a resolution going from 2.5 % at 2 GeV for a 1 G uncertainty to 4 % at 2 GeV for a 5 G uncertainty on the magnetic field radial component.

These results can finally be included in the momentum resolution of the whole SAND detector, including the 3DST and the TPC, by replacing the theoretical formula, giving the -transverse momentum resolution of the TPC based on the track's sagitta, from Equation 4.6 by the fitted results for the different field uncertainties presented in Figure 4.54. The result is shown in Figure 4.55 where we can see that it will be necessary to constrain as much as possible the uncertainty on the magnetic field in order to limit its impact on the resolution of the reconstructed particles momentum. However, even with a magnetic field resolution of 5 G (worse than what was achieved for

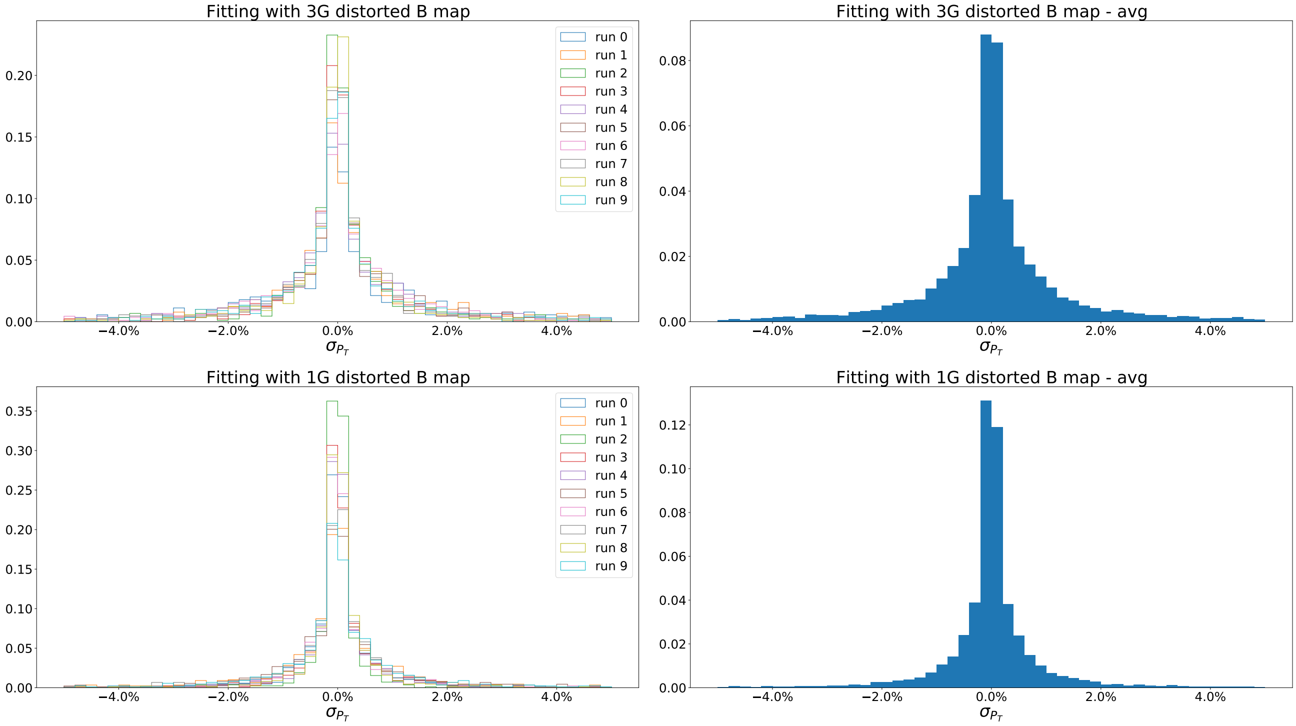

Figure 4.52: Obtained resolutions of the transverse momentum after the track fit with different distorted maps. On the left are shown the obtained results for ten different simulated distorted fields with a 3 G (top) and 1 G (bottom) deviation to the nominal field. The averaged results over the ten maps are shown on the right.

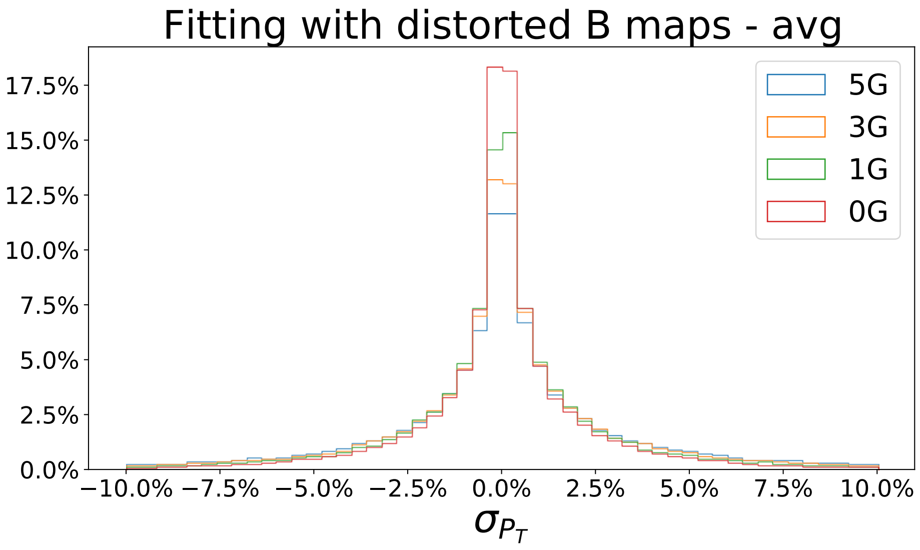

Figure 4.53: Average transverse momentum resolution distributions, including TPC spatial resolution effects, for different σ_B values.

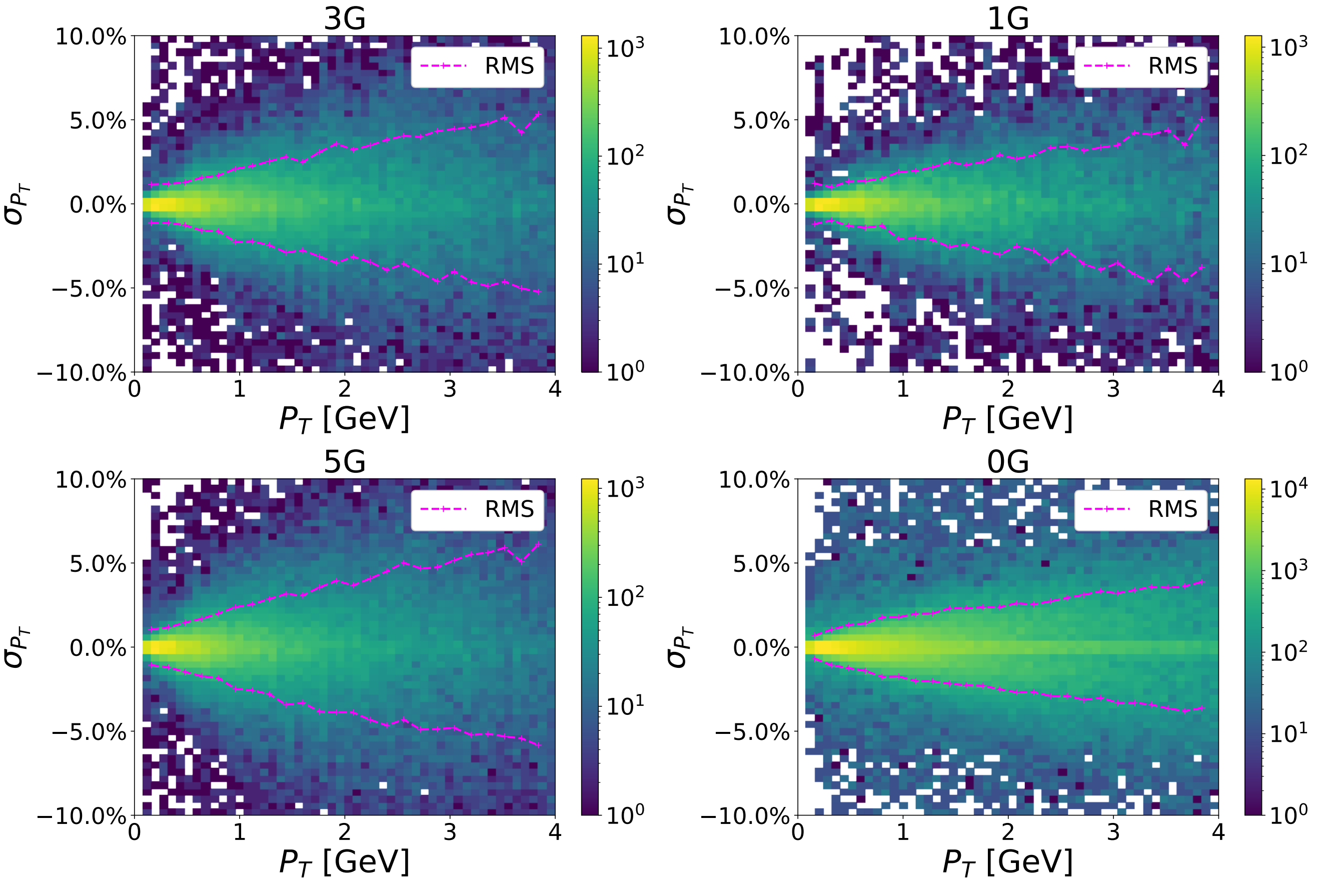

Figure 4.54: Evolution of the transverse momentum resolution as function of the transverse momentum, including TPC spatial resolution effects, for different σ_B values.

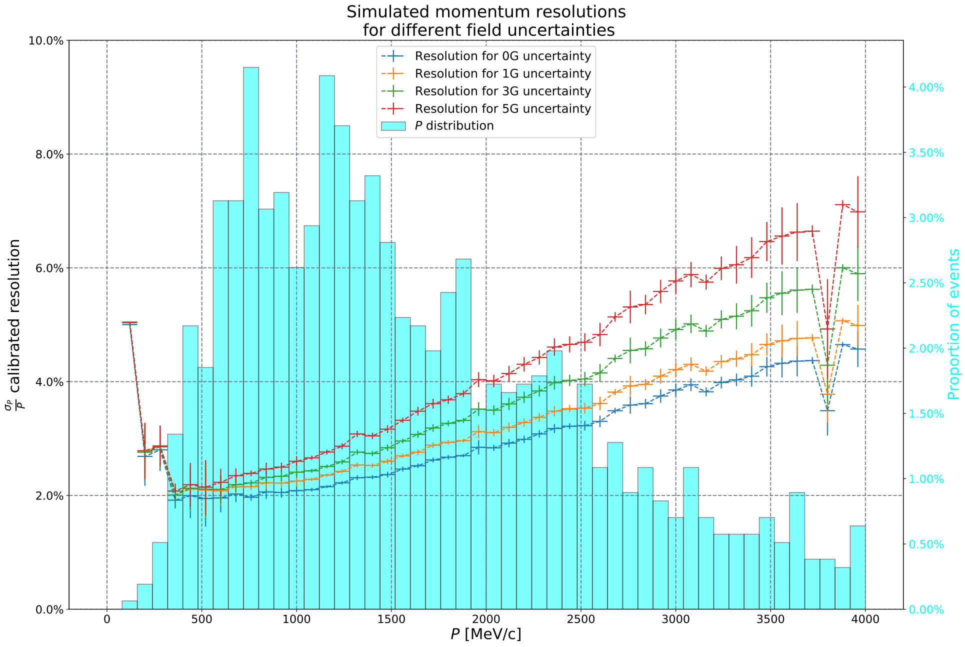

Figure 4.55: Total resolution on the particle momentum for different σ_B

KLOE), the momentum resolution of the TPCs remain in the DUNE SAND specifications.

Depending on the specific simulated field map, the impact of the field inhomogeneities can be different depending on the charge of the particle. This phenomenon can be seen in Figure 4.56 where the resolution on the reconstructed transverse momentum is shown for two different simulated maps, differentiated by particle charge. This asymmetry could introduce a systematic error on the ν vs $\bar{\nu}$ analysis. However, this might also help calibrating the field by using a sample of $K^0 \rightarrow \mu^+\mu^-$.

4.7 Detecting neutrons in the 3DST

We assess here the neutron detection capabilities of the 3DST using the available simulations.

4.7.1 Neutron tagging and reconstruction

As discussed previously the neutron detection capabilities of 3DST-like detectors allow to greatly improve the resolution on the neutrino energy. To reach this target, we need to discriminate neutron hits from energy deposited by other (possibly numerous) particles inside the detector. As neutrons are neutral particles, they do

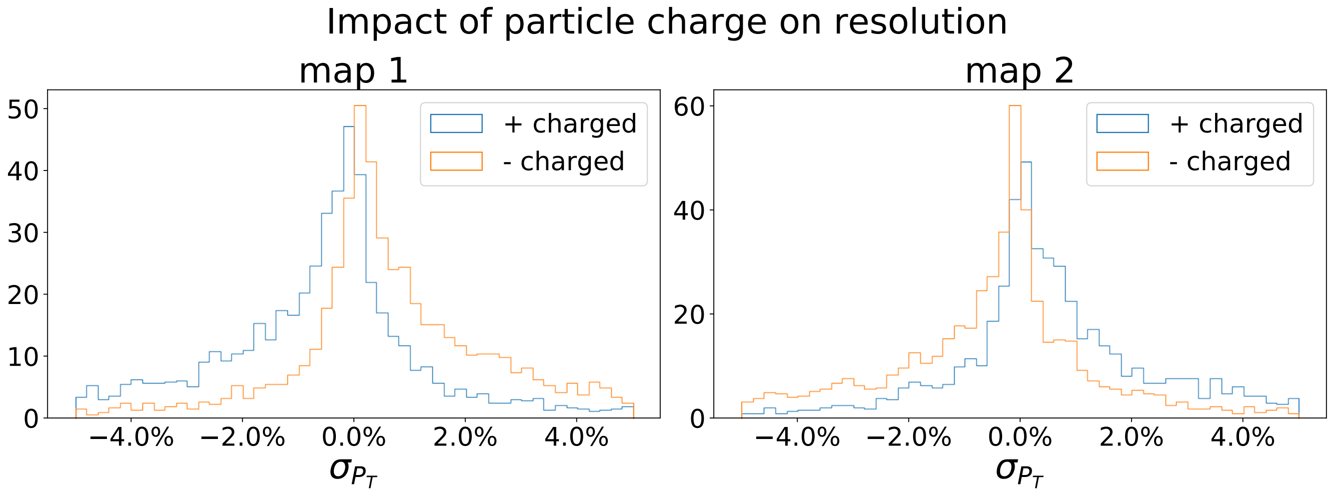

Figure 4.56: Resolution on the reconstructed transverse momentum as function of the charge for two different simulated magnetic field maps with a 3 G uncertainty.

not deposit energy continuously in the detector forming tracks. However, they scatter periodically on nuclei inside the scintillating material giving energy to charged particles that lead to localised energy deposits within the detector which, in turn, yield some light which can be detected. Thus neutrons will appear in the reconstruction as a succession of isolated clusters marking the locations in the detector where they interacted. For sub-GeV neutrons, as it is the case for neutrons produced in most of $\bar{\nu}$ interactions in DUNE, the amount of energy transferred to the secondary particle is almost independent of the initial neutron energy. As a consequence, the neutron energy has to be inferred by measuring the time-of-flight (ToF) and the distance between the $\bar{\nu}$ interaction vertex and the earliest cluster linked to the interaction of the neutron inside the detector, as shown in Figure 4.57. The relative velocity β of the neutron is determined as

$$\beta = \frac{L}{(t_2 - t_1)c} \tag{4.16}$$

where t_1 is the time of the interaction vertex and t_2 is the time of the first hit of the earliest cluster, L is the distance between the earliest cluster and the interaction vertex, called the lever-arm, and c is the speed of light. From this measurement of β, one can determine the Lorentz factor associated to the neutron,

$$\gamma = \frac{1}{\sqrt{1 - \beta^2}} \tag{4.17}$$

and finally the neutron kinetic energy:

$$T_n = (\gamma - 1)m_n \tag{4.18}$$

where m_n = 939.57 MeV is the neutron mass.

All the isolated clusters are potential neutron interactions however these clusters can be linked with particles that are not primary neutrons such as γ, δ or secondary neutrons coming from n, p, π interactions in the detector.

In the case of CCQE-like channel, we expect primary neutrons to be the main source of isolated clusters. This interaction channel is thus the simplest to study, as it provides only a lepton and a neutron in the final state (noted CC0π in the following). In order to select events meeting the pattern of this interaction channel, we select the CC events (with a lepton in the final state) that contain no pions. This selection is made in the simulated data by requiring the events to only contain a single reconstructed track that should correspond to the lepton produced at the vertex. Selecting the first cluster in time allows then to pick up the first interaction of the primary neutron and thus measure its energy after the neutrino interaction.

4.7.2 Nuclear effects at the interaction

Final State Interactions (FSI) are reinteractions with the nuclear medium of particles produced by the neutrino-nucleus interaction. All the final state particles produced by the neutrino interaction can undergo FSI inside the nucleus of a carbon atom. Different processes leading to FSI can occur inside the nucleus:

- Absorption of the particle inside the nucleus. This can notably happen to pions created by a resonant decay leading to the impossibility of their detection and the mis-classification of the event as CCQE.
- Quasi-elastic scattering in which the kinematics of the particle is changed.
- Hadron production in which the particle undergoes inelastic processes that leads to the production of pions or other nucleons.

Multi-nuclon interactions (2p2h) are also possible. This term describes interactions of the neutrino with a nucleon that is itself correlated with other nucleons inside the nucleus. Neutrino interaction on nucleons that are bound together can lead to multi-nucleon final states [129].

These FSI and 2p2h processes complicate the analyses of neutrino-nucleus interactions as the particles detected in the detector can be different from the final state particles of the neutrino interaction, both in nature and momentum. In the case of CCQE interactions, there is sometimes no primary neutron to be detected because it

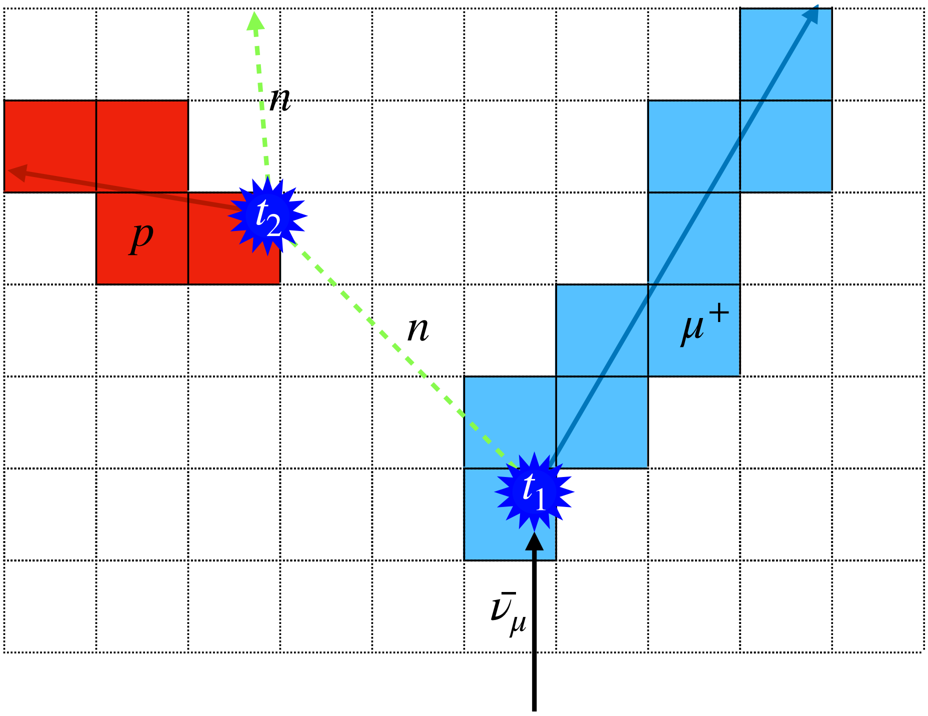

Figure 4.57: The first cluster after the neutrino interaction is identified as a neutron event

is reabsorbed inside the nucleus, in some other cases, the number of neutrons exiting the nucleus is larger than 1 because some reinteractions occured inside the nucleus by FSI or because of 2p2h. In the first case where no primary neutron can be detected, we can expect the absence of isolated cluster. For events with multiple primary neutrons, the applied method only considers a single neutron, the fastest to interact in the detector. This will lead to an underestimation of the incoming neutrino energy given that we don't account for all the particles in the final state.

4.7.3 Neutron selection

For some of the preselected events with a single reconstructed track, the first cluster in time is not linked to the primary neutron as shown in Figure 4.58. Some other preselected events correspond to non QES processes, such as resonant interactions and DIS, as shown in Figure 4.59. This can be due either to the absorption of some particles in the nucleus by FSI or the impossibility to reconstruct tracks inside the detector. In order to discard all these backgrounds, additional selections are applied to the events. For most of the cases where the first cluster in time is not related to the primary neutron, the energy deposit has been made by either a δ electron from the μ^+ track, a secondary neutron created by the primary neutron or a primary proton produced by some FSI effects or mis-selection of a non CC0π event. Secondary neutrons cannot be distinguished from primary

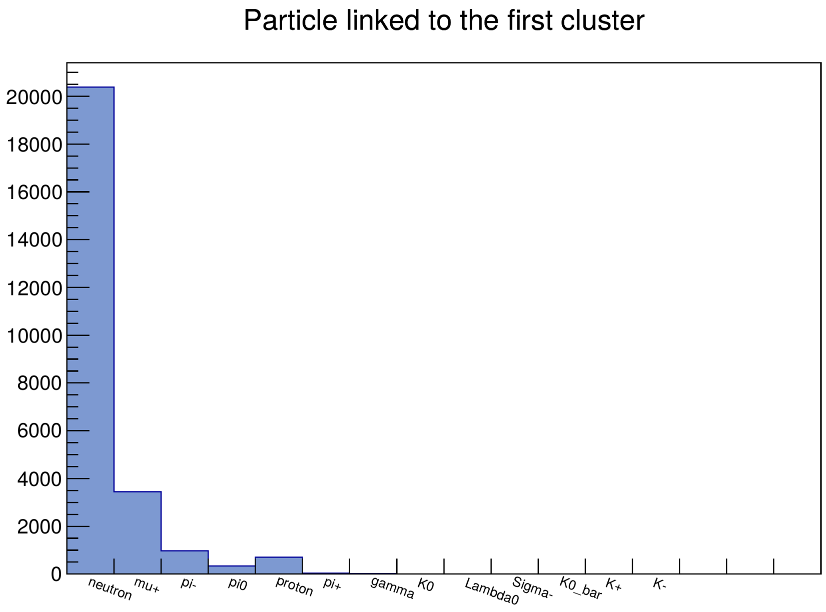

Figure 4.58: Proportion of the primary particles that created the first cluster in time for CC0π events. The cluster might have been created by a daughter particle, like the μ^+ contribution that comes from emitted δ electrons.

neutrons because they have the same topology. However, it is possible to remove most of the δ electrons and meson-linked background by applying a cut on the angle between the μ^+ track and the vertex-to-first cluster direction, as shown on Figure 4.60. The nature of the particle linked to the energy deposition of the first cluster in time is discriminated according to the following categories:

Signal Energy deposited by a primary neutron (by interacting with a proton for instance)

Signal induced Energy deposited by a neutron that acquired kinetic energy from an interaction with a primary neutron

δ **electron** Energy deposited by a δ electron from a muon track

Primary proton Energy deposited by a primary proton

Background neutron Energy deposited by a neutron that was neither created in the primary interaction nor created by a primary neutron

Background other Energy deposited by other kind of particles, such as mesons

Applying a cut of 30° on the angle between the vertex-to-cluster direction and the μ^+ allows to increase the selection purity from 69 % to 81 % with a loss of only 2 % of signal.

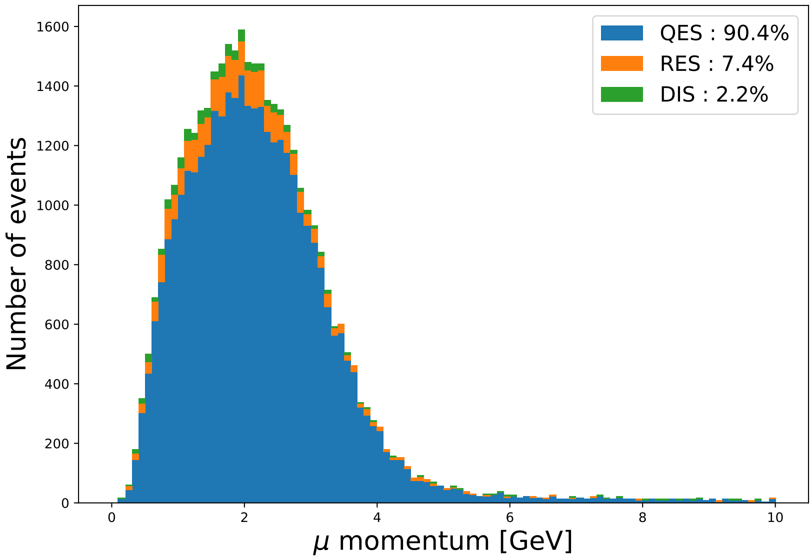

Figure 4.59: Stacked plot of the μ energy distribution after the preselection of CC0π events for the different processes.

Furthermore, an additional selection can be made by requiring a minimal distance between the $\bar{\nu}$ vertex and the earliest cluster in order to select a subset of events with neutrons that travel a sufficient distance for the energy reconstruction by ToF to be precise enough. Indeed, the spatial resolution is fixed by the cube size (1.5 cm) and does not depend on the lever-arm, so that, selecting larger lever-arm events allows to obtain a smaller relative error on the lever-arm. The lever-arm distributions for the different backgrounds and the signal are shown in Figure 4.61. The effect is similar for what concerns the time-of-flight that has a fixed error of around 1 ns, mostly due to the electronics time resolution, independent of the time-of-flight or lever-arm. Estimating the impact of the time resolution on the analysis results is important to optimize the design of the electronics and is one of the aim of this study.

Selecting events with larger lever-arm allows to improve both the relative resolution on the lever-arm and time-of-flight, thus improving the resolution on the β and the neutron energy measurement. This is demonstrated in Figure 4.62 that shows how the resolution on the neutron energy varies as function of the lever-arm cuts. Moreover, we can see that the impact of the time resolution on the neutron kinetic energy resolution is really relevant. This emphasises the importance of the electronics time resolution to achieve good neutron energy resolutions.

Finally an additional kinematic variable allows to select a subset of events for which the energy reconstruction is

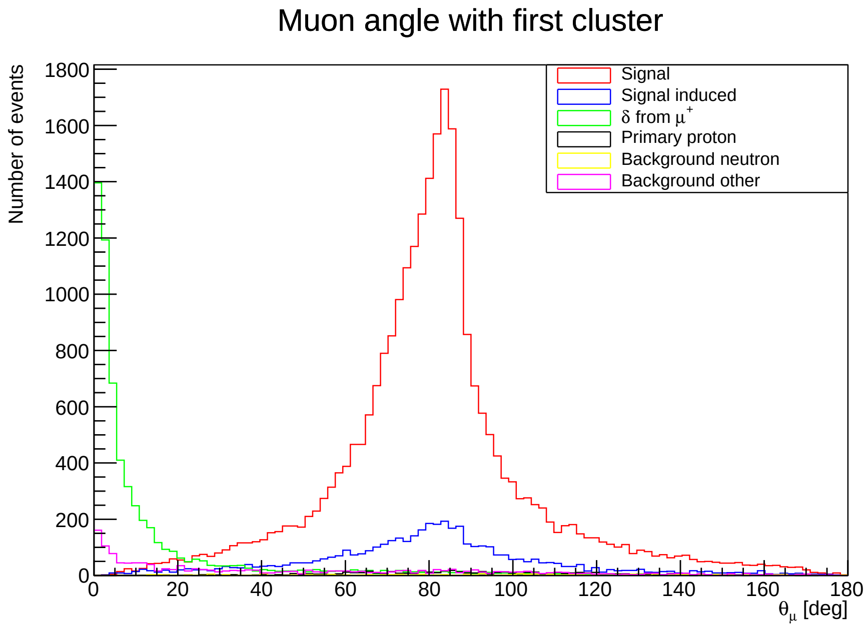

Figure 4.60: Distributions of the angular separation between the μ^+ and the first cluster in time for the different kind of particles

better controlled and, as a consequence, the anti-neutrino energy resolution improved: the transverse momentum imbalance δp_T. This variable was first introduced for this kind of analysis in Ref [109]. In the case of a CCQE anti-neutrino interaction, $\bar{\nu} p \rightarrow l^+ n$, the transverse momentum imbalance is simply defined as:

$$\delta p_T = \left| \vec{p^l}_T + \vec{p^n}_T \right| \tag{4.19}$$

where p^n and p^l are the outgoing neutron and lepton momenta respectively. The T subscript refers to the projection of the vector into the plane transverse to the incoming neutrino direction.

For an interaction on a free nucleon (the case of an hydrogen target), there is no transverse momentum imbalance in the final state. On the other hand, nuclear targets as carbon are composite particles and their nucleons are subject to Fermi motion and binding energy, thus leading to a non-zero δp_T. Furthermore, the scattering of a neutrino off a bound state of two nucleons (2p2h interactions) or the production of a pion which is re-absorbed inside the nucleus (because of FSI) are examples of inelastic scattering with no reconstructed meson in the final state. In these events, the unseen nucleon in the case of 2p2h or absorbed pion in the case of FSI carries transverse momentum that is not measured and leads to the measurement of a large δp_T. As a consequence, selecting events with low δp_T allows to enrich the selection with interactions on hydrogen for which no nuclear effect has to be taken into account in the energy reconstruction. As shown in Figure 4.63, when no

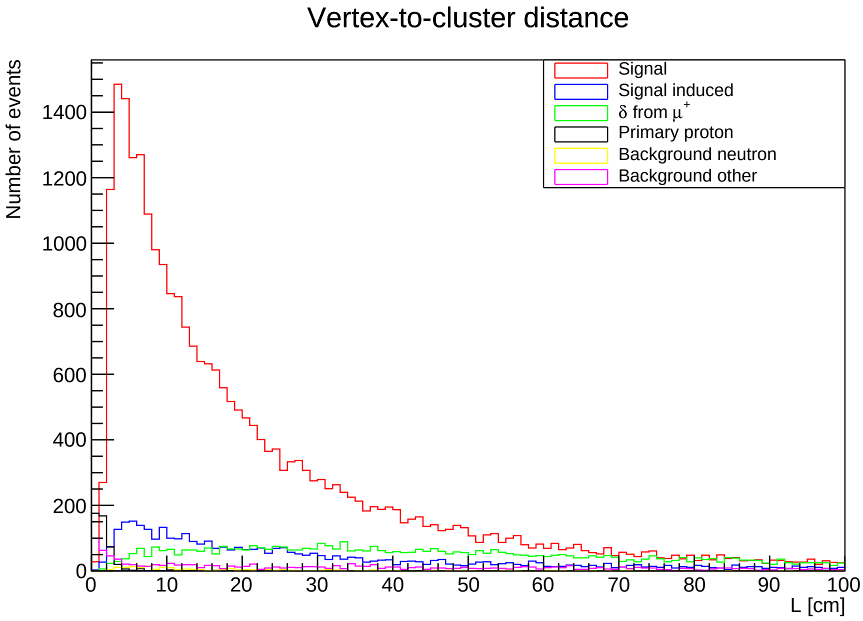

Figure 4.61: Distributions of the distance between the vertex and the first cluster for the different types of particles.

δp_T selection is made, the selected fraction of ν interactions on hydrogen is around 25 % while applying a cut on the δp_T values allows for the selection of samples enriched in hydrogen interactions. The reconstructed δp_T distributions for both hydrogen and carbon interactions are shown in Figure 4.64. Selecting only events with δp_T < 40 MeV increases the purity of the selection to 93 % and allows to have a subset enriched in hydrogen interactions (more than 60 %). As the proportions of interactions and C and H vary with δp_T, it is possible to analyze subsamples within a specific range of δp_T in order to study H or C enriched samples. This allows for different analysis and corrections to be applied on H and C interactions, using all the available interactions.

Moreover, the interactions on carbon nuclei with low δp_T value tend to be those for which the perturbations due to FSI and 2p2h are minimal. Therefore, applying a cut on δp_T allows to reject some additional events for which the primary neutron is misidentified or a meson not reconstructed given that these background events do not match the CCQE kinematic and thus have a large transverse momentum imbalance. As shown in Figure 4.65, applying even a loose cut on δp_T, such as δp_T < 400 MeV, can remove some background enhancing the selection purity from 80 % to 87 %.

Figure 4.66 shows the β distributions that are obtained with and without the cuts. It can be seen that most of the contamination is removed by the various cuts. Moreover, the wrongly selected clusters that pass the cuts are mostly secondary neutrons that are themselves children of the primary neutron. As a consequence, it can be seen that the β spectrum of these clusters is similar to the spectrum of primary neutrons. This means that if a

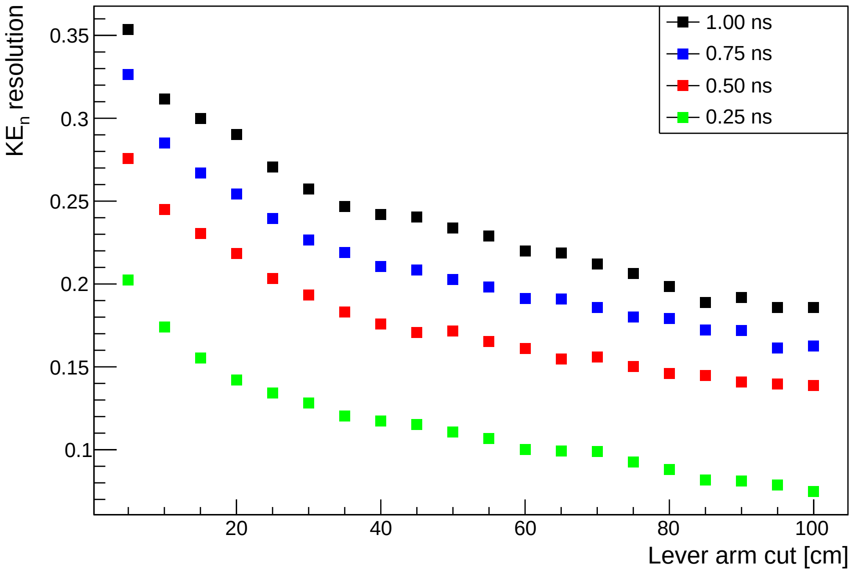

Figure 4.62: Neutron kinetic energy resolution as a function of the lever-arm cut for different time resolutions.

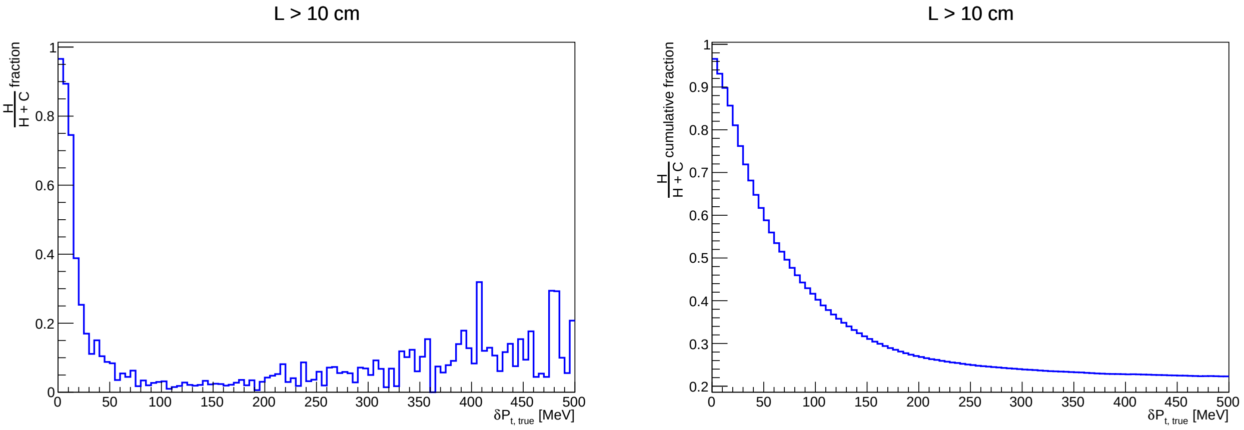

Figure 4.63: Evolution of the hydrogen ν interactions as a function of the δp_T true value (left) with the corresponding cumulative distribution (right).

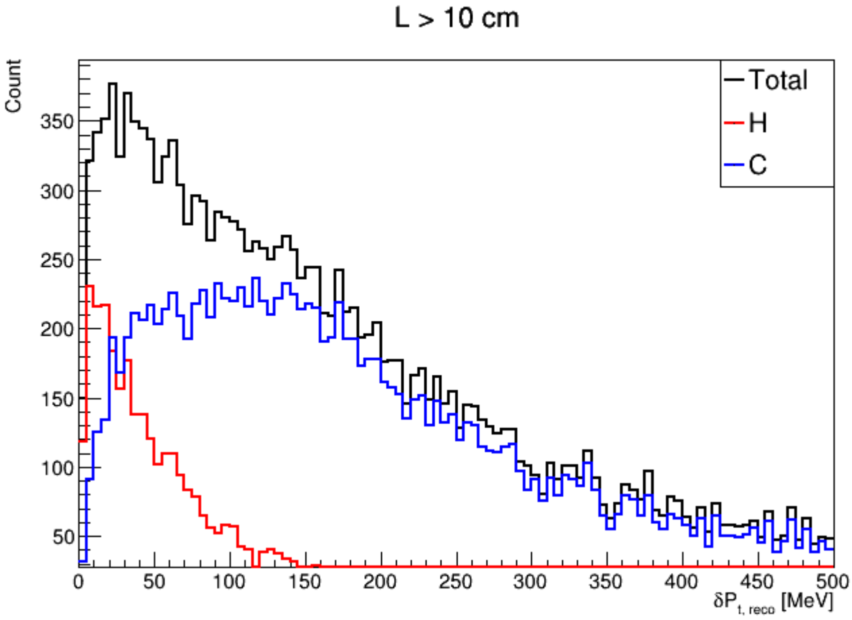

Figure 4.64: Reconstructed δp_T distributions for interactions on Hydrogen and Carbon

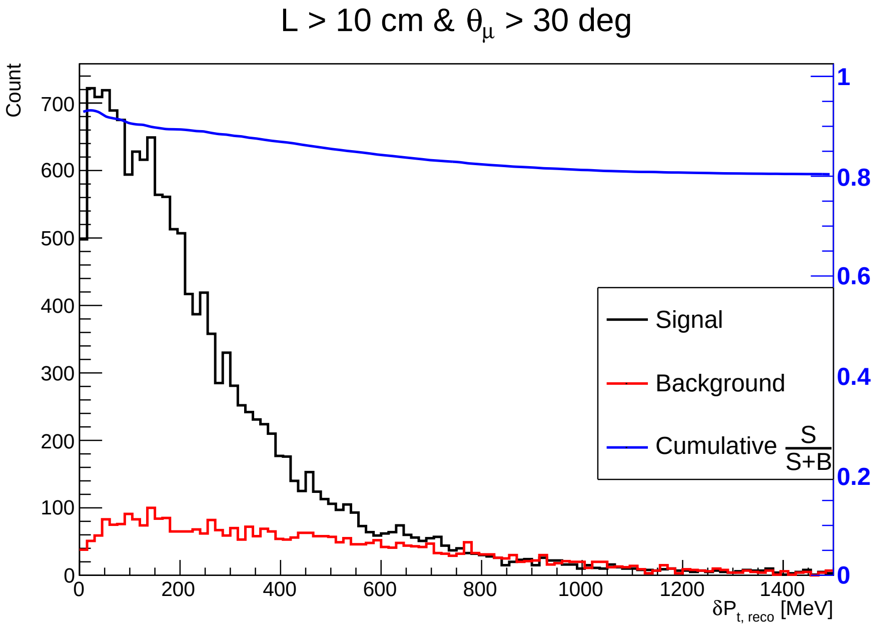

Figure 4.65: Signal and background distributions as a function of reconstructed δp_T.

mis-selection is made, it consists most of the time in the selection of a children particle of the primary neutron that leads to the reconstruction of a β value similar to that of its parent. The efficiencies of the cuts are shown for various variables in Figure 4.67. We can see that the efficiencies, once all the cuts added, seem to be relatively independant of the kinematics variables.

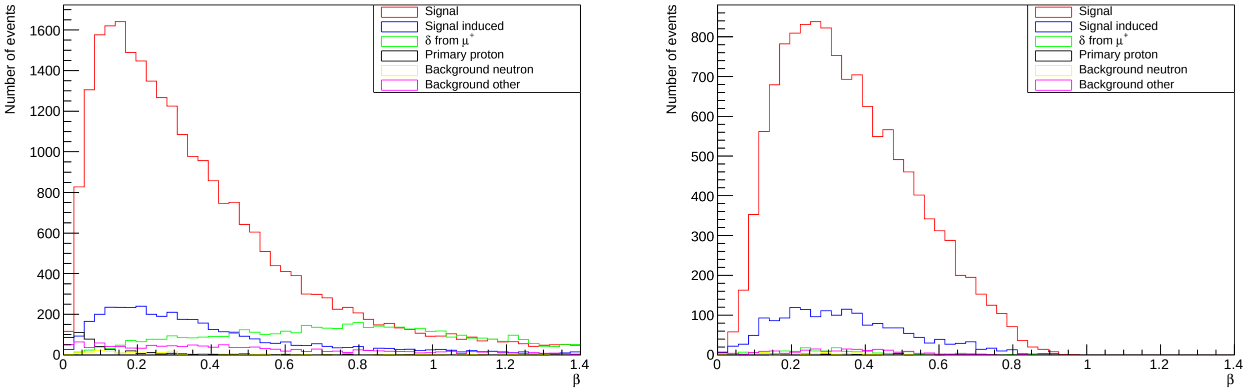

Figure 4.66: Measured β distributions of the first cluster in time considering all the events (left) or only those passing the $L < 10\,\text{cm}$, $\theta_\mu < 30°$ and $\delta p_T < 500\,\text{MeV}$ cuts (right).

The effects on the different resolutions leading to the estimation of the primary neutron energy are shown in Figure 4.68. It can be seen that the selection that helps to improve the energy resolution the most is the δp_T selection. In Figure 4.69, we can see the neutron energy resolution after the cuts showing a resolution of about 20 %.

In summary, we apply the following selection cuts:

1. We make sure that the reconstructed charged tracks are coherent with a CC0π interaction: reconstruction of a μ^+ particle with no additional reconstructed charged track.

2. We select the first cluster in time assuming that it corresponds to the first interaction of the primary neutron inside the detector.

3. We apply cuts in order to remove as much as possible the events for which the first cluster in time does not correspond to the interaction of a primary neutron: $L > 10\,\text{cm}$, $\theta_\mu > 30°$ and $\delta p_T < 40\,\text{MeV}$. The cut on δp_T will be varied in the following in order to evaluate its impact on the energy reconstruction.

4. The neutron momentum is estimated from the measured lever-arm and time-of-flight.

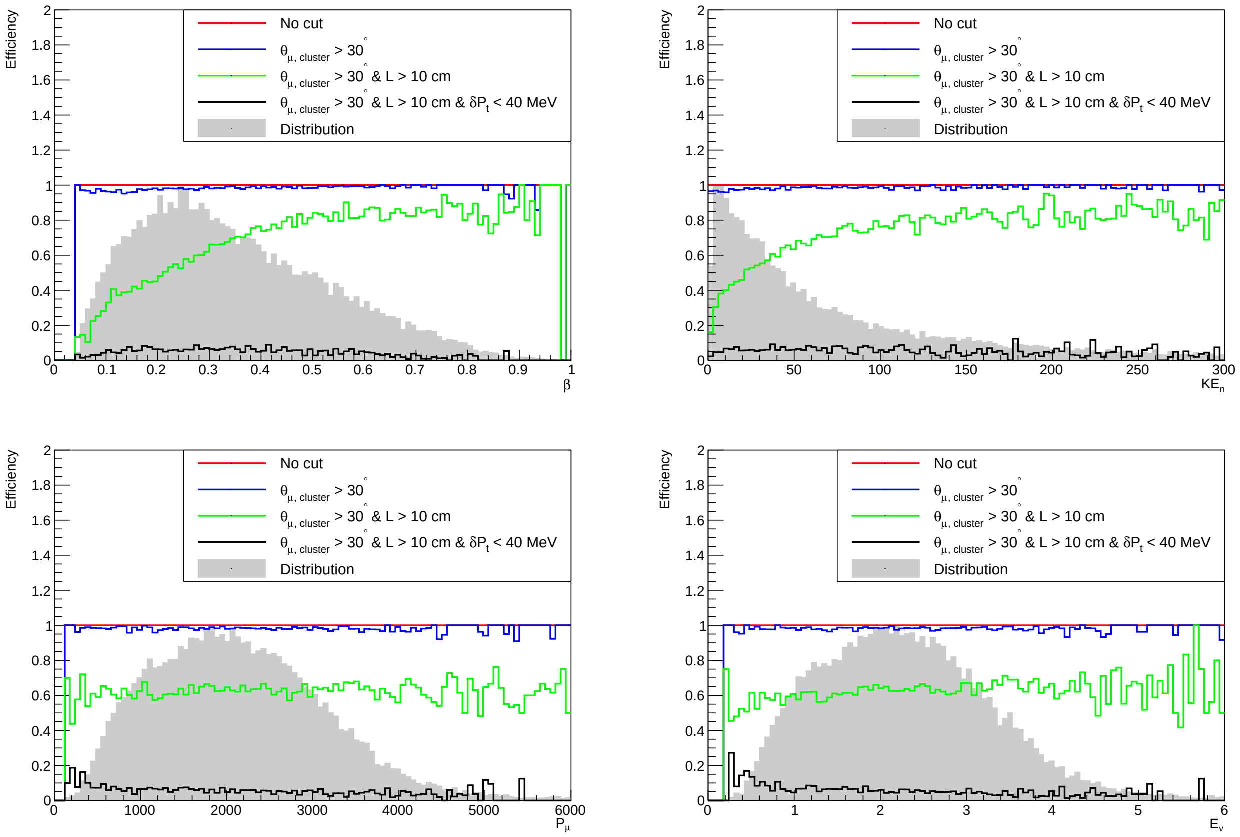

Figure 4.67: Efficiencies of the different cuts as a function of the different variables.

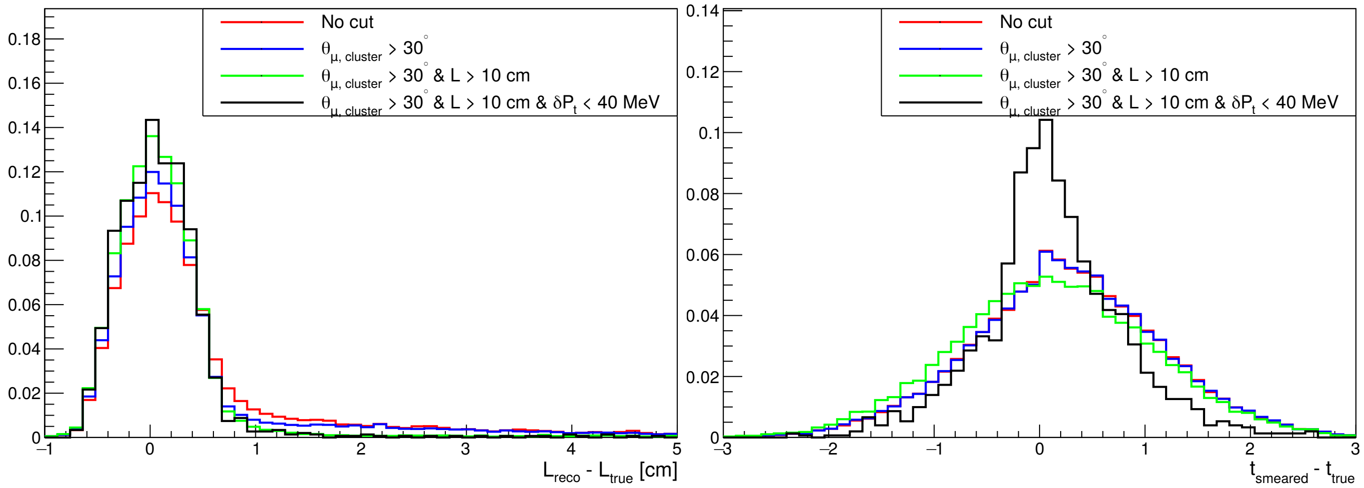

(a) Lever-arm resolution

(b) Time resolution

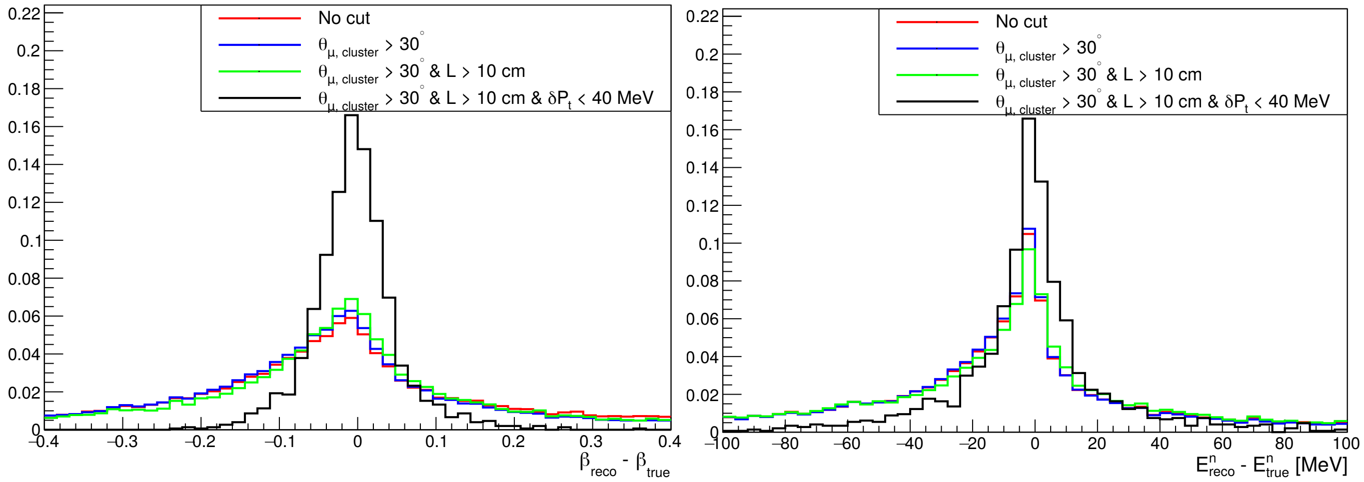

(c) β resolution

(d) Neutron energy resolution

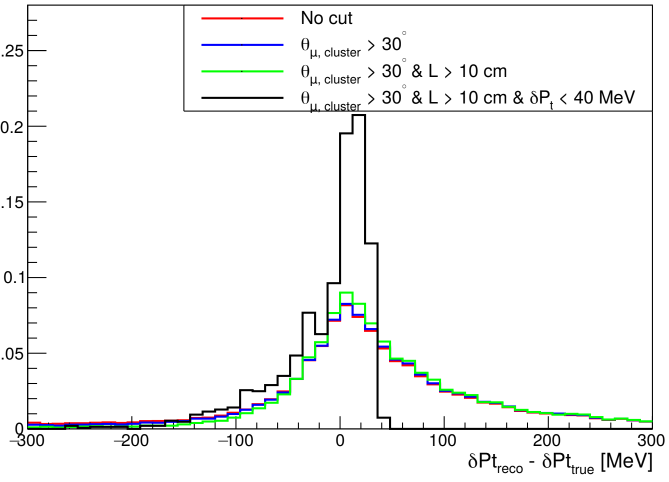

(e) δp_T resolution

Figure 4.68: Resolution normalized distributions on the lever arm and time-of-flight and their impact on the reconstructed β, neutron energy and δp_T

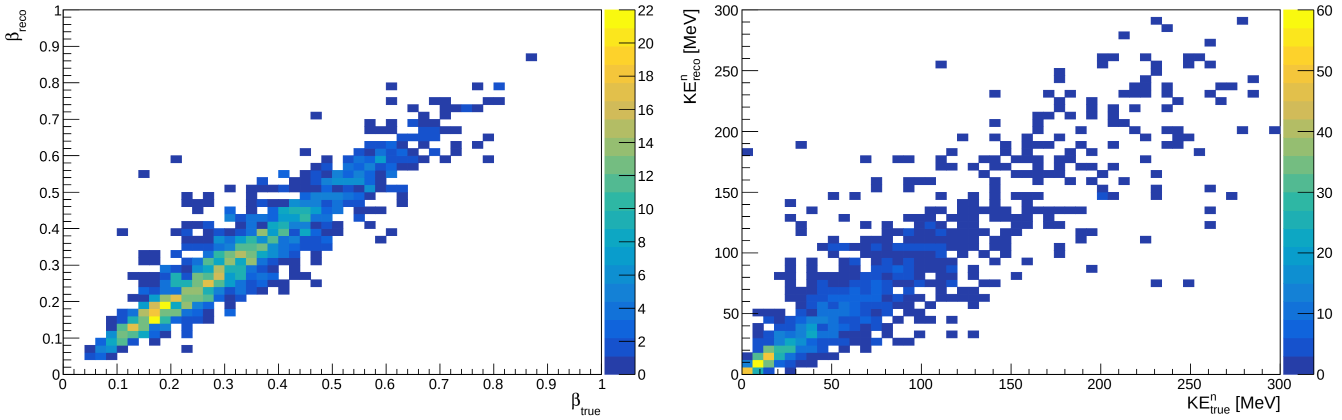

(a) β resolution

(b) Neutron energy resolution

Figure 4.69: β and neutron energy resolutions after applying all the cuts

4.8 Impact of neutron detection on neutrino energy resolution

We study how the detection of the primary neutrons, with the performance shown previously, allows to improve the neutrino energy measurement. This study focuses on the detection of neutrons in CCQE-like channel, for anti-neutrinos, given that this is the simplest interaction channel to study. However, the detection of neutrons can obviously also be very useful to better reconstruct the neutrino and anti-neutrino energy for all the interaction channels.

The following assumptions are made:

- the PID of charged particles is supposed to be perfect given the performances of 3DST ;
- a muon momentum resolution of 4 % is applied manually. This resolution is chosen conservatively given the typical momentum resolutions reachable by spectrometers that would be placed around 3DST as demonstrated in Section 4.6 ;
- an angular resolution of 1° is applied for the azimutal and polar angles of the muon as demonstrated in section 4.6 ;

For CCQE interaction of anti-neutrinos, it is possible to rely on the μ^+ kinematics alone in order to compute

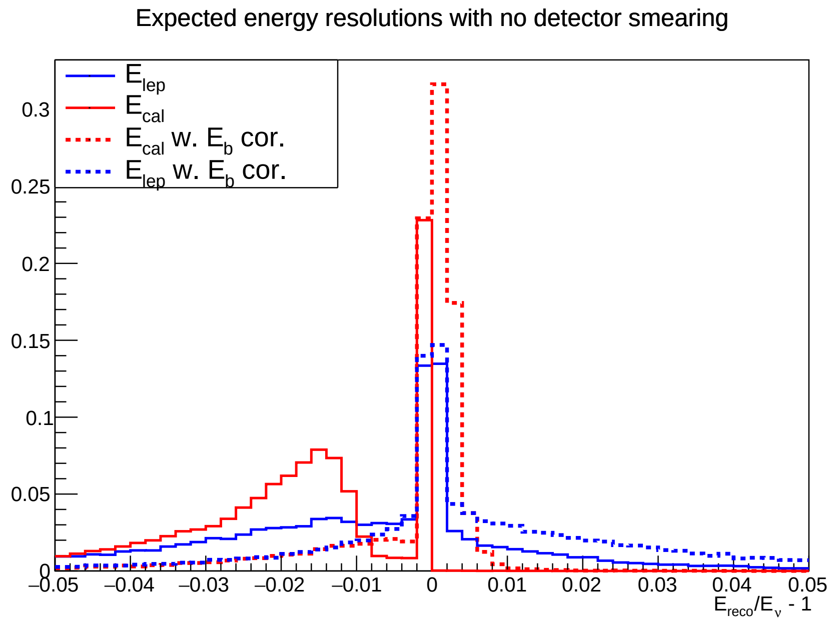

Figure 4.70: Expected neutrino resolutions for the two reconstruction methods assuming no detector smearing. Additional dashed curves show the obtained results if the binding energy (E_b) is accounted for in the reconstruction of C interactions.

the $\bar{\nu}$ energy:

$$E_{\bar{\nu}}^{\text{lep}} = \frac{m_n^2 - m_p^2 - m_\mu^2 + 2m_p E_\mu}{2\left(m_p - E_\mu + p_\mu \cos\theta_\mu\right)} \tag{4.20}$$

where m_n, m_p and m_μ are the masses of the neutron, proton and muon respectively whilst E_μ, p_μ and θ_μ are the energy, momentum and angle of the outgoing μ^+. This formula is exact only in the case of a pure Quasi-Elastic interaction on a free proton (hydrogen interaction) but underestimates or overestimates the anti-neutrino energy in presence of Fermi momentum and binding energy. This can be clearly seen on Figure 4.70 that shows the energy resolution with no detector smearing where there is a peak at zero corresponding to a perfect resolution for hydrogen interactions surrounded by a wide distribution due to Fermi momentum smearing. The second distribution, due to interaction on C, is shifted from 0 because the binding energy of the nucleon (E_b) is not taken into account in the reconstruction formula. A dashed line shows the obtained result if the ν interactions on carbon are corrected for E_b. Figure 4.71 shows the resolutions on E_ν using Equation 4.20 and the associated mean and RMS values are given in Table 4.5. Applying a cut on δp_T decreases the magnitude of the tail that corresponds to an underestimation of the anti-neutino energy mostly due to 2p2h and FSI. This shows that the information that the neutron brings on the event topology through the δp_T variable allows to improve the energy resolution even without using the neutron energy in the formula for the reconstruction of the neutrino energy.

Detecting the primary neutron of the anti-neutrino interaction, allows to estimate the anti-neutrino energy

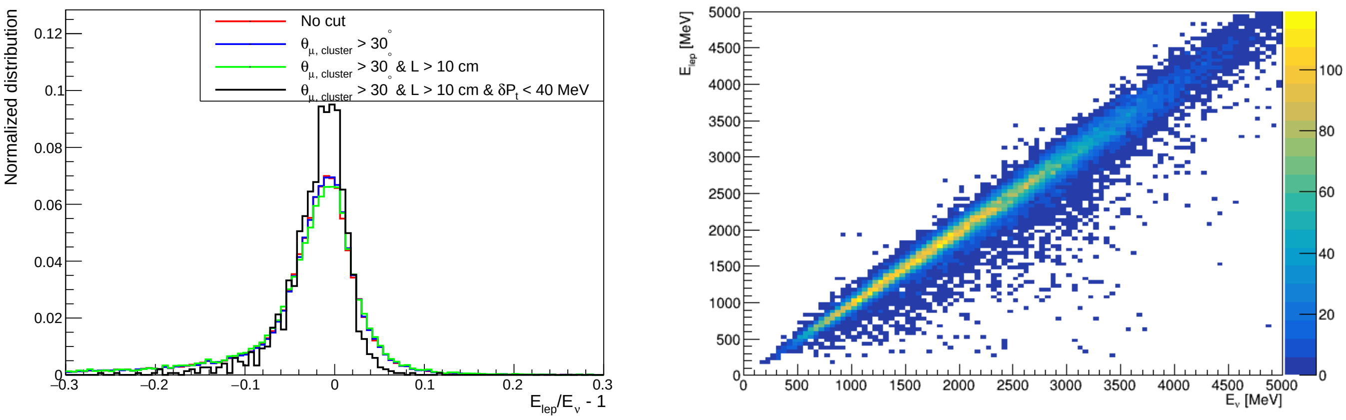

Figure 4.71: $E_{\bar{\nu}}^{\text{lep}}$ resolution

Table 4.5: Evolution of $E_{\bar{\nu}}^{\text{lep}}$ resolution with the successive cuts.

Additional cut	Mean	RMS
No cut	−2.8 %	7.2 %
Angle with muon	−2.7 %	7.1 %
Distance to vertex	−2.7 %	7.1 %
δp_T	−2.0 %	4.0 %

by using a complete measurement of the total energy in the final state:

$$E_{\bar{\nu}}^{\text{cal}} = E_\mu + E_n - m_p \tag{4.21}$$

where m_p is the proton mass whilst E_μ and E_n are the muon energy and neutron energy measured from their momentum and ToF respectively. As shown on Figure 4.70, when no detector smearing is considered, the calorimetric energy reconstruction displays a better resolution than the reconstruction without neutron thus demonstrating the usefulness of a detector able to reconstruct neutrons. The shift in energy of the C distribution is more visible in the $E_{\bar{\nu}}^{\text{cal}}$ reconstruction since it is a permanent underestimation of the ν energy while it is smeared in the $E_{\bar{\nu}}^{\text{lep}}$ reconstrution. Correctly accounting for E_b solves this. Figure 4.72 shows the obtained resolutions using this $E_{\bar{\nu}}^{\text{cal}}$ estimation of the neutrino energy and the associated mean and RMS values are given in Table 4.6. We can see that once again the various selections allow to improve the neutrino energy estimation.

For all the selected events, the anti-neutrino energy is reconstructed using the two formulas (4.20) and (4.21). The result of the anti-neutrino energy resolution after applying a cut on δp_T is given in Figure 4.73. It can be seen that both reconstruction methods give very similar result with an energy resolution around 4.5 %.

Furthermore, the impact of the δp_T cut value and of the time resolution of the detector on the final neutrino

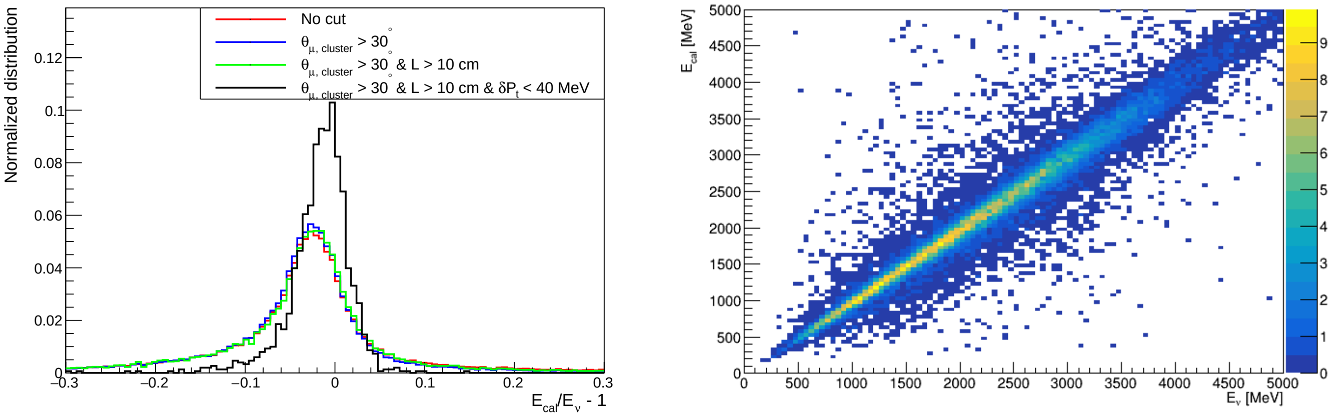

Figure 4.72: $E_{\bar{\nu}}^{\text{cal}}$ resolution

Table 4.6: Evolution of $E_{\bar{\nu}}^{\text{cal}}$ resolution with the successive cuts.

Additional cut	Mean	RMS
No cut	–3.4 %	10.0 %
Angle with muon	–3.3 %	9.9 %
Distance to vertex	–2.8 %	9.9 %
δp_T	–1.8 %	3.5 %

energy resolution has been studied and the results are presented on Figures 4.74 and 4.75. Figure 4.74 shows that for a time resolution of 0.5 ns or lower, the E_{cal} estimator performs better. This improvement in resolution is only noticeable for the calorimetric estimation of the energy because it directly impacts the uncertainty on the time-of-flight of the neutron that is used in order to estimate its kinetic energy. Imposing stricter δp_T cuts allows to improve the neutrino energy resolution for both E_ν reconstruction methods with a slightly largr improvement seen in E_ν^{cal}.

The energy resolution is not the only parameter to take into account in order to assess the performances of such a detector. It is also necessary to check that the reconstructed neutrino energy spectrum is not distorted and that no bias was introduced in the reconstructions procedure. For such a detector to be installed as a near detector for a long baseline neutrino oscillation experiment, it is crucial to be able to reconstruct the full neutrino spectrum without introducing any distortion in order to characterize the neutrino energy flux. Figure 4.76 shows that the energy reconstruction procedure presented here does not distort the reconstructed neutrino energy spectrum in any way and that the type of event (H or C interaction) has no impact on the shape of the reconstructed spectrum with χ^2 test p-values above 0.2 for both cases.

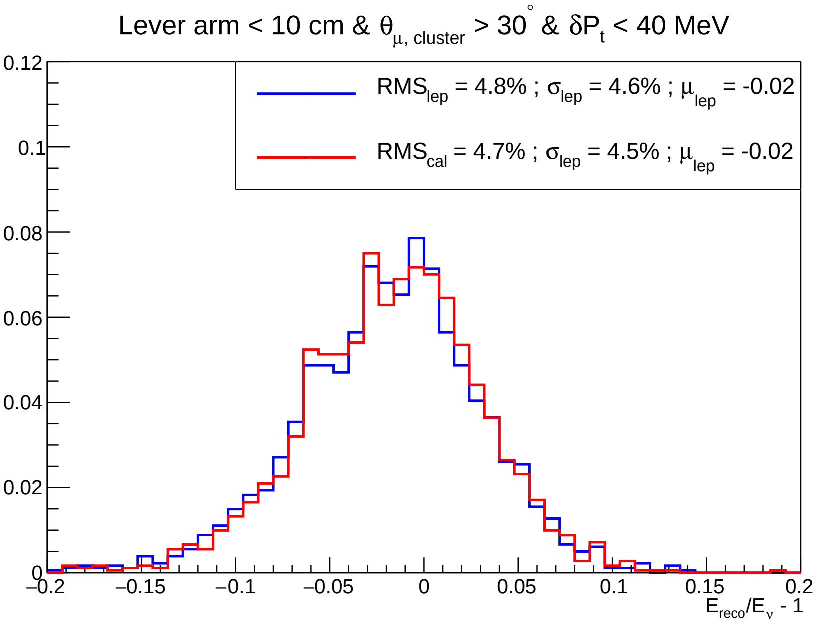

Figure 4.73: Obtained resolution on the interacting anti-neutrino with the two different formulas for $\delta p_T < 40\,\mathrm{MeV}$

4.9 Conclusion

The conducted studies on both the 3DST and TPC detectors are important in order to define their design for the SAND near detector of DUNE. These studies prove that the proposed designs for the TPC were consistent with the SAND requirements both in term of acceptances and resolutions. The impacts on the TPC performances of the electronics time response and the pad size have been studied. Moreover, the known inhomogeneities of the KLOE magnetic field have been considered and we ensured that they affect the TPC performances to acceptable levels.

The studies conducted on the 3DST allowed to tune the cube granularity and the time resolution to achieve the best physics performances. We showed that the timing resolution was a crucial parameter for what concerns the measurement of the neutron energy, and that improving it could significantly improve the final resolution on the neutrino energy. Moreover, it was showed that a multidimensional analysis in the δp_T vs $E_{\bar{\nu}}^{\mathrm{cal}}$ could be conducted in order to select specific samples enriched in C or H interactions. We focused for this study on the QES channel where the neutron selection is more easy to achieve. This is also the channel where $E_{\bar{\nu}}^{\mathrm{lep}}$ performs the best. Therefore, the improvement in neutrino resolution using the neutron information was limited. Here we used QES as a case study to evaluate the performance of the detector and optimize the design. However, for all the other channels that will be dominant for DUNE, the importance of reconstructing the neutrons for a full

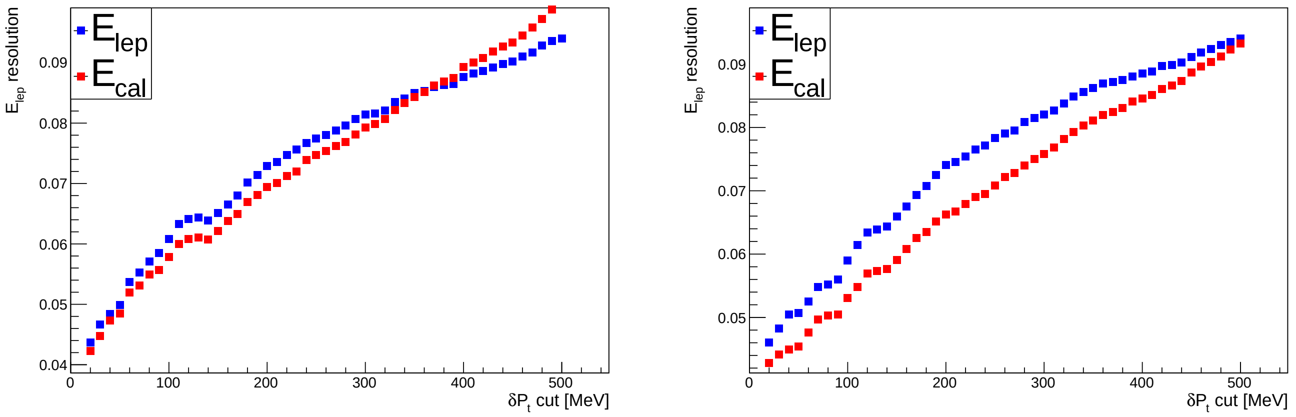

(a) Time resolution: 0.5 ns

(b) Time resolution: 0.25 ns

Figure 4.74: Evolution of the resolution on the reconstructed $\bar{\nu}$ energy as a function of the δp_T cut for two different time resolutions

calorimetric measurement of the neutrino energy will be even more important.

Despite the numerous qualities of the proposed inner tracker design, SAND made the choice of an other technology for financial reasons. However the developed studies stay relevant to demonstrate how suitable and flexible this detector design is also at higher rate and allows targeting better precision in future experiments.

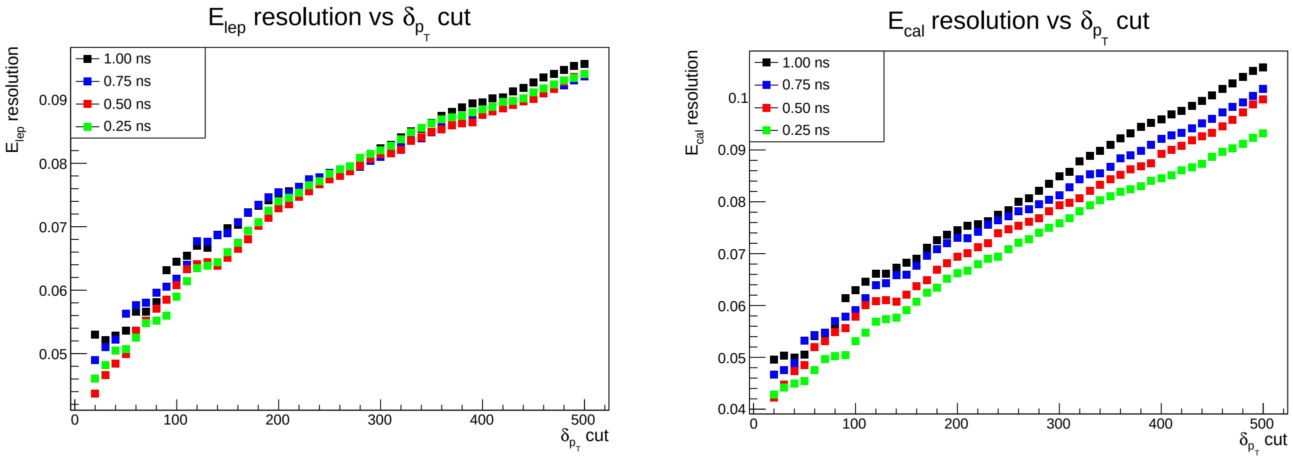

(a) $E_{\bar{\nu}}^{\text{lep}}$ resolution

(b) $E_{\bar{\nu}}^{\text{cal}}$ resolution

Figure 4.75: Evolution of the resolution on the reconstructed $\bar{\nu}$ energy as a function of the δp_T cut for different time resolutions

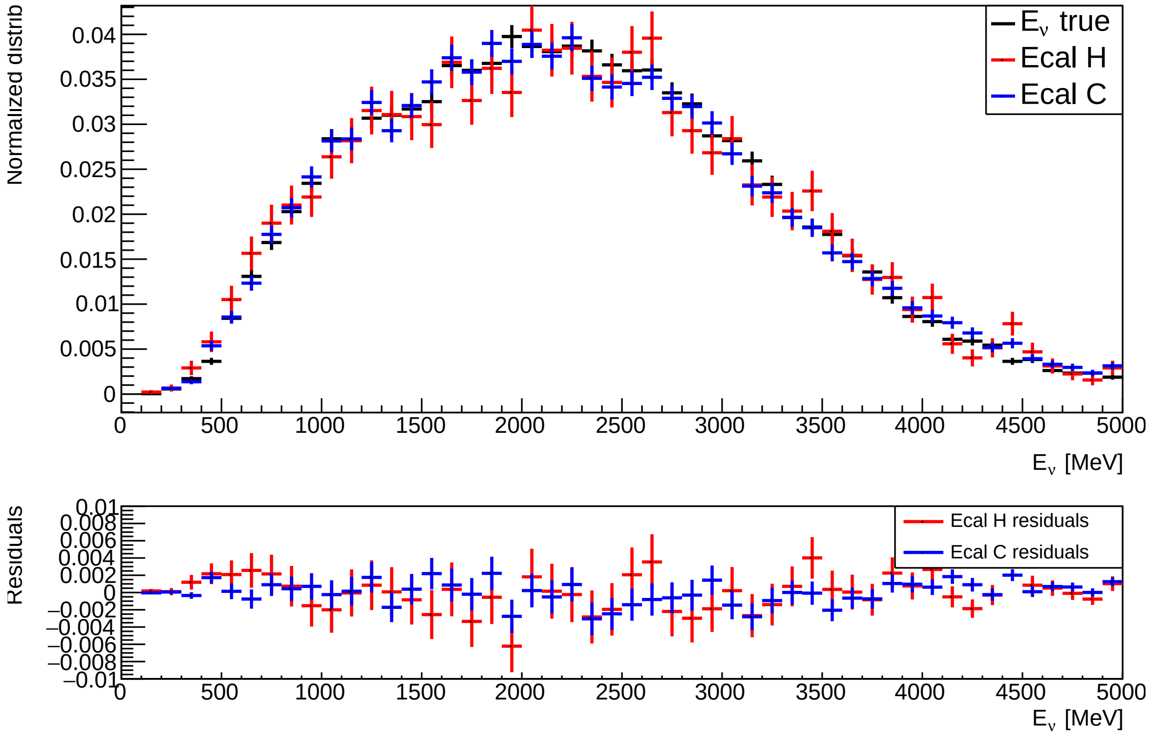

Figure 4.76: Reconstructed neutrino spectra and difference with the true one

Conclusion

The discovery neutrino oscillations have opened a new field in particle physics. This observation is so far the only experimental evidence of massive neutrinos, and thus the first indication of physics beyond the Standard Model. In the last decades, this field has seen immense progresses with the determination of all the mixing angles and mass-square differences. Two main unknowns however remain: the determination of δ_{CP} that could lead to the observation of CP-violation in the lepton sector, and the establishment of the correct mass hierarchy that would constrain multiple theories trying to explain the neutrino masses. Measuring these parameters requires new high precision long baseline neutrino experiments with powerful beams and large active volumes. TPCs are tracking detectors that have been extensively used in particle physics experiments, and the next-generation TPCs can be great detectors for the challenges of precision measurements in the field of neutrino oscillations. DUNE is one of these next-generation experiments and it made the choice of using TPCs as detectors both for the near and far detectors.

The promising LArTPC-DualPhase technology was considered as an option to instrument part of the far detector modules, as it had shown impressive gain results on small-scale prototypes. A large-scale prototype, ProtoDUNE-DualPhase, was built at CERN in order to evaluate the feasability of this technology at large scale and assess its performances. Several issues were encountered during the operations of this prototype that did not allow for stable operations. In these conditions, the DualPhase technology could not be completely demonstrated. The high purification of the liquid argon (lifetime $> 3\,\mathrm{ms}$) and the possibility to obtain signal amplification with the LEMs have however been demonstrated by my studies on the gains and electron lifetime with cosmogenic muons. In order to limit the possible stability risks introduced by the DualPhase technology, the choice was made by the DUNE collaboration to shift to the so-called Vertical Drift design with immersed 2D anodes without extraction and amplification.

The SAND near detector of DUNE will precisely measure the neutrino flux on the beam axis. An inner tracker design composed of a finely grained 3D scintillating target surrounded by three TPCs instrumented with resistive

MicroMegas was proposed. I could demonstrate the adequation of the proposed TPC design with the DUNE beam flux, as well as their impressive momentum resolution (largely better than the requirements). Moreover I demonstrated the innovant neutron detection capabilities of the 3DST, as well as, their beneficial impact on the reconstruction of the neutrino energy. The combination of these two new technologies would have allowed for a precise monitoring of the DUNE neutrino beam, however, another design was prefered for financial considerations.

Despite the specific choices made by the DUNE collaboration, in this thesis I could demonstrate the invaluable role that TPCs will keep playing in the study of neutrino oscillation in long-baseline accelerator-based neutrino experiments. Both such type of experiments and the TPC technology have a bright future and the investigation of innovative solutions, like the dual-phase LArTPC or the resistive MicroMegas are of important value to shape such future.

Appendix A

Application of the $\vec{\mathrm{E}} \times \vec{\mathrm{B}}$ simulation to DESY test beam

In order to test the resistive MicroMegas technology for the ND280 High-Angle TPC, test beams have been conducted. Among these, tests were conducted at the DESY beam with a small TPC embedded in a solenoid allowing to reach a magnetic field of 1 T. It directly appeared in the data that a large $\vec{\mathbf{E}} \times \vec{\mathbf{B}}$ was present, modifying the drift of the electrons in the TPC. The main visible effect in the data was the reconstruction of tilted tracks in the anode plane whereas the beam was aligned along the pad lines. This apparent tilt angle was measured and depends on the magnetic field nominal value, as shown in Figure A.1. This evolution of the tilt angle with the nominal magnetic field value can be explained by looking back at the Langevin equation (4.13). Indeed, as $\left\|\vec{\mathbf{B}}\right\|$ increases, $\omega\tau$ also increases and the term colinear to the magnetic field becomes dominant over the $\vec{\mathbf{E}} \times \vec{\mathbf{B}}$ term. The apparent tilt angle is mostly due to the $\vec{\mathbf{E}} \times \vec{\mathbf{B}}$ term, and is therefore more important for intermediate values of the nominal magnetic field.

As the magnetic field of the DESY electromagnet had been previously mapped, I attempted to apply the previously developed method in order to simulate the $\vec{\mathbf{E}} \times \vec{\mathbf{B}}$ effect and reproduce the DESY data. The geometry of the DESY test beam setup is shown in Figure A.2, with electric and magnetic fields oriented along the Z axis and the beam entering along X. Note that the TPC is not centered in Y. The simulated electric field is $E = 275\,\mathrm{V\,cm^{-1}}$, the drift velocity is taken as $v_d = 6.8\,\mathrm{cm\,\mu s^{-1}}$.

The mapped magnetic field for a nominal field value of 1 T is shown in Figure A.3. We can see that the radial component of the field can be relatively strong near the TPC cathode and anode with values that can be

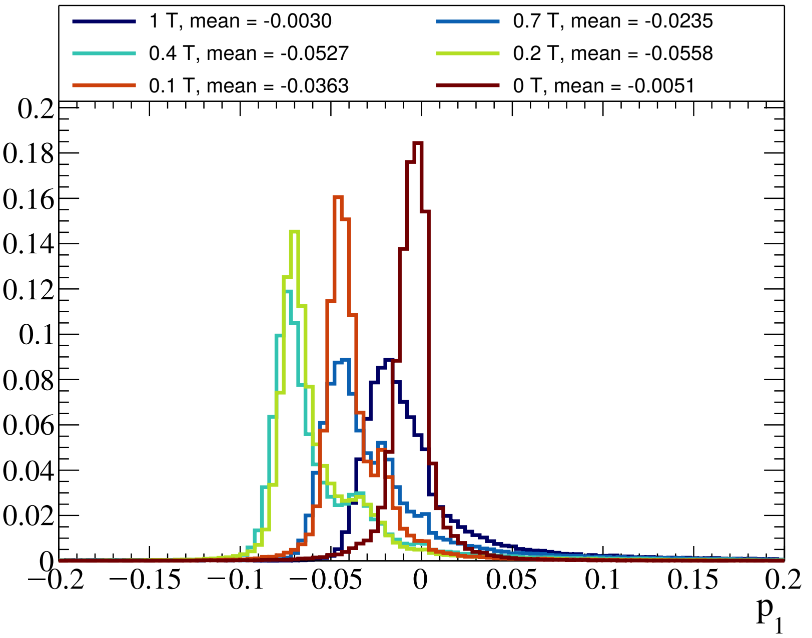

Figure A.1: Distribution of the measured tilt slope (p_1) of the tracks measured in the DESY data for different magnetic fields.

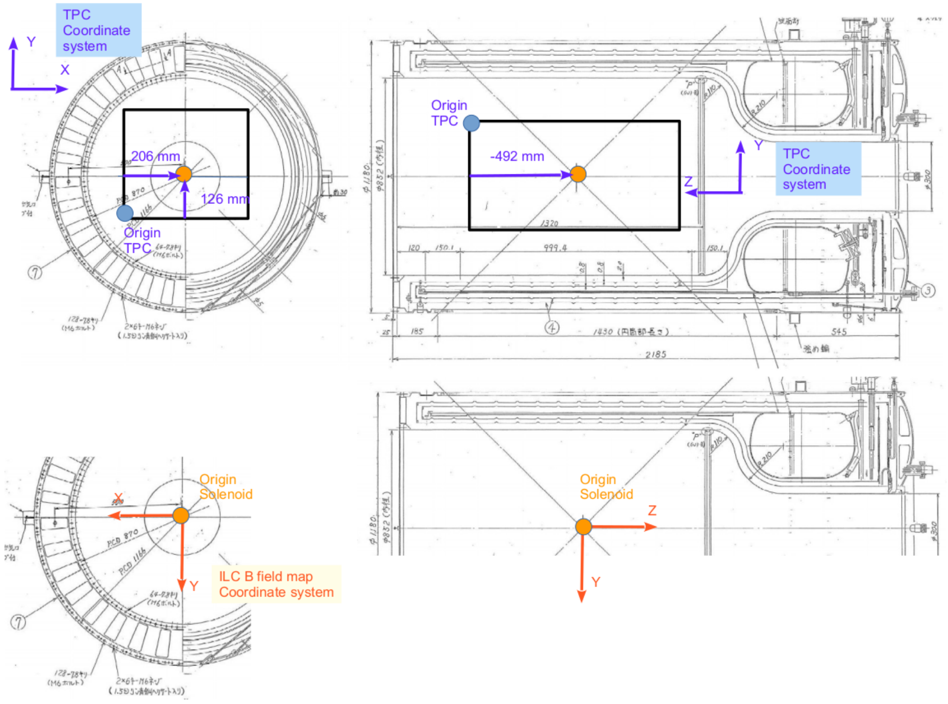

Figure A.2: Scheme of the DESY test beam setup.

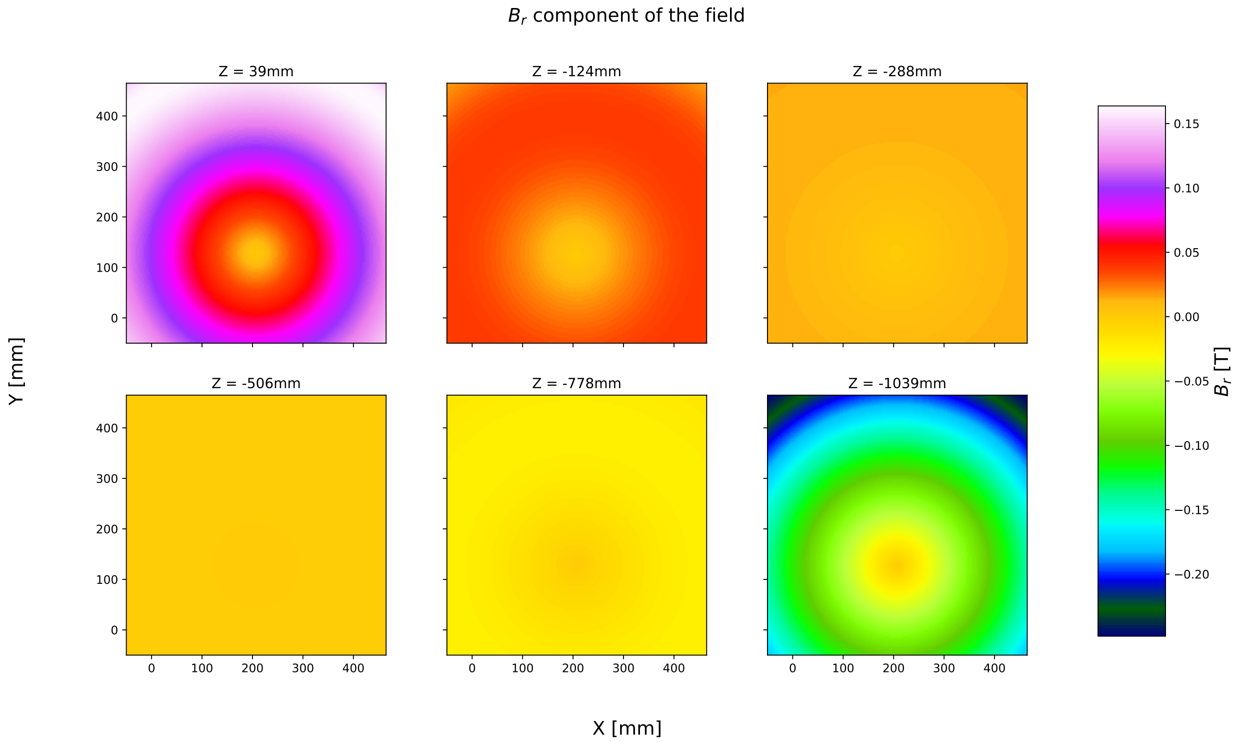

Figure A.3: Radial component of the magnetic field for different slices along the drift direction (Z) from the cathode plane ($Z = 39\,\text{mm}$) to the anode plane ($Z = -1039\,\text{mm}$).

as high as 15 $\%$ of the nominal field. One can compute the projection map corresponding to this magnetic field map for different starting positions inside the TPC. Displacement values at fixed Z are displayed in Figure A.4. We can see that the displacement is maximal for tracks in the middle of the TPC. This can be explained by the antisymmetry of the magnetic field that leads no $\vec{\mathbf{E}} \times \vec{\mathbf{B}}$ effect cancellations along the electrons drift for drift distances above half the TPC length. This was not the case in SAND simulation ad the cathode was placed in the middle of the TPC. The directions of the displacement are shown in Figure A.5 for different nominal fields. We can see that the displacement along the Y direction varies as tracks travel along the X direction, thus introducing an apparent tilt angle.

To be able to reproduce the observed test beam data, I simulated 3 GeV electron tracks entering the TPC and simulated the measured anode track for different nominal magnetic fields. The obtained results are produced in Figure A.6, where we can see the track on the anode for electrons entering around $Y = 15\,\text{cm}$. We can clearly see the apparition of a tilt angle for tracks on the anode with a maximal effect around 0.2 T to 0.4 T as observed in the data. This effect can be quantified by fitting the anode tracks with lines as it is done for the data in order to compare the obtained slopes. The measured angles depend on the Y position as it is shown in Figure A.7. Accumulating the data for all the positions, we obtain the Figure A.8. We can see that the simulated effect is

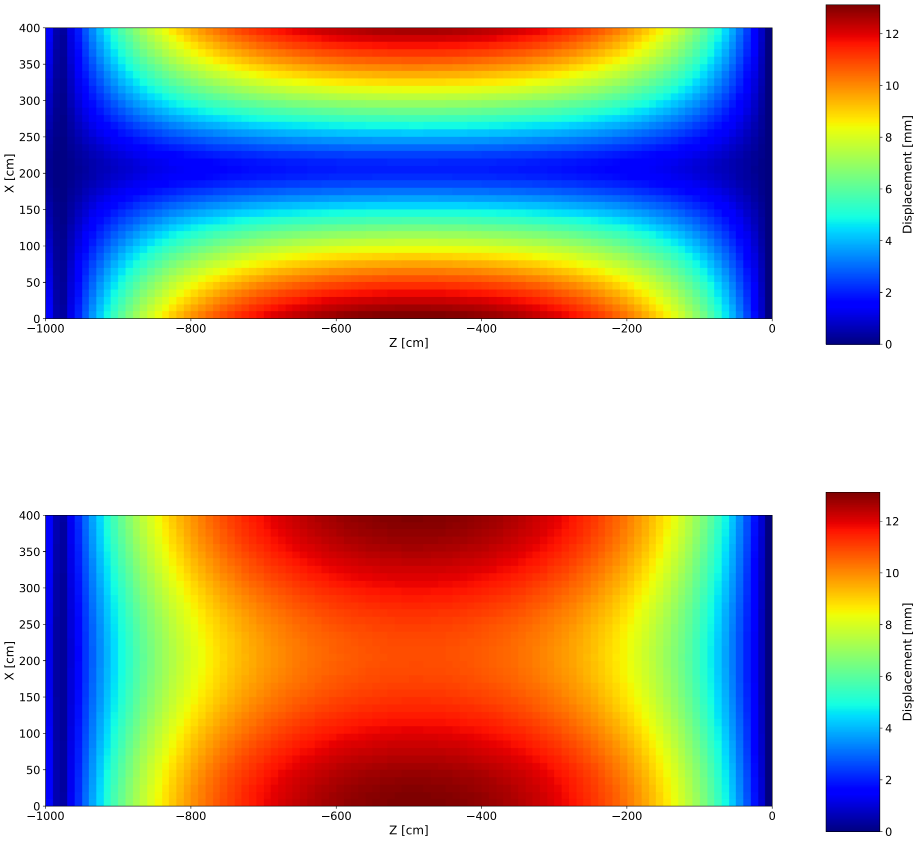

Figure A.4: Displacement maps at Y = 154 cm (top) and Y = 308 cm (bottom) for a nominal field of 1 T.

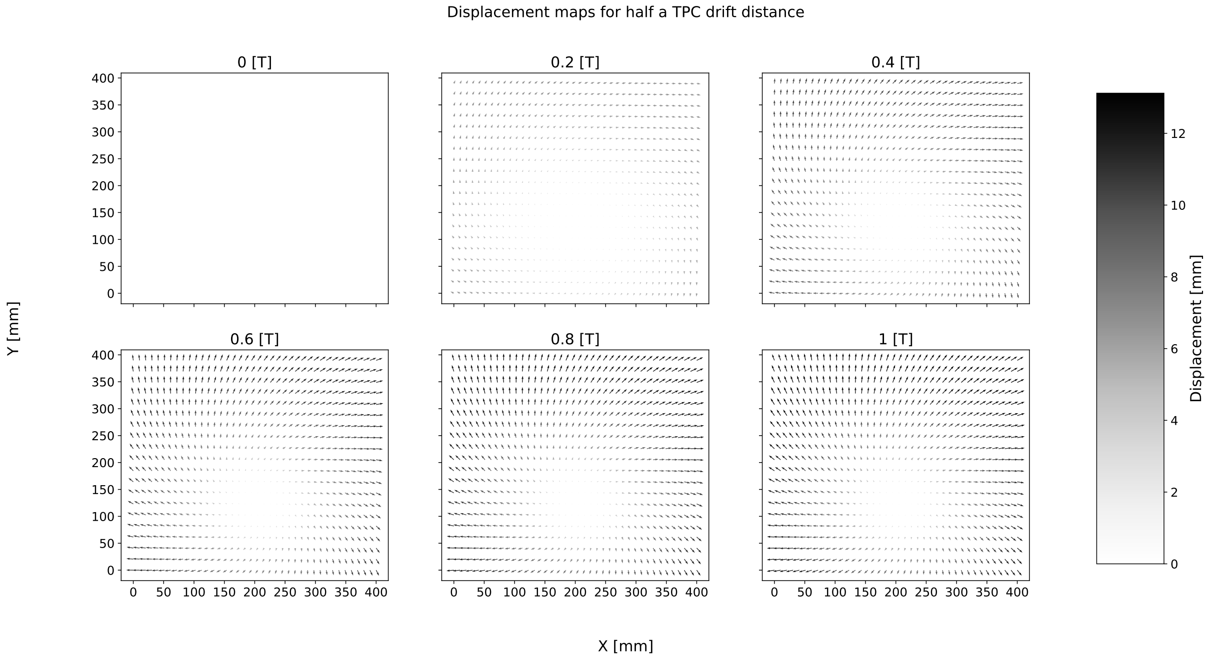

Figure A.5: Displacement maps represented with arrows for half a TPC distance for different nominal fields. The base of the arrow is the expected position on the anode for a homogenous magnetic field and its tip is the actual position with DESY magnetic field.

qualitatively in agreement with the test beam data, however, the simulation provides apparent tilt angles that are smaller with respect to what is obeserved in the test beam data. This disagreement needs to be further investigated.

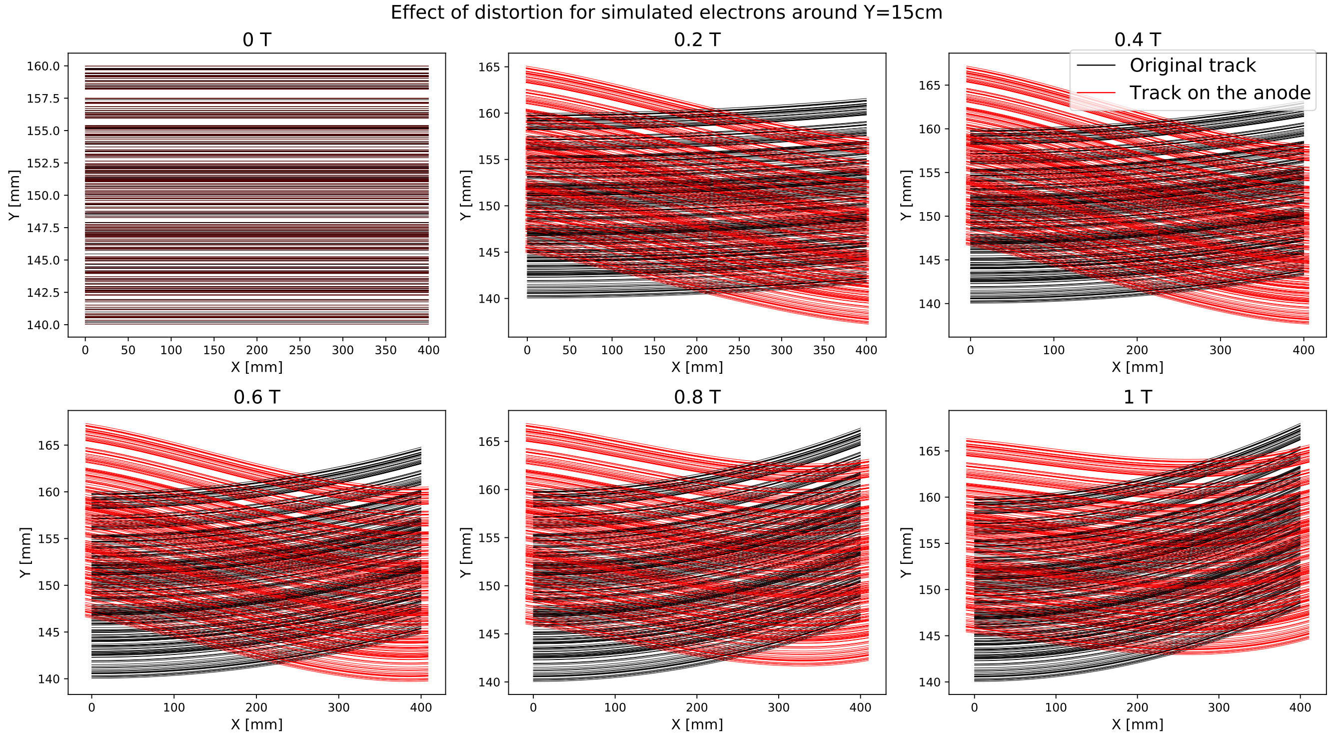

Figure A.6: Effect of the magnetic field distortions on the measured anode tracks for different nominal magnetic fields.

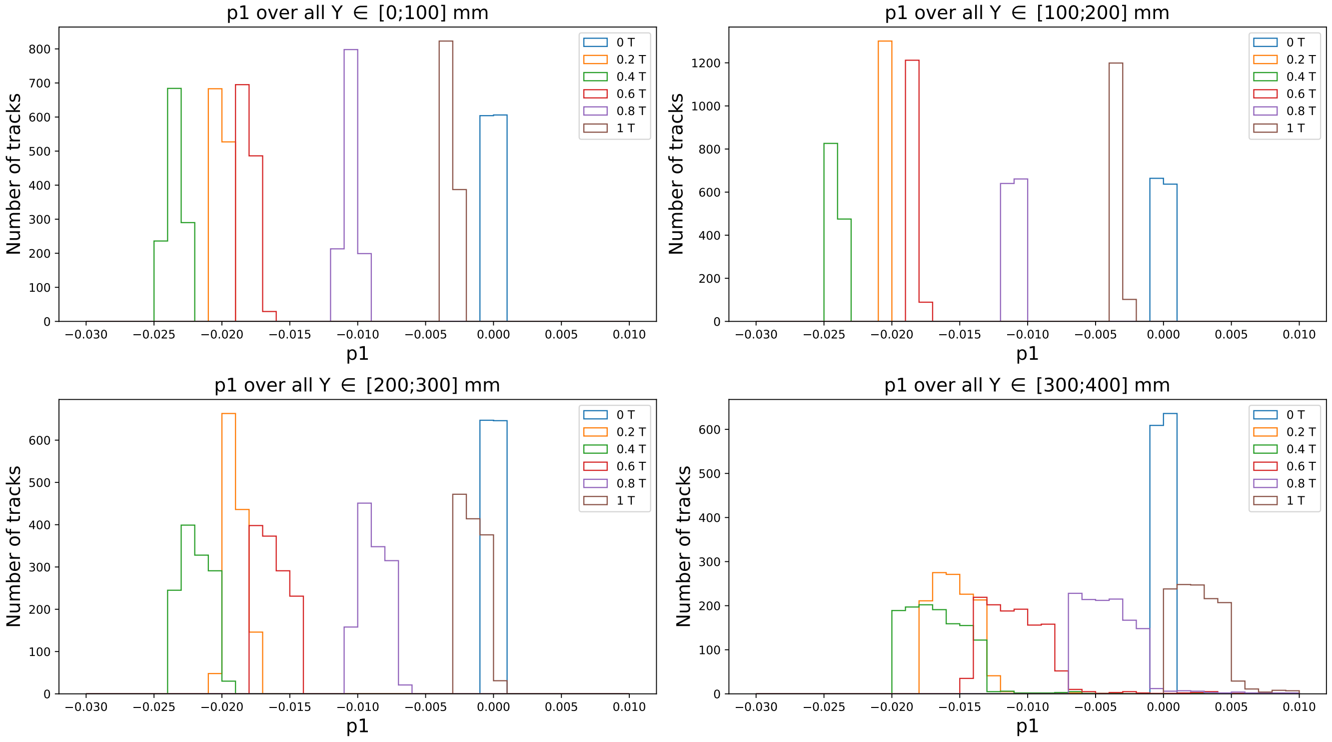

Figure A.7: Fitted slopes on simulated anode tracks for different nominal magnetic fields and Y positions.

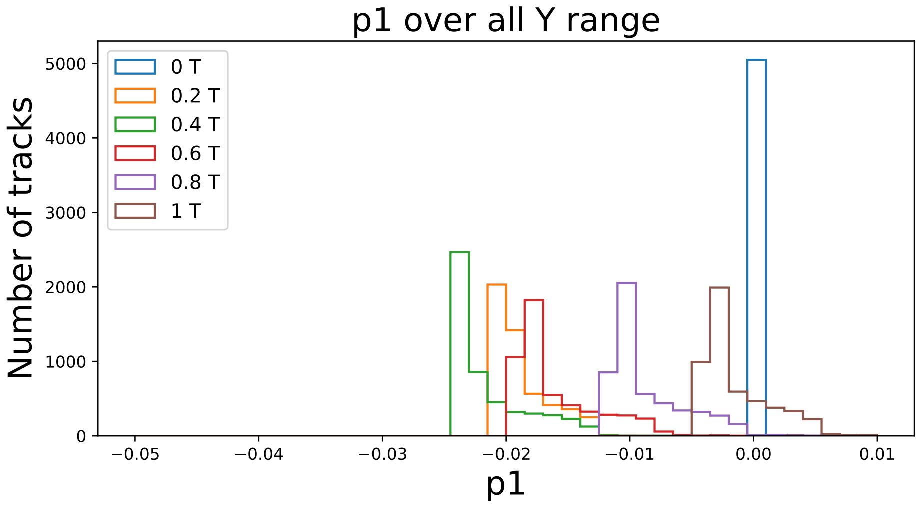

Figure A.8: Fitted slopes on simulated anode tracks for different nominal magnetic fields.

Bibliography

[1] Henri Becquerel. “Sur les radiations émises par phosphorescence”. In: *Comptes Rendus à l’Académie des sciences* (1896), pp. 420–421.

[2] Marie Sklodowska Curie. “Recherches sur les substances radiocatives”. PhD thesis. 1903.

[3] Ernest Rutherford. “Uranium Radiation and the Electrical Conduction Produced by It”. In: *Philosophical Magazine* 47 (1899), pp. 109–163.

[4] Paul Villard. “Sur le rayonnement du radium”. In: *C. R. Acad. Sci.* 130 (1900), pp. 1178–1179.

[5] Henri Becquerel. “Sur l’analyse magnétique du rayonnement du radium et du rayonnement secondaire provoqué par ces rayons”. In: *Comptes rendus de l’Académie des Sciences* 132 (1901), p. 1289.

[6] Ernest Rutherford and Frederick Soddy. “The Cause and Nature of Radioactivity”. In: *Philosophical Magazine* 4.21 (1902), pp. 370–396. DOI: https://doi.org/10.1080/14786440209462856.

[7] Frederick Soddy. “The Radio-elements and the Periodic Law”. In: *Chemical News* 107 (1913), pp. 97–99.

[8] James Chadwick. “Intensitatsverteilung im magnetischen spektrum der beta-strahlen von radium B+C”. In: *Verhandlungen der deutschen Physikalischen Gesellschaft* 16 (1914), p. 383.

[9] James Chadwick. “The existence of a neutron”. In: *Proceedings of the Royal Society of London. Series A, Containing Papers of a Mathematical and Physical Character* 136.830 (June 1932), pp. 692–708. ISSN: 0950-1207. DOI: 10.1098/rspa.1932.0112. URL: https://royalsocietypublishing.org/doi/10.1098/rspa.1932.0112.

[10] Enrico Fermi. "Tentativo di una teoria dell'emissione dei raggi beta". In: *La Ricerca Scientifica* 4 (1933), pp. 491–495.

[11] F. Reines and C. L. Cowan. "Detection of the Free Neutrino". In: *Physical Review* 92.3 (Nov. 1953), pp. 830–831. ISSN: 0031-899X. DOI: `10.1103/PhysRev.92.830`. URL: `https://link.aps.org/doi/10.1103/PhysRev.92.830`.

[12] G. Danby et al. "Observation of high-energy neutrino reactions and the existence of two kinds of neutrinos". In: *Physical Review Letters* 9.1 (1962), pp. 36–44. ISSN: 00319007. DOI: `10.1103/PhysRevLett.9.36`.

[13] M. L. Perl et al. "Evidence for anomalous lepton production in e+-e- annihilation". In: *Physical Review Letters* 35.22 (1975), pp. 1489–1492. ISSN: 00319007. DOI: `10.1103/PhysRevLett.35.1489`.

[14] The ALEPH Collaboration et al. "Precision Electroweak Measurements on the Z Resonance". In: *Physics Reports* 427.5-6 (Sept. 2005), pp. 257–454. ISSN: 03701573. DOI: `10.1016/j.physrep.2005.12.006`. arXiv: `0509008 [hep-ex]`. URL: `https://linkinghub.elsevier.com/retrieve/pii/S0370157305005119%20http://arxiv.org/abs/hep-ex/0509008%20http://dx.doi.org/10.1016/j.physrep.2005.12.006`.

[15] Ziro Maki, Masami Nakagawa, and Shoichi Sakata. "Remarks on the Unified Model of Elementary Particles". In: *Progress of Theoretical Physics* 28.5 (Nov. 1962), pp. 870–880. ISSN: 0033-068X. DOI: `10.1143/PTP.28.870`. URL: `http://ptp.oxfordjournals.org/content/28/5/870%20https://academic.oup.com/ptp/article-lookup/doi/10.1143/PTP.28.870`.

[16] B. Pontecorvo. "Neutrino Experiments and the Problem of Conservation of Leptonic Charge". In: *Zh. Eksp. Teor. Fiz.* 53 (1967), pp. 1717–1725. DOI: `10.1016/b978-0-12-395657-6.50020-3`.

[17] V. Gribov and B. Pontecorvo. "Neutrino astronomy and lepton charge". In: *Physics Letters B* 28.7 (Jan. 1969), pp. 493–496. ISSN: 03702693. DOI: `10.1016/0370-2693(69)90525-5`. URL: `https://linkinghub.elsevier.com/retrieve/pii/0370269369905255`.

[18] E. Kh. Akhmedov and A. Yu. Smirnov. “Paradoxes of neutrino oscillations”. In: *Physics of Atomic Nuclei* 72.8 (Aug. 2009), pp. 1363–1381. ISSN: 1063-7788. DOI: 10.1134/S1063778809080122. URL: http://link.springer.com/10.1134/S1063778809080122.

[19] C. Giganti, S. Lavignac, and M. Zito. “Neutrino oscillations: The rise of the PMNS paradigm”. In: *Progress in Particle and Nuclear Physics* 98 (Jan. 2018), pp. 1–54. ISSN: 01466410. DOI: 10.1016/j.ppnp.2017.10.001. URL: https://linkinghub.elsevier.com/retrieve/pii/S014664101730087X.

[20] Bruno Pontecorvo. *Inverse beta process*. Tech. rep. 1946, PD–205.

[21] B. T. Cleveland et al. “Update on the measurement of the solar neutrino flux with the Homestake chlorine detector”. In: *Nuclear Physics B (Proceedings Supplements)* 38.1-3 (1995), pp. 47–53. ISSN: 09205632. DOI: 10.1016/0920-5632(94)00732-B.

[22] W.C. Haxton, R.G. Hamish Robertson, and Aldo M. Serenelli. “Solar Neutrinos: Status and Prospects”. In: *Annual Review of Astronomy and Astrophysics* 51.1 (Aug. 2013), pp. 21–61. ISSN: 0066-4146. DOI: 10.1146/annurev-astro-081811-125539. URL: https://www.annualreviews.org/doi/10.1146/annurev-astro-081811-125539.

[23] W. C. Haxton, R. G. Hamish Robertson, and Aldo M. Serenelli. “Solar neutrinos: Status and prospects”. In: *Annual Review of Astronomy and Astrophysics* 51.November (2013), pp. 21–61. ISSN: 00664146. DOI: 10.1146/annurev-astro-081811-125539. arXiv: 1208.5723.

[24] J. N. Abdurashitov et al. “Measurement of the solar neutrino capture rate with gallium metal. III. Results for the 2002–2007 data-taking period”. In: *Physical Review C* 80.1 (July 2009), p. 015807. ISSN: 0556-2813. DOI: 10.1103/PhysRevC.80.015807. URL: https://link.aps.org/doi/10.1103/PhysRevC.80.015807.

[25] W. Hampel et al. “GALLEX solar neutrino observations: results for GALLEX IV”. In: *Physics Letters B* 447.1-2 (Feb. 1999), pp. 127–133. ISSN: 03702693. DOI: 10.1016/S0370-2693(98)01579-2. URL: https://linkinghub.elsevier.com/retrieve/pii/S0370269398015792.

[26] M. Altmann et al. “Complete results for five years of GNO solar neutrino observations”. In: *Physics Letters B* 616.3-4 (June 2005), pp. 174–190. ISSN: 03702693. DOI: 10.1016/j.physletb.2005.04.068. URL: https://linkinghub.elsevier.com/retrieve/pii/S0370269305005149.

[27] K. Abe et al. “Constraint on the matter–antimatter symmetry-violating phase in neutrino oscillations”. In: *Nature* 580.7803 (Apr. 2020), pp. 339–344. ISSN: 0028-0836. DOI: 10.1038/s41586-020-2177-0. URL: http://www.nature.com/articles/s41586-020-2177-0.

[28] K. S. Hirata et al. “Observation of B8 solar neutrinos in the Kamiokande-II detector”. In: *Physical Review Letters* 63.1 (July 1989), pp. 16–19. ISSN: 0031-9007. DOI: 10.1103/PhysRevLett.63.16. URL: https://link.aps.org/doi/10.1103/PhysRevLett.63.16.

[29] Y. Fukuda et al. “Solar Neutrino Data Covering Solar Cycle 22”. In: *Physical Review Letters* 77.9 (Aug. 1996), pp. 1683–1686. ISSN: 0031-9007. DOI: 10.1103/PhysRevLett.77.1683. URL: https://link.aps.org/doi/10.1103/PhysRevLett.77.1683.

[30] K. Abe et al. “Solar neutrino measurements in Super-Kamiokande-IV”. In: *Physical Review D* 94.5 (Sept. 2016), p. 052010. ISSN: 2470-0010. DOI: 10.1103/PhysRevD.94.052010. URL: https://link.aps.org/doi/10.1103/PhysRevD.94.052010.

[31] B. Aharmim et al. “Combined analysis of all three phases of solar neutrino data from the Sudbury Neutrino Observatory”. In: *Physical Review C* 88.2 (Aug. 2013), p. 025501. ISSN: 0556-2813. DOI: 10.1103/PhysRevC.88.025501. URL: https://link.aps.org/doi/10.1103/PhysRevC.88.025501.

[32] Q. R. Ahmad et al. “Direct Evidence for Neutrino Flavor Transformation from Neutral-Current Interactions in the Sudbury Neutrino Observatory”. In: *Physical Review Letters* 89.1 (2002), pp. 6–11. ISSN: 10797114. DOI: 10.1103/PhysRevLett.89.011301. arXiv: 0204008 [nucl-ex].

[33] Borexino Collaboration. “First real time detection of Be7 solar neutrinos by Borexino”. In: (Aug. 2007). DOI: 10.1016/j.physletb.2007.09.054. arXiv: 0708.2251. URL: http://arxiv.org/abs/0708.2251%20http://dx.doi.org/10.1016/j.physletb.2007.09.054.

[34] Borexino Collaboration. “Neutrinos from the primary proton–proton fusion process in the Sun”. In: *Nature* 512.7515 (Aug. 2014), pp. 383–386. ISSN: 0028-0836. DOI: 10.1038/nature13702. URL: http://www.nature.com/articles/nature13702.

[35] M. Agostini et al. “Experimental evidence of neutrinos produced in the CNO fusion cycle in the Sun”. In: (June 2020). DOI: 10.1038/s41586-020-2934-0. arXiv: 2006.15115. URL: http://arxiv.org/abs/2006.15115%20http://dx.doi.org/10.1038/s41586-020-2934-0.

[36] Alessandro Strumia and Francesco Vissani. “Precise quasielastic neutrino/nucleon cross-section”. In: *Physics Letters B* 564.1-2 (July 2003), pp. 42–54. ISSN: 03702693. DOI: 10.1016/S0370-2693(03)00616-6. URL: https://linkinghub.elsevier.com/retrieve/pii/S0370269303006166.

[37] Carlo Bemporad, Giorgio Gratta, and Petr Vogel. “Reactor-based neutrino oscillation experiments”. In: *Reviews of Modern Physics* 74.2 (2002), pp. 297–328. ISSN: 00346861. DOI: 10.1103/RevModPhys.74.297.

[38] KamLAND Collaboration. “First Results from KamLAND: Evidence for Reactor Anti-Neutrino Disappearance”. In: (Dec. 2002). DOI: 10.1103/PhysRevLett.90.021802. arXiv: 0212021 [hep-ex]. URL: http://arxiv.org/abs/hep-ex/0212021%20http://dx.doi.org/10.1103/PhysRevLett.90.021802.

[39] *NuFIT 5.1 (2021)*. URL: www.nu-fit.org.

[40] A. Gando et al. “Reactor on-off antineutrino measurement with KamLAND”. In: *Physical Review D - Particles, Fields, Gravitation and Cosmology* 88.3 (2013), pp. 1–10. ISSN: 15507998. DOI: 10.1103/PhysRevD.88.033001. arXiv: 1303.4667.

[41] M. Honda et al. “Improvement of low energy atmospheric neutrino flux calculation using the JAM nuclear interaction model”. In: *Physical Review D - Particles, Fields, Gravitation and Cosmology* 83.12 (2011), pp. 1–34. ISSN: 15507998. DOI: 10.1103/PhysRevD.83.123001. arXiv: 1102.2688.

[42] The MACRO Collaboration and M. Ambrosio et Al. “Measurement of the atmospheric neutrino-induced upgoing muon flux using MACRO”. In: (July 1998). DOI: 10.1016/S0370-2693(98)00885-5. arXiv: 9807005 [hep-ex]. URL: http://arxiv.org/abs/hep-ex/9807005%20http://dx.doi.org/10.1016/S0370-2693(98)00885-5.

[43] W.W.M. Allison et al. “Measurement of the atmospheric neutrino flavour composition in Soudan 2”. In: *Physics Letters B* 391.3-4 (Jan. 1997), pp. 491–500. ISSN: 03702693. DOI: 10.1016/S0370-2693(96)01609-7. URL: https://linkinghub.elsevier.com/retrieve/pii/S0370269396016097.

[44] Y. Fukuda et al. “Evidence for oscillation of atmospheric neutrinos”. In: *Physical Review Letters* 81.8 (Aug. 1998), pp. 1562–1567. ISSN: 10797114. DOI: 10.1103/PhysRevLett.81.1562. arXiv: 9807003 [hep-ex]. URL: https://journals.aps.org/prl/abstract/10.1103/PhysRevLett.81.1562.

[45] K. Abe et al. “T2K neutrino flux prediction”. In: *Physical Review D - Particles, Fields, Gravitation and Cosmology* 87.1 (2013), pp. 1–36. ISSN: 15507998. DOI: 10.1103/PhysRevD.87.012001. arXiv: arXiv:1211.0469v3.

[46] M. H. Ahn et al. “Measurement of neutrino oscillation by the K2K experiment”. In: *Physical Review D* 74.7 (Oct. 2006), p. 072003. ISSN: 1550-7998. DOI: 10.1103/PhysRevD.74.072003. URL: https://link.aps.org/doi/10.1103/PhysRevD.74.072003.

[47] P. Adamson et al. “Measurement of Neutrino and Antineutrino Oscillations Using Beam and Atmospheric Data in MINOS”. In: *Physical Review Letters* 110.25 (June 2013), p. 251801. ISSN: 0031-9007. DOI: 10.1103/PhysRevLett.110.251801. URL: https://link.aps.org/doi/10.1103/PhysRevLett.110.251801.

[48] P. Adamson et al. “The NuMI neutrino beam”. In: *Nuclear Instruments and Methods in Physics Research Section A: Accelerators, Spectrometers, Detectors and Associated Equipment* 806 (Jan. 2016), pp. 279–306. ISSN: 01689002. DOI: 10.1016/j.nima.2015.08.063. URL: https://linkinghub.elsevier.com/retrieve/pii/S016890021501027X.

[49] Ciro Riccio. “Recent results from T2K”. In: *Proceedings of The 22nd International Workshop on Neutrinos from Accelerators — PoS(NuFact2021)*. Vol. 36. 6. Trieste, Italy: Sissa Medialab, Mar. 2022, p. 001. DOI: `10.22323/1.402.0001`. arXiv: `2105.06732`. URL: `https://pos.sissa.it/402/001`.

[50] N Agafonova et al. “Discovery of τ Neutrino Appearance in the CNGS Neutrino Beam with the OPERA Experiment”. In: *Physical Review Letters* 115.12 (2015), pp. 1–10. ISSN: 10797114. DOI: `10.1103/PhysRevLett.115.121802`. arXiv: `1507.01417`.

[51] M. Kaplon, B. Peters, and D. M. Ritson. “Emulsion Cloud-Chamber Study of a High Energy Interaction in the Cosmic Radiation”. In: *Physical Review* 85.5 (Mar. 1952), pp. 900–903. ISSN: 0031-899X. DOI: `10.1103/PhysRev.85.900`. URL: `https://link.aps.org/doi/10.1103/PhysRev.85.900`.

[52] N. Agafonova et al. “Latest results of the OPERA experiment on nu-tau appearance in the CNGS neutrino beam”. In: *Physical Review Letters* 1 (2019), pp. 1–7. ISSN: 10797114. DOI: `10.21468/SciPostPhysProc.1.028`. arXiv: `1804.04912`.

[53] M. Apollonio et al. “Search for neutrino oscillations on a long base-line at the CHOOZ nuclear power station”. In: (Jan. 2003). DOI: `10.1140/epjc/s2002-01127-9`. arXiv: `0301017 [hep-ex]`. URL: `http://arxiv.org/abs/hep-ex/0301017%20http://dx.doi.org/10.1140/epjc/s2002-01127-9`.

[54] K. Abe et al. “Indication of Electron Neutrino Appearance from an Accelerator-Produced Off-Axis Muon Neutrino Beam”. In: *Physical Review Letters* 107.4 (July 2011), p. 041801. ISSN: 0031-9007. DOI: `10.1103/PhysRevLett.107.041801`. URL: `https://link.aps.org/doi/10.1103/PhysRevLett.107.041801`.

[55] Daya Bay Collaboration et al. “A new measurement of antineutrino oscillation with the full detector configuration at Daya Bay”. In: *Physical Review Letters* 115.11 (May 2015), pp. 1–8. ISSN: 10797114. DOI: `10.1103/PhysRevLett.115.111802`. arXiv: `1505.03456`. URL: `http://arxiv.org/abs/1505.03456%20http://dx.doi.org/10.1103/PhysRevLett.115.111802`.

[56] RENO Collaboration and J. K. Ahn. "RENO: An Experiment for Neutrino Oscillation Parameter theta_13 Using Reactor Neutrinos at Yonggwang". In: (Mar. 2010). arXiv: 1003.1391. URL: http://arxiv.org/abs/1003.1391.

[57] Maury Goodman Thierry Lasserre. "Double Chooz, A Search for the Neutrino Mixing Angle theta-13". In: (June 2006). arXiv: 0606025 [hep-ex]. URL: http://arxiv.org/abs/hep-ex/0606025.

[58] Martin Freund. "Analytic Approximations for Three Neutrino Oscillation Parameters and Probabilities in Matter". In: (Mar. 2001). DOI: 10.1103/PhysRevD.64.053003. arXiv: 0103300 [hep-ph]. URL: http://arxiv.org/abs/hep-ph/0103300%20http://dx.doi.org/10.1103/PhysRevD.64.053003.

[59] Justyna Lagoda. "Latest oscillation results from T2K". In: *Proceedings of The 22nd International Workshop on Neutrinos from Accelerators — PoS(NuFact2021)*. Trieste, Italy: Sissa Medialab, Mar. 2022, p. 054. DOI: 10.22323/1.402.0054. URL: https://pos.sissa.it/402/054.

[60] M. A. Acero et al. "An Improved Measurement of Neutrino Oscillation Parameters by the NOvA Experiment". In: (2021). arXiv: 2108.08219. URL: http://arxiv.org/abs/2108.08219.

[61] Ivan Esteban et al. "The fate of hints: updated global analysis of three-flavor neutrino oscillations". In: (July 2020). DOI: 10.1007/JHEP09(2020)178. arXiv: 2007.14792. URL: http://arxiv.org/abs/2007.14792%20http://dx.doi.org/10.1007/JHEP09(2020)178.

[62] Jonathan Asaadi et al. "A New Concept for Kilotonne Scale Liquid Argon Time Projection Chambers". In: *Instruments* 4.1 (Feb. 2020), p. 6. ISSN: 2410-390X. DOI: 10.3390/instruments4010006. URL: https://www.mdpi.com/2410-390X/4/1/6.

[63] A. Abed Abud et al. "Deep underground neutrino experiment (DUNE) near detector conceptual design report". In: 5.4 (Dec. 2021). ISSN: 2410390X. DOI: 10.3390/INSTRUMENTS5040031. arXiv: 2103.13910. URL: https://arxiv.org/abs/2103.13910v1.

[64] DUNE Collaboration et al. “Snowmass Neutrino Frontier: DUNE Physics Summary”. In: (Mar. 2022). arXiv: 2203.06100. URL: http://arxiv.org/abs/2203.06100.

[65] B. Abi et al. “Long-baseline neutrino oscillation physics potential of the DUNE experiment: DUNE Collaboration”. In: *European Physical Journal C* 80.10 (2020). ISSN: 14346052. DOI: 10.1140/epjc/s10052-020-08456-z. arXiv: arXiv:2006.16043v2.

[66] JUNO Collaboration et al. “JUNO Physics and Detector”. In: (Apr. 2021). DOI: 10.1016/j.ppnp.2021.103927. arXiv: 2104.02565. URL: http://arxiv.org/abs/2104.02565%20http://dx.doi.org/10.1016/j.ppnp.2021.103927.

[67] KM3NeT Collaboration et al. “Combined sensitivity of JUNO and KM3NeT/ORCA to the neutrino mass ordering”. In: *Journal of High Energy Physics* 2022.3 (Aug. 2021), pp. 1–25. DOI: 10.1007/jhep03(2022)055. arXiv: 2108.06293. URL: http://arxiv.org/abs/2108.06293.

[68] Laura-Iuliana Munteanu. “Long-baseline neutrino oscillation sensitivities with Hyper-Kamiokande”. In: *Proceedings of The 22nd International Workshop on Neutrinos from Accelerators — PoS(NuFact2021)* Trieste, Italy: Sissa Medialab, Mar. 2022, p. 056. DOI: 10.22323/1.402.0056. URL: https://pos.sissa.it/402/056.

[69] Maddalena Antonello et al. “Muon momentum measurement in ICARUS-T600 LAr-TPC via multiple scattering in few-GeV range”. In: *Journal of Instrumentation* 12.4 (Dec. 2017). ISSN: 17480221. DOI: 10.1088/1748-0221/12/04/P04010. arXiv: 1612.07715. URL: http://arxiv.org/abs/1612.07715%20http://dx.doi.org/10.1088/1748-0221/12/04/P04010.

[70] P. A. Zyla et al. *Review of particle physics*. Aug. 2020. DOI: 10.1093/ptep/ptaa104. URL: https://academic.oup.com/ptep/article/2020/8/083C01/5891211.

[71] Hans Bichsel. *A method to improve tracking and particle identification in TPCs and silicon detectors*. 2006. DOI: 10.1016/j.nima.2006.03.009.

[72] Kevin Ingles. *Muon Energy Loss in Liquid Argon*. Tech. rep.

[73] M. Miyajima et al. “Average energy expended per ion pair in liquid argon”. In: *Physical Review A* 9.3 (Mar. 1974), pp. 1438–1443. ISSN: 10502947. DOI: 10.1103/PhysRevA.9.1438. URL: https://journals.aps.org/pra/abstract/10.1103/PhysRevA.9.1438.

[74] Ö Şahin et al. “Penning transfer in argon-based gas mixtures”. In: *Journal of Instrumentation* (2010). ISSN: 17480221. DOI: 10.1088/1748-0221/5/05/P05002.

[75] S Amoruso et al. “Study of electron recombination in liquid argon with the ICARUS TPC”. In: *Nuclear Instruments and Methods in Physics Research, Section A: Accelerators, Spectrometers, Detectors and Associated Equipment* 523.3 (2004), pp. 275–286. ISSN: 01689002. DOI: 10.1016/j.nima.2003.11.423.

[76] I. Gil-Botella. “Scintillation light detection in the 6-m drift length ProtoDUNE Dual Phase liquid argon TPC”. In: *Journal of Instrumentation* 17.1 (2022), p. 31. ISSN: 17480221. DOI: 10.1088/1748-0221/17/01/C01012.

[77] S. Palestini and F. Resnati. “Space charge in liquid argon time-projection chambers: a review of analytical and numerical models, and mitigation methods”. In: *Journal of Instrumentation* (2021). ISSN: 17480221. DOI: 10.1088/1748-0221/16/01/P01028.

[78] B. Abi et al. “First results on ProtoDUNE-SP liquid argon time projection chamber performance from a beam test at the CERN Neutrino Platform”. In: *Journal of Instrumentation* 15.12 (Dec. 2020), P12004. ISSN: 1748-0221. DOI: 10.1088/1748-0221/15/12/P12004. arXiv: 2007.06722. URL: https://iopscience.iop.org/article/10.1088/1748-0221/15/12/P12004%20https://iopscience.iop.org/article/10.1088/1748-0221/15/12/P12004/meta.

[79] Anna Peisert and Fabio Sauli. “Drift and diffusion of electrons in gases: a compilation (with an introduction to the use of computing programs)”. In: *European organization for nuclear research* July (1984). DOI: 10.5170/CERN-1984-008.

[80] A Delbart et al. *TIME PROJECTION CHAMBERS AND ASSOCIATED ELECTRONICS*. Apr. 2017. URL: https://indico.in2p3.fr/event/14279/contributions/17563/attachments/14563/

17841/MeV%7B%5C_%7DTPC%7B%5C_%7DWorkshop%7B%5C_%7Ddelbart%7B%5C_%7Dapril12%7B%5C_%7D2107.pdf.

[81] A. Herzenberg. “Attachment of slow electrons to oxygen molecules”. In: *The Journal of Chemical Physics* 51.11 (Sept. 1969), pp. 4942–4950. ISSN: 00219606. DOI: 10.1063/1.1671887. URL: https://aip.scitation.org/doi/abs/10.1063/1.1671887.

[82] Alan Hahn et al. “The LBNE 35 Ton Prototype Cryostat”. In: *2014 IEEE Nuclear Science Symposium and Medical Imaging Conference, NSS/MIC 2014*. Institute of Electrical and Electronics Engineers Inc., Mar. 2016. ISBN: 9781479960972. DOI: 10.1109/NSSMIC.2014.7431158.

[83] M. Antonello et al. “Experimental observation of an extremely high electron lifetime with the ICARUS-T600 LAr-TPC”. In: *Journal of Instrumentation* 9.12 (Sept. 2014). ISSN: 17480221. DOI: 10.1088/1748-0221/9/12/P12006. arXiv: 1409.5592. URL: http://arxiv.org/abs/1409.5592%20http://dx.doi.org/10.1088/1748-0221/9/12/P12006.

[84] M. Huk, P. Igo-Kemenes, and A. Wagner. “Electron attachment to oxygen, water, and methanol, in various drift chamber gas mixtures”. In: *Nuclear Inst. and Methods in Physics Research, A* 267.1 (Apr. 1988), pp. 107–119. ISSN: 01689002. DOI: 10.1016/0168-9002(88)90635-3.

[85] Maxim Titov and Leszek Ropelewski. “Micro-pattern gaseous detector technologies and RD51 collaboration”. In: *Modern Physics Letters A* 28.13 (May 2013). ISSN: 02177323. DOI: 10.1142/S0217732313400221.

[86] V Peskov and P Fonte. “Research on discharges in micropattern and small gap gaseous detectors”. In: (2009). arXiv: 0911.0463. URL: http://arxiv.org/abs/0911.0463.

[87] ALICE Collaboration. *Upgrade of the ALICE Time Projection Chamber*. Tech. rep. CERN-LHCC-2013-020 / ALICE-TDR-016, 2014. URL: https://cds.cern.ch/record/1622286/files/?ln=fr.

[88] C. Cantini et al. “Long-term operation of a double phase LAr LEM Time Projection Chamber with a simplified anode and extraction-grid design”. In: *Journal of Instrumentation* (2014). ISSN: 17480221. DOI: 10.1088/1748-0221/9/03/P03017. arXiv: 1312.6487.

[89] C. Cantini et al. “Performance study of the effective gain of the double phase liquid Argon LEM time projection chamber”. In: *Journal of Instrumentation* (2015). ISSN: 17480221. DOI: 10.1088/1748-0221/10/03/P03017.

[90] D. Attié. “TPC review”. In: *Nuclear Instruments and Methods in Physics Research, Section A: Accelerators, Spectrometers, Detectors and Associated Equipment* 598.1 (2009), pp. 89–93. ISSN: 01689002. DOI: 10.1016/j.nima.2008.08.114.

[91] DUNE Collaboration et al. “The DUNE Far Detector Interim Design Report, Volume 3: Dual-Phase Module”. In: 3 (2018). arXiv: 1807.10340. URL: http://arxiv.org/abs/1807.10340.

[92] A. Curioni et al. “A regenerable filter for liquid argon purification”. In: *Nuclear Instruments and Methods in Physics Research, Section A: Accelerators, Spectrometers, Detectors and Associated Equipment* 605.3 (Mar. 2009), pp. 306–311. ISSN: 01689002. DOI: 10.1016/j.nima.2009.04.020. arXiv: 0903.2066v1. URL: http://arxiv.org/abs/0903.2066%20http://dx.doi.org/10.1016/j.nima.2009.04.020.

[93] C. Cuesta. “Photon detection system for ProtoDUNE dual phase”. In: *Journal of Instrumentation* 12.12 (Dec. 2017). ISSN: 17480221. DOI: 10.1088/1748-0221/12/12/C12048.

[94] A Rubbia. “Experiments For CP-Violation: A Giant Liquid Argon Scintillation, Cerenkov And Charge Imaging Experiment ?” In: (2004). arXiv: 0402110 [hep-ph]. URL: http://arxiv.org/abs/hep-ph/0402110.

[95] B. Aimard et al. “A 4 tonne demonstrator for large-scale dual-phase liquid argon time projection chambers”. In: *Journal of Instrumentation* 13.11 (June 2018). ISSN: 17480221. DOI: 10.1088/1748-0221/13/11/P11003. arXiv: 1806.03317. URL: http://arxiv.org/abs/1806.03317%20http://dx.doi.org/10.1088/1748-0221/13/11/P11003.

[96] Guillaume Eurin, PierreMazzucato Granger, and Edoardo Mazzucato. *ProtoDUNE-DP: Summary of CRP sparking rate analysis*. Tech. rep. 2020.

[97] Ruth Pordes and Erica Snider. “The Liquid Argon software toolkit (LArSoft): Goals, status and plan”. In: *Proceedings of Science*. Vol. Part F1285. Proceedings of Science (PoS), 2016. DOI: 10.22323/1.282.0182.

[98] Etienne Chardonnet. “Study of the response of the dual-phase liquid argon TPC, ProtoDUNE Dual-Phase at CERN, and the development of tools improving the detector performances for the DUNE experiment at Fermilab.” PhD thesis. 2021.

[99] W. Walkowiak. “Drift velocity of free electrons in liquid argon”. In: *Nuclear Instruments and Methods in Physics Research, Section A: Accelerators, Spectrometers, Detectors and Associated Equipment* 449.1 (July 2000), pp. 288–294. ISSN: 01689002. DOI: `10.1016/S0168-9002(99)01301-7`.

[100] D. W. Swan. “Electron attachment processes in liquid argon containing oxygen or nitrogen impurity”. In: *Proceedings of the Physical Society* 82.1 (July 1963), pp. 74–84. ISSN: 03701328. DOI: `10.1088/0370-1328/82/1/310`. URL: `https://iopscience.iop.org/article/10.1088/0370-1328/82/1/310%20https://iopscience.iop.org/article/10.1088/0370-1328/82/1/310/meta`.

[101] A. Bettini et al. “A study of the factors affecting the electron lifetime in ultra-pure liquid argon”. In: *Nuclear Inst. and Methods in Physics Research, A* (1991). ISSN: 01689002. DOI: `10.1016/0168-9002(91)90532-U`.

[102] The Wa105 Collaboration et al. “Performance study of a 3×1×1 m3dual phase liquid Argon Time Projection Chamber exposed to cosmic rays”. In: *Journal of Instrumentation* 16.8 (2021). ISSN: 17480221. DOI: `10.1088/1748-0221/16/08/P08063`.

[103] Philippe (CEA/Irfu) Cotte. “Le projet WA105 : un prototype de Chambre à Projection Temporelle à Argon Liquide Diphasique utilisant des détecteurs LEMs”. PhD thesis. 2019.

[104] Paolo Franzini and Matthew Moulson. *The physics of DAΦNE and KLOE*. 2006. DOI: `10.1146/annurev.nucl.56.080805.140459`. URL: `www.annualreviews.org`.

[105] David S. Ayres. “Detectors for the MINOS long-baseline neutrino oscillation experiment”. In: *Nuclear Physics B - Proceedings Supplements* (1998). ISSN: 09205632. DOI: `10.1016/S0920-5632(97)00533-1`.

[106] L. Aliaga et al. “Design, calibration, and performance of the MINERvA detector”. In: *Nuclear Instruments and Methods in Physics Research, Section A: Accelerators, Spectrometers, Detectors and Associated Equipment* (2014). ISSN: 01689002. DOI: 10.1016/j.nima.2013.12.053. arXiv: 1305.5199.

[107] T2K Collaboration. “T2K ND280 Conceptual Design Report”. In: *Internal Report* (2005).

[108] A. Blondel et al. “A fully active fine grained detector with three readout views”. In: (July 2017). DOI: 10.1088/1748-0221/13/02/P02006. arXiv: 1707.01785. URL: http://arxiv.org/abs/1707.01785%20http://dx.doi.org/10.1088/1748-0221/13/02/P02006.

[109] L. Munteanu et al. “New method for an improved antineutrino energy reconstruction with charged-current interactions in next-generation detectors”. In: *Physical Review D* 101.9 (2020), pp. 1–11. ISSN: 24700029. DOI: 10.1103/PhysRevD.101.092003. arXiv: 1912.01511.

[110] Guang Yang. “Neutron beam test with 3D-projection scintillator tracker prototypes for long-baseline neutrino oscillation experiments”. In: *Proceedings of Science* 390 (2021), pp. 0–2. ISSN: 18248039. DOI: 10.22323/1.390.0221.

[111] A. M. Ankowski et al. “Missing energy and the measurement of the CP -violating phase in neutrino oscillations”. In: *Physical Review D - Particles, Fields, Gravitation and Cosmology* 92.9 (Nov. 2015), p. 091301. ISSN: 15502368. DOI: 10.1103/PhysRevD.92.091301. arXiv: 1507.08561. URL: https://journals.aps.org/prd/abstract/10.1103/PhysRevD.92.091301.

[112] David Rivera. *Neutron cross section measurement in ProtoDUNE-SP*. 2021. URL: https://docs.dunescience.org/cgi-bin/private/RetrieveFile?docid=24163%7B%5C&%7Dfilename=Plenary%7B%5C_%7Dtalk%7B%5C_%7Dneutron%7B%5C_%7Dxs%7B%5C_%7Drivera%7B%5C_%7Ddavid%7B%5C_%7Dv3.pdf%7B%5C&%7Dversion=2.

[113] Maria Martinez-Casales. *Cross section model tuning and multiplicity studies in NOvA*. 2019.

[114] K. Abe et al. “First combined measurement of the muon neutrino and antineutrino charged-current cross section without pions in the final state at T2K”. In: *Physical Review D* 101.11

(June 2020), p. 112001. ISSN: 24700029. DOI: 10.1103/PhysRevD.101.112001. arXiv: 2002.09323. URL: https://journals.aps.org/prd/abstract/10.1103/PhysRevD.101.112001.

[115] S. Dolan et al. “Sensitivity of the Upgraded T2K Near Detector to constrain neutrino and anti-neutrino interactions with no mesons in the final state by exploiting nucleon-lepton correlations”. In: (Aug. 2021). arXiv: 2108.11779. URL: https://arxiv.org/abs/2108.11779v2%20http://arxiv.org/abs/2108.11779.

[116] K. Abe et al. “T2K ND280 Upgrade – Technical Design Report”. In: (Jan. 2019). arXiv: 1901.03750. URL: https://arxiv.org/abs/1901.03750v2%20http://arxiv.org/abs/1901.03750.

[117] J Fleury et al. “Petiroc and Citiroc: front-end ASICs for SiPM read-out and ToF applications”. In: *Journal of Instrumentation* 9.01 (Jan. 2014), pp. C01049–C01049. ISSN: 1748-0221. DOI: 10.1088/1748-0221/9/01/C01049. URL: https://iopscience.iop.org/article/10.1088/1748-0221/9/01/C01049.

[118] Konrad Briggl et al. “Characterization results and first applications of KLauS - An ASIC for SiPM charge and fast discrimination readout”. In: *IEEE Nuclear Science Symposium Conference Record*. 2013. ISBN: 9781479905348. DOI: 10.1109/NSSMIC.2013.6829778.

[119] A. Blondel et al. “The SuperFGD Prototype charged particle beam tests”. In: *Journal of Instrumentation* (2020). ISSN: 17480221. DOI: 10.1088/1748-0221/15/12/P12003. arXiv: 2008.08861.

[120] M. S. Dixit et al. “Position sensing from charge dispersion in micro-pattern gas detectors with a resistive anode”. In: *Nuclear Instruments and Methods in Physics Research, Section A: Accelerators, Spectrometers, Detectors and Associated Equipment* 518.3 (2004), pp. 721–727. ISSN: 01689002. DOI: 10.1016/j.nima.2003.09.051. arXiv: 0307152 [physics].

[121] D. Attié et al. “Performances of a resistive Micromegas module for the Time Projection Chambers of the T2K Near Detector upgrade”. In: *Nuclear Instruments and Methods in Physics Research, Section A: Accelerators, Spectrometers, Detectors and Associated Equipment*

957 (Mar. 2020), p. 163286. ISSN: 01689002. DOI: 10.1016/j.nima.2019.163286. arXiv: 1907.07060. URL: https://doi.org/10.1016/j.nima.2019.163286.

[122] D. Attié et al. "Characterization of resistive Micromegas detectors for the upgrade of the T2K Near Detector Time Projection Chambers". In: *Nuclear Instruments and Methods in Physics Research, Section A: Accelerators, Spectrometers, Detectors and Associated Equipment* 1025 (Feb. 2022), p. 166109. ISSN: 01689002. DOI: 10.1016/j.nima.2021.166109. arXiv: 2106.12634. URL: https://doi.org/10.1016/j.nima.2021.166109.

[123] P. A. Amaudruz et al. "The T2K fine-grained detectors". In: *Nuclear Instruments and Methods in Physics Research, Section A: Accelerators, Spectrometers, Detectors and Associated Equipment* 696 (2012), pp. 1–31. ISSN: 01689002. DOI: 10.1016/j.nima.2012.08.020. arXiv: 1204.3666.

[124] T2K Collaboration. "Document for ND280 review Contents". In: (2006).

[125] M. Tanabashi et al. *Review of Particle Physics*. 2018. DOI: 10.1103/PhysRevD.98.030001.

[126] R. L. Gluckstern. "Uncertainties in track momentum and direction, due to multiple scattering and measurement errors". In: *Nuclear Instruments and Methods* 24.C (1963), pp. 381–389. ISSN: 0029554X. DOI: 10.1016/0029-554X(63)90347-1. URL: https://ui.adsabs.harvard.edu/abs/1963NucIM..24..381G/abstract.

[127] N Abgrall et al. "Time projection chambers for the T2K near detectors". In: *Nuclear Instruments and Methods in Physics Research, Section A: Accelerators, Spectrometers, Detectors and Associated Equipment* 637.1 (2011), pp. 25–46. ISSN: 01689002. DOI: 10.1016/j.nima.2011.02.036. arXiv: 1012.0865.

[128] Simone Dell'Agnello. *Assembly, Alignment and Magnetic Measurements of KLOE at DAPHNE*. Tech. rep. CERN, 1999. URL: https://indico.cern.ch/event/412705/attachments/842125/1171270/190499.pdf.

[129] R. Gran et al. "Neutrino-nucleus quasi-elastic and 2p2h interactions up to 10 GeV". In: *Physical Review D - Particles, Fields, Gravitation and Cosmology* (2013). ISSN: 15502368. DOI: 10.1103/PhysRevD.88.113007. arXiv: 1307.8105.